Une variation sur les propriétés magiques de modèles de Boltzmann pour l'écoulement microscopique et macroscopique

Irina Ginzburg

Une variation sur les propriétés magiques de modèles de Boltzmann pour l'écoulement microscopique et macroscopique

Thèse d'Habilitation à diriger des recherches
de l'Université Pierre et Marie Curie

Spécialité : Sciences pour l'ingénieur

présentée par

Irina Ginzburg

Unité de Recherche "Hydrosystèmes et Bioprocédés" (HBAN)
Cemagref, groupement d'Antony

Soutenance le 16 Janvier 2009 devant le jury composé de:

François Dubois	Rapporteur
Pierre Sagaut	Examinateur
Christian Saguez	Examinateur
Jonathan Summers	Rapporteur
Jonas Tölke	Rapporteur
Stéphane Zaleski	Examinateur

A Vladimir Markovich Entov

REMERCIEMENTS

Ce mémoire est une synthèse de mes travaux sur la théorie et les applications des équations de Boltzmann sur réseau (Lattice Boltzmann Equation ou LBE), afin d'obtenir l'Habilitation à diriger des recherches de l'Université Pierre et Marie Curie. Je dédie cette thèse à la mémoire du Professeur Vladimir Markovich Entov, qui a fait de moi "une vraie chercheuse".

Directrice scientifique du Cemagref, Claude Schmidt-Lainé m'a encouragée à préparer ce mémoire; les Professeurs François Dubois, Jonathan Summers et Jonas Tölke ont gentiment accepté la lourde tâche de lecture ; les Professeurs Pierre Sagaut, Stéphane Zaleski et Christian Saguez m'ont fait l'honneur de compléter le jury: je les en remercie tous vivement. Je tiens à remercier tout particulièrement Jonas Tölke et Stéphane Zaleski pour les occasions diverses mais toujours très agréables de nos collaborations et leurs confiance en mes résultats. J'espère que nous entamerons encore de nouvelles aventures scientifiques !

Un travail passionnant au Laboratoire "Applications Scientifiques du Calcul Intensif (ASCI)" du CNRS a suivi mon Doctorat. J'ai beaucoup appris sur la nature de méthodes de Boltzmann grâce à l'intuition et compréhension de Professeurs Pierre Lallemand et Dominique d'Humières, deux des fondateurs de cette approche. Leurs absence de préjugés a su libérer ma pensée et m'a appris la créativité "rigoureuse". Mon travail ultérieur n'aurait pas été possible sans leurs soutien constant. Je suis très redevable envers Dominique pour avoir pris au sérieux mes paramètres magiques qu'il a su éclairer de sa brillante lumière.

Mon séjour de trois ans à l'Institut d'Applications Numériques à l'Université de Stuttgart fut très enrichissante grâce à la vaste expérience du Professeur Gabriel Wittum, et de son équipe, dans les méthodes d'éléments et de volumes finis, les solveurs multi-grilles et programmation moderne. Je n'oublierais jamais la beauté du code "UG" et sa versatilité pour les grilles non-structurées en mouvement ! Je remercie Gabriel de m'avoir accueillie à un moment difficile.

J'ai pu revenir ensuite au monde de méthodes "cinétiques" au Fraunhofer Institut für Techno- und Wirtschaftsmathematik (ITWM) à Kaiserslautern. Je garde de très précieux souvenirs des années à ITWM. Dr. Franz-Josef Pfreundt, je me souviendrai toujours de votre respect pour mon travail et de mon premier écran plasma, encore rare à l'époque et tellement nécessaire pour moi. Une phrase ne suffira pas pour exprimer ma reconnaissance à Peter Klein pour notre travail commun sur le code ParPac que j'utilise encore aujourd'hui. Konrad Steiner et Margarite Beck, un très grand merci pour votre énorme support, numérique et humain.

Évidemment encore, l'activité d'un chercheur requiert un cadre pour s'épanouir. J'ai beaucoup apprécie l'esprit du travail et l'atmosphère scientifique de notre équipe de "drainage" au Cemagref, qui m'a permis d'élargir les modèles de Boltz-

mann à l'échelle de petits bassins versants et de commencer enfin à soulever certains secrets magiques de cette méthode, les idées ayant attendues longtemps depuis ASCI... Je tiens aussi à remercier Cyril Kao et Yves Nédélec, pour leurs explications hydrologiques et hydrauliques, et leur patience à mon égard. J'espère mener ces travaux à bout. Un grand merci à Françis Goeta pour m'avoir aidée survivre avec la "partition magique" sous Windows lors de mon arrivé au Cemagref. Je remercie Pierrick Givone et Gilles Bonnet qui m'ont installés les PC parallèles sous mon système d'exploitation préféré.

Je remercie sincèrement toutes les autres personnes dont les suggestions, les conseils et la confiance m'ont aidée: mes collègues en Allemagne, Christian Wagner et Peter Bastian à Stuttgart, Joachim Linn, Doris Reinel-Bitzer, Carsten Lojewski, Dirk Kehrwald, Michael Junk, Andreas Wiegmann, Arnulf Latz, Dimitar Stoyanov, Oleg Iliev, Serge Antonov et Julia Orlik à Kaiserslautern; mes collègues de LBE, L. Giraud à Orsay, Li-Shi Luo en Virginie, Frederick Verhaeghe à Leuven, Manfred Krafczyk à Braunschweig, Abdulmajeed A. Mohamad à Calgary; les post-doctorants Jean Philippe Carlier et Eloise Beaugendre, avec qui j'ai eu l'occasion de collaborer au Cemagref; Michel Poirson avec qui nous avons partagé l'expérience douloureuse du débogage de code, quelle que soit la méthode; et mes collègues d'aujourd'hui: Valérie Pot à l'INRA, les chercheurs du projet "Méthode", et plus particulièrement, Alexandre Ern à l'ENPC et Olivier Delestre à l'Université d'Orléan, et mes collègues de HBAN: Cécile Loumagne, Sophie Morin, Julien Tournebize et Bernard Vincent pour leur accueil quotidien.

Il ne me reste qu'à remercier mes lecteurs. Mes remerciements vont à ceux qui ont pu se débrouiller dans nos longs papiers et m'envoyer leurs questions. La premiers lectrice de la partie française de ce manuscrit a été ma fille Julia Skalova: "many thanks" dans ta langue préférée ! Ses corrections ont été raffinées par Dominique d'Humières, Yves Nédélec et Bénédicte Augeard et complétées avec les remarques de Dirk Kehrwald et mes étudiants "virtuels", Hassan Hammou et Alexander Kuzmin. Je les remercie tous chaleureusement.

Enfin, je remercie mes parents, ma famille et mes chiens pour pouvoir supporter ma mauvaise humeur quand la théorie et le numérique divergent, donc souvent...

Contents

Part I

Synthèse des travaux

CURRICULUM-VITAE

Irina Ginzburg ingénieur de recherche.
Née le 07/11/1966, à Moscou, Russie.
Adresse Cemagref, Antony, Regional Centre, HBAN,
Parc de Tourvoie, BP 44, 92163 Antony cedex, France.
Tél.: 33-1-40966060. Fax: 33-1-40966270.
email: irina.ginzburg@cemagref.fr.

Diplômes

1994 **Docteur en Mécanique de l'Université Paris 6.**

1988 **Ingénieur-mathématicien de l'Académie du gaz et du pétrole de Moscou.**
Spécialité: Mathématiques appliquées.

Parcours professionel

1983 – 1988 Assistant scientifique à l'Académie du gaz et du pétrole et à l'Insitut du transport du pétrole, Moscou.

1988 – 1991 Chercheur à l'Institut des Problèmes en Mécanique, Académie des Sciences de Russie.
Directeur de recherche: Professeur V. M. Entov.

1991 – 1994 Préparation d'une thèse doctorale au CNRS.
Laboratoire d'Aérothermique, Meudon, France.
Sujet: Les problèmes de conditions aux limites dans les méthodes des gaz sur réseaux à plusieurs phases.
Directeur: Professeur P. M. Adler.
Mention: très honorable avec les félicitations du jury.
Contrats: CNRS/IFP, BRITE/EURAM.

1994 –1995 Chercheur associé au CNRS.
Laboratoire Applications Scientifiques du Calcul Intensif, Orsay, France.
Travail post-doctoral en collaboration avec Professeurs P. Lallemand et D. d'Humières (LPS/ENS).

1995 –1999 Poste contractuel de recherche.
Institut Applications Numériques III (ICA III), Université de Stuttgart, Allemagne.
Directeur de recherche: Professeur G. Wittum.
Projet SFB 412, programme Franco-Allemand CNRS-DFG de recherche en mécanique des fluides.

1999 – 2002 Poste contractuel/permanent de recherche.
Fraunhofer Institut für Techno- und Wirtschaftsmathematik (ITWM), Kaiserslautern, Allemagne.
Contrats: ParPac, MAGMA GmbH, Mann+Hummel GmbH, Neumag, HegerGuss, Pfleider.
Projets de recherche: DFG, BNBF.

9/2002- **Ingénieur de recherche en analyse numérique.**
Institut de recherche pour l'ingénierie de l'agriculture et de l'environnement, Cemagref, Antony, France.
Projets de recherche:
Arc DYNAS ("Dynamique des nappes souterraines"),
Germano-Swisse FIMOTUM ("FIrst-principle-based MOdeling of Transport in Unsaturated Porous Media"),
Projet ANR multidisciplinaire METHODE ("Modélisation de l'Ecoulement sur une Topographie avec des Hétérogénéités Orientées et des Différences d'Echelle"),
Projet innovant INRA "Modélisation spatialisée de la dynamique des pesticides dans la porosité du sol".

Co-encadrement des doctorants et post-doctorants.

1. Co-encadrement de la thèse de Laurent Giraud, intitulée: "Fluides visco-élastiques par la méthode de Boltzmann sur réseau.", Université Paris VI, 1997, avec une contribution de 80% environ pendant mon année post-doctorale à ASCI, Orsay. Le travail a porté sur l'analyse de la localisation des parois solides par réflexions simples dans les méthodes LBE et l'estimation de la précision des perméabilités obtenues (le Chapitre 4 de la thèse). Les solutions pour les paramètres libres du modèle LBE ainsi déduites permettent les calculs efficaces dans un milieux poreux. Ils ont permis par la suite la paramétrisation des modèles LBE par les nombres physiques sans dimensions et par les paramètres cinétiques libres, Réf. [23].

2. Co-encadrement de la thèse de Dirk Kehrwald, intitulée: "Numerical analysis of Immiscible Lattice BGK", Universität Kaiserslautern, 2002, avec une contribution de 30% environ, lors de mon travail à ITWM sur les modèles diphasiques avec grand rapports de viscosités et modèles à surface libre. L'analyse mathématique des opérateurs d'advection d'une phase par rapport à l'autre, et anti-diffusifs à l'interface, a été développée (Chapitres 2-4 de la thèse).

3. Co-encadrement du travail de Jean Philippe Carlier lors de son séjour post-doctoral au Cemagref en 2004, avec une contribution de 70% environ. Ce travail porte sur l'extension d'une approche dite "milieu effectif" pour remplacer un système de drains situés dans le sol par un milieu hétérogène anisotrope de perméabilité équivalente, afin d'éviter la discretisation individuelle de chaque drain lors de la modélisation du petit bassin versant. Nous avons aussi élargi les solutions analytiques de l'équation de Richards pour l'infiltration dans un sol variablement saturé. Ces résultats sont décrits dans les références [19,26] et rapportés à la Conférence Internationale "Computational Methods in Water Resources", 2004.

4. Co-encadrement du travail de la post-doctorante Eloise Beaugendre (laboratoire Cermics de l'ENPC) dans le cadre de l'ARC DYNAS, l'initiative de coopération de l'INRIA 2004, avec co-encadrement de 30% environ. Deux modèles numériques, celui par LBE en 3D et celui par éléments finis en 2D, ont été développés pour étudier les mécanismes de genèse de l'écoulement surfacique lors de pluies intenses, sur la base de l'équation de Richards. Les résultats ont été présentés dans les références [16,27] et rapportés à International DYNAS Workshop, à Rocquencourt, 2004.

5. Co-encadrement du travail de Frederik Verhaeghe lors de sa thèse à Katholeike Universiteit of Leuven, Belgium, 2005-2007, avec une contribution de 30% environ. Ce travail a porté sur la construction de conditions précises de Dirichlet aux parois arbitraires, pour la vitesse, la pression et leur combinaison. Ces travaux sont décrits dans les références [20,21].

6. Co-encadrement du travail de la post-doctorante Nadia Elyeznasni (2007-2008) et du doctorant Hassan Hammou (2008-) en stage de 6 mois (2ème année en Faculté des sciences, Université Mohammed I Oujda-Maroc, thèse intitulée "Modélisation numérique d'écoulements de l'eau et de transport des polluants dans les milieux poreux variablement saturés", avec une contribution de 40% environ pour encadrement.

7. Co-encadrement du travail de doctorant Alexandre Kuzmin (Université de Calgary, Canada) sur l'étude de stabilité de LBE pour AADE, depuis début 2008.

<u>Activités d'intérêt collectif</u>

1. Cours sur la théorie de LBE (6h) pour les doctorants à l'Université de Calgary (Canada), 29.10-6.11, 2008, invitation de Professeur A. A. Mohamad.

2. Organisation avec Professeur F. Dubois d'un atelier scientifique internationale: "Schéma scientifique sur réseau: méthodes et applications", au Cemagref, 5 décembre 2008.

3. Organisation d'un colloque le 18/19 avril 2002 à Kaiserslautern, réunissant l'ensemble de la communauté allemande travaillant sur les méthodes de Boltzmann sur réseau (10 équipes), dans le cadre du projet DFG.

4. Organisation d'un séminaire annuel à Kaiserslautern pendant l'année 2002 réunissant des étudiants de deuxième cycle, doctorants (D. Kehrwald, M. Rheinländer) et professeurs (D. d'Humières, M. Junk, A. Klar), autour de la théorie et applications de LBE.

5. Participation à des comités de lecture: J. Comp. Physics, J. Stat. Physics, Physics of Fluids, Advances in Water Resource, Water Res. Research, Computations & Fluids, J. Comp. and Applied Math., Phys. Rev. E, Phys. Letters, Int. J. Comp. Fluid Dynamics, Progress in Comput. Fluid Dynamics, Computers and Math. with Applications, Computations and Vizualization in Science (CVS), Applied Math. Modeling, J. Heat & Mass Transport.

6. Participation au comité d'organisation de Conférence Internationale "Méthodes Mésoscopiques en Engineering et Science", ICMMES, autour du comité de lecture pour les actes de ce congres.

Communications à des congrès, symposiums, séminaires (2000-2008)

- N. Elyeznasni, V. Pot, P. Benoit, I. Ginzburg, F. Sellami, and A. Genty, "Fate of pesticides in soil porosity using Lattice Boltzmann and X-ray computed tomography", Int. Conf. Eurosoil, Vienne, August, 2008.

- N. Elyeznasni, V. Pot, I. Ginzburg and A. Genty, "Transport modeling of pesticides in soil porosity using Lattice Boltzmann simulations and 3D maps provided from X-ray computed tomography", Int. Conference CMWR, San Francisco, July 2008.

- D. d'Humières and I. Ginzburg, "Some analytical results about the stability of the Lattice Boltzmann Model", Int. Conf. ICMMES, Hampton, Virginia, July 2006.

- I. Ginzburg et D. d'Humières, "Quelques éléments de la méthode de Boltzmann sur reseaux pour les problémes hydrodynamiques et d'advection-diffusion en milieu anisotrope", Journée Thématique sur Milieux Poreux, Saclay, Mars 2007.

- I. Ginzburg and D. d'Humières, "Some elements of Lattice Boltzmann modeling for hydrodynamic and anisotropic advection-diffusion problems", Seminair MoMAS, Paris, CNAM, December 2006, et Seminair de l'Institut des Problèmes en Mécanique, Moscow, November 2006.
- I. Ginzburg, "Lattice Boltzmann modeling with discontinuous collision components focused on Richard's equation in heterogeneous anisotropc aquifers", Int. Workshop "Multi-Scale Modeling of Transport in Porous Media", Monte Verita, April 2006.
- I. Ginzburg, "Lattice Boltzmann formulations for modeling variably saturated flow in anisotropic heterogeneous soils", Int. Workshop of DYNAS Project, Rocquencourt, December 2004, and Int. Workshop of FIMOTUM Project, Stuttgart, April 2005.
- I. Ginzburg, "Variably saturated flow described by Lattice Boltzmann advection and anisotropic dispersion equations", Int. Conference ICMMES, Braunschweig, July 2004.
- I. Ginzburg, J.-P. Carlier, C. Kao, Lattice Boltzmann approach to Richards' Equation. Int. Conference CMWR, North Caroline, June 2004.
- E. Beaugendre, A. Ern, I. Ginzburg, C. Kao, "Finite element modeling of variably saturated flows in hillslopes with shallow water tables", Int. Conference CMWR, North Caroline, June 2004.
- D. d'Humières and I. Ginzburg, "Boundary condition analysis: multi-reflection schemes", Int. DFG Workshop "Lattice Boltzmann methods", Kaiserslautern, April, 2002.
- I. Ginzburg and D. d'Humières, "LB calculations with static and moving boundaries", Int. DFG Workshop "Lattice Boltzmann methods", Kaiserslautern, April, 2002.
- I. Ginzburg, "Lattice Boltzmann method with free interface for filling process in casting", Int. ECMI Glass Days, Kaiserslautern, October, 2001.
- I. Ginzburg, "A free-surface Lattice Boltzmann method for Newtonian and Bingham fluids", Int. Conference DSFD, Cargesse, July 2001.
- I. Ginzburg, "Introduction of upwind and free boundary into lattice Boltzmann method", Int. Gamm Workshop, Braunschweig, December, 2000.
- I. Ginzburg, "Efficient Lattice Boltzmann Method for porous media", Int. Workshop on Porous Media, Lambrecht, June, 2000.

RÉSUME DES PUBLICATIONS

1. Application de la théorie des groupes de renormalisation et construction de solutions auto-semblables, exactes ou asymptotiques, pour des problèmes non linéaires de transfert de soluté par convection-diffusion en présence d'adsorption irréversible: Réfs. [1,2,3,24].

2. Extension des méthodes "Volumes de Fluides" et "Multigrille" pour décrire et résoudre les équations de Navier-Stokes à deux phases avec une discrétisation alternée (pression et vitesses définies en des points différents) sur un maillage nonstructuré, aligné avec l'interface et localement raffiné. Simulations de l'ascension d'une bulle pour un large spectre de paramètres physiques: Réfs. [7,8].

3. Développement d'une approche mathématique et élaboration de nouveaux algorithmes pour les méthodes cinétiques permettant de localiser de façon précise (du deuxième et troisième ordre) les parois solides et obstacles mobiles de forme arbitraire en restant sur une grille régulière: Réfs. [4,6,12,29].

4. Extension des modèles LBE pour l'écoulement à deux phases avec forts effets capillaires en présence de grands rapports de viscosité cinématique. Construction de l'opérateur de collision à l'interface entre deux fluides. Calcul des perméabilités relatives dans des micro-structures: Réfs. [5,17,29].

5. Construction de modèles LBE à temps de la relaxation multiples pour les problèmes hydrodynamiques. Ces modèles permettent d'augmenter la précision, l'efficacité et la stabilité de l'approche de Boltzmann et incorporent naturellement les modèles de turbulence simples: Réfs. [9,25].

6. Introduction du modèle LBE avec surface libre pour un fluide newtonien. Application à la simulation et visualisation des différentes étapes du remplissage de moules par des métaux liquides: Réfs. [10,30].

7. Extension du modèle LBE avec surface libre pour un fluide visco-élastique de Bingham: Réfs. [11].

8. Extension des modèles LBE pour décrire l'équation d'advection-diffusion non-linéaire, avec anisotropie arbitraire du tenseur de diffusion. Introduction du modèle à deux temps de relaxation (TRT) valable pour l'écoulement et le transport. Estimation de la diffusion numérique et des erreurs d'ordres élevés, en termes de paramètres libres d'équilibre et de collision. Développement des conditions aux limites adéquates: Réfs. [13,14].

9. Extension de l'approche LBE pour résoudre l'équation de Richards (2D et 3D), décrivant l'écoulement de l'eau dans un sol variablement saturé, homogène ou stratifié, isotrope ou anisotrope. Les critères de stabilité ont été établis dans les régimes les plus difficiles (sol secs, interface saturé/insaturé) et pour les principaux modèles de sols: Réfs. [15,26].

10. Développement d'une approche mathématique pour remplacer un système de drains situé dans le sol par un milieu hétérogène anisotrope de perméabilité équivalente. L'évolution temporelle des débits et des hauteurs de nappe est en bonne accord avec les calculs directs d'un système de drains: Réf. [19].

11. Étude d'affleurement de la nappe lors des épisodes de pluie avec la méthode de discretisation de l'équation de Richards par les méthodes des éléments finies: Réfs. [16,27].

12. Construction de solutions analytiques, analyse des conditions implicites et construction d'une couplage explicite pour un cas tridimensionnel dans lequel l'anisotropie du sol stratifié est hétérogène et le tenseur de perméabilité n'est plus diagonal: Réfs. [17,18].

13. Introduction de classes infinies (ayant une précision équivalente) de conditions aux limites avec la pour la vitesse, la pression et leur combinaison et extension pour des géométries complexes. Analyse de l'exactitude de leur paramétrisation, du support des invariants alternés et de l'unicité des solutions obtenues. Le modèle TRT avec des conditions aux limites adaptées s'avère être très efficace pour la plupart des problèmes (et leurs couplages) traités par LBE dans les milieux poreux: Réfs. [20,21].

14. Adaptation d'une schéma LBE à deux temps de relaxation pour le modèle de Brinkman permettant le couplage simple d'un milieu poreux et de l'écoulement libre. Construction de solutions exactes du schéma LBE-Brinkman pour l'écoulement simple. La solution exacte des coefficients de la série infinie de Chapman-Enskog pour les solutions stationnaires: Réf. [22].

15. Dérivation et analyse des équations de récurrence discrétisées équivalentes aux schémas de Boltzmann, sous forme d'opérateurs de différences-finies directionnels. Construction de solutions généralisées stationnaires et paramétrisation cohérente (physique) de la série infinie de termes de troncature par les combinaisons libres des valeurs propres de la matrice de collision. Cette paramétrisation fait complètement disparaître un artefact numérique connu de schémas LBE, à savoir: une dépendance non-physique de la perméabilité du milieu poreux avec la viscosité cinématique du fluide modélisé: Réf. [23].

PUBLICATIONS

1. I. S. Ginzburg, V. M. Entov. Investigation of the dynamics of a thin impurity plug in a seepage flow. in Numerical methods of solving seepage problems, *Dynamics of Multiphase Media*, Izd. Inst. Hydrodinamiki SO Akad. Nauk SSSR, Novosibirsk, pp. 76–81, 1989.

2. I. S. Ginzburg, V. M. Entov, E. V. Teodorovich. Renormalization group method for the problem of convective diffusion with irreversible sorption. *J. Appl. Maths. Mechs.*, 56(1):59, 1992.

3. I. S. Ginzburg, V. M. Entov. Thin slug dynamics with allowance for diffusion and sorbtion irreversibility. *Fluid Dynamics*, 28:373, 1993.

4. I. Ginzbourg, P. M. Adler. Boundary flow condition analysis for the three-dimensional lattice Bolzmann model. *J. Phys. II France*, 4:191–214, 1994.

5. I. Ginzbourg, P. M. Adler. Surface Tension Models with Different Viscosities. *Transport in Porous Media*, 20:37-75, 1995.

6. I. Ginzbourg, D. d'Humières. Local Second-Order Boundary method for Lattice Boltzmann models. *J. Stat. Phys.*, 84(5/6):927–971, 1996.

7. I. Ginzburg, G. Wittum. Multigrid Methods for Two Phase Flows. in *Numerical Flow Simulation*, Notes on Numerical Fluid Mechanics, E. H. Hirschel ed., Vieweg, 66:144-167, 1998.

8. I. Ginzburg, G. Wittum. Two-Phase Flows on interface refined grid modelled with VOF, staggered finite volumes, and spline interpolants. *J. of Comp. Phys.*, 166:302–335, 2001.

9. D. d'Humières, I. Ginzburg, M. Krafczyk, P. Lallemand, L.-S. Luo. Multiple-relaxation-time lattice Boltzmann models in three dimensions. *Phil. Trans. R. Soc. Lond. A*, 360:437–451, 2002.

10. I. Ginzburg, K. Steiner. A free-surface Lattice Boltzmann method for modelling the fillling of expanding cavities by Bingham Fluids. *Phil. Trans. R. Soc. Lond. A*, 360:453-466, 2002.

11. I. Ginzburg, K. Steiner. Lattice Boltzmann model for free-surface flow and its application to filling process in casting. *J. Comp. Phys.*, 185:61–99, 2003.

12. I. Ginzburg, D. d'Humières. Multi-reflection boundary conditions for lattice Boltzmann models. *Phys. Rev. E*, 68:066614-1–30, 2003.

13. I. Ginzburg. Equilibrium-type and Link-type Lattice Boltzmann models for generic advection and anisotropic-dispersion equation. *Adv. Water Resour.*, 28:1171–1195, 2005.

14. I. Ginzburg. Generic boundary conditions for Lattice Boltzmann models and their application to advection and anisotropic-dispersion equations. *Adv. Water Resour.*, 28:1196–1216, 2005.

15. I. Ginzburg. Variably saturated flow described with the anisotropic Lattice Boltzmann methods. *J. Comp. & Fluids*, 25: 831–848, 2006.

16. E. Beaugendre, A. Ern, T. Esclaffer, E. Gaume, I. Ginzburg, C. Kao. A seepage face model for the interaction of shallow water tables with the ground surface: Application of the obstacle-type method. *J. of Hydrology*, 1-2:258-273, 2006.

17. I. Ginzburg. Lattice Boltzmann modeling with discontinuous collision components. Hydrodynamic and advection-diffusion equations. *J. Stat. Phys.*, 126:157–203, 2007.

18. I. Ginzburg, D. d'Humières. Lattice Boltzmann and analytical modeling of flow processes in anisotropic and heterogeneous stratified aquifers. *Adv. Water Resour.*, 30, 2202-2234, 2007

19. J.-P. Carlier, C. Kao, I. Ginzburg. Field-scale modeling of sub-surface tile-drained soils using an effective medium approach. *J. of Hydrology*, 341:105-115, 2007.

20. I. Ginzburg, F. Verhaeghe, D. d'Humières. Two-relaxation-time Lattice Boltzmann scheme: about parametrization, velocity, pressure and mixed boundary conditions. *Commun. Comput. Physics*, 3(2), 427-478, 2008.

21. I. Ginzburg, F. Verhaeghe, D. d'Humières. Study of simple hydrodynamic solutions with the two-relaxation-times Lattice Boltzmann scheme. *Commun. Comput. Physics*, 3(3):519–581, 2008.

22. I. Ginzburg. Consistent Lattice Boltzmann schemes for the Brikman model of porous flow and infinite Chapman-Enskog expansion. *Physical Review E*, 77, 066704-1-12, 2008.

23. D. d'Humières, I. Ginzburg. Viscosity independent numerical errors for Lattice Boltzmann models:from recurrence equations to "magic" collision numbers. *à paraître dans Computers & Mathematics with Applications*, 2008.

Actes de congrès

24. V. M. Entov, I. S. Ginzburg, E. V. Teodorovich. Irreversible adsorption and desorption effect in propagation of thin slugs in chemicals, *Proc. 6th European Symposium of Improved Oil Recovery*, Stavanger, Norvège, 1, Book II, pp. 619–628, 1991.

25. I. Ginzbourg. Introduction of upwind and free boundary into lattice Boltzmann method. *in Discrete Modelling and Discrete Algorithms in Continuum Mechanics*, eds. T. Sonar & I. Thomas, 97–109, Logos-Verlag, Berlin, 2001.

26. I. Ginzburg, J.-P. Carlier, C. Kao. Lattice Boltzmann approach to Richards' Equation. *in Computational methods in Water resources*, Ed. by C. T. Miller, 583-597, Elsevier, 2004.

27. E. Beaugendre, A. Ern, I. Ginzburg, C. Kao. Finite element modeling of variably saturated flows in hillslopes with shallow water tables. *in Computational methods in Water resources*, Ed. by C. T. Miller, 1427-1429, Elsevier, 2004.

Mémoires

28. I. Ginzbourg. L'analyse mathématique et numérique des problèmes de transfert de soluté dans les milieux poreux saturés, Diplôme de fin d'études de l'académie du Gaz et du Pétrole de Moscou, (en russe), 1988.

29. I. Ginzbourg. Les problèmes des conditions aux limites dans les méthodes de gaz sur réseau à plusierues phases, Thèse de doctorat de l'Université Paris VI, 1994.

Brevet

30. I. Ginzburg. Europäische Patentanmeldung, 01112579.6, 23.05.2001. Lattice-Boltzmann-Verfahren zur Berechnung von Strömungsvorgängen mit freien Oberflächen.

PROJETS ET PERSPECTIVES.

Les modèles de l'équation de Boltzmann développés permettent de modéliser l'écoulement microscopique à un ou deux phases dans des conduites ou en milieux poreux, l'écoulement macroscopique dans un sol variablement saturé, le couplage de l'écoulement libre avec l'écoulement macroscopique ainsi que le transport de soluté dans un champ donné de vitesse et avec les fonctions prédéfinies de diffusion. On peut prévoir l'intérêt de la modélisation des phénomènes couplés (transport + écoulement) dans le cadre du même formalisme. Ce type de couplage devient très répandu pour étudier, par exemple, l'influence des propriétés du milieu poreux (anisotropie, fractures, interaction avec la matière solide) sur le transport. Le travail sur le couplage de l'écoulement avec le transport dans le régime temporel nécessite de déterminer les critères de stabilité (linéaires ou non-linéaires) du schéma LBE pour la modélisation des phénomènes physiques en jeu et d'établir ensuite des stratégies efficaces pour le choix des paramètres numériques, hydrodynamiques ainsi que cinétiques. Mes projets de recherche à court terme se focalisent alors sur trois axes principaux:

1. application des méthodes développées pour l'écoulement et le transport des polluants et leur couplage;

2. développment de nouveaux schémas LBE;

3. analyse de l'équation de Boltzmann et interprétation de cette méthode en termes de discrétisation directe (différences ou volumes finis).

Projet innovant de l'INRA (2007-2008):

"Modélisation spatialisée de la dynamique des pesticides dans la porosité du sol".

Pendant les deux dernières années, j'ai travaillé en collaboration avec Valérie Pot, chercheur à l'INRA Grignon, UMR AgroParisTech EGC, Equipe "SOL", l'une des responsables de ce projet. Le projet s'intéresse à modéliser le transport et le devenir des pesticides dans les sols à une échelle microscopique, en prenant en compte la description des hétérogénéités bio-physico-chimiques du sol. Les hétérogénéités du sol peuvent fortement influencer le transport, la rétention/libération et la biodégradation des pesticides. Le modèle de Boltzmann a été choisi pour décrire l'écoulement saturé et le transport dans un espace poral, extrait d'images 3D d'échantillons de sol non perturbé, obtenues par mesures tomographiques à haute résolution. On envisage de superposer aux frontières de cet espace poral

des sites de rétention/libération des pesticides et de résidence de micro-organismes du sol capables de dégrader les pesticides. L'accessibilité des pesticides à ces sites lors de leur transport et l'impact des hétérogénéités de ce processus sur les paramètres physiques (comme le coefficient de la dispersion hydrodynamique) sont les premières questions à quantifier.

La mise en place d'un logiciel basé sur le modèle LBE à deux temps de relaxation (modèle TRT) pour le transport et l'écoulement de Stokes/Navier-Stokes en deux et trois dimensions a constitué la première phase du travail numérique, assistée par la post-doctorante Nadia Elyeznasni. Dans le même temps, les sites réactifs d'un espace poral d'échantillons de sol sélectionnés ont été identifiés. Ensuite, la validation et l'extension du modèle numérique ont été initiées par Hassan Hammou, doctorant de l'Université Mohammed I à Oujda (Maroc), qui effectue un stage de six mois à l'INRA. Compte tenu des objectifs communs du projet et de la thèse, le travail s'est focalisé d'abord sur la validation du modèle TRT de transport. La dispersion de Taylor dans l'écoulement parabolique établie dans un canal infini a été premièrement examiné. La rétention d'un traceur à la paroi solide a ensuite été introduite dans le modèle de transport. Une augmentation du coefficient de la dispersion hydrodynamique (un effet de "retard") a été constatée. Les résultats ont montré un bon accord avec les prédictions théoriques à condition que les artefacts numériques, déjà relevés par notre analyse théorique, aient été atténués. Les trois facteurs principaux sont: (i) le tenseur de diffusion numérique (compensé à l'aide des corrections d'équilibre): (ii) l'impact des coefficients de diffusion élevés sur la précision (neutralisé par le choix adéquat de la valeur propre libre); (iii) l'artefact numérique des conditions aux limites en utilisant le rebond pour l'ADE. En effet, le rebond contraint le flux parallèle, en plus de la condition souhaitée d'imperméabilité à la paroi (flux normal égal à zéro). Pour réduire cet effet, nous avons remplacé (uniquement pour le transport) le modèle $d2Q9$ avec les vitesses diagonales par les modèle minimaux ($d2Q5$ et $d3Q7$). Notons que ces modèles sont incapables d'éliminer les composantes transversales de la diffusion numérique en multi-dimensions. Il nous reste à comprendre pourquoi les corrections introduites pour le rebond, efficaces dans le champ de vitesse uniforme, ne sont pas satisfaisantes dans ces simulations. Il faudra aussi d'estimer les différents sources possibles d'erreurs numériques, et notamment la diffusion numérique, et la précision du mécanisme d'adsorption. Les premiers résultats ont été présentés aux Conférences Internationales, CMWR 2008 et Eurosoil 2008, et illustrés sur Figures 1 et 2.

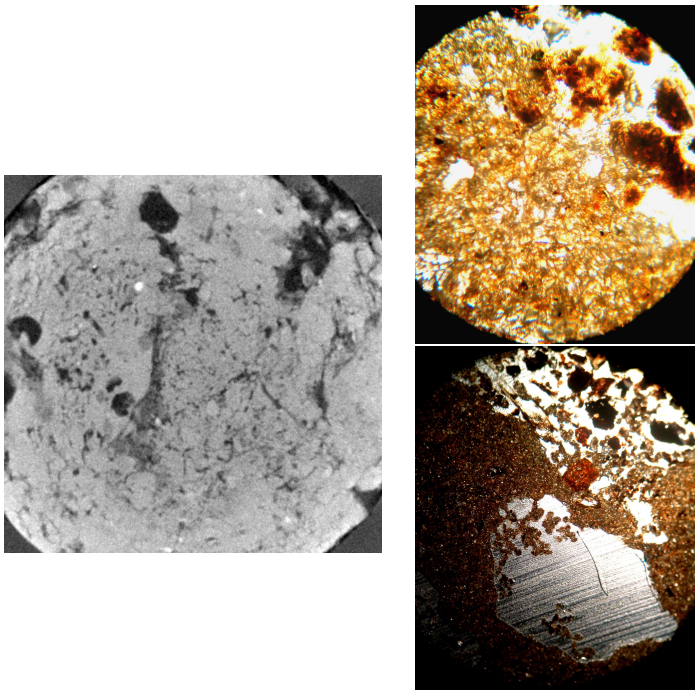

Figure 1: Image tomographique d'un milieu poreux (à gauche) et deux lames minces microscopiques obtenues à partir de cette image (à droite), Eurosoil 2008.

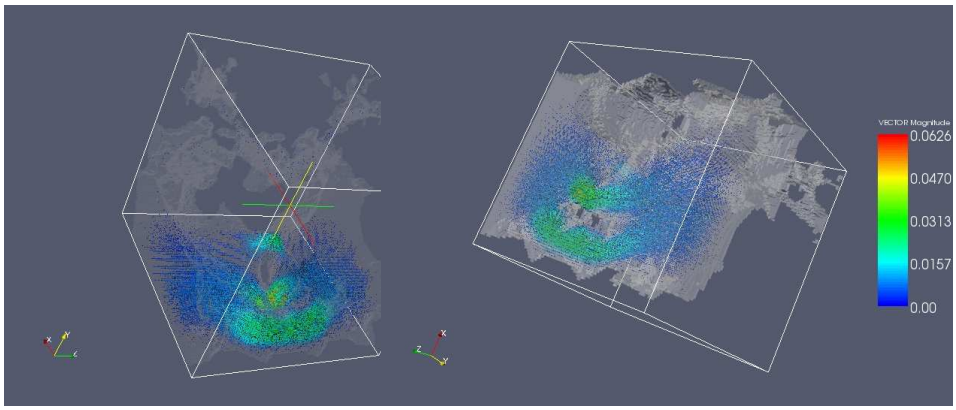

Figure 2: Ecoulement de Stokes dans la porosité du sol (les couleurs sont données en unité du réseau), Eurosoil 2008.

Dans la suite, on souhaite pouvoir transporter les pesticides à l'intérieur d'un milieu poral variablement saturé. En effet, le mécanisme physique du transport par l'interface n'est pas encore suffisamment maîtrisé. La modélisation de l'écoulement microscopique non saturé nécessitera un développement du modèle diphasique particulièrement fiable aux interfaces. Nous pouvons commencer par l'étude des modèles LBE existants, avancés au cours de ces dernières années, avec les outils de l'analyse présentés dans ce mémoire.

Thèse de H. Hammou (2007-)

"Modélisation numérique d'écoulements de l'eau et de transport des polluants dans les milieux poreux variablement saturés".

La méthode de Boltzmann a été choisie pour résoudre l'équation de Richards pour l'écoulement à l'échelle macroscopique et l'ADE pour le transport, par son directeur de thèse au Maroc, Professeur M. Boulerhcha, et je l'encadre pour la compréhension, le développement et l'implantation de la méthode. En parallèle avec le travail sur l'équation du transport, H. Hammou développe le code pour résoudre l'équation de Richards. Dans un premièr temps, il modélise l'infiltration dans une colonne de sol et valide ces résultats par des tests analytiques, déjà établis lors de mon développement de LBE pour ce problème. Des comparaisons avec les solutions obtenues avec le code HYDRUS, couramment utilisé dans ce domaine, sont envisagées également. Cette étude pourrait raffiner les éléments de connaissances acquis sur la stabilité et la précision des techniques LBE et aider à mieux maîtriser les conditions d'application pour des simulations à grande échelle. D'après mes études, ce problème fortement non-linéaire nécessite la variation des paramètres caractéristiques du système LBE au cours des calculs. Signalons que l'adaptation dynamique des paramètres internes aux critères de stabilité est encore très peu abordée (voire inexistante) dans LBE, car elle nécessite un traitement particulier de la partie hors équilibre. Cependant, les premiers résultats d'un changement du pas du temps lors d'un processus d'imbibition dans un sol initialement sec sont prometteurs.

Dans le cadre de son travail de thèse, H. Hammou envisage l'application du modèle LBE développé pour reproduire les résultats expérimentaux sur le transport d'un traceur NaCl dans un sol remanié et non-remanié, acquis lors de son stage dans l'équipe du Professeur M. Vanclooster à l'Université Catholique de Louvain. Ce type de modélisation pose deux questions : est-ce que l'équation d'advection-diffusion est capable de décrire les courbes d'élution observées ? et quelle est la dépendance des coefficients de transport (notamment de la dispersivité) avec la distribution de la teneur en eau ? Il faudra donc déterminer si les courbes d'élution observées manifestent une dissymétrie prononcée et anticiper les difficultés potentielles. Compte tenu de la multitude d'approches existantes dans la littérature, quel est le bon modèle à utiliser ? Par ailleurs, cette question est déjà abordée par mon collègue de l'équipe, Julien Tournebize, et un travail commun est envisagé sur cette thématique avec Alain Cartalade (CEA/Saclay). De plus, il sera intéressant d'examiner si on peut élargir le modèle de Boltzmann pour prendre en compte, si nécessaire, les effets "anormaux" de la diffusion. Quand ces étapes seront franchies, on pourra réfléchir au choix de la stratégie pour la modélisation du transport dans l'écoulement transitoire ainsi que dans un sol hétérogène et/ou anisotrope.

Projet ANR multidisciplinaire METHODE (2008-2011):

"Modélisation de l'Ecoulement sur une Topographie avec des Hétérogénéités Orientées et des Différences d'Echelle".

L'objectif de ce projet est d'étudier, de comprendre et de modéliser le ruissellement sur un sol en pente en présence de sillons agricoles. Des travaux empiriques ont montré que le ruissellement suit la direction de la pente topographique lors de forts écoulements, alors qu'il prend la direction des sillons pour des faibles écoulements. La rugosité orientée (sillons parallèles entre eux) joue également un rôle non négligeable sur le stockage d'eau. Il est nécessaire de comprendre les principaux mécanismes régissant ces écoulements pour améliorer l'aménagement des bassins versants. Afin de rester dans un cadre opérationnel, les effets des détails les plus fins de la topographie doivent être intégrés dans un modèle hydrologique global. L'idée de ce projet est d'essayer de prendre en compte l'orientation de l'écoulement à l'aide de modifications adéquates des lois de frottement, sans tenir compte de manière explicite de la présence de sillons. Ces corrections anisotropes vont probablement dépendre des paramètres significatifs physiques et géométriques (nombre physique sans dimension, orientation de la rugosité par rapport à la pente principale, dimension et périodicité des sillons, etc.). Des interactions étroites entre les études expérimentales et numériques sont en cours de développement afin de quantifier ces effets.

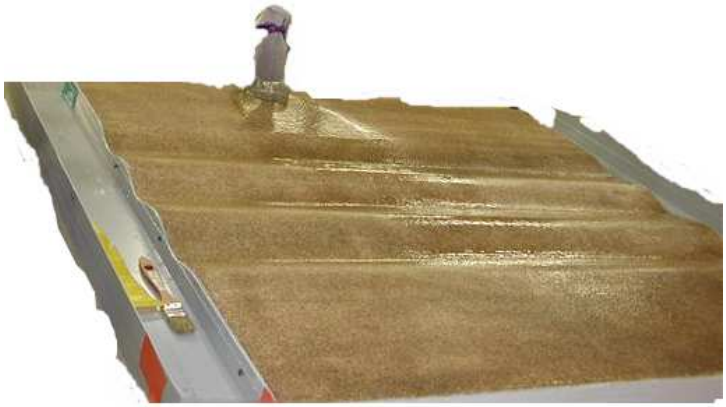

Figure 3: Ecoulement sur une maquette de laboratoire avec une source d'eau ponctuelle (collaboration avec l'équpe de l'INRA d'Orléans).

Les travaux expérimentaux de description physique des écoulements dans les sillons sont menés par F. Darboux (l'INRA d'Orléans) en collaboration avec le

LTHE à Grenoble et mes collègues du Cemagref, Y. Nédélec et B. Augeard. Ainsi, un premier travail préparatoire a été mené par l'INRA et le Cemagref avec le stage de fin d'étude de Stéphanie Becque : "Étude expérimentale et numérique de l'influence d'une rugosité orientée sur le ruissellement". Dans ce cadre, un protocole de mesure de la hauteur des lames d'eau de quelques millimètres d'épaisseur ainsi que de son champ de vitesse a été défini et appliqué au cas d'une maquette composée de trois sillons sinusoïdaux et alimentée par une source d'eau ponctuelle (Fig. 3). Les données acquises en régime permanent permettent d'observer la répartition de l'eau entre les différents sillons. Ces données ont été exploitées par une première approche monodimentionnelle pour estimer les coefficients effectifs de frottement pour différentes configurations expérimentales, et sélectionner ensuite la loi de frottement la plus adaptée. En outre, ces données seront d'une grande utilité pour la modélisation numérique.

Deux approches de la modélisation numérique sont envisagées dans le projet. L'approche principale consiste à décrire le ruissellement sur la surface comportant les sillons à l'aide des équations de Barré Saint-Venant à deux dimensions. Ces équations, aussi appelées "shallow water equations", décrivent traditionnellement l'écoulement profond sur une pente relativement faible (rivières, fossés) en hydraulique à surface libre. Les équations de Saint-Venant expriment la conservation de masse en termes d'épaisseur d'eau et déterminent une vitesse horizontale moyennée suivant la hauteur de l'écoulement. Elles sont déduites soit des équations d'Euler, soit des équations de Navier-Stokes (en prenant en comptes les termes visqueux) avec l'hypothèse de faible vitesse verticale, ce qui conduit à l'approximation hydrostatique pour la pression. Les méthodes de résolution de ces équations sont déjà étudiées par la plupart d'équipes participantes au projet. Ainsi, le schéma de différences-finies de MacCormack a été adapté à l'écoulement surfacique dans les travaux de l'équipe de M. Esteves (LTHE, Grenoble), le solveur de Riemann basé sur la discretisation de volumes finis est étudié dans l'équipe de l'Université d'Orléans (S. Cordier, F. James et O. Délestre) ; les méthodes cinétiques avec différents degrés d'approximation sont développées dans les travaux des chercheurs de l'INRIA et l'EDF (Marie-Odile Bristeau, E. Audusse et J. Sainte-Marie). De plus, une approche des éléments finis de type Galerkin discontinus est développée par l'équipe du Cermics à l'ENPC (A. Ern et P. Tassi). Cependant, quelle que soit la méthode de résolution, des difficultés croissantes sont à prévoir quand la hauteur d'eau s'approche de zéro (sol sec), qui représente la limite formelle de l'approche moyennée.

La deuxième approche envisage le traitement du ruissellement dans les trois dimensions par l'équation de Navier-Stokes à interface libre, afin de valider les limites d'application des équations moyennées. Il s'agit donc de la résolution de l'écoulement vertical à échelle millimétrique dans chaque sillon discrétisé sur une

grille de calculs, et de la description métrique dans le plan de sillons. L'approche avec l'équation de Navier-Stokes vient compléter celle de Saint-Venant pour deux raisons. D'une part, il est souvent plus facile de confronter deux approches numériques aux mêmes scénarios que d'obtenir un système numérique équivalent au système expérimental, surtout pour des conditions aux limites. D'autre part, les méthodes de la résolution de l'équation de Navier-Stokes à l'interface libre sont assez fragiles et elles doivent être adaptées au phénomène considéré: décrire un grand spectre de comportement d'une lame mince du fluide à grand nombres de Reynolds et pour des nombres de Froude très variables, avec les passages automatiques entre les régimes fluviaux et torrentiels dans des géométries complexes. Ce type de modélisation est encore très peu abordé et nécessite une réflexion préliminaire pour le choix de cas tests pertinents et une comparaison de deux approches.

Mon travail prévu dans le cadre de ce projet est de contribuer à ce deuxième volet de modélisation en collaboration avec l'équipe de Cermics (A. Ern, P. Tassi, S. Piperno et T. Lelièvre). Leur approche est basée sur la formulation Lagrangienne de l'équation de Navier-Stokes avec une discretisation d'un mouvement de front sur une grille adaptive. La méthode alternative Eulerienne sur une grille statique, basée sur l'équation de Boltzmann sur réseau, a été développée lors de mon travail à l'ITWM à Kaiserslautern (1999-2002) et appliquée à la modélisation du remplissage de cavités confinées. Le travail sur le ruissellement suppose (i) d'élargir le modèle et le code existant pour des géométries non-confinées et l'échelle spatiale très dispersée, (ii) d'introduire de nouvelles conditions aux limites, (iii) d'incorporer les termes de sources ponctuelles et, (iv), éventuellement, d'amener la pluie sur la surface libre. Afin aborder cette tâche, j'ai commencé par l'extension du code de Navier-Stokes (2D ou 3D) aux équations de Saint-Venant (1D ou 2D), avec deux objectifs en vue. Le premier est de pouvoir comparer facilement les solutions de deux approximations à l'interface libre ayant une discretisation similaire (voir équivalente). L'autre objectif est le couplage de ces deux approches en régime transitoire qui intéresse par ailleurs notre équipe, notamment pour les études sur la compréhension de la mise en charge de l'écoulement dans les drains souterrains. Ensuite, nous pourrions envisager un couplage du ruissellement avec l'écoulement souterrain et le transport de soluté (pesticides) associé à ces deux écoulements. Les modules de transport et de la résolution de l'équation de Richards dans un sol variablement saturé ont déjà été développés pendant mon travail au Cemagref et ils sont implantés dans le même code, toujours dans la formalisme mathématique et numérique uniforme présenté par les modèles de Boltzmann.

En effet, les modèles de Boltzmann pour la résolution des équations de Saint-Venant en 2D existent déjà dans la littérature: la masse de fluide est reliée alors à la hauteur d'eau qui devient une quantité conservée. Dans le même temps, la dépendance de la pression avec la quantité conservée, qui est linéaire pour

l'équation de Navier-Stokes, devient cubique pour la description hydrostatique en présence de l'interface libre. Les équations de Saint-Venant s'écrivent naturellement dans le cadre de modèles de Boltzmann pour des fluides compressibles. Les modifications nécessaires, n'étant pas compliquées pour un code, soulèvent néanmoins les problèmes importants d'analyse numérique. Signalons le problème de stabilité de la méthode avec une fonction non-linéaire d'équilibre et une force de frottement fortement non-linéaire, et, plus généralement, une modélisation dans un régime très peu visqueux, qui est la limite la plus sévère de stabilité du modèle. De plus, la topographie apparaît dans les équations de Saint-Venant à travers le terme de force extérieure. Il est montré que la description non-locale de cette force (qui n'est pas naturelle pour le modèle de Boltzmann) est nécessaire afin d'obtenir une description cohérente de l'état hydrostatique du système, quand la pente de la topographie n'est plus constante. Cette description, connue comme "well balanced schemes" par les méthodes directes, a été construite lors de mon travail sur le projet et validée par des calculs numériques. Les premières simulations ont montré qu'il faudrait également comprendre comment imposer les conditions aux limites, différentes pour beaucoup de cas dans les régimes fluviaux et torrentiels, dans les modèles de Boltzmann. En effet leur reconstruction à l'aide de caractéristiques du système est encore très peu étudiée pour ces méthodes. On peut s'attendre à ce que l'un des problèmes difficiles sera alors d'assurer l'unicité des solutions obtenues.

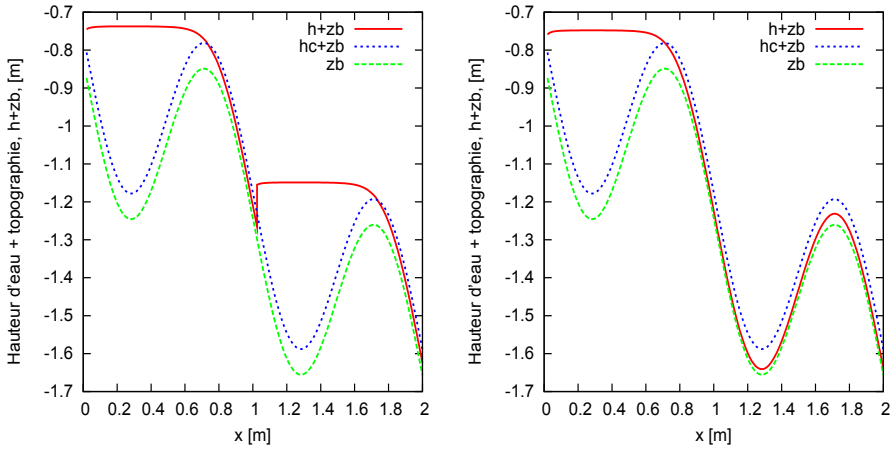

Figure 4: Hauteur d'eau dans l'écoulement mixte (fluvial/torrentiel) paralléle à la pente, avec (à gauche) et sans (à droite) ressaut hydraulique.

La possibilité de contrôler méthodiquement les solutions par des conditions aux limites et par des conditions du ressaut a été examinée à l'aide d'un code de résolution de l'équation de Sant-Venant en 1D, dans le régime stationnaire. Ce

code, inspiré par certaines idées d'un logiciel hydraulique (Canal 9) utilisé au Cemagref, a été développé en collaboration avec mon collègue Y. Nédélec. Le nouveau code permet d'imposer une topographie arbitraire et une variation libre des conditions aux limites, ainsi que des stratégies possibles pour le couplage des régimes fluviaux et torrentiels. On provoque alors facilement les différents scénarios d'une distribution de l'eau dans la suite de sillons. Dans la gamme des paramètres étudiés expérimentalement, les résultats (avec le "petit" ressaut illustrées sur la Fig. 4) s'accordent bien avec les solutions de Olivier Delestre et P. Tasso. Nous avons également pu établir les solutions analytiques de ce modèle pour une hauteur de l'écoulement selon la pente constante à un débit donné, disponibles pour les deux lois de frottement, de Darcy-Weisbach et de Manning-Strickler. On peut supposer que certains éléments caractéristiques d'un comportement de l'écoulement dans un système présentant des sillons sinusoïdaux peuvent être déduits d'un système approché, où les sillons sont représentés par des morceaux linéaires, montant ou descendant. Cette piste reste encore à explorer.

Ainsi, il me semble intéressant de pouvoir poursuivre les deux approches proposées, celle basée sur les équations de Sant-Venant et celle basée sur les équations de Navier-Stokes. A l'heure actuelle il n'est pas clair encore si les régimes souhaités d'écoulement sont abordables par ces approches dans le cadre traditionnel des modèles de Boltzmann. Il est possible que des éléments supplémentaires de stabilisation, comme le modèle de turbulence simple ou d'équilibre entropique, garantissant la positivité de la hauteur d'eau, soient nécessaires. Les solutions de référence (analytiques, numériques et expérimentales) seront exploitées pour valider les simulations directes pour les deux approches à l'interface libre.

AVANT-PROPOS

Étudiante à l'académie du Gaz et du Pétrole de Moscou, j'ai commencé à participer aux travaux de recherche menés dans le département de Physique et d'Hydrodynamique. Vladimir Markovich Entov, chercheur à l'Institut de Mécanique de Moscou, m'a fait découvrir le passionnant univers des méthodes numériques. Mon mémoire de fin d'études en 1988 et les deux années suivantes de recherche sous sa direction ont porté sur l'analyse mathématique des problèmes de transfert de soluté dans les milieux poreux saturés. Trois mécanismes physiques ont été mis en jeu : le transfert d'un additif par convection, la dispersion par diffusion, et l'adsorption à la surface du squelette d'un milieu poreux. L'irréversibilité de l'adsorption rend ce problème non-linéaire et à frontières libres. L'originalité de ce travail a été la construction de solutions auto-semblables exactes ou asymptotiques pour la distribution de la concentration des solutés dans un écoulement unidimensionnel ou axisymétrique. Nous avons pu démontrer l'équivalence des exposants de renormalisation avec les exposants d'auto-similarité pour ces solutions. Vladimir Markovich Entov a suivi mon travail et m'a encouragée de loin jusqu'aux derniers mois de sa vie. Je lui dédie ce mémoire qui résume mes travaux sur les modèles de Boltzmann sur réseau.

En effet, à l'exception de quelques années (1996-1999) pendant lesquelles j'ai travaillé avec Gabriel Wittum à l'Institut pour Applications Numériques à Stuttgart (où il s'agissait de développer de nouvelles discrétisations mixtes élément-finis/-volumes finis et des solveurs multi-grilles associés pour la modélisation d'écoulements diphasiques sur un maillage adaptatif aux interfaces), mon travail principal s'est focalisé sur les méthodes de Boltzmann sur réseau. Ces recherches ont commencé pendant ma thèse dans l'équipe de Pierre Adler au CNRS à Meudon. Au début des années quatre-vingt-dix, le schéma numérique dit équation de Boltzmann sur réseau (Lattice Boltzmann Equation ou LBE) venait juste d'être dérivé des modèles de gaz sur réseau. Aujourd'hui ces modèles constituent des approches indépendantes et originales de modélisation en mécanique des fluides. Les avantages de cette méthode se manifestent dans sa versatilité pour un changement d'échelle (nano, micro ou macro) et de dimension du problème, ce qui la classe parmi les méthodes dites mésoscopiques.

Ce schéma décrit des lois de conservation : masse, quantité de mouvement, énergie, ou leurs combinaisons, par des règles de collisions très simples sur les nœuds d'un réseau régulier. La collision détermine la relaxation de la partie des populations hors équilibre, l'équilibre etant une fonction prédite des quantités conservées. Le passage de LBE vers les équations macroscopiques aux dérivées partielles se fait naturellement par le développement d'une perturbation de la partie hors équilibre sous la forme d'une série infinie de gradients des quantités con-

servées. Cette méthode, introduite par Chapman (1916) et Enskog (1917) dans leurs travaux sur la théorie cinétique de gaz, obtient les coefficients de transport de la solution de l'équation de Boltzmann décrivant le fluide à l'échelle moléculaire.

Les conditions aux limites sont aussi diffèrentes entre les modèles cinétiques et ceux basés sur la discrétisation directe des équations différentielles. Les populations sorties de nœuds frontières doivent être remplacées par des populations qui entrent, en respectant autant que possible les conditions souhaitées. La première idée a été d'utiliser le rebond (inversion de vitesse) pour le non-glissement et la réflexion spéculaire pour le glissement libre, suivant les idées de Maxwell. En effet, en utilisant le rebond dans un canal infini, on obtient le profil parabolique prédit par la solution de Poiseuille pour l'équation de Navier-Stokes. Nous avons cependant été surpris d'observer que la vitesse ne s'annule pas à la paroi solide où la population a rebondi. Qu'est ce que cela signifie ? Et comment trouver où s'annule la vitesse ? Ma thèse répond à ces premières questions et soulève par la suite des questions plus complexes. Les règles établies pour un écoulement parallèle sont elles également valables pour un point de stagnation ? Est-il possible d'imposer la vitesse en un endroit précis pour un écoulement arbitraire?

Afin d'y répondre, une approche mathématique d'analyse des conditions aux limites des modèles cinétiques a été développée et poursuivie dans le cadre de mon année postdoctorale au laboratoire ASCI (CNRS), en collaboration avec Pierre Lallemand et Dominique d'Humières. Nous avons ainsi construit les populations entrantes sous la forme de leur approximation prédite par le développement de Chapman-Enskog, qui permet également déduire toute l'information hydrodynamique nécessaire des populations connues localement. Des années plus tard, cette approche a pris la forme élégante et simple d'une multi-réflexion, où chacune des populations sortantes est remplacée par une combinaison linéaire de quelques populations connues de vitesses parallèles ou opposées. Le choix adéquat des coefficients permet de faire correspondre les conditions de fermeture avec le développement directionnel de Taylor, soit de la partie symétrique de l'équilibre, soit de sa partie antisymétrique, avec une précision du deuxième ou troisième ordre et cela pour une forme arbitraire de la paroi.

Cette notion de symétrie par rapport à la distribution du champ de vitesse va guider nos études. Intuitivement naturelle, la décomposition de l'équation d'évolution sur deux parties, symétrique et antisymétrique, est formalisée par l'opérateur à deux temps de relaxation. Cet opérateur de collision, dit two-relaxation-times model (TRT), attribue un paramètre de relaxation pour la partie paire (symétrique) hors équilibre (la demi-somme des quantités associées des vitesses opposées) et un autre pour la partie impaire (leurs demi-différence). Il inclut alors l'opérateur le plus répandu Bhatnagar-Gross-Krook (BGK), dit aussi single-relaxation-time model (SRT), comme cas particulier. Le paramètre de relaxation unique de BGK

détermine soit la valeur de la viscosité cinématique, soit le coefficient de diffusion isotrope. Pour les deux types de problèmes, les équations hydrodynamiques et d'advection-diffusion, le modèle à deux temps possède donc un nouveau paramètre libre auquel nous réservons un rôle particulier par la suite. Signalons que le modèle TRT lui-aussi constitue une sous-classe des modèles à plusieurs temps de relaxation, dit multiple-relaxation-times models (MRT), qui sont les modèles les plus riches pour les équations hydrodynamiques.

Après tous ces efforts pour construire des modèles hydrodynamiques suffisamment isotropes, est-il possible de les étendre aux équations anisotropes ? Je me suis posé cette question au début de mon travail au Cemagref, afin de pouvoir porter les modèles de Boltzmann à une échelle supérieure, et notamment pour l'écoulement macroscopique d'eau souterraine décrit par la loi de Darcy dans un sol variablement saturé et avec une conductivité anisotrope. Deux approches ont été développées. La première technique utilise l'opérateur isotrope de collision (le même que pour l'équation de Navier-Stokes, c'est-à-dire MRT, TRT, ou BGK) et introduit l'anisotropie du tenseur de diffusion à l'aide d'une fonction d'équilibre anisotrope. La seconde technique consiste à modifier les règles de collision de façon anisotrope avec un opérateur de collision "par lien", dit opérateur L, qui généralise l'opérateur à deux temps de relaxation : les deux paramètres peuvent alors différer d'un lien à l'autre. En prenant la même valeur pour toutes les parties symétriques, la seconde classe de modèle permet de garder une fonction d'équilibre isotrope. On se retrouve alors avec deux hiérarchies de modèles : les opérateurs à temps multiples d'un côté (ayant les polynômes orthogonaux de vitesse comme base de leur matrice de collision), et les opérateurs par "lien" de l'autre côté. Ces derniers se révèlent plus riches pour les équations anisotropes. Quant au modèle à deux temps de relaxation, il représente leur intersection et joue pour cette raison un rôle central dans ce mémoire.

En effet, la solution exacte pour un écoulement de Poiseuille a montré que, dans le cas du rebond, la position effective de la paroi solide (la domaine où la vitesse s'annule pour la solution numérique avec la méthode LBE) dépend de la viscosité du fluide modélisé. On peut facilement imaginer l'impact de cette propriété inattendue sur les mesures de perméabilité d'un milieu poreux, une des applications favorites du modèle de Boltzmann depuis sa naissance ! Ainsi toutes les mesures de perméabilité effectuées avec le modèle BGK ont, comme artefact numérique, une dépendance de la perméabilité avec la viscosité, l'erreur étant approximativement proportionnelle au carré de la viscosité utilisée pour l'écoulement de Stokes. D'autre part, la position effective de la paroi solide dépend des paramètres libres de relaxation, qui n'interviennent pas dans les équations hydrodynamiques. Déjà en 1994, nous avons constaté avec Laurent Giraud (alors doctorant à l'ASCI), que la perméabilité d'un milieu poreux arbitraire devient indépendante de la viscosité

quand certaines combinaisons des temps de relaxation sont maintenues constantes. Nous avons ensuite réalisé que ces combinaisons ”magiques” relient entre elles de façon particulière les paramètres de relaxation des modes symétriques et antisymétriques de l'opérateur de collision. Comment peut-on expliquer ce fait ? À cette époque nous avons cherché à exprimer les coefficients de la série infinie de Chapman-Enskog, afin de faire apparaître les combinaisons ”magiques” dans la condition de fermeture imposée par le rebond. Mais nous n'y sommes parvenus que jusqu'à un certain ordre...

C'est seulement une dizaine années plus tard que, avec D. d'Humières, nous avons réussi à démontrer ce résultat rigoureusement. En effet, l'équation d'évolution de l'opérateur L a été reformulée en termes d'opérateurs directionnels de type différences-finies. Ainsi, quatre relations entre les populations de trois nœuds voisins (un central et deux en positions symétriques) ont été remplacées par quatre équations de récurrence le long de chaque axe du réseau. Leurs variables sont les parties symétriques et antisymétriques hors équilibre et dépendent de la fonction d'équilibre. Ce système est fermé par les conditions de conservation et par les conditions aux limites.

Après avoir introduit certaines factorisations de la solution stationnaire de ce système, la forme exacte de ses composantes montre que les modes symétriques et antisymétriques n'interviennent que par leurs combinaisons ”magiques”. Cela nous a permis de faire un grand pas en avant pour la compréhension de la méthode! Tout d'abord, nous avons pu prouver que, dans le régime de Stokes, l'équation macroscopique exacte, déduite du modèle à deux temps de relaxation, n'est linéaire (par rapport à la perméabilité comme paramètre caractéristique) que quand leur combinaison “magique” garde une valeur fixe pour toute variation de la viscosité. Cette propriété est également vérifiée par la condition de clôture de type rebond, et elle se généralise pour le modèle à temps multiples de relaxation. Ces deux faits réunis expliquent les résultats observés auparavant !

Finalement, grâce aux solutions des équations de récurrence nous avons pu donner une forme explicite à tous les coefficients de la série infinie de Chapman-Enskog, pour les solutions stationnaires. Ces deux solutions sont en effet équivalentes en volume, c'est-à-dire quand les conditions aux frontières n'interviennent pas dans l'analyse. De plus, l'extension des équations de récurrence aux nœuds frontières nous a permis de trouver une forme de couches d'accommodation selon chaque axe du réseau coupé par la paroi. Ces couches d'accommodation sont provoquées par l'écart entre les conditions effectives de fermeture et la forme exacte de la solution en volume : leur amplitude décroît de façon exponentielle avec la distance à la paroi. Les quantités conservées, la partie (hydrodynamique) des populations hors équilibre et les couches d'accommodation sont toutes ensemble définies par un système global d'équations différentielles discrétisées sur le réseau.

On prouve que maintenir constante la combinaison “magique” du modèle à deux temps de relaxation est une condition suffisante pour que les solutions stationnaires de ce système, pour la fonction d’équilibre hydrodynamique de Navier-Stokes, soient paramétrées (à tout ordre) par les nombres physiques sans dimension, comme les nombres de Froude et de Reynolds, et le nombre de Mach dans un régime compressible. L’équation d’advection-diffusion possède des propriétés similaires. Cela signifie que leurs solutions adimensionnelles restent les mêmes sur une grille donnée quelle que soit la variation des paramètres physiques et cinétiques, pourvu que les conditions exactes de clôture soient elles aussi paramétrées. Pour le modèle BGK, la combinaison “magique” est proportionnelle au carré de la viscosité et l’erreur relative dépend inévitablement de sa valeur, contrairement (par exemple) à ce que prévoit la linéarité de d’équations de Stokes et Brinkman. Après avoir compris cette propriété, nous avons formulé des conditions suffisantes pour les coefficients de multi-réflexions et conçu des classes de schémas paramétrées exactement pour la vitesse et la pression, avec un nombre infini d’éléments formellement équivalents en ordre de précision.

Toutefois, la modélisation avec des valeurs numériques très élevées de coefficients de transport nécessite au moins deux temps de relaxation pour diminuer l’importance des artefacts numériques en volumes, aux bords du domaine et aux interfaces. Les valeurs fortes des coefficients de transport accélèrent la convergence vers l’état stationnaire. Elles sont inévitables pour des modèles à deux phases en cas de grands contrastes de viscosité cinématique, pour certains modèles rhéologiques, ainsi que pour décrire les phénomènes dominés par la diffusion, ce qui est souvent le cas de l’équation de Richards pour l’écoulement dans un sol variablement saturé. D’autre part, la modélisation avec des valeurs numériques proches de zéro de coefficients de transport, qui est inévitable pour l’écoulement rapide aux grand nombres de Reynolds et pour l’advection des polluants, est plus précise mais mois robuste. Ces modèles peuvent améliorer sa stabilité à l’aide des choix adéquat de paramètres libres. Certaines règles précises sont déjà établies afin d’obtenir la stabilité optimale, un vision complète reste encore à découvrir.

Il reste également à comprendre comment quantifier l’impact des couches d’accommodation sur les quantités macroscopiques. On peut se demander si elles possèdent, pour certains types de conditions aux limites, les propriétés cinétiques des couches de Knudsen. Ainsi, bien que la compréhension des schémas de Boltzmann se soit améliorée avec le temps, plusieurs questions restent encore ouvertes. Peut-être l’une des plus importantes est de clarifier leur place, aussi bien en termes formels de précision numérique que de stabilité, par rapport aux autres méthodes numériques, en particulier les différences finies. Pour l’instant, supposons que la ”magie” des schémas de Boltzmann est cachée dans sa partie ”cinétique” et partiellement aperçue lors de l’analyse numérique de ses équations de récurrences.

SYNTHÈSE DU MÉMOIRE.

Un simple argument de symétrie par rapport aux vitesses des populations va servir de guide, tout d'abord pour élargir les équations d'évolution aux problèmes d'advection-diffusion anisotrope dans le premier chapitre, ensuite pour déduire les équations de récurrence et construire leurs solutions dans le deuxième chapitre, concevoir les conditions aux limites appropriées dans le troisième, et enfin, dans le quatrième chapitre, pour analyser la continuité de la solution macroscopique quand les opérateurs de collision ont des éléments discontinus. Une grande partie de résultats analytiques présentés dans ces quatre premières chapitres sont développés en collaboration avec Dominique d'Humières, chercheur à Laboratoire de Physique Statistique de l'ENS à Paris. Tous ces développements ont été motivés par la modélisation de phénomènes physiques concrets. Ceux qui ont été abordés dans mon travail sont décrits dans le cinquième chapitre. Il s'agit de la modélisation d'écoulements microscopiques de Stokes et de Navier-Stokes à une et deux phases dans un milieu poreux, d'un modèle de Brinkman pour le couplage d'écoulements macroscopiques et microscopiques, d'un modèle à deux fluides non miscibles et de la modélisation avec l'interface libre pour des fluides newtonien ou à rhéologie plus complexe. Nous décrivons aussi l'écoulement macroscopique d'eau dans un sol variablement saturé à l'aide de l'équation de Richards. Le sixième chapitre contient quelques solutions exactes du schéma de Boltzmann, avec les algorithmes adéquats aux limites.

Le premier chapitre rappelle tout d'abord les idées principales de l'équation linéarisée de Boltzmann, décrivant l'évolution d'ensemble des populations $\{f_q(\vec{r},t)\}$ de vitesse $\vec{c}_q$ sur des nœuds $\{\vec{r}\}$ d'un réseau régulier (voir Figure 5) comme la relaxation de leur partie hors d'équilibre $\{n_q(\vec{r},t)\}$ par la matrice de collision $\mathbf{A}$:

$$f_q(\vec{r}+\vec{c}_q,t+1) = f_q(\vec{r},t) + g_q \ , \ g_q = (\mathbf{A}\cdot\mathbf{n})_q \ , \ q = 0,\dots Q-1 \ .$$

Nous proposons une décomposition *par lien* (par paire des vitesses opposées), aussi bien des populations que de leurs fonctions d'équilibre $\{e_q\}$, sur leurs parties symétriques et antisymétriques :

$$f_q^{\pm} = \frac{1}{2}(f_q \pm f_{\bar{q}}) \ , \ e_q^{\pm} = \frac{1}{2}(e_q \pm e_{\bar{q}}) \ , \ n_q^{\pm} = (f_q^{\pm} - e_q^{\pm}) \ , \ \vec{c}_{\bar{q}} = -\vec{c}_q \ , \ \forall\, q.$$

Nous décomposons également les vecteurs propres de la matrice de collision sur les polynômes de degrés pairs et impairs, $\mathbf{v}_k^{\pm}$, et présentons le modèle à temps multiples de relaxation (MRT) avec l'argument de symétrie :

$$g_q^{\pm} = \sum_{k=1}^{N^{\pm}} \lambda_k^{\pm}(\widehat{f}_k^{\pm} - \widehat{e}_k^{\pm}) v_{kq}^{\pm} \ , \ \widehat{f}_k^{\pm} = \frac{\mathbf{f}\cdot\mathbf{v}_k^{\pm}}{||\mathbf{v}_k^{\pm}||^2} \ , \ \widehat{e}_k^{\pm} = \frac{\mathbf{e}\cdot\mathbf{v}_k^{\pm}}{||\mathbf{v}_k^{\pm}||^2} \ .$$

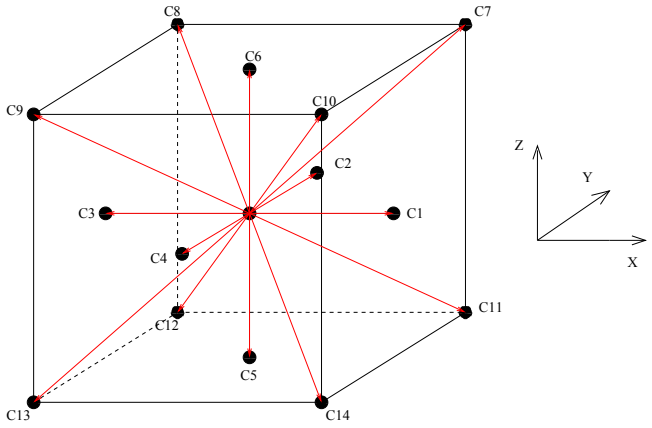

Figure 5: Champ de vitesse du modèle $d3Q15$ utilisé pour tous les calculs dans ce mémoire, avec la population immobile de vitesse $c_0 = 0$.

Les valeurs propres $\{\lambda_k^{\pm}\}$ des modes conservés sont égaux à zéro ; pour les autres modes, nous introduisons les combinaisons "magiques" $\Lambda^{eo\,(k,j)}$:

$$\Lambda^{eo\,(k,j)} = \Lambda^{+(k)}\Lambda^{-\,(j)}\ ,\ \Lambda^{\pm(k)} = -(\frac{1}{2}+\frac{1}{\lambda_k^{\pm}})\ ,\ -2 < \lambda_k^{\pm} < 0\ .$$

Nous introduisons ensuite l'opérateur par lien (alternative à MRT), dit opérateur L, avec une paire de valeurs propres $\lambda_q^{\pm}$ associée à chaque lien:

$$g_q^{\pm} = \lambda_q^{\pm} n_q^{\pm}\ ,\ \Lambda_q^{eo} = \Lambda_q^{+}\Lambda_q^{-}\ ,\ \Lambda_q^{\pm} = -(\frac{1}{2}+\frac{1}{\lambda_q^{\pm}})\ ,\ q = 0,\ldots Q-1\ .$$

Le couplage de deux approches (MRT-L model) s'écrit alors :

$$g_q^{+} = \sum_{k=1}^{N^+} \lambda_k^{+}\widehat{n}_k^{+} v_{k\,q}^{+}\ ,\quad \text{et} \quad g_q^{-} = \lambda_q^{-} n_q^{-}\ ,\ \forall\, q\ .$$

Enfin nous présentons le modèle à deux temps de relaxation (TRT model), qui est un modèle minimal avec une combinaison "magique" et central dans notre étude:

$$g_q^{\pm} = \lambda^{\pm} n_q^{\pm}\ ,\quad \text{avec}\ \ \Lambda^{eo} = \Lambda^{-}\Lambda^{+}\ ,\ \ \Lambda^{\pm} = -(\frac{1}{2}+\frac{1}{\lambda^{\pm}})\ .$$

Le modèle TRT s'adapte facilement pour l'équation de Navier-Stokes, où la densité ρ et la quantité de mouvement $\vec{J}$ sont données, en absence de sources extérieures, tout simplement comme une somme des populations (masse) et une somme de leur quantité de mouvement:

$$\rho(\vec{r},t) = \sum_{q=0}^{Q-1} f_q = \sum_{q=0}^{Q-1} f_q^+ \ , \ \vec{J}(\vec{r},t) = \sum_{q=1}^{Q-1} f_q \vec{c}_q = \sum_{q=1}^{Q-1} f_q^- \vec{c}_q \ .$$

Les deux viscosités, cinématique et volumique, sont alors proportionnelles à Λ^+, et leurs valeurs peuvent être différentes suivant le choix de certains paramètres d'équilibre. Dans le cas de l'équation de transport avec tenseur isotrope de diffusion, et en utilisant une même forme d'équilibre avec une fonction prédite d'advection $\vec{J}(\vec{r},t)$, les coefficients de diffusion sont tous proportionnels à Λ^-. La combinaison "magique" est alors un paramètre libre pour les deux classes de problèmes. Le modèle TRT se réduit au modèle le plus populaire BGK (sans paramètres libres) quand ces deux paramétres de relaxation sont égaux:

$$\lambda^- = \lambda^+ = -\frac{1}{\tau} \ , \quad \text{avec } \Lambda^{eo}(\tau) = \frac{1}{4}(2\tau - 1)^2 \ , \ \tau > \frac{1}{2} \ .$$

Le passage vers les équations "macroscopiques" (hydrodynamiques ou d'advection diffusion) peut se faire à l'aide du développement par perturbation de Chapman-Enskog de la partie hors-équilibre autour de l'équilibre locale. En présentant la série infinie avec l'argument de symétrie :

$$g_q^{\pm}(\vec{r},t) = \sum_{k\geq 1} g_q^{\pm(2k-1)}(\vec{r},t) + \sum_{k\geq 1} g_q^{\pm(2k)}(\vec{r},t)$$

on obtient pour des solutions stationnaires de l'opérateur L avec une fonction d'équilibre arbitraire :

$$g_q^{\pm(2k-1)}(\vec{r}) = \quad \frac{a_{2k-1}\partial_q^{2k-1} e_q^{\mp}(\vec{r})}{(2k-1)!} \ , \ g_q^{\pm(2k)}(\vec{r}) = -2\Lambda_q^{\mp} \frac{a_{2k}\partial_q^{2k} e_q^{\pm}(\vec{r})}{(2k)!} \ , \ k \geq 1 \ .$$

Nous avons pu exprimer tous ses coefficients:

$$a_{2k-1} = 1 + 2(\Lambda_q^{eo} - \frac{1}{4}) \sum_{1\leq n<k} a_{2n-1} \frac{(2k-1)!}{(2n-1)!(2(k-n))!} \ , \ k \geq 2 \ , \ a_1 = 1 \ ,$$

$$a_{2k} = 1 + 2(\Lambda_q^{eo} - \frac{1}{4}) \sum_{1\leq n<k} a_{2n} \frac{(2k)!}{(2n)!(2(k-n))!} \ . \qquad k \geq 2 \ , \ a_2 = 1 \ .$$

Cette solution montre que les coefficients a_k dépendent des valeurs propres seulement à travers leurs combinaisons magiques $\{\Lambda_q^{eo}\}$! Cela signifie que tous les

erreurs de troncature des solutions stationnaires sont décrites par les combinaisons magiques. Le modèle TRT peut les contrôler, alors qu'ils sont fixés de façon non-physique par le modèle BGK, comme les polynômes de $\Lambda^{eo}(\tau)$. Signalons aussi une valeur particulière, $\Lambda_q^{eo} \equiv 1/4$, quand tous les coefficients a_k sont égaux à 1.

On distingue par la suite les quantités isotropes (égales pour des populations avec la même amplitude de leurs vitesses), des quantités anisotropes. Pour l'équation d'advection-diffusion anisotrope, deux classes d'opérateurs, MRT/TRT avec une distribution anisotrope des poids d'équilibre et opérateur L avec les paramètres de relaxation anisotropes, ont été construites. La combinaison de ces deux derniers modèles est également possible. Nous précisons les limites d'anisotropie accessibles pour les valeurs positives des populations. La diffusion numérique ainsi que des erreurs des ordres supérieurs pour l'équation d'advection-diffusion sont estimées, nous donnons ensuite les solutions pour réduire ces artefacts numériques.

Ce première chapitre se termine avec quelques résultats analytiques nouveaux sur la stabilité du modèle TRT pour l'équation d'advection-diffusion. Ils font apparaître une valeur particulière pour la combinaison "magique" de paramètres de relaxation : $\Lambda^{eo} = 1/4$, pour laquelle la bande de stabilité s'avère équivalente pour toute valeur du coefficient de diffusion. Cela nous a permis une comparaison directe entre le modèle de discretisation par différences-finies centrales explicites (FTCS) et le modèle TRT. Dans le chapitre suivant, ces propriétés intéressantes sont redécouvertes à l'aide des équations de récurrence.

Le deuxième chapitre commence avec des équations de récurrence pour les solutions stationnaires de l'opérateur L. Elles s'écrivent:

$$g_q^{\pm}(\vec{r}) = [\bar{\Delta}_q e_q^{\mp} - \Lambda_q^{\mp}\Delta_q^2 e_q^{\pm} + (\Lambda_q^{eo} - \frac{1}{4})\Delta_q^2 g_q^{\pm}](\vec{r}) \ ,$$

et

$$[\Delta_q^2 e_q^{\pm} - \Lambda_q^{\pm}\Delta_q^2 g_q^{\pm} - \bar{\Delta}_q g_q^{\mp}](\vec{r}) = 0 \ , \ q = 1, \ldots, Q-1 \ ,$$

ou

$$\bar{\Delta}_q \phi(\vec{r}) = \frac{1}{2}(\phi(\vec{r}+\vec{c}_q) - \phi(\vec{r}-\vec{c}_q)) \ \text{ et } \ \Delta_q^2\phi(\vec{r}) = \phi(\vec{r}+\vec{c}_q) - 2\phi(\vec{r}) + \phi(\vec{r}-\vec{c}_q) \ .$$

Ces équations sont équivalentes à l'opérateur L. Elles représentent les combinaisons linéaires spécifiques de ces équations d'évolution entre trois noeuds voisins selon un lien. Ces premières équations montrent que la partie hors équilibre est reliée de façon explicite à la fonction d'équilibre pour le modèle à deux temps de relaxation et quand $\Lambda_q^{eo} \equiv 1/4$. La solution de ces équations en volume, développée en série perturbative, est la même que celle du développement de Chapman-Enskog présenté dans le chapitre précédent, pour toutes les valeurs Λ_q^{eo}. Les solutions d'équations de récurrence ont été prolongées pour des noeuds frontières, et les

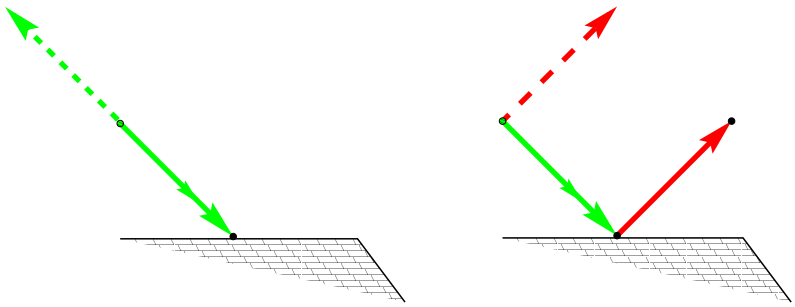

Figure 6: Réflexions simples : le rebond et la réflexion spéculaire.

équations des couches d'accommodation ont été ensuite déduites. Signalons encore que les couches d'accommodation se localisent dans les noeuds frontières, quelles que soient les conditions aux limites, quand $\Lambda_q^{eo} \equiv 1/4$. La forme de la solution obtenue, en volume et aux frontières, nous permet de paramétrer les solutions numériques de l'équation de Stokes, de Navier-Stokes et d'advection-diffusion anisotrope, par des nombres physiques sans dimension et par des combinaisons "magiques". Ainsi, le modèle à deux temps permet un paramétrisation consistante des solutions obtenues par des paramètres physiques. Les équations stationnaires de récurrence ont été aussi déduites pour l'opérateur le plus riche (MRT-L). L'analyse préliminaire des équations de récurrence pour l'opérateur TRT dans un régime dépendant du temps clarifie les propriétés inattendues de stabilité, observées auparavant par l'analyse de Fourier pour $\Lambda_q^{eo} \equiv 1/4$, et conclue ce chapitre. Nous dressons à la fin la liste des problèmes théoriques abordés mais pas encore résolus.

Le troisième chapitre s'attaque aux conditions aux limites. Nous discutons tout d'abord les problèmes de réflexions simples qui sont schématisées sur Figure 6. La solution exacte pour la largeur effective H_{eff} d'un canal infini, par rapport à un largeur attendue H:

$$H_{\text{eff}}^2 = H^2 + \frac{16}{3}\Lambda^{eo} - 1 \ , \ \Lambda^{eo} > 0 \tag{1}$$

montre clairement le problème de la localisation des parois avec le rebond. De plus, la position effective des parois dépend de leur orientation par rapport aux axes principaux du réseau. On distingue ensuite une approche par "nœud", telle que la méthode LSOB, d'une approche par "lien" qui s'exprime sous la forme de conditions de multi-réflexion (à deux points) pour la population entrante $f_{\bar{q}}(\vec{r}_{\text{b}}, t+1)$:

$$f_{\bar{q}}(\vec{r}_{\text{b}}, t+1) \rightarrow \kappa_1 \tilde{f}_q(\vec{r}_{\text{b}}, t) + \kappa_0 f_q(\vec{r}_{\text{b}}, t+1) + \overline{\kappa}_{-1} \tilde{f}_{\bar{q}}(\vec{r}_{\text{b}}, t)$$

$$+\kappa_{-1} f_q(\vec{r}_b - \vec{c}_q, t+1) + \bar{\kappa}_{-2} \tilde{f}_{\bar{q}}(\vec{r}_b - \vec{c}_q, t) \ .$$

L'idée est d'obtenir la relation de fermeture sous la forme d'une série de Taylor, le long du lien coupé par la paroi, pour la condition de Dirichlet souhaitée à une distance arbitraire δ_q:

$$[e_q^{\pm} + \delta_q \partial_q e_q^{\pm} + \frac{1}{2}\delta_q^2 \partial_q^2 e_q^{\pm} + O(\varepsilon^3)](\vec{r}_b) = e_q^{\pm}(\vec{r}_b + \delta_q \vec{c}_q).$$

Les coefficients κ_1-$\bar{\kappa}_{-2}$ sont exploités afin de décrire les conditions de Dirichlet pour la vitesse et la pression dans le cas des équations hydrodynamiques, ainsi que pour l'équation d'advection-diffusion. Notre analyse récente de ces conditions est focalisée sur l'exactitude de leur paramétrisation, leur extension pour des ouvertures minimales (coins), le support des invariants alternés et l'unicité des solutions obtenues. Ces questions sont abordées à différents degrés dans ce chapitre. On résume également les algorithmes développés pour les parois mobiles (illustrés sur Figure 7), et pour les calculs de transfert de quantité de mouvement à la paroi. En conclusion, nous signalons quelques problèmes qui ne sont pas encore résolus pour les conditions aux limites existantes.

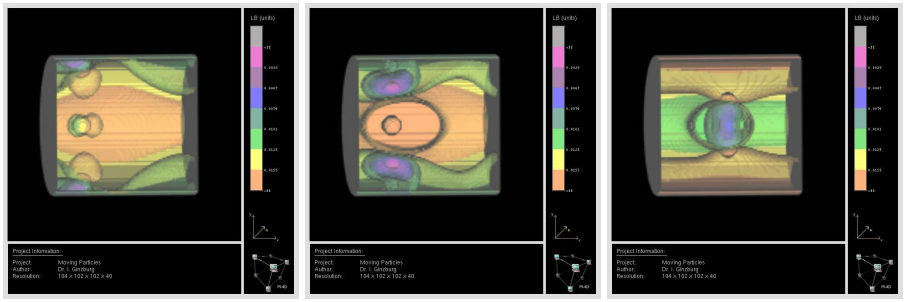

Figure 7: Champ de pression dans un tube circulaire contenant de trois bulles solides ayant un mouvement imposé dans un fluide (code ParPac, ITWM).

Le quatrième chapitre décrit les résultats de l'analyse des conditions de continuité à l'interface entre nœuds du réseau pour des composantes discontinues de l'opérateur de collision. Tout d'abord, deux conditions génériques satisfaites par chaque lien coupé par l'interface entre les nœuds $\vec{r}$ et $\vec{r} + \vec{c}_q$ sont présentées :

$$\mathcal{S}_q(\vec{r}) = \mathcal{S}_{\bar{q}}(\vec{r} + \vec{c}_q) \ , \ \mathcal{S}_q = e_q^+ + \frac{1}{2} g_q^- - \Lambda^+ g_q^+$$

et

$$\mathcal{G}_q(\vec{r}) = -\mathcal{G}_{\bar{q}}(\vec{r} + \vec{c}_q) \ , \ \mathcal{G}_q = e_q^- - \Lambda^- g_q^- + \frac{1}{2} g_q^+ \ .$$

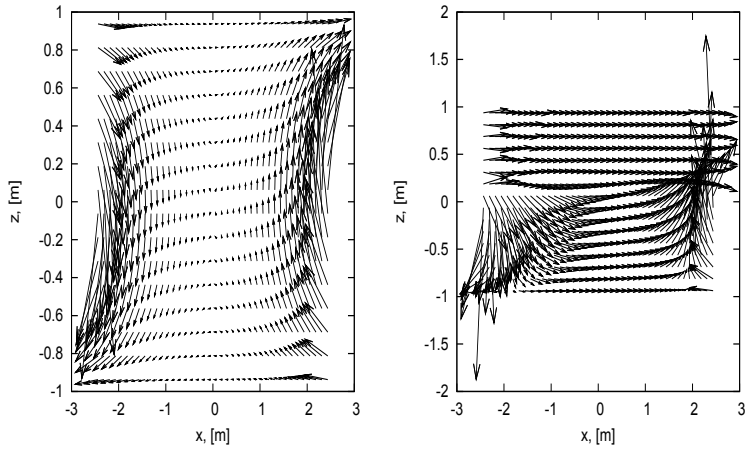

Figure 8: Champ de vitesse $\{\partial_x\phi^\star, \partial_z\phi^\star\}$ d'après la solution analytique construite pour deux couches du sol stratifié avec le tenseur diagonal $\mathbf{K}^{(\pm)} = \mathrm{diag}\{K_{xx}, K_{zz}\}$ et les conditions aux limites discontinues à l'interface : $\partial_x\phi^\star(\pm X, z) = \frac{1}{2}\mathrm{sign}(z)$. Le tenseur de perméabilité est isotrope à gauche et $K^+_{xx}/K^-_{xx} = 500$ à droite.

Ces conditions sont ensuite détaillées pour deux fluides immiscibles divisés par une interface plane, ainsi que pour deux couches de sols stratifiées avec des axes principaux orientés de façon arbitraire les uns par rapport aux autres, en présence de conductivité hétérogène. Il est montré qu'une anisotropie hétérogène peut nécessiter des corrections au niveau de la propagation des populations à travers l'interface, afin de satisfaire les conditions (tangentielles) de continuité du flux diffusif le long de l'interface et de réduire les couches d'accommodation à sa proximité. Cette situation est illustrée par la solution analytique pour un écoulement saturé qui est construite lors de nos études du comportement des schémas anisotropes et hétérogènes:

$$\nabla\cdot\mathbf{K}^{(-)}\nabla h = 0\,,\ z<0 \quad \text{et} \quad \nabla\cdot\mathbf{K}^{(+)}\nabla h = 0\,,\ z>0\,,$$

avec

$$\mathbf{K}^{(\pm)} = \begin{pmatrix} K^{\pm}_{xx} & K^{\pm}_{xy} & 0 \\ K^{\pm}_{xy} & K^{\pm}_{yy} & 0 \\ 0 & 0 & K^{\pm}_{zz} \end{pmatrix}.$$

En effet, guidée par le gradient constant de pression $\partial_y h$ selon l'axe y, la vitesse de Darcy se comporte comme un tourbillon souterrain lorsque le domaine est imperméable pour toutes ses autres extrémités (en x et z). Le champ de vitesse est déterminé par la solution générique d'un problème hétérogène à deux dimensions. Les tourbillons souterrains ont alors la vitesse $\vec{u} = -\mathbf{K}\nabla\phi^\star$ dans le plan (x,z) où

$\nabla\phi^{\star}$ est illustré sur Figure 8. Les corrections introduites pour des populations traversant l'interface permettent d'obtenir ces solutions fortement non-linéaires et discontinues avec une très bonne précision.

Le cinquième chapitre procède par glissements thématiques à partir d'applications du modèle. Il commence par les "conseils magiques" afin d'obtenir des résultats cohérents, efficaces et précis dans les milieux poreux, à l'aide de conditions aux limites exactement paramétrées et d'un choix adéquat des valeurs propres "libres" des opérateurs de collision à deux ou plusieurs temps de relaxation. Le tenseur de la perméabilité **K** d'un milieu poreux arbitraire :

$$\overline{\vec{j}} = \mathbf{K}\frac{\overline{(\vec{F} - \nabla P)}}{\nu} ,$$

obtenue à partir de la solution moyennée $\overline{\vec{j}}$ d'équation de Stokes, devient alors indépendante de la viscosité du fluide modélisé. Cela fait complètement disparaître un artefact numérique connu de schéma LBE. Les valeurs obtenues de perméabilité varient cependant avec Λ^{eo}, mais de façon peu importante pour des conditions précises aux limites (du troisième ordre) et quand le paramètre magique se trouve en dessous de certain limite, $\Lambda^{eo} \approx< 1$, ou dans les intervalles plus petits pour les méthodes aux limites plus couramment utilisées, comme le rebond : $\Lambda^{eo} \approx< \frac{1}{2}$.

La force de résistance $\vec{F} = -\nu\mathbf{K}^{-1}\vec{u}$, reliée à la vitesse par la loi de Darcy dans la partie à perméabilité faible d'un milieu fortement hétérogène, est ensuite introduite dans l'équation de Stokes en suivant le modèle de Brinkman :

$$\nabla \cdot \vec{u} = 0 , \quad \nu\mathbf{K}^{-1}\vec{u} + \frac{1}{\rho_0}\nabla\overline{P} - \vec{g} = \nu_\phi \Delta\vec{u} .$$

En effet, la variation de force avec la vitesse conduit à la déviation de valeur apparent du coefficient de viscosité ν_ϕ de sa valeur prédite par l'analyse de Chapman-Enskog. Certains auteurs ont considère cet artefact numérique du modèle comme une faillite de l'analyse de Chapman-Enskog pour le modèle de Brinkman. Très récemment nous avons pu quantifier les valeurs apparentes de la viscosité, exactement dans les écoulements simples, et de façon approchée dans un écoulement arbitraire. De nouveau, cette analyse confirme que la modélisation consistante du milieu poreux nécessite au moins deux temps de relaxation pour paramétrer correctement les erreurs de troncature et leur impacte sur la solution, ce qui est impossible avec le modèle BGK.

Ce cinquième chapitre aborde ensuite la modélisation de fluides immiscibles microscopiques par le modèle Immiscible Lattice Boltzmann (ILB), introduit dans les travaux de D. Rothman et A. Gunstensen au début des années quatre-vingt-dix.

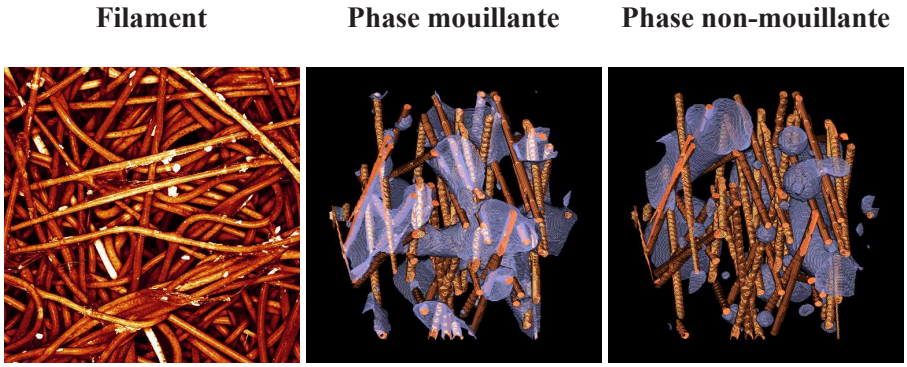

Figure 9: Distribution d'une phase huileuse sur les fibres d'un filtre par un modèle ILB (code ParPac).

Nous proposons une implémentation simplifiée et l'analyse de ce modèle, permettant par ailleurs sa meilleure interprétation pour la résolution des équations de Navier-Stokes et pour l'advection d'interface, deux éléments caractéristiques de tout le modèle diphasique. L'analyse mathématique de ce modèle a été abordée dans la thèse de Dirk Kerhwald (1999-2002), lors de nos travaux communs avec Peter Klein, Konrad Steiner et Doris Reinel-Bitzer sur les simulations d'un système huile-gaz dans un milieu poreux fibreux, issu des problèmes de production de filtres. Ces modèles ont été inscrits dans le cadre du projet ParPac (particules parallèles pour des applications industrielles) à l'Institut für Techno- und Wirtschaftsmathematik (ITWM) à Kaiserslautern et sont encore utilisés actuellement. Les images sur Figure 9 montrent les distributions d'une phase huileuse (mouillante et non-mouillante) sur les fibres d'un filtre, obtenues avec le code ParPac dans les années 2000-2001. Un modèle similaire a été adapté pour étudier l'hysteresis lors la modélisation d'un cycle d'imbibition-drainage dans le milieu poreux par mes collègues allemands (B. Ahrenholz, M. Krafczyk et J. Tölke), dans le cadre du projet FIMOTUM (2003-2008).

Pour un écoulement stationnaire de fluides immiscibles dans un milieu poreux, les équations de Stokes à grands contrastes de masse volumique (cas difficile pour l'application du modèle ILB en raison de ses contraintes de stabilité) sont décrites à l'aide de contrastes equivalents des valeurs numériques de viscosité cinématique, en respectant la condition de continuité pour les composantes du tenseur des contraintes visqueuses. Pour un écoulement non-stationnaire rapide, un tel remplacement n'est donc plus valable. Cela nous a amené à introduire un modèle microscopique LBE à interface libre pour les cas où la description de l'écoulement dans une phase gazeuse n'est pas nécessaire. Cette méthode restreint l'opérateur d'évolution aux nœuds du réseau occupés par le fluide, en imposant aux popula-

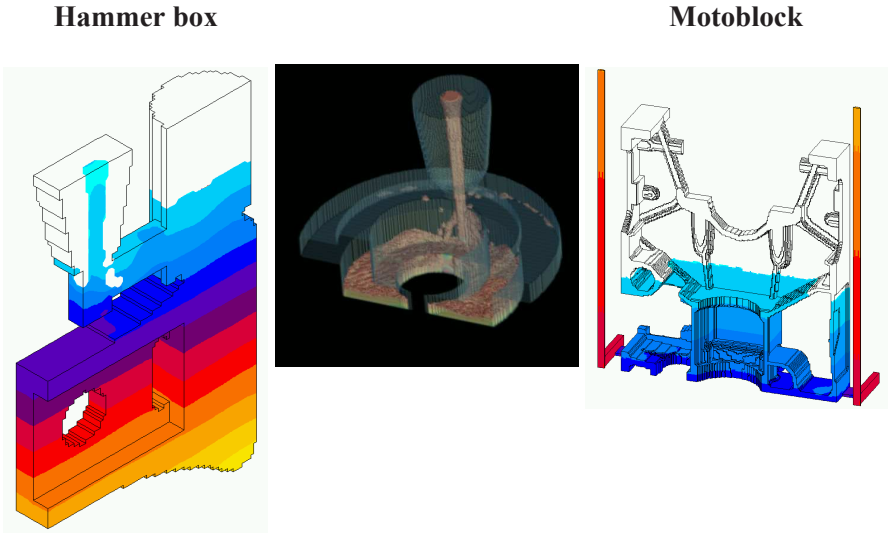

Figure 10: Le remplissage des moules de géométrie complexe par le modèle LBE à l'interface libre (code ParPac).

tions à l'interface leur solution approximative de Chapman-Enskog, et en prenant en compte la continuité des quantités physiques, comme la vitesse et la pression dans la partie à l'équilibre, et les composantes normales du tenseur visqueux dans la partie hors équilibre.

Motivé par la modélisation du remplissage de moules par le métal liquide (voir Figure 10), une des composantes du projet ParPac, cet algorithme néglige les effets de tension superficielle. La stabilisation de la méthode (de type turbulence simple) nous a permis d'étendre le domaine d'application à des nombres de Reynolds relativement élevés. Ce modèle a été complété par un module de calcul de température (de type volumes finis), ayant pour difficulté principale la compressibilité artificielle du champ de vitesse obtenu par LBE. L'ensemble constitue un code prenant en entrée la géométrie du moule (issue de la CAO ou de mesures tomographiques) et les paramètres physiques et produisant les données destinées à la visualisation des différentes étapes du processus et à l'exploitation finale.

Le fluide de Bingham (plastique) se manifeste comme un solide au dessous de certaine seuil de la magnitude du tenseur de contraints visqueuses :

$$\|\mathbf{D}\| = 0 \quad \text{if} \quad \|\tau\| < \tau_0 \,, \text{ and } \tau = (\nu + \frac{\tau_0}{\|\mathbf{D}\|})\mathbf{D} \quad \text{if} \quad \|\tau\| > \tau_0 \,.$$

Nous avons observé que, malgré un traitement explicite, le modèle LBE simple d'un fluide non-newtonien est en bon accord avec les prédictions théoriques,

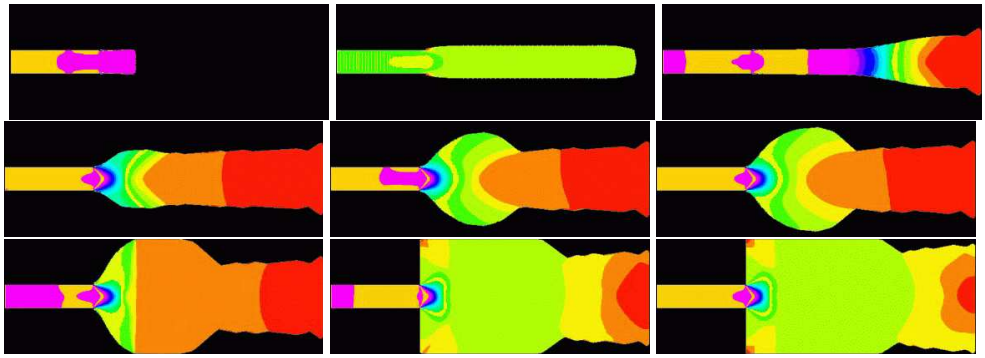

Figure 11: Remplissage de cavité par un modèle LBE à interface libre pour un fluide de Bingham à Re= 12.5 et Bi= 9.4 (Ginzburg & Steiner, 2002). Couleurs [cm/s]: rouge $(0-15)$, jaune $(15-25)$, vert $(25-55)$, bleu $(55-90)$, violet (>90).

développées dans les travaux de V. M. Entov, de la forme du front lors d'un remplissage d'une cavité rectangulaire en fonction des nombres de Reynolds et de Bingham. La formation de "bulle" est illustrée par les images sur Figure 11.

Nous changeons ensuite l'échelle spatiale et présentons la modélisation, développée au Cemagref il y a quelques années, d'un sol variablement saturé à l'aide de l'équation de Richards. Cette équation décrit la conservation de la teneur en eau θ, en supposant que la pression de gaz a une valeur constante et que la vitesse est donnée par loi de Darcy :

$$\partial_t \theta + \nabla \cdot \vec{u} = 0 \ , \ \vec{u} = -\mathbf{K}(\nabla h(\theta) + \vec{1}_z) \ , \ h(\theta) = -\frac{\psi(\theta)}{\rho_0 g} \ .$$

De nouveau, on néglige la dynamique du gaz en prenant en compte les effets capillaires de façon implicite, par des fonctions semi-heuristiques de rétention $h(\theta)$ reliant la pression et la teneur en eau. Le tenseur de perméabilité $\mathbf{K}$ varie alors avec la saturation via la fonction de conductivité hydraulique $K(h)$ et peut de plus être anisotrope : $\mathbf{K} = K(h)\mathbf{K}^a$.

Nous traitons l'équation de Richards avec les techniques LBE développées pour l'équation d'advection-diffusion anisotrope. La conservation de la masse d'eau est alors exacte en prenant la teneur en eau comme quantité conservée. L'équation de Richards est cependant fortement non-linéaire pour le terme convectif (dû à la gravité, $\mathbf{K}\vec{1}_z$) ainsi que pour sa forme diffusive à travers les fonctions de rétention. Trois formulations principales d'équilibre ont été introduites afin de gérer cette non-linéarité : la première méthode est basée sur la teneur en eau, la deuxième sur la pression (formulation mixte) et la dernière sur la transforma-

tion de Kirchhoff. Des critères approximatifs de stabilité ont été établis pour les régimes les plus difficiles (sol secs, interface saturée/insaturée). Il s'avère que ces critères sont assez différents pour les principaux modèles de sol, suivant les propriétés mathématiques de leurs fonctions hydrauliques. Nous en avons déduit que l'efficacité du modèle LBE dépend de la formulation sélectionnée pour un sol et un régime donné.

Les formulations différentes dans la zone non-saturée sont couplées avec la loi de Darcy dans la zone saturée, $\theta \equiv \theta_s$:

$$\nabla \cdot \vec{u} = 0 \ , \ \vec{u} = -K(h_s)\mathbf{K}^a(\nabla h + \vec{1}_z) \ , \ h \geq h_s \ .$$

La stratégie proposée permet le franchissement automatique de l'interface et peut être utilisée dans le cadre de méthodes numériques différentes. Les sous-itérations menées dans la zone saturée pour réduire la pseudo-compressibilité ralentissent cependant la méthode, efficace dans la zone non-saturée. Le travail commun avec mon collègue Cyril Kao et Jean-Philippe Carlier, post-doctorant au Cemagref en 2004, nous a permis élargir les solutions exactes de l'équation de Richards pour l'infiltration dans un sol variablement saturé et étudier très précisément le passage de l'interface par le modèle.

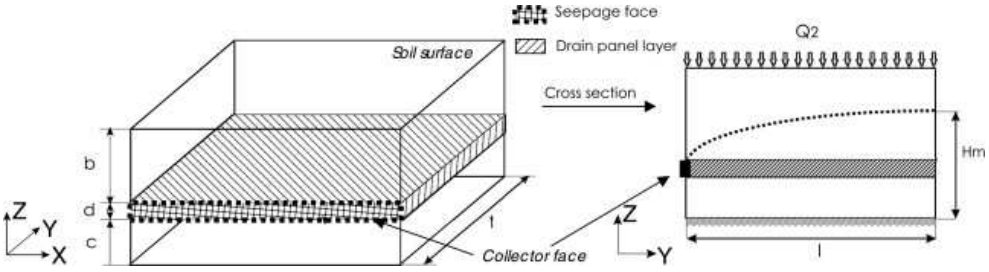

Figure 12: Système effectif stratifié du sol drainé, Carlier et al (2007).

En outre, le travail sur les modèles anisotropes nous a conduit à l'idée de remplacer une couche de drains agricoles située dans le sol par une couche homogène de perméabilité équivalente, schématisée sur Figure 12. L'ensemble constitue alors un milieu hétérogène et anisotrope, avec l'écoulement lent dans la couche du sol et l'écoulement rapide dans la couche remplaçant le réseau de drainage. Cette approche, dite aussi milieu équivalent, a été validée dans un sol variablement saturé. De façon plus générale, ce travail contribue à la réflexion sur la représentation numérique des éléments singuliers d'un bassin versant, jouant un rôle majeur dans les transfert d'eau.

Ces travaux se sont déroulés dans le cadre de l'ARC DYNAS, "Dynamique des nappes souterraines", initiative de coopération de l'INRIA, en collaboration étroite

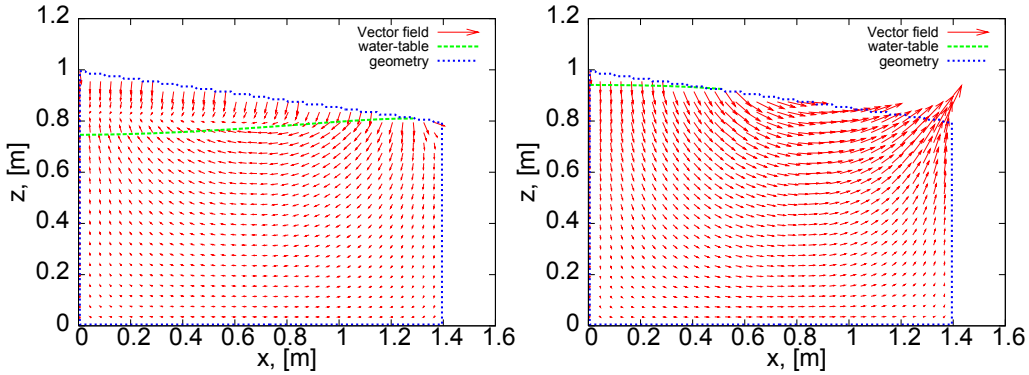

Figure 13: Évolution de la nappe lors d'un épisode pluvieux dans le sol SCL variablément saturé, simulé par le modèle LBE pour l'équation de Richards.

avec Alexandre Ern (l'ENPC) et Éloïse Beaugendre, post-doctorante au Cermics en 2004. Deux modèles numériques de résolution de l'équation de Richards, par LBE en 3D et par éléments finis en 2D, ont été confrontés aux mêmes scénarios numériques. Un bon accord entre les deux méthodes a été constaté pour la position de la nappe et pour l'évolution temporelle des flux entrants/sortants du système lors d'épisodes de pluies. La configuration étudiée est illustrée sur Figure 13. La sortie de la nappe à la surface du domaine a été traitée avec deux approches contrastées : la méthode d'éléments-finis le localise précisément (comme un obstacle), sa position approximative étant le résultat a-posteriori de l'algorithme LBE proposé. En conclusion, nous suggérons que l'alternance (dynamique) des formulations d'équilibre pourrait constituer un avantage important en terme de flexibilité du modèle LBE, car, contrairement aux méthodes de résolution directe, cela ne nécessite aucun changement fondamental de l'algorithme de base.

La dernière partie du chapitre cinq est consacrée à la modélisation d'un sol hétérogène qui nécessite, tout comme l'utilisation de grille non-uniforme, une analyse des conditions de continuité, imposées de façon implicite. Ses propriétés caractéristiques ont été déduites des relations génériques présentées dans le quatrième chapitre. Cette étude a montré que la pression est continue seulement pour la formulation mixte d'équilibre (voir Figure 14), à condition que l'anisotropie hétérogène soit traitée avec l'opérateur L (c'est-à-dire à l'aide des valeurs propres anisotropes) et non par les fonctions anisotropes d'équilibre. Notre étude numérique des corrections à l'interface couvre le cas d'un sol stratifié saturé avec une anisotropie hétérogène. Le cas non saturé n'a pas encore été abordé.

Enfin, le sixième chapitre présente les opérateurs de collisions et les schémas

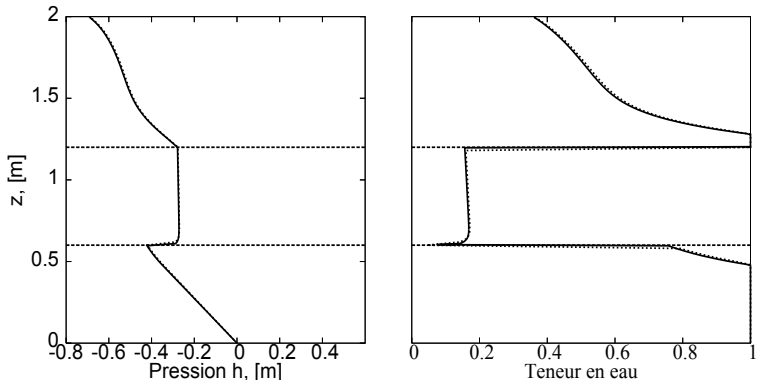

Figure 14: Épisode de drainage dans une colonne de sol hétérogène modélisé avec la formulation mixte d'équilibre (teneur en eau/pression) pour l'équation de Richards. La solution de LBE est comparée à une solution de référence (les 2 courbes coïncident).

aux limites associés afin d'obtenir quelques solutions exactes issues de problèmes hydrodynamiques ou d'advection-diffusion. Nous commençons par les écoulements de Couette et Poiseuille à une ou deux phases, et montrons ensuite leurs "équivalents" pour un écoulement de Darcy dans un sol hétérogène. Nous présentons aussi la couche d'accommodation dans un canal parallèle à l'un des axes principaux du réseau qui accompagne le profil parabolique établi en présence de termes non-linéaires (de Navier-Stokes) à l'équilibre. En effet, notre étude montre que les termes non-linéaires couramment utilisés ne sont pas compatibles avec la solution de Poiseuille dans un canal orienté de façon arbitraire, à l'exception de la valeur particulière de la combinaison magique. Quelques solutions exactes du modèle avec une distribution non-linéaire de la pression sont ensuite discutées. Nous montrons que l'équation de Brinkman admet une solution exacte par le modèle TRT lorsque le canal reste parallèle à l'un des axes du réseau. Cette solution est ensuite généralisée pour l'équation de diffusion anisotrope avec une source de masse variable. Grâce à l'anisotropie de ses valeurs propres, l'opérateur L permet d'avoir la solution exacte pour un canal arbitrairement orienté. Le lecteur trouvera aussi l'expression exacte de la diffusion numérique des modèles unidimensionnels qui peuvent inspirer des modèles naïfs de diffusion artificielle (style "upwind") ainsi qu'une solution exacte de type "onde de température", obtenue à l'aide d'une transformation intégrale de l'équilibre. Bien qu'à des degrés différents, ces solutions ont aidé tout au cours ce travail à valider les développements théoriques et leur implémentation dans le code numérique. Certaines entre eux nécessitent les valeurs particulières de la combinaison "magique" qui sont rassemblées dans la dernière

section de ce mémoire.

Les valeurs ”magiques” principales pour le modèle à deux temps de relaxation sont :

- $\Lambda^{eo} = \frac{1}{4}$:

    1. La partie hors équilibre est liée de façon explicite, sous la forme d'opérateurs de différences-finies directionnels, à la fonction d'équilibre.
    2. Les coefficients a_k de la série de Chapman-Enskog pour des solutions stationnaires sont tous égaux à 1.
    3. L'opérateur d'évolution (qui est explicite en temps) obtient une forme équivalent à un système de discrétisation à trois niveaux temporels.
    4. La bande de stabilité est alors déterminée par des paramétres d'équilibre. Elle est indépendante des valeurs propres, au moins pour l'AADE.
    5. Les couches d'accommodation se localisent aux nœuds frontières.

- $\Lambda^{eo} = \frac{3}{16}$:

    La condition de rebond localise la paroi au milieu des nœuds du réseau dans l'écoulement parallèle à l'un des axes principaux du réseau.

- $\Lambda^{eo} = \frac{1}{6}$:

    1. L'erreur de discrétisation liée aux dérivées spatiales du quatrième ordre est annulée.
    2. Le modèle TRT pour l'AADE annule les corrections anisotropes du tenseur de diffusion.

- $\Lambda^{eo} = \frac{1}{12}$:

    1. L'erreur de discrétisation reliée aux dérivées spatiales du troisième ordre est annulée.
    2. Cette valeur est nécessaire pour que l'écoulement de Poiseuille dans un canal incliné de façon arbitraire par rapport aux axes du réseau soit une solution exacte du schémas LBE, lorsque le terme non-linéaire est présent à l'équilibre.
    3. Le modèle BGK pour l'ADE annule l'erreur principale sur la vitesse d'advection dans les solutions transitoires.

- $\Lambda^{eo} = \frac{3\delta^2}{4}$:
  Les schémas aux limites dits multi-réflexion ”magique linéare” à deux ou trois populations (famille MGLI) permettent d'obtenir l'écoulement exact de Poiseuille avec une distance arbitraire $0 < \delta \leq 1$ entre les nœuds frontières et la paroi solide. En particulier, les interpolations linéaires utilisés couramment, Bouzidi-Firdaouss-Lallemand rules (BFL) peuvent bénéficier de cette propriété à l'aide d'une correction locale, décrite dans ce mémoire.

Toutefois, des éléments de compréhension restent à approfondir pour la stabilité du modèle à deux temps ainsi que pour ses solutions temporelles. Des pistes pour nos recherches à venir figurent dans les sections de clôture tout au long ce mémoire.

Part II

Magic recipes for Lattice Boltzmann modeling of micro and macro flow.

PREFACE

This dissertation presents the synthesis of my research work for modelling flow problems with the Lattice Boltzmann Equation. One of my objectives has been, and remains, to understand how this method works. How can we get its exact solutions? Are they given by the Chapman-Enskog series? And how to incorporate macroscopic, boundary and interface, conditions into the kinetic-type scheme? What equations obey the induced accommodation layers? And what is their impact on the macroscopic solutions? How can we extend the method for highly nonlinear and anisotropic equations? What are its advantages over the explicit finite-difference schemes? I aim to answer these and similar questions without resorting to any kinetic interpretation of the method, just taking it as a given numerical scheme.

The principal recent elements of the first chapter are (i) link-wise collisions (L operator) and (ii) anisotropic equilibrium functions, both suitable for modeling non-linear advection-diffusion equations with fully anisotropic diffusion tensors, (iii) the two-relaxation-times (TRT) model, a common sub-class of the multiple-relaxation-times (MRT) operators and L operators, (iv) the explicit form of all coefficients of the infinite Chapman-Enskog series (on steady solutions) and (v) the high-order corrections for convective velocity and diffusion tensors. This chapter introduces magic combinations of the collision eigenvalues, an essential component of our analysis. One particular choice of this parameter makes especially transparent the link between the forward time central finite-difference scheme and the TRT scheme, in what concern their approximation and stability properties.

The second chapter presents directional central finite-differences type, recurrence equations of the LBE evolution operators, very recently derived. Their variables are the symmetric and non-symmetric non-equilibrium components. They are functions of the corresponding (with respect to the symmetry argument) equilibrium components. The system is closed by conservation relations and the boundary conditions. This approach extends the Chapman-Enskog approximation of the non-equilibrium components to their exact equations and allows us to take the boundary points into consideration. Then we obtain exact dependency of the conservation relations on the equilibrium and collision parameters. This shows that physical non-dimensional numbers control the macroscopic steady solutions when the magic collision combinations of eigenvalues are given. This parametrization property may cure several important numerical artefacts of the LBE modeling of creeping flow in porous media, but only when the collision operator offers at least one free relaxation parameter. This motivates our preference for the TRT and MRT models. Furthermore, exact time-dependent recurrence equations make it possible to reinterpret the temporal evolution of the LBE schemes in terms of three level finite-

difference schemes. This would explain several distinctive stability properties. The whole picture of the influence of free relaxation parameters on the stability is not yet understood and we are working on this.

The third chapter summarizes the works on highly-accurate boundary techniques for arbitrarily shaped boundaries, with a focus on the multi-reflection schemes for hydrodynamic and advection-diffusion equations. Specific conditions on their coefficients select schemes with the exactly same parametrization properties as the bulk solutions, among the infinite classes of multi-reflections with equal formal accuracy. Further choices can be guided by the wish to avoid staggered invariants and to guarantee a unique solution. A discussion on the accurate computations of the momentum transfer on the boundaries and moving obstacles concludes this chapter.

The fourth chapter deals with discontinuous collision elements: equilibrium weights, relaxation parameters, or both. The question is how to analyse the continuity properties of the solutions and enforce the desired macroscopic conditions? We take our starting point from link-wise exact relations for implicit interface tracking, valid for any equilibrium function. They are then elaborated for immiscible fluids on a flat interface (in the frame of "color gradient" model) and for fully anisotropic heterogeneous diffusion tensors in stratified sub-domains.

Essentially, all these theoretical tools are motivated by modelling concrete physical phenomena. Some of the problems encountered in my work are described in the fifth chapter. They include (i) permeability measurements in porous media, and how to make them viscosity independent, (ii) the Brinkman model for coupling the microscopic and macroscopic flow in highly contrasted structures, and how to estimate its apparent viscosity coefficient, (iii) two phase flows and (iv) free interface approach, (v) Bingham plastics and (vi) water flow in variably saturated, heterogeneous and anisotropic soil, described by the highly non-linear Richard's equation. Although these topics cover the major aspects of flow modeling at micro and macro scales, they represent only a very small part in very broad spectre of the actual applications of the LBE method.

The last chapter contains several exact solutions of the LBE schemes, together with the adequate boundary and interface conditions. They are indispensable components of our exact analysis, and the best validation tools of numerical code. Some of these solutions need the specific values of magic combinations. Their list concludes this work. Open questions and unsolved problems are reported in the concluding sections of the different chapters. They motivate my future research work.

Chapter 1

Lattice Boltzmann Equation

Originated from the Lattice-gas cellular automata [53], (U. Frisch, D. d'Humières, B. Hasslacher, P. Lallemand, Y. Pomeau and J. P. Rivet), the ideas of the Lattice Boltzmann numerical scheme first appear in the works by G. R. McNamara & G. Zanetti [138], F. J. Higuera & J. Jiménez [91], at the end of the eighties. Intensively developed, these models manifest them now as independent ways to simulate fluid flows. Extensive reviews [12, 34, 37, 163, 169, 187, 189, 210, 212, 217] cover different aspects of the theory and applications of this method but mostly restrict it to the very particular single-relaxation-time collision operator. In this chapter different formulations of the LBE schemes with a focus on the symmetry and anti-symmetry of their components with respect to the lattice directions are proposed. This approach, first formulated in author's works [69, 72] for anisotropic advection-diffusion and hydrodynamic equations, is central for the presented work.

1.1 Evolution Equation

Lattice Boltzmann schemes are specified by three main components: a set of d-dimensional velocities, each velocity connecting two lattice nodes, a linear collision operator, and an equilibrium distribution that is a given function of the conserved quantities. We assume that the velocity set contains Q vectors: one zero, $\vec{c}_0 = \vec{0}$, for the rest population, and $Q-1$ non-zero vectors, $\vec{c}_q = \{c_{q\alpha},\ \alpha \in \{1,\dots,d\}\}$, $q \in \{1,\dots,Q-1\}$, for the moving populations. Note that we are using "arrows" to denote vectors in the d-dimensional (physical) space, while "bold" face denotes vectors in the Q-dimensional (population) space, e.g., $\mathbf{c}_\alpha = \{c_{q\alpha},\ q = 0,\dots,Q-1\}$, $\alpha \in \{1,\dots,d\}$. Each nonzero velocity $\vec{c}_q$ has an opposite one $\vec{c}_{\bar{q}} = -\vec{c}_q$ in the velocity set. Hereafter we call "*links*" such pairs of anti-parallel velocities $(\vec{c}_q, \vec{c}_{\bar{q}})$. Velocity vectors $\vec{c}_q$ are said to belong to the same class

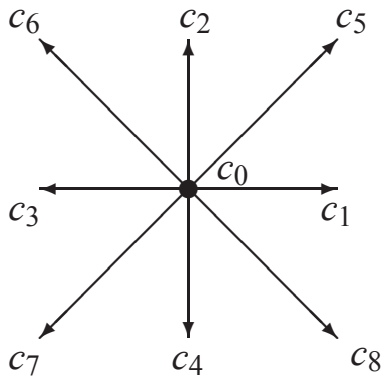

Figure 1.1: Velocity set of $d2Q9$ model.

$p = \|\vec{c}_q\|^2$ if they have equal magnitudes. A vector in the population space is said *isotropic* when its components have the same value per velocity class.

Cubic velocity sets [161] with two moving classes are mostly assumed, e.g., $d2Q9$ set with 8 moving velocities (see Fig. 1.1): $\vec{c}_q = \{(\pm 1,0),(0,\pm 1),(\pm 1,\pm 1)\}$ and $d3Q15$ set with 14 moving velocities: $\vec{c}_q = \{(\pm 1,0,0),\ (0,\pm 1,0),\ (0,0,\pm 1),\ (\pm 1,\pm 1,\pm 1)\}$. They allow us to formulate uniform schemes for the hydrodynamic (Navier-Stokes) equation and for the anisotropic, linear or non-linear, advection-diffusion equation. The simplest $d2Q4$ and $d3Q7$ models are only sufficient for diagonal diffusion tensors. The extension to the $d3Q13$ [99], $d3Q19$ and $d3Q27$ sets [161] is mostly straightforward. The $d3Q15$ velocity set is used for all numerical computations of this study.

The unknown variable of the scheme at time t is the $Q-$dimensional population vector $\mathbf{f}(\vec{r},t) = \{f_q,\ q = 0,\ldots,Q-1\}$, specified on the nodes $\vec{r}$ of the $d-$dimensional computational mesh Ω. Let $q-$bulk node $\vec{r} \in \Omega_q$ have its two neighbors $\vec{r} \pm \vec{c}_q$ in the computational domain Ω. We will distinguish bulk and boundary nodes in Ω. The bulk nodes $\vec{r}$ are such that $\vec{r} \in \Omega_q$ for all q. All others are boundary nodes and denoted $\vec{r}_{\rm b}$: they have at least one neighbor along the link q which is not in Ω. Assuming that the initial distribution $\mathbf{f}(\vec{r},0)$ is prescribed, the evolution of the population vectors obeys the following update rule:

$$\begin{aligned} f_q(\vec{r}+\vec{c}_q,t+1) &= \tilde{f}_q(\vec{r},t)\,, \qquad q \in \{0,\ldots,Q-1\}\,, \\ \tilde{f}_q(\vec{r},t) &= f_q(\vec{r},t) + g_q\,,\ g_q = (\mathbf{A}\cdot\mathbf{n})_q\,,\ n_q = f_q - e_q\,. \end{aligned} \tag{1.1}$$

The update is fully defined for bulk node $\vec{r}$ once the equilibrium function $\mathbf{e} = \{e_q\}$ and the set of post-collision corrections $\{g_q\}$, given by the products of collision

matrix $\mathbf{A}[Q][Q]$ and the non-equilibrium vector $\{n_q\}$, are computed for local immobile population $f_0(\vec{r},t)$ and for all neighbor nodes $\vec{r}-\vec{c}_q$. In boundary nodes $\vec{r}_\mathrm{b}$, when $\vec{r}_\mathrm{b}-\vec{c}_q \notin \Omega$, then $f_q(\vec{r}_\mathrm{b},t+1)$ is computed with the help of the boundary schemes discussed in Chapter 3.

The post-collision correction can be divided into its symmetric and anti-symmetric parts for any pair of opposite velocities:

$$g_q = g_q^+ + g_q^- \ , \ g_q^\pm = \frac{1}{2}(g_q \pm g_{\bar{q}}) \ , \ \vec{c}_{\bar{q}} = -\vec{c}_q \ , \ \forall\, q. \tag{1.2}$$

Here and below, any relation with "$\pm$" and/or "$\mp$" addresses *two* different relations: one with the "upper" sign and another one with the "lower" sign, for all the variables. This construct is applied to the populations, their equilibrium and non-equilibrium components:

$$f_q^\pm = \frac{1}{2}(f_q \pm f_{\bar{q}}) \ , \ e_q^\pm = \frac{1}{2}(e_q \pm e_{\bar{q}}) \ , \ n_q^\pm = (f_q^\pm - e_q^\pm) = \frac{1}{2}(n_q \pm n_{\bar{q}}) \ . \tag{1.3}$$

The symmetric parts are equal: $\psi_q^+ = \psi_q^\pm = \frac{1}{2}(\psi_q + \psi_{\bar{q}})$, $\psi_0^+ = \psi_0$, whereas the anti-symmetric parts have opposite signs: $\psi_q^- = -\psi_{\bar{q}}^- = \frac{1}{2}(\psi_q - \psi_{\bar{q}})$, $\psi_0^- = 0$, $\forall\, \psi$.

1.2 External source terms

Let $M(\vec{r},t)$ and $\vec{F}(\vec{r},t)$ be the external mass and momentum source quantities, such that the local mass and momentum in *pre-collision* state $\{f_q(\vec{r},t)\}$ and outgoing state $\{\tilde{f}_q(\vec{r},t)\}$ are connected as:

$$\sum_{q=0}^{Q-1} \tilde{f}_q(\vec{r},t) = \sum_{q=0}^{Q-1} f_q(\vec{r},t) + M(\vec{r},t) \ , \tag{1.4}$$

$$\sum_{q=1}^{Q-1} \tilde{f}_q(\vec{r},t)\vec{c}_q = \sum_{q=1}^{Q-1} f_q(\vec{r},t)\vec{c}_q + \vec{F}(\vec{r},t) \ . \tag{1.5}$$

Hereafter, only mass conservation constraint is relevant for modeling advection-diffusion equations. Then momentum conserved quantities are defined only for hydrodynamic equations. Let $\mathcal{M}$ and $\vec{\mathcal{F}}$ represent the contributions coming from the sources quantities $S_q^\pm$, directly added to outgoing populations:

$$\mathcal{M} = \sum_{q=0}^{Q-1} S_q^+ \ , \ \vec{\mathcal{F}} = \sum_{q=1}^{Q-1} S_q^- \vec{c}_q \ . \tag{1.6}$$

Then the solvability conditions of the system become:

$$\begin{array}{rcl} \sum_{q=0}^{Q-1} g_q^+(\vec{r},t) + \mathcal{M} & = & M\,, \\ \sum_{q=1}^{Q-1} g_q^-(\vec{r},t)\vec{c}_q + \vec{\mathcal{F}} & = & \vec{F}\,. \end{array} \tag{1.7}$$

The second-order order accurate approximation of these relations, for suitable collision operators and equilibrium functions, defines the modeled macroscopic equations. Let us define the microscopic (numerical) mass and momentum quantities as:

$$\begin{array}{rcl} \rho & = & \displaystyle\sum_{q=0}^{Q-1} f_q = \sum_{q=0}^{Q-1} f_q^+\,, \\ \vec{J} & = & \displaystyle\sum_{q=1}^{Q-1} f_q\vec{c}_q = \sum_{q=1}^{Q-1} f_q^-\vec{c}_q\,. \end{array} \tag{1.8}$$

It was recognized in the early works [56, 57, 124], and confirmed by later contributions [25, 66, 86] that the macroscopic momentum, $\vec{j}$ hereafter, has to be redefined with half the forcing $\vec{F}(\vec{r},t)$:

$$\vec{j} = \vec{J} + \frac{\vec{F}}{2}\,. \tag{1.9}$$

This redefinition follows from consistency of the derived mass conservation equation, [56, 57], or the equality of the population flux to the momentum, [66]. With a similar argument of consistency, the macroscopic conserved mass variable ρ^m is redefined in the presence of the mass source (see Appendix A of [74]):

$$\rho^m = \rho + \frac{M}{2}\,. \tag{1.10}$$

The mass sources are relatively rare in LBE studies, although they appear, for instance, in flow modeling during rainfall events or in advection-diffusion phenomena. Let us define now the mass and momentum of equilibrium, $\rho^{\rm eq}$ and $\vec{j}^{\rm eq}$, respectively:

$$\rho^{\rm eq} = \sum_{q=0}^{Q-1} e_q^+\,, \text{ and } \vec{j}^{\rm eq} = \sum_{q=1}^{Q-1} e_q^-\vec{c}_q\,. \tag{1.11}$$

When the external source quantities are added directly to outgoing populations, the equilibrium conserves the local mass and local momentum:

$$\begin{array}{rcl} \mathcal{M} = M & : & \rho^{\rm eq} = \rho\,, \\ \vec{\mathcal{F}} = \vec{F} & : & \vec{j}^{\rm eq} = \vec{J}\,. \end{array} \tag{1.12}$$

One should bear in mind that the source terms can be hidden in the equilibrium, then $S_q^{\pm} = 0$ and relations (1.7) become:

$$\begin{aligned} \sum_{q=0}^{Q-1} g_q^{+}(\vec{r},t) &= M(\vec{r},t)\ ,\ \mathcal{M} = 0\ ,\ \text{and} \\ \sum_{q=1}^{Q-1} g_q^{-}(\vec{r},t)\vec{c}_q &= \vec{F}(\vec{r},t)\ ,\ \vec{\mathcal{F}} = 0\ . \end{aligned} \tag{1.13}$$

We adapt the last approach for the link-wise operators: they may arbitrary split the mass quantity M between ρ^{eq} and $\mathcal{M}$, and momentum quantity $\vec{F}$ between $\vec{j}^{\text{eq}}$ and $\vec{\mathcal{F}}$. Two examples are given by equilibrium distributions (1.42) and (1.48) for hydrodynamic and advection-diffusion equations, respectively.

1.3 Collision operators

1.3.1 Matrix and GLBE/MRT forms

In the original LBE models, the post-collision corrections $\{g_q\}$ are computed as a product of the collision matrix by a non-equilibrium vector. A possible way to define **A** is to choose its eigenvectors and eigenvalues. They were first specified by Higuera & Jimenez [91] for the two-dimensional six-velocity Frisch-Hasslacher-Pomeau (FHP) model with immobile particles and for the four-dimensional face-centered hypercubic (FCHC) model [97] without them. The eigenvectors are built as the polynomials of the velocity components for the FCHC model with the immobile population ($d4Q25$) in [56, 57], for $d2Q9$ in [98], $d3Q13$ [99], $d3Q15$ in [64, 67, 100] and for $d3Q19$ in [100]. The basis vectors are summarized in a common form in the Appendix A of [69].

The idea of the *generalized lattice Boltzmann equation* (GLBE) method of d'Humières [98] is to compute the collision operator directly in the momentum space, spanned by the eigenvector basis of the collision matrix, hence, reconstructing neither the matrix nor any individual equilibrium e_q. The GLBE form, mostly known as the (multiple-relaxation-time) **MRT**-model [100], is much more numerically efficient than the matrix form.

Let us divide the basis eigenvectors on the N^+ symmetric vectors $\mathbf{v}_k^+ = \{v_{k\,q}^+\}$ ($v_{k\,q}^+ = v_{k\,\bar{q}}^+$, $\forall\, q$) and N^- anti-symmetric vectors $\mathbf{v}_k^- = \{v_{k\,q}^-\}$ ($v_{k\,q}^- = -v_{k\,\bar{q}}^-$, $\forall\, q$), with non-zero eigenvalues $\lambda_k^{\pm}$. The equivalent MRT form of equation (1.1) with relation (1.2) becomes:

$$g_q^{\pm} = \sum_{k=1}^{N^{\pm}} \lambda_k^{\pm}(\widehat{f}_k^{\pm} - \widehat{e}_k^{\pm}) v_{kq}^{\pm}\ ,$$

$$\widehat{f}_k^{\pm} = \frac{\mathbf{f}\cdot\mathbf{v}_k^{\pm}}{||\mathbf{v}_k^{\pm}||^2}\,,\ \widehat{e}_k^{\pm} = \frac{\mathbf{e}\cdot\mathbf{v}_k^{\pm}}{||\mathbf{v}_k^{\pm}||^2}\,,\ -2<\lambda_k^{\pm}<0\,. \tag{1.14}$$

The coefficients $\mathbf{f}\cdot\mathbf{v}_k^{\pm}$ are usually called "moments". If the eigenvectors are chosen properly, the first few moments define the local conserved quantities, such that $\mathbf{f}\cdot\mathbf{v}_k^{\pm}=\mathbf{e}\cdot\mathbf{v}_k^{\pm}$, and their eigenvalues are not relevant. The eigenvalues λ_k of some other eigenvectors specify the transport coefficients of the derived macroscopic equations, while the remaining eigenvalues are free ("kinetic") parameters. The number of the free eigenvalues depends on the chosen set of velocities and the nature of the conservation laws. In one of the first works [92], the free eigenvalues were all set equal to -1, the mid-point of the linear stability interval [91, 127] of the evolution equation.

Let us define collision combinations $\Lambda^{eo\,(k,j)}$ as the products of positive eigenvalue functions $\Lambda^{+(k)}$ and $\Lambda^{-\,(j)}$:

$$\begin{aligned}\Lambda^{eo\,(k,j)} &= \Lambda^{+(k)}\Lambda^{-\,(j)}\,,\ k=1,\ldots,N^+\,,\ j=1,\ldots,N^-\,,\\ \Lambda^{+(k)} &= -(\frac{1}{2}+\frac{1}{\lambda_k^+})\,,\ \Lambda^{-\,(j)}=-(\frac{1}{2}+\frac{1}{\lambda_j^-})\,.\end{aligned} \tag{1.15}$$

It appears in our work that the specific combinations $\Lambda^{eo\,(k,j)}$ of the hydrodynamic and free eigenvalues control the numerical errors of the LBE steady solutions beyond the second order and determine the accuracy of boundary and interface closure relations at the second and higher orders, [57]-[59], [74]-[76], and [103]. The free eigenvalues have some impact on the stability, understood only to little extent, [73, 104, 127, 173, 179].

1.3.2 Link-based L operator

To be contrasted with the hydrodynamic models for which great care has been taken to recover isotropic macroscopic equations, many applications of advection-dispersion equations require anisotropic models. A similar mathematical problem appears when transferring a space with anisotropic discretization in different domains on an equidistant computational grid. One possibility to extend the isotropic advection-diffusion models to anisotropic diffusion and/or dispersion form is offered by link (L) operator. The L operator is introduced in [69] such that the projections of any population space vector on the pair of basis vectors associated with the q^{th}-link are equal to its symmetric and anti-symmetric components. Let us abbreviate the basis vectors of L operator as:

$$\mathbf{v}_k^{\pm}=\delta_k\pm\delta_{\bar{k}}\,,\ k=0,\ldots,\frac{Q-1}{2}\,, \tag{1.16}$$

where k^{th} element of population vector δ_k is equal to 1 and all others elements are equal to zero. The projections (1.14) are given by relations (1.3):

$$\widehat{f}_k^{\pm} = f_k^{\pm} \, , \, \widehat{e}_k^{\pm} = e_k^{\pm} \, , \, k = 0, \ldots , \frac{Q-1}{2} \, . \tag{1.17}$$

Specifying an equilibrium distribution $\{e_q^{\pm}\}$ and a pair of collision rates per link $\{\lambda_q^+, \lambda_q^-\}$, the L operator is:

$$g_q^{\pm} = \lambda_q^{\pm} n_q^{\pm} \, , \, \lambda_q^{\pm} = \lambda_{\bar{q}}^{\pm} \, , \, -2 < \lambda_q^{\pm} < 0 \, , \, q = 0, \ldots , Q-1 \, . \tag{1.18}$$

This operator has at most $(Q-1)/2$ distinct positive link-wise "magic" values Λ_q^{eo}, given by the products of the positive eigenvalue functions Λ_q^+ and Λ_q^-:

$$\Lambda_q^{eo} \;\; = \;\; \Lambda_q^+ \Lambda_q^- \, , \, \Lambda_q^{\pm} = -(\frac{1}{2} + \frac{1}{\lambda_q^{\pm}}) \, , \; q = 1, \ldots , \frac{Q-1}{2} \, . \tag{1.19}$$

Using one common eigenvalue λ^+ for all the symmetric components:

$$\lambda_q^+ = \lambda^+ \, , \, q = 0, \ldots , \frac{Q-1}{2} \, , \tag{1.20}$$

the L operator is able to conserve the mass with mass conserving equilibrium functions (1.12). The restriction (1.20) is applied for modeling of all mass conservation equations in our study. Then relations (1.7) and (1.11) become:

$$\Sigma_{q=0}^{Q-1} g_q^+(\vec{r},t) \;\; = \;\; \lambda^+(\rho - \rho^{\rm eq}) \, , \quad \text{i.e.,} \quad \rho^{\rm eq} \;\; = \;\; \rho - \tfrac{M-\mathcal{M}}{\lambda^+} \, . \tag{1.21}$$

The magic combinations of the L operator with the choice (1.20) are denoted as Λ_q^e:

$$\Lambda_q^e \;\; = \;\; \Lambda^+ \Lambda_q^- \, , \, q = 1, \ldots , \frac{Q-1}{2} \, . \tag{1.22}$$

1.3.3 MRT-L operator

A combination of the unit mass vector and $(Q-1)/2$ even order orthogonal polynomial eigenvectors from the MRT basis and $(Q-1)/2$ anti-symmetric L eigenvectors is called MRT-L basis in [71]. This combination has Q (the highest possible value) distinct eigenvalues for the AADE. Its "magic" combinations become:

$$\Lambda_q^{eo\,(k)} = \Lambda^{+(k)} \Lambda_q^- \, , \, q = 1, \ldots , \frac{Q-1}{2} \, , \, k = 1, \ldots , \frac{Q-1}{2} \, . \tag{1.23}$$

One common eigenvalue λ^- for all the anti-symmetric components: $\lambda_q^- = \lambda^-, \forall \, q$, enables the MRT-L model to match the hydrodynamic equations with the momentum conserving equilibrium function (1.12). Then the MRT-L operator becomes equivalent to MRT operator, commonly applied with one relaxation rate for all the non-conserved anti-symmetric modes.

1.3.4 Two-relaxation-times (TRT) operator

The TRT model sets all λ_q^+ equal to λ^+ and all λ_q^- equal to λ^-:

$$g_q^{\pm} = \lambda^{\pm} n_q^{\pm} \ , \ \forall \ q \ . \tag{1.24}$$

This enables the TRT operator to model both mass and momentum conservation relations with conserving equilibrium functions (1.12). In the presence of the source terms, relation (1.21) relates the mass variables. The equilibrium momentum $\vec{j}^{\rm eq}$ is related to population momentum $\vec{J}$, for the hydrodynamic equations:

$$\Sigma_{q=1}^{Q-1} g_q^-(\vec{r},t)\vec{c}_q \ = \ \lambda^-(\vec{J}-\vec{j}^{\rm eq}) \ , \quad \text{i.e.,} \quad \vec{j}^{\rm eq} \ = \ \vec{J} - \tfrac{\vec{F}-\vec{\mathcal{F}}}{\lambda^-} \ . \tag{1.25}$$

The TRT operator is the sub-class of the MRT-operators when all λ_k^+ are equal to λ^+ and all λ_k^- are equal to λ^-. This configuration is often used in previous studies, e.g., [59, 66, 78, 179]. The link-based form (1.24) greatly simplifies the evolution equation and its subsequent analysis.

The TRT operator has only one free "magic" parameter, called Λ^{eo} hereafter:

$$\Lambda^{eo} = \Lambda^- \Lambda^+ \ , \ \Lambda^{\pm} = -(\frac{1}{2} + \frac{1}{\lambda^{\pm}}) \ . \tag{1.26}$$

When λ^+ is fixed via the kinematic viscosity, which is proportional to Λ^+, or when λ^- is fixed via the mean diagonal diffusion coefficient, proportional to Λ^-, the TRT operator can maintain Λ^{eo} at any positive value with the help of the second (free) eigenvalue. We show below that $\Lambda^{eo} = \frac{1}{4}$ has distinctive properties.

1.3.5 Single-relaxation-time (SRT) or BGK operator

The diagonalized (Bhatnagar-Gross-Krook) BGK operator [32, 161] with equal relaxation parameter τ for all collision modes is the sub-class of the TRT operator, with

$$\lambda^- = \lambda^+ = -\frac{1}{\tau} \ , \ \Lambda^{eo}(\tau) = \frac{1}{4}(2\tau - 1)^2 \ . \tag{1.27}$$

The BGK $d2Q9$ model is also directly derived from the continuous Boltzmann equation with the BGK collision by He & Luo [88]. The BGK scheme has no free relaxation parameters. Advocated for the simplicity of its coding and numerical efficiency, the SRT operator gains actually not so much (about $10\% - 15\%$) against the MRT operators when they are coded carefully (see [100]). It is noted that computing the symmetric and anti-symmetric components only once per link, the BGK and TRT are equal in efficiency. Then the BGK operator has not any advantage over the TRT but it lacks its possibility for improvement and control of the

truncation errors, roughly related to powers of $\Lambda^{eo}(\tau)$. Using of smaller transport coefficients ($\tau \to \frac{1}{2}$) is more accurate but quite inefficient for the convergence to steady state and is not robust.

1.4 Chapman-Enskog analysis

Chapman [31] and Enskog [50] independently developed a perturbative approach for solving the Boltzmann equation [19] based on the expansion of the particle distribution around its equilibrium, where each subsequent term brings the correction to all lower-order approximations. Frisch et al [53] adapt this idea for Lattice Gas Methods and relate the values of bulk viscosity and kinematic viscosity to several collision eigenvalues, which are associated with the second order polynomial eigenvectors, hereafter called viscous modes. Developed for mean distributions, this approach naturally fits the Lattice Boltzmann schemes. The GLBE approach of d'Humières [98] and equivalent partial differential equations of Dubois [45] extend it for describing the evolution of all moments. Exact explicit form for all coefficients of the Chapman-Enskog expansion of steady solutions was derived recently in author's work [76], for any equilibrium distribution. This solution is presented in the next section. The Chapman-Enskog approximation takes a simple directional form for L operator, [69, 74]. We demonstrate it for the classical two-times perturbation analysis in Section 1.4.2.

1.4.1 The coefficients of the infinite series for steady solutions

At steady state, the immobile population is found at the equilibrium, hence:

$$n_0 = n_0^+ = g_0^+ = g_0 \equiv 0 \,. \tag{1.28}$$

The subsequent solution addresses the moving populations only. Following the idea of Chapman and Enskog, let us assume that the non-equilibrium steady solution in bulk nodes is sufficiently smooth and may take the form of Taylor expansion around the equilibrium component:

$$f_q^{\pm}(\vec{r},t+1) \;=\; e_q^{\pm}(\vec{r},t) + n_q^{\pm}(\vec{r},t) \;,\; n_q^{\pm}(\vec{r},t) = \sum_{l\geq 1} n_q^{\pm(l)}(\vec{r},t) \,. \tag{1.29}$$

The solution of L operator is looked for in the form:

$$g_q^{\pm}(\vec{r},t) \;=\; \sum_{l\geq 1} g_q^{\pm(l)}(\vec{r},t) \;,\; g_q^{\pm(l)} = \lambda_q^{\pm} n_q^{\pm(l)} \;,\; \forall \; q \,. \tag{1.30}$$

where the post-collision components are related to directional derivatives of the equilibrium:

$$\begin{aligned} g_q^{\pm(2k-1)}(\vec{r}) &= \frac{a_{2k-1}\partial_q^{2k-1}e_q^{\mp}(\vec{r})}{(2k-1)!}\ ,\ k\geq 1\ , \\ g_q^{\pm(2k)}(\vec{r}) &= -2\Lambda_q^{\mp}\frac{a_{2k}\partial_q^{2k}e_q^{\pm}(\vec{r})}{(2k)!}\ ,\ k\geq 1\ , \end{aligned} \tag{1.31}$$

with $\partial_q = (\nabla\cdot\vec{c}_q)$ and $\partial_q^{(l)} = \partial_q\partial_q^{(l-1)}$. The obtained solution for the coefficients $\{a_{2k-1}, a_{2k}\}$, $k\geq 1$, reads:

$$a_1 = 1\ ,\ a_2 = 1\ , \tag{1.32}$$

$$\begin{aligned} a_{2k-1} &= 1+2(\Lambda_q^{eo}-\frac{1}{4})\sum_{1\leq n<k} a_{2n-1}\frac{(2k-1)!}{(2n-1)!(2(k-n))!}\ ,\ k\geq 2\ , \\ a_{2k} &= 1+2(\Lambda_q^{eo}-\frac{1}{4})\sum_{1\leq n<k} a_{2n}\frac{(2k)!}{(2n)!(2(k-n))!}\ ,\ k\geq 2\ . \end{aligned} \tag{1.33}$$

This solution shows an explicit dependency for all coefficients on the "magic" collision combinations Λ_q^{eo} ! We show in the next Chapter that the obtained series presents exact steady solution of the L operator. It follows that all non-dimensional solutions in bulk and their truncation errors are fixed by Λ_q^{eo} and the physical governing parameters of the given problem. When Λ_q^{eo} are fixed, the convergence behaviour with grid refining becomes consistent. It should be remembered that the second-order equations of mass and momentum conservation account only for two first terms, given by $a_1 = 1$ and $a_2 = 1$. The special cases are given by two following values, which annihilate the coefficients of truncation errors related to third and fourth order derivatives of the equilibrium component, respectively :

$$\Lambda_q^{eo} = \frac{1}{12}\ ,\ \text{then}\ a_3 = 0\ , \tag{1.34}$$

$$\Lambda_q^{eo} = \frac{1}{6}\ ,\ \text{then}\ a_4 = 0\ . \tag{1.35}$$

The BGK Navier-Stokes solutions [95], $\tau_3 = \frac{1}{2}+\frac{\sqrt{3}}{6}$ and $\tau_4 = \frac{1}{2}+\frac{\sqrt{6}}{6}$ are given by these relations replacing Λ_q^{eo} with its BGK value: $\Lambda^{eo}(\tau) = (\tau-\frac{1}{2})^2$ (cf. relation (1.27)). In contrast with the BGK model, the TRT model can get any Λ^{eo} value for any selected value of the transport coefficient, which is fixed either by Λ^+ for bulk and kinematic viscosities or by Λ^- for the diffusion coefficient.

When $\Lambda_q^{eo}\equiv\frac{1}{4}$, all coefficients reduce to one ($a_k\equiv 1, \forall\, k$) and the post-collision components become:

$$\Lambda_q^{eo}\equiv\frac{1}{4}:\quad g_q^{\pm(2k-1)}(\vec{r}) = \frac{\partial_q^{2k-1}e_q^{\mp}(\vec{r})}{(2k-1)!}\ ,$$

$$g_q^{\pm(2k)}(\vec{r}) \;=\; -2\Lambda_q^{\mp}\frac{\partial_q^{2k}e_q^{\pm}(\vec{r})}{(2k)!}\,, \tag{1.36}$$

or, using the finite difference operators:

$$\bar{\Delta}_q\psi \;=\; \sum_{k\geq 1}\frac{\partial_q^{2k-1}\psi}{(2k-1)!}\,,\ \Delta_q^2\psi = 2\sum_{k\geq 1}\frac{\partial_q^{2k}\psi}{(2k)!}\,,\ \forall\psi\,, \tag{1.37}$$

one gets:

$$\Lambda_q^{eo} = \frac{1}{4}:\ g_q^{\pm}(\vec{r}) \;=\; \bar{\Delta}_q e_q^{\mp} - \Lambda_q^{\mp}\Delta_q^2 e_q^{\pm}\,,\ \forall\, q\,. \tag{1.38}$$

This relation expresses the non-equilibrium components via the link-wise central finite-difference operators, which are applied to the equilibrium components. In the next Chapter, the recurrence equations (2.5) extend relations (1.38) to any Λ_q^{eo} and to boundary nodes.

1.4.2 Second-order expansion for link-wise operators

We follow classical form of two-times multi-scale expansion for a typical perturbation length ε^{-1}, where ε is a small parameter going to zero in the continuous limit. We develop then a link-wise expansion in terms of $\partial_{q'}$, $\partial_{q'}^2$ and ∂_{t_1}, ∂_{t_2}, such that:

$$\partial_q = \varepsilon\partial_{q'}\,,\ \partial_q^2 = \varepsilon^2\partial_{q'}^2\,,\ \text{and}\ \ \partial_t = \varepsilon\partial_{t_1} + \varepsilon^2\partial_{t_2}\,. \tag{1.39}$$

Assuming that the source terms are included into the equilibrium, the formal expansion of L operator reads:

$$\begin{aligned}
g_q^{\pm(1)} &= \varepsilon(\partial_{t_1}e_q^{\pm} + \partial_{q'}e_q^{\mp})\,,\\
g_q^{\pm(2)} &= \varepsilon^2\partial_{t_2}e_q^{\pm} - \varepsilon^2[\partial_{q'}\Lambda_q^{\mp}\partial_{t_1}e_q^{\mp} + \partial_{q'}\Lambda_q^{\mp}\partial_{q'}e_q^{\pm}]\\
&- \varepsilon^2[\partial_{t_1}\Lambda_q^{\pm}\partial_{t_1}e_q^{\pm} + \partial_{t_1}\Lambda_q^{\pm}\partial_{q'}e_q^{\mp}]\\
&= \varepsilon^2\partial_{t_2}e_q^{\pm} - \varepsilon\partial_{q'}\Lambda_q^{\mp}g_q^{\mp(1)} - \varepsilon\partial_{t_1}\Lambda_q^{\pm}g_q^{\pm(1)}\,.
\end{aligned} \tag{1.40}$$

This form is suitable for any sufficiently smooth equilibrium distribution. The MRT models need to project each subsequent vector $\{g_q^{\pm(l)}\}$ on the eigenvector basis. The TRT and L operators do this very easily, with the simple argument of symmetry. At steady state, relations (1.40) reduce to:

$$g_q^{\pm(1)}(\vec{r}) = \;\; \partial_q e_q^{\mp}(\vec{r})\,,\ \text{and}\ g_q^{\pm(2)}(\vec{r}) = -\Lambda_q^{\mp}\partial_q^2 e_q^{\pm}(\vec{r}). \tag{1.41}$$

This solution coincides with the steady solution (1.31) written for $k = 1$: $a_1 = 1$ and $a_2 = 1$ (cf. relation (1.32)). Following this approach, the TRT and L operators are adapted for anisotropic advection-diffusion equations in [69] and discussed in Section 1.6. The hydrodynamic solutions of the TRT model are discussed in the next section.

1.5 Hydrodynamic equations of the TRT model

The Navier-Stokes equations with variable source terms are derived from the TRT model in Appendix A of [74]. They are resumed in two next sections. *Exact* form of the hydrodynamic TRT based steady equations is presented for Stokes and Navier-Stokes equilibrium in [75, 103] and summarized in Sections 2.4.2 and 2.4.3, respectively. The simple incompressible and compressible solutions of the hydrodynamic TRT scheme are studied in [74, 75]. They include approximate solutions for compressible pulsatile flow, derived in Appendix B of [75].

1.5.1 Equilibrium function

Based on the ideas of [89, 127, 161] and the relations above for ρ, $\rho^{\rm eq}$, ρ^m and $\vec{J}$, $\vec{j}^{\rm eq}$, $\vec{j}$, let us define the equilibrium functions and external source quantities $S_q^{\pm}$, assuming $d2Q9$, $d3Q15$ or $d3Q19$ models:

$$\begin{aligned}
e_q^- &= t_q^\star(\vec{j}^{\rm eq}\cdot\vec{c}_q)\ ,\ S_q^- = t_q^\star(\vec{\mathcal{F}}\cdot\vec{c}_q)\ ,\ q=1,\dots,Q-1\ ,\\
e_0^+ &= e_0 = \rho^{\rm eq} - \sum_{q=1}^{Q-1} e_q^+\ ,\ S_q^+ = t_q^m\mathcal{M}\ ,\ S_0^+ = \mathcal{M} - \sum_{q=1}^{Q-1} S_q^+\ ,\\
e_q^+ &= \mathcal{P}_q^\star(\rho^{\rm eq},\vec{j},\tilde{\rho})\ ,\ \mathcal{P}_q^\star(\rho,\vec{j},\tilde{\rho}) = t_q^\star P + g_S E_q^{(u)}(\vec{j},\tilde{\rho})\ ,\ P = c_s^2\rho\ ,\\
E_q^{(u)}(\vec{j},\tilde{\rho}) &= t_q^\star\frac{3j_q^2 - ||\vec{j}||^2}{2\tilde{\rho}} - \frac{||\vec{j}||^2}{\tilde{\rho}}\alpha_{\varepsilon^\star}\varepsilon_q^\star\ ,
\end{aligned} \tag{1.42}$$

where, for the TRT model :

$$\begin{aligned}
\rho^{\rm eq} &= \rho^m + \Lambda^+ M + \frac{\mathcal{M}}{\lambda^+}\ ,\ \rho^m = \rho + \frac{1}{2}M\ ,\ \rho = \sum_{q=0}^{Q-1} f_q\ ,\\
\vec{j}^{\rm eq} &= \vec{j}\ + \Lambda^-\vec{F} + \frac{\vec{\mathcal{F}}}{\lambda^-}\ ,\quad \vec{j} = \vec{J} + \frac{1}{2}\vec{F}\ ,\ \vec{J} = \sum_{q=1}^{Q-1} f_q\vec{c}_q\ .
\end{aligned} \tag{1.43}$$

We assume $g_S = 1$, $\tilde{\rho} = \rho^m$ (or $\tilde{\rho} = \rho_0$) for modeling the compressible (incompressible, respectively) Navier-Stokes equations and $g_S = 0$ for Stokes equation.

Isotropic equilibrium weights $\{t_q^\star\}$ are uniquely defined by the following (isotropic) conditions:

$$\sum_{q=1}^{Q-1} t_q^\star c_{q\alpha} c_{q\beta} = \delta_{\alpha\beta} \ , \ \forall \alpha, \beta \ , \ \text{and} \ 3 \sum_{q=1}^{Q-1} t_q^\star c_{q\alpha}^2 c_{q\beta}^2 = 1 \ , \ \forall \alpha \neq \beta \ . \tag{1.44}$$

They have one value per velocity class : $\{t_I^\star = \frac{1}{3} \ , \ t_{II}^\star = \frac{1}{12}\}$ for $d2Q9$, $\{t_I^\star = \frac{1}{3} \ , \ t_{III}^\star = \frac{1}{24}\}$ for $d3Q15$, $\{t_I^\star = \frac{1}{6} \ , \ t_{II}^\star = \frac{1}{12}\}$ for $d3Q19$, where Roman number equals $p = ||\vec{c}_q||^2$.

The equilibrium parameter c_s^2 represents the sound velocity in derived equations. Higher order corrections of the transport hydrodynamic coefficients are derived with the help of the dispersion analysis in [21, 102, 127, 164]. The results [127, 164] show that $c_s^2 = \frac{1}{3}$ eliminates the first-order effect of advective velocity on the value of bulk viscosity, and several apparent second-order correction terms for kinematic viscosity. The value $c_s^2 = \frac{1}{3}$ also follows from the *a priori* derivation [88]. We keep c_s^2 as free parameter in our study, restricted to interval $]0, \frac{2}{3}[$ for the positivity of bulk viscosity (see below).

The non-linear (Navier-Stokes) term (1.42) takes its original form [89, 161] (restricted there to $c_s^2 = \frac{1}{3}$) when $\alpha_{\varepsilon^\star} = 0$ and the external sources are either absent or added directly to outgoing populations ($\rho^{\text{eq}} = \rho$ and $\vec{j}^{\text{eq}} = \vec{J}$). The isotropic distribution $\varepsilon^\star = \{\varepsilon_q^\star\}$ has one value per velocity class and is given by the components of the fourth order polynomial, mass and momentum conserving, basis vectors of the MRT model, e.g., $\{\varepsilon_0^\star = 4 \ , \ \varepsilon_I^\star = -2 \ , \ \varepsilon_{II}^\star = 1\}$ for $d2Q9$, $\{\varepsilon_0^\star = 8 \ , \ \varepsilon_I^\star = -2 \ , \ \varepsilon_{III}^\star = 1/2\}$ for $d3Q15$, and $\{\varepsilon_0^\star = 12 \ , \ \varepsilon_I^\star = -4 \ , \ \varepsilon_{II}^\star = 1\}$ for $d3Q19$, see [69, 98, 100, 127]. Its second order moments vanish, $\sum_{q=1}^{Q-1} \varepsilon_q^\star c_{q\alpha} c_{q\beta} = 0$, $\forall \alpha$, $\forall \beta$; hence, the equilibrium projections on this vector do not influence the second-order conservation equations. A particular choice $\alpha_{\varepsilon^\star} = -\frac{1}{24}$ is of special interest for finite-difference interpretation of the obtained LBE stencils (to be reported). This choice presents a necessary condition for compatibility of the parabolic flow in arbitrarily rotated channel with the LBE scheme in the presence of the non-linear equilibrium term, $g_S = 1$ (this is derived in [76] and discussed in Section 6.1.5).

In summary, the equilibrium function (1.42) is defined with two free parameters, c_s^2 and $\alpha_{\varepsilon^\star}$. There exist also the alternative choices for the weights of the forcing term S_q^- (e.g., the anisotropic weights [76], using free projections on the third order polynomial MRT vectors) and for the weights of the pressure and mass terms (using again free projections on $\varepsilon^\star$). In our opinion, when the weights are proportional to $t_q^\star$ for momentum, pressure, $E_q^{(u)}$ and source terms, their link-wise coupling (for all orders) is greatly simplified, as well as the theoretical investigations.

1.5.2 Navier-Stokes equation

Taking the moments of the distribution $g_q^{\pm(2)}$, given by relations (1.40), and substituting there the equilibrium distribution (1.42), one gets the compressible type Navier-Stokes equations with the variable source terms:

$$\begin{aligned}
\partial_t \rho^m &+ \nabla\cdot\vec{j} = M\,,\\
\partial_t \vec{j} &+ g_S\nabla\cdot(\frac{\vec{j}\otimes\vec{j}}{\tilde{\rho}}) = -\nabla P + \vec{F} + \nabla\cdot(\nu\nabla\vec{j}) + \nabla(\nabla\cdot\nu_\xi\vec{j}) + err(\vec{F})\,,\\
P &= c_s^2\rho^m\,,\ \nu = \frac{\Lambda^+}{3}\,,\ \nu_\xi = \Lambda^+(\frac{2}{3}-c_s^2)\,,\ 0<c_s^2<\frac{2}{3}\,,\\
err(\vec{F}) &= \nabla\cdot\frac{\Lambda^+}{3}\nabla\Lambda^-\vec{F} + \nabla\frac{2\Lambda^+}{3}\nabla\cdot\Lambda^-\vec{F}\,.
\end{aligned} \tag{1.45}$$

These equations have the same form as the MRT second order equations. The reader can find the expressions of bulk and kinematic viscosity for MRT $d2Q9$ model in [98, 127], $d3Q13$ in [99], for $d3Q15$ and $d3Q19$ models in [67, 100], for $d4Q25$ in [56]. Both bulk viscosity and kinematic viscosity of the TRT model are however defined via one eigenvalue and they coincide when $c_s^2 = \frac{1}{3}$. We assume hereafter that Λ^+ is fixed by the choice of the kinematic viscosity. The MRT model is more advantageous for the compressible flow, owing to its additional eigenvalue of the viscous modes. The term $err(\vec{F})$ is examined for Brinkman model where the forcing is proportional to velocity. Further corrections may appear from the neglected terms, as $\varepsilon^2\partial_{t_2}\Lambda^-\vec{F}$, $\varepsilon^2\partial_{t_2}\Lambda^+M$ and $\varepsilon\Lambda^+\partial_{t_1}\nabla\cdot E_q^{(u)}(\vec{u})$. Their investigation is left for future work.

The velocity solution (in lattice units) is given as

$$\vec{u} = \frac{\vec{j}}{\tilde{\rho}}\,,\ \vec{j} = \vec{J} + \frac{\vec{F}}{2}, \tag{1.46}$$

where $\tilde{\rho} = \rho_0$ for incompressible Navier-Stokes and Stokes equations, and $\tilde{\rho} = \rho^m$ for compressible Navier-Stokes equations. Further rescaling of this solution to physical variables follows through a standard procedure, equating the governing non-dimensional parameters, as Froude and Reynolds numbers in incompressible regime, plus Mach number in compressible regime, on the physical and computational grids. The macroscopic approximation (1.45) of the LBE solutions is controlled by these numbers. We show in Section 2.4 that the constant values of the magic parameters extend this property for all truncation errors in space.

1.6 Anisotropic advection-diffusion equations (AADE)

Dropping momentum conservation, the BGK scheme was first adapted for the isotropic diffusion equation (see review by D. Wolf-Gladrow [210]), and later for the anisotropic advection-diffusion equations by Zhang et al. [214], using one relaxation parameter per direction. Two alternative modeling approaches are developed for the AADE in the author's work [69]. One is based on the MRT/TRT operators and the anisotropic equilibrium functions. The another one is based on the L operator with the anisotropic set of anti-symmetric eigenvalues. Unlike Zhang's model, both anisotropic approaches [69] make possible to keep the equilibrium mass variable equal to local mass quantity.

The numerical analysis of the anisotropic models is addressed in a series of works in collaboration with D.d Humières: their second order tensors of the numerical diffusion and high-order dispersion relations are presented in [69], available anisotropic diffusion tensors and several analytical results of linear stability analysis are discussed in [73]. These findings are summarized in this section, along with a comparative study of the TRT and forward time central scheme (FTCS) scheme in stability. The extension of the AADE LBE models for stratified sub-domains with the heterogeneous (full) diffusion tensors is investigated in [72, 73] and reviewed in section 4.3. These schemes are adapted for highly non-linear Richards's equation in variably saturated anisotropic heterogeneous aquifers in [68, 71, 72] and reviewed in Section 5.6. Finally, all these new models are supported by the boundary schemes, [70, 71, 73], which are addressed in Section 3.3.6. With their help, several exact solutions of the AADE LBE schemes are constructed in Section 6.3.

1.6.1 Equilibrium function

Let $\mathcal{L} = L'/L$ and $\mathcal{U} = U'/U$ be the ratios of the characteristic values for length and velocity variables between the computational and physical grids. The scaling factors along the coordinate directions with respect to the characteristic scaling $\mathcal{L}$ are presented by the diagonal elements of matrix $\mathbf{L}$, $\mathbf{L} = \mathrm{diag}(L_x, L_y, L_z)$. Then the components of the modeled diffusion tensor $K'_{\alpha\beta}$ (in lattice units) are related to the physical values of diffusion components $H_{\alpha\beta}$ through following relations:

$$K'_{\alpha\beta} = \frac{H_{\alpha\beta}\Delta_t}{\Delta_\alpha \Delta_\beta}\ ,\ \Delta_\alpha = \frac{1}{\mathcal{L}L_\alpha}\ ,\ \Delta_t = \frac{\mathcal{U}}{\mathcal{L}}\ . \tag{1.47}$$

Suitable anisotropic grid transformation with non-uniform spacings ($L_\alpha \neq 1$) (see sketch in Fig. 1.2) makes possible to solve the problems with disperse characteristic lengths, on the reasonable size cuboid computational grids We emphasize

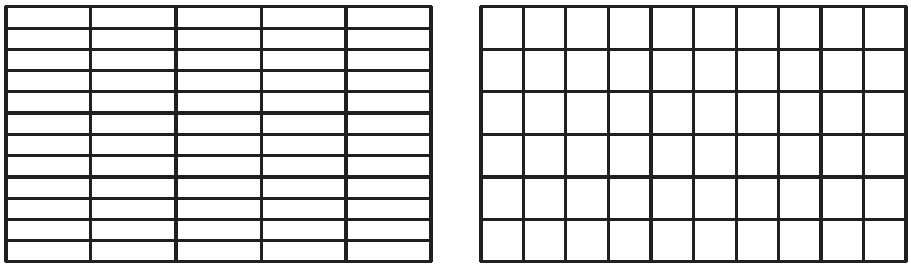

Figure 1.2: Sketch for grid rescaling with $L_z = 4L_x$ from the anisotropic physical grid (left picture) to computational cuboid grid of the LBE (right picture).

that this approach differs principally from the extension of the LBE method on the stretched grids, [21, 127, 154], or the hierarchical grids, [184, 200].

We will distinct "simple" or "minimal stencil" $d1Q3$, $d2Q5$ and $d3Q7$ models, then $d3Q13$ model and two moving velocity classes models. We show in [69] that the MRT operator can match all d anisotropic diagonal components with the help of the distinct velocity eigenvalues, based on usual isotropic equilibrium. The MRT operator should however take equal velocity eigenvalues in the presence of the symmetric cross-diffusion elements, hence using the anisotropic equilibrium functions, like the TRT. In what follows, we restrict ourselves to two "extreme" techniques, referred to as the TRT-E model, based on the TRT operator and anisotropic equilibrium weights $\{E_q\}$ and L model, based on the L operator with all equal symmetric eigenvalues and isotropic equilibrium: $\{E_q = t_q^\star\}$. We again include the sources into the equilibrium functions $\{e_q\}$ (hence $S_q^\pm = 0$) and define it as:

$$\begin{aligned} e_q^- &= t_q^\star(\vec{J}\cdot\vec{c}_q)\,, \quad q\in\{1,\dots,Q-1\}\,,\ e_0^- = 0\,,\\ e_q^+ &= \bar{\mathcal{D}}(s)E_q - \frac{M_q}{\lambda^+}\,,\ E_q = E_{\bar{q}}^-\,,\ M_q = t_q^m M\,,\ q\in\{1,\dots,Q-1\}\,,\\ e_0^+ &= e_0 = s + \Lambda^+ M - \sum_{q=1}^{Q-1} e_q^+\,,\ s = \sum_{q=0}^{Q-1} f_q + \frac{M}{2}\,. \end{aligned} \tag{1.48}$$

The mass weights t_q^m are usually taken proportional to isotropic weights $t_q^\star$. The weights $\{t_q^\star\}$ are defined with relations (1.44) (only first condition is relevant for simple stencils). Alternatively, they can all be set equal to zero: then the mass quantity is introduced by e_0. The solution for weights E_q is discussed below. The "diffusion function" $\bar{\mathcal{D}}(s)$ and "advection function" $\vec{J}(s)$ are prescribed (linear or non-linear) functions of the conserved quantity s. The $d-$dimensional vector $\vec{J} = \{\mathcal{U}L_\alpha K_\alpha\}$ presents the rescaled vector $\vec{K}$, $\nabla\cdot\vec{K}$ being the advection term in physical space. The linear convective-diffusion equation is matched with $\bar{\mathcal{D}}(s) = H^{\rm eq}s$

(where $H^{\rm eq}$ is some constant) and $\vec{J} = s\vec{U}$, where $\vec{U} = \mathcal{U}\mathbf{L}\vec{u}$ and $\vec{u}$ is physical advective velocity.

Motivated by modeling of Richard's equation, which is mainly diffusion-dominant problem, our study of choice of the eigenvalues and equilibrium parameters was first concentrated in this domain. Necessary diffusion-dominant linear stability condition constrains the equilibrium weight of the rest population to interval $[0\,,1]$ for minimal models and $d3Q15$ models:

$$0 \leq E_0^+ = \frac{e_0}{s} \leq 1\ ,\ \text{or}\ \ 0 \leq \left[\sum_{q=1}^{Q-1} E_q\right] \bar{\mathcal{D}}(s)/s \leq 1 \quad \text{if} \quad M = 0\ . \tag{1.49}$$

The velocity models where $\sum_\alpha c_{q\alpha}$ does not take odd values $\forall q \neq 0$, as $d2Q9$ and $d3Q19$, do not necessarily constraint E_0^+, [104]. Further details are given in Sections 1.6.6 and 1.6.7. We interpret this stability condition below for two collision strategies, given by relations (1.60)- (1.62) and (1.63)- (1.65).

1.6.2 Generic AADE

The second-order approximation of the solvability condition $\sum_{q=0}^{Q-1} g_q^+ = M$ takes the following form:

$$\partial_t s \ + \ \nabla\cdot\vec{J} = \nabla\cdot\vec{D} + M\ ,\ \vec{D} = -\vec{\Phi}\ ,\ \vec{\Phi} = \{\Phi_\beta = (\Phi\cdot\mathbf{c}_\beta)\}\ , \tag{1.50}$$

$$\Phi \ = \ \{\Phi_q = -\Lambda_q^- g_q^-\}\ ,\ \mathbf{c}_\beta = \{c_{q\beta}\}\ ,\ \beta \in \{1,\ldots,d\}\ . \tag{1.51}$$

Hereafter, $d-$dimensional vector $\vec{\Phi} = \{\Phi_\beta\}$ is called the "diffusive flux". Its components are given by the projections of the non-equilibrium vector $\{\Phi_q\}$ on the velocity vectors. For a pure diffusion equation, or when the numerical diffusion induced by the advective term $\partial_q\partial_t e_q^-$ is neglected or removed by the proper equilibrium corrections (see Section 1.6.3), the first order expansion (1.41) yields:

$$\Phi_q \ = \ -\Lambda_q^-\partial_q[\bar{\mathcal{D}}(s)E_q] + O(\varepsilon^2)\ . \tag{1.52}$$

Then the diffusion term $\nabla\cdot\vec{\Phi}$ is obtained from relations (1.50) with (1.51). Assuming uniform weights $\{E_q\}$, it takes a form:

$$\nabla\cdot\vec{\Phi} \ = \ \partial_\alpha\left[K'_{\alpha\beta}\partial_\beta\bar{\mathcal{D}}(s)\right]\ , \tag{1.53}$$

$$K'_{\alpha\beta} \ = \ 2\sum_{q=1}^{(Q-1)/2} \mathcal{T}_q c_{q\alpha}c_{q\beta}\ ,\ \mathcal{T}_q = \Lambda_q^- E_q\ . \tag{1.54}$$

The diffusion tensor is related to Λ_q^- and E_q by their product only. Using notation $\mathcal{T}_\alpha$ for coordinate links ($c_{q\alpha}c_{q\beta}=0$ for all $\beta\neq\alpha$) and $\mathcal{T}_q$ for diagonal (remaining) links, the solution to equations (1.54) takes a form:

$$\mathcal{T}_\alpha = \frac{1}{2}(K'_{\alpha\alpha}-s_{\alpha\alpha})\ ,\ \alpha\in\{1,\ldots,d\}\ , \tag{1.55}$$

$$\mathcal{T}_q = \frac{1}{\sum_{q=1}^{Q-1} c_{q\alpha}^2 c_{q\beta}^2}(s_{\alpha\beta}+\sum_{\alpha\neq\beta} K'_{\alpha\beta}c_{q\alpha}c_{q\beta})\ ,\ s_{\alpha\beta}=2\sum_{q(diag)}\mathcal{T}_q c_{q\alpha}^2 c_{q\beta}^2\ ,\forall\,\alpha\ ,\ \forall\,\beta\ . \tag{1.56}$$

Models having only the coordinate links ($d2Q5$, $d3Q7$) yield $s_{\alpha\alpha}=0$ and they cannot handle off-diagonal elements. The $d3Q13$ set has no links along the axes and relations (1.56) set the $\mathcal{T}_q$ values for its 6 diagonal links (with $s_{\alpha\alpha}=K'_{\alpha\alpha}$ and $s_{\alpha\beta}=(s_{\alpha\alpha}+s_{\beta\beta}-s_{\gamma\gamma})/2$). For the $d2Q9$ and $d3Q15$ sets, the $\{s_{\alpha\alpha}\}$ have the same value, s_d hereafter, that is the only free parameter:

$$d2Q9\ ,\ d3Q15:\ \ s_{\alpha\beta}=s_{\beta\beta}=s_d\ ,\ \forall\,\alpha\ ,\ \forall\,\beta\ . \tag{1.57}$$

For the $d3Q19$ set, the three independent values s_{xx}, s_{yy} and s_{zz} present three free parameters.

The non-negativity of the diagonal diffusion elements and the collision combinations $\{\mathcal{T}_q\geq 0\}$ restricts free parameters to

$$s_{\alpha\alpha}\leq K'_{\alpha\alpha}\ ,\ \text{and}\ |K'_{\alpha\beta}|\leq s_{\alpha\beta}\ \ \text{for}\ \alpha\neq\beta. \tag{1.58}$$

The range of the available off-diagonal elements is estimated by relations (28) to (30) in [73] for positive set $\{\mathcal{T}_q\}$. They show that the largest off-diagonal element is smaller than the smallest diagonal element for $d2Q9$ and $d3Q15$ and the sum of two off-diagonal elements is smaller than the diagonal element, per each line of the diffusion tensor, for $d3Q19$ model. We stress that these conditions are not proved as necessary stability conditions, although numerical simulations with positive equilibrium weights E_q (hence $\mathcal{T}_q>0$ since $\Lambda_q^->0$) are often more stable.

1.6.3 Second order anti-diffusion tensor

In the presence of the equilibrium (advective) term e_q^-, the diffusion tensor obtained using relations (1.55)-(1.56) gets an apparent correction $\vec{D}^-$, which is the numerical diffusion of the scheme. This term is derived with the second-order Chapman-Enskog analysis in [69]. Using the TRT operator, it becomes:

$$\vec{D}_\alpha^- \approx -\Lambda^- U_\alpha\partial_\beta J_\beta \approx -\Lambda^-\partial_\beta U_\alpha U_\beta s\ ,\ \vec{J}=s\vec{U}. \tag{1.59}$$

The diagonal components of the numerical diffusion tensor (1.59) are negative. One can remove this tensor with the help of the following equilibrium correction: $e_q^+ \to e_q^+ + E_q^{(u)}(s\vec{U},s)$, where two argument function $E_q^{(u)}(\cdot,\cdot)$ is the same as the one used for Navier-Stokes term, and given by relation (1.42) for $d2Q9$, $d3Q15$ and $d3Q19$ models. We refer to the work [99] for the non-linear equilibrium term of $d3Q13$ model. A similar construct takes place for the MRT operator (relation (30) of [69]).

The minimal diffusion models, $d2Q5$ and $d3Q7$ cannot remove the tensor of the numerical diffusion, except when the velocity is parallel to one of the coordinate axes or the off-diagonal elements $U_\alpha U_\beta$ are neglected. Hereafter, we set for the minimal models: $E_q^{(u)}(s\vec{U},s) = \frac{1}{2}s\sum_\alpha U_\alpha^2 c_{q\alpha}^2$, $q \neq 0$. An annihilation of the off-diagonal elements of the tensor of the numerical diffusion with "pseudo-velocities", which present explicit finite-difference equilibrium correction, is proposed in a very recent work [173]. However, from their results, the $d2Q9$ behaves better with the non-linear equilibrium term $E_q^{(u)}$ than with the "pseudo-velocities".

The tensor of the numerical diffusion of the L operator (relation (44) of [69]) is not symmetric for general (anisotropic) set of the eigenvalues and no simple way was found to remove it by the L model itself. Finally, very little attention was paid to the numerical diffusion induced by the non-linear and time dependent advection functions $\vec{J}(s)$ (very simplified estimations are proposed by relations (25)-(26) in [71]).

1.6.4 Anisotropic weights or anisotropic eigenvalues

Two principal techniques to select $\{\Lambda_q^-\}$ and $\{E_q\}$ giving their product $\mathcal{T}_q$ (relations (1.55)- (1.56)) are introduced in [69] and generalized in [71, 73]. They are referred to as the L model and the TRT-E model.

The **L model** combines an anisotropic eigenvalue set $\{\Lambda_q^-\}$ with a conventional *isotropic* equilibrium function:

$$E_q = c_e t_q^\star \text{ , and } \Lambda_q^- = \mathcal{T}_q/(c_e t_q^\star) \text{ , } \quad q \in \{1,\ldots,Q-1\} \text{ .} \tag{1.60}$$

Then, using linear diffusion function

$$\bar{\mathcal{D}}(s) = H^{\text{eq}} s \text{ , } H^{\text{eq}} > 0 \text{ ,} \tag{1.61}$$

and when the non-linear term $E_q^{(u)}$ is omitted or neglected, the immobile population is restricted to interval $[0,1]$ if

$$c_e \leq \frac{c_e^{\max}}{H^{\text{eq}}} \text{ , } c_e^{\max} = [\sum_{q=1}^{Q-1} t_q^\star]^{-1} \text{ .} \tag{1.62}$$

When $\{E_q\}$ are specified, relations (1.55)-(1.56) yield the linear system of equations for $\{\Lambda_q^-\}$. The so-called "local" eigenvalue strategy, given by relations (B.10) to (B.12) in [73], yields the positivity of Λ_q^- by selecting the free parameter s_d between the largest value of the linear combination $\sum_{\alpha\beta} K'_{\alpha\beta} c_{q\alpha} c_{q\beta}$ and the smallest diagonal element $K'_{\alpha\alpha}$. The isotropic tensors get the isotropic set $\{\Lambda_q^-\}$.

The **TRT-E model** combines the TRT operator and *anisotropic* equilibrium weights $\{E_q\}$ (called E model in [69]). When Λ^- is selected, then the relations (1.55)-(1.56) yield the equilibrium weights $E_q = \mathcal{T}_q/\Lambda^-$, in function of the free parameters $s_{\alpha\beta}$. One can project the obtained set $\{E_q\}$ on any selected basis. The reader can find in [71] (Tables 1 and 2) and in [73] (Appendix B) their projections on the symmetric vectors from the MRT basis, for $d2Q9$ and $d3Q15$ models. Selecting free projection on the fourth order polynomial basis vector $\varepsilon^\star$, one sets s_d value for these models (cf. relation (20) in [71] and relation (B.4) in [73]). Let us decompose $\{E_q\}$ onto their isotropic and anisotropic components, $\{I_q\}$ and $\{A_q\}$, respectively:

$$E_q = I_q + A_q \;,\; q = 0, \ldots, Q-1 \;,\; A_0 = 0 \;. \tag{1.63}$$

The isotropic components are equal for all velocities of the same magnitude. It can be shown that $\sum_q E_q = \sum_q I_q$ for each class of moving velocities. We also define the reduced tensor $(\mathcal{D}_{\alpha\beta})$ and its mean value c_e:

$$\mathcal{D}_{\alpha\beta} = \frac{K'_{\alpha\beta}}{\Lambda^-} \;, \qquad c_e = \frac{1}{d} \sum_{\alpha \in \{1,\ldots,d\}} \mathcal{D}_{\alpha\alpha} \;. \tag{1.64}$$

The natural choice is to set

$$I_q = c_e t_q^\star \;, \text{ then } \; s_d = \sum_\alpha K'_{\alpha\alpha}/(3d) = \frac{\Lambda^- c_e}{3} \;. \tag{1.65}$$

The last relation is derived taking a sum of relations (1.55) for all coordinate links. Then the rest population is found inside stability interval $[0,1]$ when Λ^- obeys the following constraint for linear diffusion set-up (1.61), again assuming $E_q^{(u)} = 0$:

$$\Lambda^- \geq \frac{\sum_\alpha K'_{\alpha\alpha}}{d} \frac{H^{\mathrm{eq}}}{c_e^{\max}} \;. \tag{1.66}$$

We compare this condition to FTCS stability criteria in Section 1.6.6.

The M model [73], a particular combination of the E and L models is built with distinct eigenvalues for the coordinate and diagonal links; all diagonal links

get equal eigenvalues. Then the off-diagonal elements are captured through the equilibrium projections on the polynomial vectors $\mathbf{p}^{(\alpha\beta)} = \{c_{q\alpha}c_{q\beta}\}$, as for the E model.

It has been a difficult task to give a priority to anisotropic eigenvalues or anisotropic equilibrium distributions, due to the number of available strategies and the way they mix the different sources of error. It has been found that the TRT-E model and partially the M model may smooth truncation errors with a proper choice of the free eigenvalue λ^+. An important advantage of the TRT-E model is that it can keep one value of magic combination for all links. At the same time, TRT-E and M models handle the variation of anisotropic properties through variable (or discontinuous) equilibrium weights, thus they generally require equilibrium corrections on the interfaces for continuity of the diffusion function, unlike the L model. We come back to this problem in Section 4.3.

1.6.5 High-order corrections for linear AADE.

The next order corrections for the coefficients of anisotropic diffusion tensors and advection velocity were obtained with the help of the dispersion analysis by D. d'Humières. Their synthesis is presented in Appendix B of [69]. The solution of the evolution equation with the anisotropic equilibrium function (1.48) and $\bar{\mathcal{D}}(s) = s$ and $\vec{J} = s\vec{U}$ is looked for in the form: $\mathbf{f}_0 \exp(i[\vec{k}\cdot(\vec{r}-\vec{U}t) - \omega t])$, where $\omega(\vec{k}) = -i\nu(\vec{k})k^2$, $\nu(\vec{k}) = \sum_{\alpha,\beta} K'_{\alpha\beta}\frac{k_\alpha k_\beta}{k^2}$ and $\vec{k} = (k_x,k_y,k_z) = k(\cos\theta\sin\phi, \sin\theta\sin\phi, \cos\phi)$ is a given wave vector. Also, $z = \exp(-i(\omega + \vec{k}\cdot\vec{U})t)$ and $\mathbf{f}_0$ are the eigenvalues and eigenvectors, respectively, of the linear operator $\Xi = \mathbf{S}^{-1}\cdot(\mathbf{I} + \mathbf{A}\cdot(\mathbf{I} - \mathbf{E}^{\mathrm{eq}}))$, $\mathbf{e} = \mathbf{E}^{\mathrm{eq}}\cdot\mathbf{f}$ and $\mathbf{S} = \mathrm{diag}(\exp(\vec{k}\cdot\vec{c}_j))$. The solution [69] examines the k^2 and k^4 relative corrections $\nu_1^{(\mathrm{r})}$ and $\nu_2^{(\mathrm{r})}$ with respect to the assumed (derived from the second-order Chapman-Enskog analysis) anisotropic diffusion form $\nu(\vec{k})$:

$$\nu^{\mathrm{LB}}(\vec{k}) = \nu(\vec{k})(1 + \nu_1^{(\mathrm{r})}(\vec{k})k^2 + \cdots + \nu_n^{(\mathrm{r})}(\vec{k})k^{2n} + \cdots)\ . \tag{1.67}$$

The general form of $\nu_1^{(\mathrm{r})}(\vec{k})$ for the TRT-E model is presented by relation (B.2) of [69]. When $K'_{\alpha\beta}$ is isotropic and $E_q = c_e t_q^\star$ ($a_e = 0$, $c_s^2 = c_e$ in notations [69]), then $\nu_1^{(\mathrm{r})}(\vec{k})$ is isotropic (and becomes equal to function $f_1(\lambda^-,\lambda^+,c_e)$ in relation (B.2) of [69]). Let us elaborate this term as:

$$\nu_1^{(\mathrm{r})}(\vec{k}) \quad = \quad c_e((\Lambda^-)^2 - \frac{1}{4}) + (1-c_e)(\Lambda^{eo} - \frac{1}{4}) + \frac{1}{4}(c_e - \frac{1}{3})\ ,\ c_e \le 1\ . \tag{1.68}$$

This form tells us that the TRT model with $\Lambda^{eo} > (\Lambda^-)^2$ has higher values of the diffusion correction than the BGK model, where $\nu_1^{(\mathrm{r})}(\vec{k}) = ((\Lambda^-)^2 - \frac{1}{4}) + \frac{1}{4}(c_e - \frac{1}{3})$.

Moreover, when $c_e = \frac{1}{3}$, the BGK correction vanishes for $\tau = 1$, a choice often found as most accurate. Then $\nu_1^{(r)}(\vec{k})$ becomes negative for $\Lambda^- < \frac{1}{2}$ ($\tau < 1$).

Using the TRT model, the correction $\nu_1^{(r)}(\vec{k})$ vanishes if the free eigenvalue λ^+ is set equal to λ_e^{is}, given by relation (B7) of [69], or, equivalently, if $[\Lambda^{eo}(\Lambda^-, c_e)]^{is}$ is given as :

$$[\Lambda^{eo}(\Lambda^-, c_e)]^{is} = \frac{1}{4} + \frac{(c_e(\Lambda^-)^2 - \frac{1}{12})}{(c_e - 1)} \, , \; 0 < c_e < 1 \, . \tag{1.69}$$

Here, $\Lambda^{eo}(\Lambda^-, c_e)]^{is} = \Lambda^-[\Lambda^+]^{is}$, $[\Lambda^+]^{is} = -(\frac{1}{2} + \frac{1}{\lambda_e^{is}})$,

then:

$$[\Lambda^{eo}(\Lambda^-)]^{is} = \frac{3 - 4(\Lambda^-)^2}{8} \, , \; i.e., \; \lambda_e^{is} = \lambda^-(2 + \lambda^-) \;\; \text{if} \;\; c_e = \frac{1}{3} \, . \tag{1.70}$$

This solution reduces to mentioned above case: $[\Lambda^{eo}]^{is} = \frac{1}{4}$ for $\Lambda^- = \frac{1}{2}$ ($\tau = 1$). The solution for the next order correction $\nu_2^{(r)}(\vec{k})$ is given by relation (B.9) of [69], assuming that $\nu_1^{(r)}(\vec{k})$ vanishes with the help of the relation (1.69). The particular values given there by relation (B.10) for λ^- and by relation (B.11) for c_e annihilate $\nu_2^{(r)}$, such that the relative error becomes in k^6.

The specific magic value

$$\Lambda^{eo} = \frac{1}{6} \tag{1.71}$$

annihilates the anisotropic component in $\nu_1^{(r)}(\vec{k})$ (so-called "optimal diffusion solution"). The correction is anisotropic when either $\vec{k}$ is inclined with respect to the coordinate axis and the isotropic weights are not proportional to $t_q^\star$, or the diffusion tensor is anisotropic. The magic combination becomes equal to $\frac{1}{6}$ on the solution $\lambda^+ = \lambda_e^{is}(\lambda^-, c_e)$ for one particular value, $\lambda^- = \lambda_D^0$:

$$\lambda_D^0 = -3 + \sqrt{3} \, , \; \forall \;\; c_e \, . \tag{1.72}$$

The combination of this value with $\lambda_e^{is}(\lambda_D^0)$ eliminates $\nu_1^{(r)}(\vec{k})$ for isotropic and anisotropic tensors. The BGK operator with the "optimal convective" solution

$$\Lambda^{eo} = \frac{1}{12} \, , \; \lambda^+ = \lambda^- = \lambda_D^0 \tag{1.73}$$

annihilates the k^2-correction $u_1^{(r)}(\vec{k})$ to the advective velocity:

$$\vec{k} \cdot \vec{U}^{LB} = \vec{k} \cdot \vec{U}(1 + u_1^{(r)}(\vec{k})k^2 + \cdots + u_n^{(r)}(\vec{k})k^{2n} + \cdots) \, . \tag{1.74}$$

It follows that both $u_1^{(\mathrm{r})}(\vec{k})$ and $\nu_1^{(\mathrm{r})}(\vec{k})$ cannot be canceled simultaneously via the free eigenvalue.

All derived analytical estimations for high-order apparent corrections and second order numerical diffusion were confirmed in multi-dimensions by evolution of the concentration wave and Gaussian pick (see [69]). Also, the third order Chapman-Enskog analysis and numerical study [173] for isotropic advection-diffusion equation confirm that the solution (1.73) removes the numerical dispersion. Another example of using this choice is given by study [184].

1.6.6 Optimal TRT scheme

This is given by a specific value of magic combination:

$$\Lambda^{eo} = \frac{1}{4}\,. \tag{1.75}$$

It was first shown in [104] with the help of the Neumann analysis that the stability bounds of the TRT model with $\Lambda^{eo} = \frac{1}{4}$ are independent of the eigenvalues for any AADE equilibrium function and all considered velocity sets. This result is signalized in [73] (without proof) and confirmed by our numerical linear stability analysis. Then, for any Λ^-, and when $\Lambda^+ = \frac{1}{4\Lambda^-}$, the stability bounds for equilibrium variables are equivalent to those of the BGK scheme $\Lambda^- = \Lambda^+ = \frac{1}{2}$ ($\tau = 1$). In this work, we propose an alternative derivation of this special property of $\Lambda^{eo} = \frac{1}{4}$ directly from the time-dependent recurrence equations in Sections 2.6 and 2.7. It appears that this unexpected property has the same origin as the unconditional stability of the Du Fort-Frankel diffusion scheme (see, e.g., [155, 122]).

As a next step, the equilibrium stability bounds can be set using the results known for the forward Euler in time and central in space scheme (FTCS) or, when the second order numerical diffusion is removed with $E_q^{(u)}$, for the (modified) MFTCS scheme. The MFTCS scheme is also known as Lax-Wendorf scheme. The minimal stencil FTCS scheme for advection-diffusion equation reads:

$$\frac{s(\vec{r},t+\Delta_t)-s(\vec{r},t)}{\Delta_t} + \sum_\alpha U_\alpha \frac{s(x_\alpha+\Delta_\alpha,t)-s(x_\alpha-\Delta_\alpha,t)}{2\Delta_\alpha} = \sum_\alpha H_{\alpha\alpha}\Delta_\alpha^2 s(\vec{r},t)\,, \tag{1.76}$$

where s is grid laplace operator: $\Delta_\alpha^2 s(\vec{r}) = (s(x_\alpha+\Delta_\alpha) - 2s(\vec{r}) + s(x_\alpha-\Delta_\alpha))/\Delta_\alpha^2$. Hindmarsch et al. [93] prove that this scheme is stable in von Neumann sense, if and only if the following conditions take place:

$$0 \le \sum_\alpha m_{\alpha\alpha} \le 1\,, \tag{1.77}$$

and

$$\sum_\alpha \frac{U_\alpha^2}{m_{\alpha\alpha}} \quad \leq \quad 1 \text{ , or equivalently , } \sum_\alpha U_\alpha Pe_\alpha \leq 1 \text{ ,} \tag{1.78}$$

where the dimensionless parameters are:

$$m_{\alpha\alpha} \quad = \quad 2\frac{H_{\alpha\alpha}\Delta_t}{\Delta_\alpha^2} \text{ , } U_\alpha = \frac{u_\alpha \Delta_t}{\Delta_\alpha} \text{ , } Pe_\alpha = \frac{u_\alpha \Delta_\alpha}{2H_{\alpha\alpha}} = \frac{U_\alpha}{m_{\alpha\alpha}} \text{ .} \tag{1.79}$$

The condition (1.77) is more restrictive when all $Pe_\alpha < 1$ whereas (1.78) prevails when all $Pe_\alpha > 1$. The conditions (1.78) necessary imply Courant-Friedrichs-Lewy conditions $U_\alpha \leq 1$. The stability results for the MFTCS scheme are obtained replacing $m_{\alpha\alpha}$ by $m_{\alpha\alpha} + U_\alpha^2$. Let us interpret these conditions for the TRT model.

1.6.7 The TRT against the FTCS

The stability bounds of the minimal BGK models with $\Lambda^- = \frac{1}{2}$ are first set for $d1Q3$, $d2Q5$ and $d3Q7$ models. Their equilibrium weights are restricted to coordinate weights: $E_q = E_\alpha = \frac{1}{2}\frac{K'_{\alpha\alpha}}{\Lambda^-}$ when $c_{q\alpha} \neq 0$. They become all equal to isotropic weights $E_\alpha = \frac{1}{2}c_e$ when $K'_{\alpha\alpha}$ are all equal. The *necessary and sufficient* stability bounds of the BGK model with $\tau = 1$ are set by relations (1.77) and (1.78), replacing there $m_{\alpha\alpha}$ by $2K'_{\alpha\alpha} = 2E_\alpha$ when $E_q^{(u)} = 0$; otherwise: $m_{\alpha\alpha} \to 2E_\alpha + {U_\alpha}^2$. The "diffusive" conditions (1.77) and "convective" conditions (1.78) become:

$$0 \leq E_0 \leq 1 \text{ ,} \tag{1.80}$$

and

$$\sum_\alpha \frac{{U_\alpha}^2}{2E_\alpha} \quad \leq \quad 1 \text{ , } \quad \text{if} \quad E_q^{(u)} = 0 \text{ ,} \tag{1.81}$$

$$\sum_\alpha \frac{{U_\alpha}^2}{2E_\alpha + {U_\alpha}^2} \quad \leq \quad 1 \text{ , } \quad \text{if} \quad E_q^{(u)} \neq 0 \text{ .} \tag{1.82}$$

For isotropic tensor, two first conditions become:

$$E_q^{(u)} = 0 \quad : \quad c_e \leq \frac{1}{d} \text{ , and } ||U||^2 \leq c_e \text{ .} \tag{1.83}$$

Then, replacing c_e with $c_e + U_\alpha$, and taking a sum over $\alpha = 1, \ldots, d$, these conditions become:

$$E_q^{(u)} \neq 0 \quad : \quad ||U||^2 \leq 1 - c_e d \text{ , } \forall d \text{ , and } ||U||^2 \leq c_e \frac{d}{d-1} \text{ , } d \geq 2 \text{ .} \tag{1.84}$$

We stress that the conditions (1.83) and (1.84) present necessary and sufficient stability conditions for minimal isotropic models, and the conditions (1.80)-(1.82) present necessary and sufficient stability conditions for minimal anisotropic models. The proof of their sufficiency can be borrowed from [104]. For any dimension, the largest velocity is reached on the "diffusion" boundary ($c_e = 1$) when the numerical diffusion is present. For $d1Q3$ model this condition is equivalent to the CFL criteria when $c_e = 1$: $||U||^2 \leq 1$. This particular case, corresponding to $d1Q2$ model without rest populations, is a subject of study [165]. Several analytical estimations for BGK model at $\tau = 1$ and $E_q^{(u)} = 0$ are also presented in [188] for $d2Q4$ (with $c_e = \frac{1}{2}$) and $d2Q9$ model (with $c_e = \frac{1}{3}$), they satisfy the condition (1.83).

When the numerical diffusion is removed, the conditions (1.84) suggest the following (optimal) values c_e in two and three dimensions where "convective" and "diffusion" curves intersect and yield the largest velocity: $c_e = \frac{1}{4}$ then $||U||^2 < \frac{1}{2}$ for $d2Q5$ and $c_e = \frac{2}{9}$ then $||U||^2 < \frac{1}{3}$ for $d3Q7$. In one dimension, the highest velocity amplitude $||U||^2 = 1$ is reached for $c_e = 0$.

It appears from the Fourier analysis [104] that the necessary stability condition for $d3Q15$ model also constrains the equilibrium weight of the immobile population as given by condition (1.80), then $||U||^2 < 3 - 7c_e$ with the choice (1.65): $I_q = c_e t_q^\star$. We estimate the optimal stability bounds of $d3Q15$ model using $||U||^2 \leq 2c_e$ as the second (necessary) condition, then $c_e = \frac{1}{3}$ and $||U||^2 < \frac{2}{3}$ for $d3Q15$. We are working on the extension of this analysis to $d2Q9$ model and $d3Q15$ models with the most possible number of free equilibrium parameters.

In physical units, the condition (1.80) becomes for diffusion problem ($\vec{U} = 0$) or when $E_q^{(u)} = 0$:

$$\Delta_t \quad \leq \quad \Lambda^- \sum_\alpha \frac{\Delta_\alpha^2}{H_{\alpha\alpha}} \,. \tag{1.85}$$

When $\Lambda^- = \frac{1}{2}$, this condition is equivalent to diffusion-dominant condition (1.77). Selecting $\Lambda^- > \frac{1}{2}$, the TRT scheme gains in computational efficiency against the FTCS.

The inverse situation takes place when $\Lambda^- < \frac{1}{2}$ in convection-dominant regime, where the major condition $||U||^2 \leq Const\ c_e$ becomes (in physical units)

$$\Delta_t \quad \leq \quad Const \frac{\sum_\alpha H_{\alpha\alpha}}{\Lambda^- ||u||^2} \,. \tag{1.86}$$

The TRT model gets more advantageous stability limits when $\Lambda^- < \frac{1}{2}$. It follows that it is worthwhile to work with $\Lambda^- > \frac{1}{2}$ in the diffusion domain, and then to maintain the space accuracy with suitable range of Λ^+. In contrast, it is more

efficient to take $\Lambda^- < \frac{1}{2}$ in convection domain, then to maintain stability with a proper choice of Λ^+. One can then use $\Lambda^{eo} = \frac{1}{4}$ (or close values) in both cases, unless other choice is prescribed.

1.7 Concluding remarks

Consistent LBE schemes for the hydrodynamic and anisotropic advection-diffusion problems are developed. Their further numerical investigation is needed to select the optimal solutions for free collision components, which are problem dependent. The interface analysis [72, 73] (summarized in Section 4) brings a light on the choice between anisotropic equilibrium functions and anisotropic sets of eigenvalues (see in Section 4). It is worthwhile to explore the advantages of the integral transforms offered by the proposed equilibrium schemes for proper choice of the diffusion function $\mathcal{D}(s)$. Temperature wave solution in Section 6.3.4 presents one example. Two others are the Kirchhoff transformation based and mixed forms of the Richard's equation [71] (see in Section 5.6.2).

Among the remaining "technical" problems, let us mention the high-order analysis and the numerical diffusion of the L model, estimation of the numerical diffusion for non-constant velocity, extension of necessary and sufficient stability conditions beyond the minimal models and in the presence of cross-diffusion elements, strong derivation of the consistency conditions, necessary and sufficient conditions of the positivity of the conserved variable, an important point for many transport problems, and, especially, further investigation of the stability role of the free eigenvalues (or Λ^{eo}_q values) beyond the particular choice $\Lambda^{eo} = \frac{1}{4}$.

This specific value yields the same stability bounds as the BGK model with $\tau = 1$, for any eigenvalue function Λ^-, and that is why we call it "optimal". The paper in progress presents the necessary and sufficient conditions for the minimal stencils and extend them for two moving classes models, in two and three dimensions. When taking *arbitrary (small)* Λ^{eo} value for given Λ^-, it may occur that the TRT stability bounds *diminue* against the BGK model in the convective limit $\Lambda^- \to 0$, even if $\Lambda^{eo} > [\Lambda^-]^2$. We aim to establish the rigorous optimal stability bounds for $\Lambda^{eo}(\Lambda^-)$.

Chapter 2

Recurrence equations of the LBE

Equivalent equations of the LBE are very recently derived in common work [103] with D. d'Humières and called *recurrence equations*. They express the LBE via the directional central finite-difference operators and incorporate the closure relations. Based upon, we try to assess the applicability of the steady Chapman-Enskog expansion in the presence of boundaries. The coefficients of the recurrence equations determine parametrization of the bulk *steady* solutions with the non-dimensional physical parameters and collision combinations Λ_q^{eo}. When the boundary scheme obeys the parametrization properly, the numerical solutions obey exactly the non-dimensional properties predicted for bulk solutions. The parametrized solutions are physically consistent since all their numerical errors are independent of the transport coefficients when all Λ_q^{eo} are set. Properly parametrized solutions of the Stokes equation result in viscosity independent permeability measurements. This parametrization is not possible with the BGK operator. For the sake of completeness, we also present the recurrence equations for the MRT-L operators but they have not been yet fully explored.

Time dependent recurrence equations conclude this Chapter. We derive from them new interesting results on the consistence of the time approximation and the general stability properties of the LBE solutions, at least for the "optimal choice" $\Lambda_q^{eo} \equiv \frac{1}{4}$.

2.1 Steady recurrence equations

At steady state, the immobile population takes its equilibrium value then $g_0 = g_0^+ \equiv 0$. The subsequent developments are then relevant only for moving populations, $q = 1, \ldots, Q-1$. We assume that the collision rates are link-wise constant and the source quantities $\frac{-S_q^\pm}{\lambda_q^\pm}$ are put into $e_q^\pm$ using the L operator (1.18). The recur-

rence equations represent four specific linear combinations of four evolution equations (1.1) along one link: from $q-$bulk grid node $\vec{r} \in \Omega_q$, having its two neighbors $\vec{r} \pm \vec{c}_q$ in the computational domain Ω, to these neighbors and back. Keeping in mind that that the populations and their post-collision values can be written as:

$$f_q = e_q^+ + e_q^- - \left(\frac{1}{2} + \Lambda_q^+\right) g_q^+ - \left(\frac{1}{2} + \Lambda_q^-\right) g_q^- \ , \tag{2.1}$$

$$\tilde{f}_q = e_q^+ + e_q^- + \left(\frac{1}{2} - \Lambda_q^+\right) g_q^+ + \left(\frac{1}{2} - \Lambda_q^-\right) g_q^- \ , \tag{2.2}$$

we first write down two steady-state evolution equations of L operator from $\vec{r}$ to $\vec{r} \pm \vec{c}_q$, using that $g_q^{\pm} = g_q^+$ and $g_{\bar{q}}^- = -g_q^-$:

$$\begin{aligned} &[e_q^+ \pm e_q^- - (\frac{1}{2} + \Lambda_q^+) g_q^+ \mp (\frac{1}{2} + \Lambda_q^-) g_q^-](\vec{r} \pm \vec{c}_q) = \\ &[e_q^+ \pm e_q^- + (\frac{1}{2} - \Lambda_q^+) g_q^+ \pm (\frac{1}{2} - \Lambda_q^-) g_q^-](\vec{r}) \ , \ \vec{r} \in \Omega_q \ , \end{aligned} \tag{2.3}$$

then back, from $\vec{r} \pm \vec{c}_q$ to $\vec{r}$:

$$\begin{aligned} &[e_q^+ \mp e_q^- + (\frac{1}{2} - \Lambda_q^+) g_q^+ \mp (\frac{1}{2} - \Lambda_q^-) g_q^-](\vec{r} \pm \vec{c}_q) = \\ &[e_q^+ \mp e_q^- - (\frac{1}{2} + \Lambda_q^+) g_q^+ \pm (\frac{1}{2} + \Lambda_q^-) g_q^-](\vec{r}) \ , \ \vec{r} \in \Omega_q \ . \end{aligned} \tag{2.4}$$

Then the solution of evolution equation $\{g_q^{\pm}(\vec{r}) \ , \ q = 1, \ldots, Q-1\}$ satisfies four recurrence equations:

$$g_q^{\pm}(\vec{r}) \ = \ [\bar{\Delta}_q e_q^{\mp} - \Lambda_q^{\mp} \Delta_q^2 e_q^{\pm} + (\Lambda_q^{eo} - \frac{1}{4}) \Delta_q^2 g_q^{\pm}](\vec{r}) \ , \ \vec{r} \in \Omega_q \ , \tag{2.5}$$

and

$$[\Delta_q^2 e_q^{\pm} - \Lambda_q^{\pm} \Delta_q^2 g_q^{\pm} - \bar{\Delta}_q g_q^{\mp}](\vec{r}) = 0 \ , \ \ \vec{r} \in \Omega_q \ . \tag{2.6}$$

They are obtained as linear combinations of four relations (2.3) and (2.4) (this is worked out in [103]), with the help of the link-wise finite-difference operators,

$$\begin{aligned} \bar{\Delta}_q \phi(\vec{r}) \ &= \ \frac{1}{2}(\phi(\vec{r} + \vec{c}_q) - \phi(\vec{r} - \vec{c}_q)) \ , \\ \Delta_q^2 \phi(\vec{r}) \ &= \ \phi(\vec{r} + \vec{c}_q) - 2\phi(\vec{r}) + \phi(\vec{r} - \vec{c}_q) \ . \end{aligned} \tag{2.7}$$

Any steady solution of the evolution equation (1.1) with relations (1.18) is also solution of equations (2.5) and (2.6) and inversely. In section 2.3 we extend these relations to boundary nodes and represent the whole solution as:

$$g_q^{\pm}(\vec{r}) = \gamma_q(e_q^{\mp}) - 2\Lambda_q^{\mp} \Gamma_q(e_q^{\pm}) + \delta g_q^{\pm}(\vec{r}) \ , \ \forall \, \vec{r} \, , \tag{2.8}$$

where $\Gamma_q(\phi)$ and $\gamma_q(\phi)$ are solutions of the following recurrence equations:

$$2\Gamma_q(\phi) = \Delta_q^2\phi + 2(\Lambda_q^{eo} - \frac{1}{4})\Delta_q^2\Gamma_q(\phi)\,, \tag{2.9}$$

$$\gamma_q(\phi) = \bar{\Delta}_q\phi + (\Lambda_q^{eo} - \frac{1}{4})\Delta_q^2\gamma_q(\phi)\,,\ \vec{r}\in\Omega_q\,, \tag{2.10}$$

and $\delta g_q^{\pm}(\vec{r})$ satisfy the following system:

$$\delta g_q^{\pm}(\vec{r}) = (\Lambda_q^{eo} - \frac{1}{4})\Delta_q^2\delta g_q^{\pm}(\vec{r})\,, \tag{2.11}$$

$$[\Lambda_q^{\pm}\Delta_q^2\delta g_q^{\pm} + \bar{\Delta}_q\delta g_q^{\mp}](\vec{r}) = 0\,,\ \vec{r}\in\Omega_q\,. \tag{2.12}$$

The solutions of the recurrence equations (2.5) and (2.6) are the same if $\delta g_q^{\pm}(\vec{r}) \equiv 0$. This correction is needed to incorporate boundary nodes and it vanishes for periodic solutions, where relations (2.9) and (2.10) are defined for all grid nodes.

2.2 Bulk solution of the recurrence equations

Let us first consider a special choice $\Lambda_q^{eo} \equiv \frac{1}{4}$. Then the last terms vanish in equations (2.9) and (2.11) and the post-collision variables become directly related to the equilibrium components:

$$\Lambda_q^{eo} = \frac{1}{4}:\ 2\Gamma_q(\phi) = \Delta_q^2\phi\,,\ \gamma_q(\phi) = \bar{\Delta}_q\phi\,,\ \delta g_q^{\pm}(\vec{r}) = 0\,,\ \vec{r}\in\Omega_q\,. \tag{2.13}$$

We emphasize that the accommodation term $\delta g_q^{\pm}(\vec{r})$ vanishes in bulk and the solution (2.8) becomes:

$$\Lambda_q^{eo} = \frac{1}{4}:\ g_q^{\pm}(\vec{r}) = \gamma_q(e_q^{\mp}) - 2\Lambda_q^{\mp}\Gamma_q(e_q^{\pm})\,,\ \vec{r}\in\Omega_q\,. \tag{2.14}$$

The solution in a form (2.14) with relations (2.13) coincides with the solution (1.38), obtained from the Chapman-Enskog analysis. Let us now extend the connection between these two solution forms for arbitrary Λ_q^{eo}.

We replace the finite-difference operators Δ_q and Δ_q^2 by their infinite Taylor expansion (1.37). Assuming the solution of the recurrence equations (2.9) and (2.10) in the form of the expansion around the equilibrium:

$$\gamma_q(\phi) = \sum_{k\geq 1}\frac{a_{2k-1}\partial_q^{2k-1}\phi}{(2k-1)!}\,,\qquad \Gamma_q(\phi) = \sum_{k\geq 1}\frac{a_{2k}\partial_q^{2k}\phi}{(2k)!}\,, \tag{2.15}$$

and substituting this form into relations (2.9) and (2.10), we get the same solution for the coefficients $\{a_{2k-1}, a_{2k}\}$ as one given by relations (1.33). Then the Chapman-Enskog solution (1.30), (1.31) with the coefficients (1.33) coincides with the solution (2.8) when $\delta g_q^{\pm}(\vec{r}) = 0$:

$$\begin{aligned} \sum_{k\geq 1} g_q^{\pm(2k)}(\vec{r}) &= -2\Lambda_q^{\mp}\Gamma_q(e_q^{\pm}) , \\ \sum_{k\geq 1} g_q^{\pm(2k-1)}(\vec{r}) &= \gamma_q(e_q^{\mp}) , \vec{r}\in\Omega_q , \forall\ \Lambda_q^{eo} . \end{aligned} \tag{2.16}$$

It follows that the *bulk* macroscopic equations, commonly derived without taking into account any possible boundary corrections, are the same either using the infinite Chapman-Enskog expansion or expanded solutions of the recurrence equations. Taking the moments of relations (2.5) for the TRT operator, exact form of bulk conservation relations (1.13) is:

$$\sum_{q=1}^{Q-1} \bar{\Delta}_q e_q^- = M + \sum_{q=1}^{Q-1} \Lambda^- \Delta_q^2 e_q^+ - (\Lambda^{eo} - \frac{1}{4}) \sum_{q=1}^{Q-1} \Delta_q^2 g_q^+ , \tag{2.17}$$

$$\sum_{q=1}^{Q-1} \bar{\Delta}_q e_q^+ \vec{c}_q = \vec{F} + \sum_{q=1}^{Q-1} \Lambda^+ \Delta_q^2 e_q^- \vec{c}_q - (\Lambda^{eo} - \frac{1}{4}) \sum_{q=1}^{Q-1} \Delta_q^2 g_q^- \vec{c}_q . \tag{2.18}$$

Substituting here the equilibrium distribution, this form is very useful for subsequent analysis of truncation errors. This enabled us to derive exact apparent corrections of transport coefficients in simple cases. It follows from these relations that all truncation errors in bulk are controlled by the physical numbers and Λ^{eo}. When the solution varies only along one of the lattice axis, say $e_q^{\pm}(y')$, then

$$\sum_{q=1}^{Q-1} \Delta_q^2 g_q^+ = \Delta_{y'}^2 \sum_{q=1}^{Q-1} g_q^+ , \sum_{q=1}^{Q-1} \Delta_q^2 g_q^- c_{q\alpha'} = \Delta_{y'}^2 \sum_{q=1}^{Q-1} g_q^- c_{q\alpha'} , \tag{2.19}$$

where $\Delta_{y'}^2$ are Laplace differences along $y'-$axis. These sums vanish due to solvability relations (1.13) when the source terms are constant in space. Then we suggest that macroscopic steady solutions are independent of Λ^{eo} under assumptions above. One known example (beyond the parabolic solutions where $\Delta_{y'}^2 g_q^{\pm}$ vanishes) is the one-dimensional exact steady convection-diffusion solution (6.37), which is independent of free eigenvalues. However, the numerical solutions of this problem may in principle depend on Λ^{eo}, because of accommodation corrections. Also, the variation of the forcing induces the apparent corrections for Brinkman channel solution, [76, 146]. They are discussed in Sections 5.2 and 6.2: we get the

exact finite-difference equivalent of Brinkman TRT model in simple channel from eq. (2.18) and its approximate solution in rotated channels.

In general, the derived equations are explicit functions of the equilibrium variables only for $\Lambda^{eo} = \frac{1}{4}$. We should bear in mind that the commonly used second-order Chapman-Enskog analysis neglects the variation of the non-equilibrium components beyond the first order. Hence, it neglects the terms $\sum_{q=0}^{Q-1} \Delta_q^2 g_q^+$ and $\sum_{q=1}^{Q-1} \Delta_q^2 g_q^- \vec{c}_q$, for any Λ^{eo}. Then the second-order approximations of the macroscopic equations are independent of Λ^{eo} and they reduce to steady form of Navier-Stokes equation (1.45) or advection-diffusion equation (1.50).

2.3 Boundary conditions for the recurrence equations

2.3.1 Generic conditions

It can be shown that $\gamma_q(\phi)$ can also be written as (see Appendix A of [103]):

$$\gamma_q(\phi) \;=\; \bar{\Delta}_q \phi + 2(\Lambda_q^{eo} - \frac{1}{4}) \bar{\Delta}_q \Gamma_q(\phi) \,. \tag{2.20}$$

Indeed, starting from this form and using relation (2.9) for γ_q it appears that

$$\Delta_q^2 \gamma_q(\phi) = 2\bar{\Delta}_q \Gamma_q(\phi) \,, \tag{2.21}$$

then two forms (2.10) and (2.20) coincide. Taking the sum of $\Gamma_q(\phi)$ at $\vec{r} - \vec{c}_q$ and $\vec{r}$ plus $\gamma_q(\phi)$ at $\vec{r} - \vec{c}_q$, where $\vec{r} - \vec{c}_q$ and $\vec{r}$ are both q-bulk nodes, it comes from relations (2.9) and (2.20):

$$[\Gamma_q(\phi)]\,(\vec{r}) + [\Gamma_q(\phi) + \gamma_q(\phi)](\vec{r} - \vec{c}_q) = [\gamma_q(\phi)](\vec{r}) \,. \tag{2.22}$$

This relation is used to extend solution (2.8) from the $q-$bulk nodes to boundary nodes $\vec{r}_{b_1}$ and $\vec{r}_{b_2} = \vec{r}_{b_1} + N_q \vec{c}_q$ (ends of a segment of $N_q + 1$ consecutive nodes all in Ω):

$$\begin{aligned}
[\gamma_q(\phi)]\,(\vec{r}_{b_1}) &= [\gamma_q(\phi)](\vec{r}_{b_1} + \vec{c}_q) - [\Gamma_q(\phi)](\vec{r}_{b_1} + \vec{c}_q) - [\Gamma_q(\phi)](\vec{r}_{b_1}) \,, \quad \vec{r}_{b_1} - \vec{c}_q \notin \Omega \,, \\
[\gamma_q(\phi)]\,(\vec{r}_{b_2}) &= [\gamma_q(\phi)](\vec{r}_{b_2} - \vec{c}_q) + [\Gamma_q(\phi)](\vec{r}_{b_2} - \vec{c}_q) + [\Gamma_q(\phi)](\vec{r}_{b_2}) \,, \quad \vec{r}_{b_2} + \vec{c}_q \notin \Omega \,.
\end{aligned} \tag{2.23}$$

We emphasize that any other valid relation, e.g., relation (2.21) might be used to relate the boundary values of $\gamma_q(\phi)$ and $\Gamma_q(\phi)$, as well.

On the other side, for two given boundary values, here $\delta g_q^+(\vec{r}_{\rm b_2})$ and $\delta g_q^+(\vec{r}_{\rm b_1})$, the solution to equations (2.11) and (2.12) is:

$$\delta g_q^+(\vec{r}) = \frac{r_q^n - r_q^{-n}}{r_q^{N_q} - r_q^{-N_q}} \delta g_q^+(\vec{r}_{\rm b_2}) + \frac{r_q^{(N_q-n)} - r_q^{-(N_q-n)}}{r_q^{N_q} - r_q^{-N_q}} \delta g_q^+(\vec{r}_{\rm b_1}) \,, \tag{2.24}$$

$$\delta g_q^-(\vec{r}) = \frac{1}{\sqrt{\Lambda_q^{eo}}} [\Lambda_q^+ \delta g_q^+(\vec{r}) + \frac{2\Lambda_q^+ \delta g_q^+(\vec{r}_{\rm b_2}) r_q^{-n}}{r_q^{N_q} - r_q^{-N_q}} - \frac{2\Lambda_q^+ \delta g_q^+(\vec{r}_{\rm b_1}) r_q^{(N_q-n)}}{r_q^{N_q} - r_q^{-N_q}}] \,,$$
$$\vec{r} = \vec{r}_{\rm b_1} + n\vec{c}_q \,. \tag{2.25}$$

Here $r_q = (2\sqrt{\Lambda_q^{eo}} - 1)/(2\sqrt{\Lambda_q^{eo}} + 1)$ is one of two roots $k_{1,2}$ of $4\Lambda_q^{eo}(k-1)^2 = (k+1)^2$. A remarkable property is that the coefficients of the relation between $\delta g_q^+(\vec{r})$ and its boundary values, as well as (multiplied by Λ_q^+) coefficients relating δg_q^- to these three quantities, depend on the eigenvalues only in their magic combination Λ_q^{eo}. When $\Lambda_q^{eo} = 1/4$ then $\delta g_q^\pm(\vec{r}) = 0$ except for the boundary nodes where

$$\Lambda_q^{eo} = \frac{1}{4} \,:\, \delta g_q^\pm(\vec{r}_{\rm b_1}) = 2\Lambda^\mp \delta g_q^\mp(\vec{r}_{\rm b_1}) \,, \text{ and } \delta g_q^\pm(\vec{r}_{\rm b_2}) = -2\Lambda^\mp \delta g_q^\mp(\vec{r}_{\rm b_2}) \,. \tag{2.26}$$

The "upper" and "down" pairs (2.26) are the same using $4\Lambda_q^-\Lambda_q^+ = 1$.

The three pairs of boundary values $[\gamma_q(e_q^\mp)](\vec{r}_{\rm b})$, $[\Gamma_q(e_q^\mp)](\vec{r}_{\rm b})$ and $\delta g_q^\pm(\vec{r})$, are related via the solution obtained for $g_q^\pm(\vec{r}_{\rm b})$, then:

$$\delta g_q^\pm(\vec{r}_{\rm b}) = \left[g_q^\pm - \gamma_q(e_q^\mp)\right](\vec{r}_{\rm b}) + 2\Lambda_q^\mp [\Gamma_q(e_q^\pm)](\vec{r}_{\rm b}) \,. \tag{2.27}$$

Actually, the $q-$link closure relation of the given boundary scheme provides one (total) relation for $g_q^+(\vec{r}_{\rm b})$ and $g_q^-(\vec{r}_{\rm b})$. We have not found any independent relation to set $[\Gamma_q(e_q^\pm)](\vec{r}_{\rm b})$. The subsequent analysis of the parametrization properties of bulk and boundary closure relations suggest that main results are insensitive to this particular choice, provided that any dependency of $[\Gamma_q(e_q^\pm)](\vec{r}_{\rm b})$ on the eigenvalues is expressed via Λ_q^{eo}, e.g., as in relations (2.9), or vanishes. So far two choices were explored in details. The first follows [103] and arbitrary sets:

$$\Gamma_q(e_q^\pm)(\vec{r}_{\rm b_1}) = \Gamma_q(e_q^\pm)(\vec{r}_{\rm b_2}) = 0 \,. \tag{2.28}$$

Then the analysis [103] can be extended to relation (2.27) replacing

$$\delta g_q^\pm(\vec{r}_{\rm b}) \to \delta g_q^\pm(\vec{r}_{\rm b}) - 2\Lambda_q^\mp [\Gamma_q(e_q^\pm)](\vec{r}_{\rm b}) \,, \tag{2.29}$$

for all relevant bulk and boundary relations.

Another natural choice is adapted in Section 6.1.4 for the Poiseuille flow based on the non-linear equilibrium. There, $[\Gamma_q(e_q^\pm)](\vec{r}_{\rm b})$ is set equal to its solution given

by the exact (fourth-order accurate) Chapman-Enskog solution (2.15), as for all bulk points. The whole exact solution of the closed system confirms the presence of Knudsen-type corrections $\delta g_q^{\pm}(\vec{r})$, beyond the Chapman-Enskog solution. The correction is caused by a mismatch between the closure solutions, e.g., given by the bounce back, linear or parabolic multi-reflection type schemes, and exact bulk solution. The correction reduces in bulk where the solution tends to its approximation prescribed by the Chapman-Enskog expansion. When $\Lambda^{eo} = \frac{1}{4}$, the expansion is valid everywhere, except for the grid boundary points.

2.3.2 Example: bounce-back rule

The analysis [103] of boundary relations is illustrated in most details for the simplest parametrized rules, as the bounce-back and anti-bounce back, and for not-parametrized rule, as the BFL rule [20]. This analysis inspired us to introduce generic conditions for the parametrization of the link-wise schemes. We suggest these conditions as sufficient for the multi-reflection schemes. They are summarized in Section 3.3.1. All developed classes of the multi-reflection pressure and velocity boundary schemes are analysed with respect to these conditions in [74] and their parametrization properties were checked in numerical simulations. Let us illustrate this analysis using the simplest and mass conserving boundary rule, the bounce-back scheme for incoming populations $f_{\bar{q}}(\vec{r}_{\rm b})$:

$$f_{\bar{q}}(\vec{r}_{\rm b_2}, t+1) \;=\; \tilde{f}_q(\vec{r}_{\rm b_2}, t)\ ,\ \vec{r}_{\rm b_2} + \vec{c}_q \notin \Omega\ . \tag{2.30}$$

Replacing $f_{\bar{q}}$ and $\tilde{f}_q$ with relations (1.3) and using the TRT operator, the steady closure relation takes the form:

$$\left[e_q^- + \frac{1}{2} g_q^+ - \Lambda^- g_q^-\right](\vec{r}_{\rm b_2}) = 0\ . \tag{2.31}$$

Using relation (2.8) for $g_q^{\pm}(\vec{r}_{\rm b_2})$ and the choice $[\Gamma_q(\phi)](\vec{r}_{\rm b_2}) = 0$, this closure relation multiplied by Λ^+ becomes:

$$\begin{aligned}\Big[\Lambda^+ j_q^\star + \Lambda^{eo} F_q^\star + \frac{1}{2}\left(\gamma_q(\Lambda^+ j_q^\star) + \Lambda^{eo}\gamma_q(F_q^\star)\right)& \\ - \Lambda^{eo}\gamma_q(P_q^\star) + \frac{1}{2}\Lambda^+ \delta g_q^+ - \Lambda^{eo}\delta g_q^-\Big](\vec{r}_{\rm b_2}) \;&=\; 0.\end{aligned} \tag{2.32}$$

Replacing $\delta g_q^-(\vec{r}_{\rm b_2})$ in Eq. (2.32) by its value given by relation (2.25) makes it possible to compute $\Lambda^+ \delta g_q^+(\vec{r}_{\rm b_2})$, hence $\delta g_q^-(\vec{r}_{\rm b_2})$, as unique functions of $\Lambda^+ j_q^\star + \Lambda^{eo} F_q^\star + \gamma_q(\Lambda^+ j_q^\star)/2 - \Lambda^{eo}\gamma_q(P_q^\star)$ and Λ^{eo} only. We show in the next Chapter that

this property is essential for proper parametrization of the numerical solution. Using most general form (2.29), we should add $-\Lambda^{eo}[\Gamma_q(e_q^+)](\vec{r}_{b_2})$ and $2\Lambda^{eo}[\Gamma_q(\Lambda^+ j_q^\star)](\vec{r}_{b_2})$ to closure relation (2.32). The subsequent analysis procedure will not change provided that the sufficient condition indicated above is satisfied, i.e., when $[\Gamma_q(e_q^\pm)](\vec{r}_{b_2})$ is related to equilibrium components via Λ^{eo} or vanishes.

2.4 Physical and collision numbers

Obtained explicit dependency of the non-equilibrium solution on the relaxation rates allows us to confirm the governing role of the "magic" combinations for steady solutions of the Stokes equation and to extend this property to steady solutions of the Navier-Stokes and anisotropic advection-diffusion equations.

2.4.1 Exact conservation relations

The mass and momentum equilibrium variables are related to the moments of the populations and the source quantities such that conservation relations (1.13) are satisfied. They close the system of equations for the bulk. In what follows, non-degenerated boundary conditions assume to yield a unique solution (see more detailed assumptions in [103]). Substituting solution in the form (2.8), the steady conservation relations (1.13) become in all nodes:

$$\begin{aligned}
\sum_{q=1}^{Q-1}\gamma_q(e_q^-) - 2\sum_{q=1}^{Q-1}\Lambda_q^-\Gamma_q(e_q^+) + \sum_{q=1}^{Q-1}\delta g_q^+(\vec{r}) &= M(\vec{r})\,,\\
\sum_{q=1}^{Q-1}\gamma_q(e_q^+)\vec{c}_q - 2\sum_{q=1}^{Q-1}\Lambda_q^+\Gamma_q(e_q^-)\vec{c}_q + \sum_{q=1}^{Q-1}\delta g_q^-(\vec{r})\vec{c}_q &= \vec{F}(\vec{r})\,. \qquad (2.33)
\end{aligned}$$

The total solution of the LBE system with respect to the conserved quantities is built from the solvability conditions (2.33) with the equations (2.9) and (2.10), and boundary solution (2.24) and (2.25), where, finally, $\delta g_q^+(\vec{r}_b)$ are set by the boundary closure relations of each individual scheme, as was illustrated in the previous section for the bounce-back.

2.4.2 Linearity of the Stokes equation

Owing to the linearity of the equilibrium TRT function (1.42) for Stokes flow with respect to $P_q^\star(\vec{r})$, $j_q^\star(\vec{r})$ and $\Lambda^- F_q^\star(\vec{r})$ (without mass source here):

$$\begin{aligned}
e_q^- &= j_q^\star + \Lambda^- F_q^\star\,,\ j_q^\star = t_q^\star(\vec{j}\cdot\vec{c}_q)\,,\ F_q^\star = t_q^\star(\vec{F}\cdot\vec{c}_q)\,,\\
e_q^+ &= P_q^\star\,,\ P_q^\star = t_q^\star P\,,\ P = c_s^2\rho\,, \qquad (2.34)
\end{aligned}$$

the post-collision solution can be written as a linear combination of one argument functions, here $\gamma_q(\cdot)$ and $\Gamma_q(\cdot)$:

$$\begin{aligned} \gamma_q(e_q^-) &= \gamma_q(j_q^\star) + \Lambda^- \gamma_q(F_q^\star)\ ,\ \gamma_q(e_q^+) = \Gamma_q(P_q^\star)\ , \\ \Gamma_q(e_q^-) &= \Gamma_q(j_q^\star) + \Lambda^- \Gamma_q(F_q^\star)\ ,\ \Gamma_q(e_q^+) = \Gamma_q(P_q^\star)\ . \end{aligned} \tag{2.35}$$

We substitute these relations into Eqs. (2.33), then multiply the mass equation by Λ^+. We keep in mind that $\sum_{q=1}^{Q-1} \delta g_q^-(\vec{r})\vec{c}_q$ is linearly related to $\Lambda^+ \sum_{q=1}^{Q-1} \delta g_q^+(\vec{r})\vec{c}_q$ and that the coefficients of this relation depend on the eigenvalues via Λ^{eo} only (cf. (2.25)). Also, the relation between $\delta g_q^+(\vec{r})$ and its boundary values is controlled by Λ^{eo}. Provided that the closure relations of the boundary schemes relate properly the boundary values $\delta g_q^+(\vec{r}_\mathrm{b})$ to solution components of equations (2.33), then the magic combination controls the linear relations between the $\Lambda^+ \vec{j}$ and the forcing (and/or the variation of pressure distribution), given by momentum equation, and mass conservation equation. Then the TRT model is able to yield the viscosity independent numerical errors for Stokes steady solutions. The necessary condition is to keep Λ^{eo} at a fixed value with the help of the free eigenvalue λ^- when the kinematic viscosity, $\nu = \frac{1}{3}\Lambda^+$, varies. Since the Darcy law, a linear relation between ∇P and the mean value of $\nu\vec{j}$ is controlled by Λ^{eo}, the components of the permeability tensor (for any porous structure) stay constant when the viscosity varies but Λ^{eo} is kept constant, provided that the boundary scheme obeys the parametrization. We discuss this major advantage of the TRT operator over the BGK scheme in Section 5.1.

2.4.3 Parametrization of the Navier-Stokes equations

Two equivalent forms of the parametrized equations are presented in [103] and [74], respectively based on either physical characteristic quantities or the lattice ones. We follow [74], with L' and U' as the characteristic values of the length and velocity, respectively, *in lattice units*. The hydrodynamic solutions are determined via the non-dimensional numbers: Mach number *Ma*, square of Froude number Fr^2 and Reynolds number *Re*:

$$Ma = \frac{U'}{c_s}\ ,\ Fr^2 = \frac{U'^2}{gL'}\ ,\ Re = \frac{U'L'}{\nu}\ . \tag{2.36}$$

They are computed with the lattice kinematic viscosity $\nu = \frac{1}{3}\Lambda^+$ and lattice value of the acceleration constant g. For the sake of simplicity, we assume the standard equilibrium (relation (1.42) with $\alpha_{\varepsilon^\star} = 0$, $M = 0$, $\rho^m = \rho^{\mathrm{eq}} = \rho$). Let us introduce the dimensionless velocity $\vec{j}'$, pressure P', force $\vec{F}'$ and relate other equilibrium

quantities to them:

$$\begin{aligned}
\vec{j}' &= \frac{\vec{j}}{\rho_0 U'} \, , \, P' = \frac{P-P_0}{\rho_0 U'^2} \, , \, \vec{F}' = \frac{Fr^2 L'}{\rho_0 U'^2}\vec{F} \, , \\
\rho' &= \frac{\rho}{\rho_0} = 1 + Ma^2 P' \, , \, \tilde{\rho}' = \frac{\tilde{\rho}}{\rho_0} \, , \quad \text{where } P = c_s^2 \rho \, , \\
&\text{and} \\
\mathcal{P}_q'^{\star}(\rho', \vec{j}', \tilde{\rho}') &= \frac{\mathcal{P}_q^{\star}(\rho, \vec{j}, \tilde{\rho})}{\rho_0 U'^2} = t_q^{\star}(Ma^{-2} + P') + g_S E_q^{(u)}(\vec{j}', \tilde{\rho}') \, . \quad (2.37)
\end{aligned}$$

Multiplying exact mass and momentum steady conservation relations (2.33) by $\frac{L'}{\rho_0 U'}$ and $\frac{L'}{\rho_0 U'^2}$, respectively, and writing the equilibrium and the post-collision components (2.8) in dimensionless variables, the conservation equations of the TRT operator become:

$$\begin{aligned}
3L' \sum_{q=0}^{Q-1} \gamma_q (j_q'^{\star}) &+ \frac{L'}{\rho_0 U} \sum_{q=1}^{Q-1} \Lambda^{+} \delta g_q^{+}(\vec{r}) \\
&= 2\Lambda^{eo} Re \sum_{q=0}^{Q-1} \Gamma_q (\mathcal{P}_q'^{\star}) + \frac{\Lambda^{eo}}{L'} \frac{Re}{Fr^2} \sum_{q=0}^{Q-1} \gamma_q (F_q'^{\star}) \, , \quad (2.38) \\
L' \sum_{q=1}^{Q-1} \gamma_q (\mathcal{P}_q'^{\star}) \vec{c}_q &+ \frac{L'}{\rho_0 U^2} \sum_{q=1}^{Q-1} \delta g_q^{-}(\vec{r}) \vec{c}_q \\
&= \frac{\vec{F}'}{Fr^2} + \frac{6L'^2}{Re} \sum_{q=1}^{Q-1} \Gamma_q (j_q'^{\star}) \vec{c}_q + \frac{2\Lambda^{eo}}{Fr^2} \sum_{q=1}^{Q-1} \Gamma_q (F_q'^{\star}) \vec{c}_q \quad (2.39)
\end{aligned}$$

Then, under similar conditions as for the Stokes equation (concerning relations between the boundary values $\Lambda^{+}\delta g_q^{+}(\vec{r})$ and other components of the equations (2.38) and (2.39)), the *steady* solutions for $\vec{j}'$ and P' are *exactly* the same on a given grid (L' is fixed) provided that Λ^{eo} and the Reynolds and Froude numbers are kept constant when the viscosity varies. Additionally, in compressible regimes, the Mach number should also be kept constant. When the non-dimensional solutions are the same, so are their physical equivalents, e.g., $\vec{u} = U\vec{j}'$, U being the characteristic velocity in physical units.

2.4.4 Grid refining properties

So far the recurrence equations were mainly explored on the fixed grid, with a purpose to establish their proper parametrization by the physical numbers. However, they are also helpfull to examine the convergence properties. Let us illustrate this

for leading order analysis, taking $\varepsilon = \frac{1}{L'}$ in relations (2.9)-(2.10):

$$\begin{aligned}
L'\sum_{q=0}^{Q-1}\gamma_q(j_q'^{\star}) &\approx \nabla'\cdot\vec{j}' + O(\varepsilon^2) + (\Lambda^{eo}-\frac{1}{4})\times O(\varepsilon^2)\,,\\
2\sum_{q=0}^{Q-1}\Gamma_q(\mathcal{P}_q'^{\star}) &\approx O(\varepsilon^2) + (\Lambda^{eo}-\frac{1}{4})\times O(\varepsilon^2)\,,\ \text{where}\ \ \Delta\mathcal{P}' = O(\varepsilon^2)\,,\\
L'\sum_{q=1}^{Q-1}\gamma_q(\mathcal{P}_q'^{\star})\vec{c}_q &\approx \nabla' P' + g_S\nabla\cdot'(\frac{\vec{j}'\otimes\vec{j}'}{\tilde{\rho}'}) + O(\varepsilon^2) + (\Lambda^{eo}-\frac{1}{4})\times O(\varepsilon^2)\,,\\
6L'^2\sum_{q=1}^{Q-1}\Gamma_q(j_q'^{\star})\vec{c}_q &\approx \nabla'\cdot\nabla'\vec{j}' + 2\nabla'(\nabla'\cdot\vec{j}') + O(\varepsilon^2) + (\Lambda^{eo}-\frac{1}{4})\times O(\varepsilon^2)\,.
\end{aligned} \tag{2.40}$$

In these relations, $O(\varepsilon^2)$ terms are controled by Λ^{eo} if the non-dimensional solution itself is controlled by Λ^{eo}. Of special interest here is that all coefficients of spatial truncation errors are fixed by Λ^{eo}, then the numerical schemes are consistent with grid refining. The coefficients of the truncated terms are the polynomials of $\Lambda^{eo}(\tau)$ for the BGK scheme, then the condition of consistency requires to maintain the fixed τ value while refining the grid (see Holdych et al [95]). This means the refining with constant ratio of Δ_x^2/Δ_t. We suggest that the TRT model with fixed Λ^{eo} removes this constraint for the spatial part of the solutions, at least. A consistency of temporal discretization is discussed below. Finally, the approximation errors owing to force variation are given by the last terms in (2.38) and (2.39), hence, they are $O(\varepsilon^2)$ terms provided that Froude number is set. Also, replacing $\delta g_q^{\pm}(\vec{r})$ by its bulk and boundary solution (the later depends on the boundary scheme), one can perhaps explore directly the impact of the boundary corrections on the asymptotic behaviour of the LBE scheme. This is left for future work.

2.4.5 Parametrization of the AADE

Let us address the parametrization properties of the exact mass conservation equation (2.33). Let D_0' and ρ_0 be reference values for, respectively, the components of the lattice diffusion tensor and mass variable. The equations below are based on the decomposition similar to relation (2.35) for the equilibrium function (1.48):

$$L'\sum_{q=1}^{Q-1}\gamma_q(j_q'^{\star}) \;+\; M' + \frac{L}{\rho_0 U'}\sum_{q=1}^{Q-1}\delta g_q^{+}(\vec{r}) = \frac{2L'^2}{Pe}\sum_{q=1}^{Q-1}\mathcal{T}_q'\Gamma_q(\bar{\mathcal{D}}') + 2\sum_{q=1}^{Q-1}\Gamma_q(\Lambda_q^e M_q^{\star\prime})\,,$$

where

$$\Lambda_q^e = \Lambda_q^- \Lambda^+ , \quad \bar{\mathcal{D}}' = \frac{\bar{\mathcal{D}}(s)}{\rho_0} , \quad Pe = \frac{U'L'}{D_0'} , \quad M' = \frac{M}{\rho_0}\frac{L}{U'} ,$$
$$\mathcal{T}_q' = \frac{E_q \Lambda_q^-}{D_0'}, \quad j_q'^{\star} = t_q^{\star}\frac{J_q}{\rho_0 U'} , \quad M_q^{\star\prime} = t_q^m M' . \tag{2.41}$$

The higher-order corrections to AADE, hidden in $\sum_{q=1}^{Q-1}\gamma_q(j_q'^{\star})$ and $\sum_{q=1}^{Q-1}\mathcal{T}_q'\Gamma_q(\bar{\mathcal{D}}')$, depend on $\{\Lambda_q^e = \Lambda^+\Lambda_q^-\}$. The proper rescaling of these terms requires to set all the values $\{\Lambda_q^e\}$, with the help of the free eigenvalue function Λ^+. This is possible only if the whole set $\{\Lambda_q^-\}$, then the whole set $\{E_q\}$, varies similarly when U' is changed on a given grid (L' is fixed) and *Peclet number Pe* is set. When the AADE is modeled with the TRT operator, *Pe* and Λ^{eo} control the obtained solutions provided that the closure relations scale properly with these parameters. The simplest properly rescaled Dirichlet boundary condition is the anti-bounce-back rule. The reader can find its analysis in [74, 103]. The asymptotic behaviour of the AADE scheme can be studied similar as above.

2.5 The recurrence relations of the MRT-L operator

This model, introduced in Section 1.3.3, combines the link-wise anti-symmetric vectors and the MRT polynomial symmetric vectors. Denoting $\{\mathbf{v}^{+\,(i)}\}$ the $N^+ = 1+Q/2$ vectors of the symmetric MRT-L basis, $\Lambda^{+(k)}$ the corresponding eigenvalue functions and $\{g_q^{+\,(i)}\}$ the post-collision projections (1.14), $g_q^+ = \sum_{i=1}^{N^+} g_q^{+\,(i)}$, the steady recurrence equations of the MRT-L operator are presented in Appendix C of [103] in a following form:

$$g_q^+(\vec{r}) = [\bar{\Delta}_q e_q^- - \Lambda_q^- \Delta_q^2 e_q^+ + \sum_{i=1}^{N^+}(\Lambda_q^{eo\,(i)} - \frac{1}{4})\Delta_q^2 g_q^{+\,(i)}](\vec{r}) , \tag{2.42}$$

$$g_q^-(\vec{r}) = [\bar{\Delta}_q e_q^+ - \Lambda^{+(k)}\Delta_q^2 e_q^- + \Lambda^{+(k)}\bar{\Delta}_q g_q^+ - \sum_{i=1}^{N^+}\Lambda^{+\,(i)}\bar{\Delta}_q g_q^{+\,(i)}](\vec{r})$$
$$+ \quad (\Lambda_q^{eo\,(k)} - \frac{1}{4})\Delta_q^2 g_q^-(\vec{r}) , \qquad k = 1,\ldots,N^+ ,$$

and

$$[\Delta_q^2 e_q^+ - \sum_{i=1}^{N^+}\Lambda^{+\,(i)}\Delta_q^2 g_q^{+\,(i)} - \bar{\Delta}_q g_q^-](\vec{r}) = 0 . \tag{2.43}$$

$$[\Delta_q^2 e_q^- - \Lambda_q^- \Delta_q^2 g_q^- - \bar{\Delta}_q g_q^+](\vec{r}) = 0 , \tag{2.44}$$

The form of their bulk solutions is presented there by relations (C.9) and (C.10). It is interesting that the sum of relations (2.43) for all k, divided by N^+, is controlled

by the mean values of the eigenvalue functions, $\overline{\Lambda}^{+}$ and $\overline{\Lambda}_q^{eo}$:

$$\begin{aligned} g_q^-(\vec{r}) &= [\overline{\Delta}_q e_q^+ - \overline{\Lambda}^+ \Delta_q^2 e_q^- + \overline{\Lambda}^+ \overline{\Delta}_q g_q^+ - \sum_{i=1}^{N^+} \Lambda^{+\,(i)} \overline{\Delta}_q g_q^{+\,(i)}](\vec{r}) \\ &+ (\overline{\Lambda}_q^{eo} - \frac{1}{4}) \Delta_q^2 g_q^-(\vec{r}) \,, \\ \overline{\Lambda}^{+} &= \frac{1}{N^+} \sum_{k=1}^{N^+} \Lambda^{+(k)} \,, \; \overline{\Lambda}_q^{eo} = \frac{1}{N^+} \sum_{k=1}^{N^+} \Lambda_q^{eo\,(k)} = \overline{\Lambda}^{+} \Lambda_q^- \,. \end{aligned} \tag{2.45}$$

We conjecture and confirm by the numerical simulations (in Stokes regime) that the higher-order truncation errors are rescaled properly on a given grid provided that all the collision numbers $\Lambda_q^{eo\,(i)}$, then their mean values $\overline{\Lambda}_q^{eo}$, are kept constant. Under these conditions, the bounce-back and the anti-bounce-back keep their parametrization properties. The parametrization properties of linear and parabolic pressure and velocity schemes, reviewed in next section, have not yet been rigorously checked for the MRT operators.

2.6 Time dependent recurrence equations of L operator

An extension of the first pair of recurrence equations to transient regime is summarized in concluding section [103]. The time-dependent recurrence equations represent four specific linear combinations of evolution equations (1.1) along one link: from $(\vec{r},\tilde{)} \in \Omega_q$ to $(\vec{r} \pm \vec{c}_q, \tilde{t}+1)$ and from $(\vec{r} \pm \vec{c}_q, \tilde{t})$ to $(\vec{r}, \tilde{t}+1)$, where $\tilde{t} = t$ and $\tilde{t} = t-1$. In contrast with the steady solutions, $g_0(t)$ is not zero, in general. For the sake of completeness, we present here both pairs of time-dependent recurrence equations:

$$g_q^{\pm}(\vec{r},t) = \mathcal{A}_q^{\pm}(\vec{r},t) + \mathcal{P}_q^{\pm}(\vec{r},t) \,, \; \mathcal{A}_q^{\pm}(\vec{r},t) = (\mathcal{S}_q^{\pm} + \mathcal{T}_q^{\pm})(\vec{r},t) \,, \tag{2.46}$$

and

$$\mathcal{F}_q^{\pm}(\vec{r},t) = \mathcal{X}_q^{\pm}(\vec{r},t) \,, \; q = 0, \ldots, Q-1, \tag{2.47}$$

where

$$\begin{aligned} \mathcal{S}_q^{\pm}(\vec{r},t) &= (\overline{\Delta}_q e_q^{\mp} - \Lambda_q^{\mp} \Delta_q^2 e_q^{\pm} + (\Lambda_q^{eo} - \frac{1}{4}) \Delta_q^2 g_q^{\pm})(\vec{r},t) \,, \; \mathcal{S}_0^{\pm} = 0 \,, \\ \mathcal{T}_q^{\pm}(\vec{r},t) &= (\overline{\Delta}_t e_q^{\pm} + \Lambda_q^{\mp} \Delta_t^2 e_q^{\pm} - (\Lambda_q^{eo} - \frac{1}{4}) \Delta_t^2 g_q^{\pm})(\vec{r},t) \,, \\ \mathcal{P}_q^{\pm}(\vec{r},t) &= -[\frac{1}{2} \Delta_t^2 + (\Lambda_q^{\pm} + \Lambda_q^{\mp}) \overline{\Delta}_t] g_q^{\pm}(\vec{r},t) \,, \end{aligned}$$

$$\begin{aligned}
\mathcal{F}_q^{\pm}(\vec{r},t) &= (\Delta_q^2 e_q^{\pm} - \Lambda_q^{\pm}\Delta_q^2 g_q^{\pm} - \bar{\Delta}_q g_q^{\mp})(\vec{r},t)\ ,\ \mathcal{F}_0^{\pm} = 0\ ,\\
\mathcal{X}_q^{\pm}(\vec{r},t) &= (\Delta_t^2 e_q^{\pm} - \Lambda_q^{\pm}\Delta_t^2 g_q^{\pm} - \bar{\Delta}_t g_q^{\pm})(\vec{r},t)\ ,
\end{aligned}$$

$$\begin{aligned}
\text{with} \quad & \bar{\Delta}_t\phi(t) = (\phi(t+1) - \phi(t-1))/2\ ,\\
\text{and} \quad & \Delta_t^2\phi(t) = \phi(t+1) - 2\phi(t) + \phi(t-1)\ , \qquad \forall\,\phi\ . \qquad (2.48)
\end{aligned}$$

The steady state recurrence equations (2.5) and (2.6) are:

$$g_q^{\pm}(\vec{r}) = \mathcal{S}_q^{\pm}(\vec{r})\ ,\ \text{and}\ \ \mathcal{F}_q^{\pm}(\vec{r}) = 0\ . \qquad (2.49)$$

The analysis of the time dependent equations is in progress. Let us summarize our preliminary observations and link them to the stability properties.

2.7 The TRT as a three-level time difference scheme

Let equilibrium moments be $\phi^{\pm} = \mathbf{e}^{\pm}\cdot\mathbf{v}^{\pm}$, $\mathbf{v}^{+} = \mathbf{1}$ and $\mathbf{v}^{-} = \{\mathbf{c}_\alpha\}$. We take the moments of the equations (2.46) for the TRT operator where, for the sake of simplicity, take constant (in time) source quantities, $M = S^{+}(\vec{r})$ and $\vec{F} = S^{-}(\vec{r})$. Then $(\mathbf{g}^{\pm}(\vec{r},t)\cdot\mathbf{v}^{\pm}) = S^{\pm}(\vec{r})$ and the following contributions vanish: $\bar{\Delta}_t(\mathbf{g}^{\pm}(\vec{r},t)\cdot\mathbf{v}^{\pm})$, $\Delta_t^2(\mathbf{g}^{\pm}(\vec{r},t)\cdot\mathbf{v}^{\pm})$ and $(\mathcal{P}^{\pm}(\vec{r},t)\cdot\mathbf{v}^{\pm})$. Then the time dependent conservation relations take a form:

$$\bar{\Delta}_t\phi^{\pm} + \Lambda^{\mp}\Delta_t^2\phi^{\pm} = S^{\pm}(\vec{r}) + (\mathcal{S}^{\pm}\cdot\mathbf{v}^{\pm})\ . \qquad (2.50)$$

This tells us that the temporal derivative $\partial_t\phi$ is actually described in a form of a three-level difference approximation:

$$\begin{aligned}
\partial_t\phi^{\pm} &= \Delta_t\phi^{\pm} + \Lambda^{\mp}\Delta_t^2\phi^{\pm}\\
&= (\theta + \frac{1}{2})\phi^{\pm}(t+1) - 2\theta\phi^{\pm}(t) + (\theta - \frac{1}{2})\phi^{\pm}(t-1)\ ,\ \theta = \Lambda^{\mp}\ . \qquad (2.51)
\end{aligned}$$

This property takes place independently of the spatial discretization, e.g., in uniform time-dependent solutions. When $\Lambda^{\pm} = \frac{1}{2}$, the relation (2.51) reduces to forward time approximation, most accurate at midpoint $t + \frac{1}{2}$. Otherwise, the scheme is second order accurate in time only at point $t + \Lambda^{-}$. When relations (2.50) are written in a dimensionless form, the term $\Lambda^{\mp}\Delta_t^2\phi^{\pm}$ behaves as $\frac{1}{Pe}\frac{L'^2}{T'^2}\partial_{t'}^2 s'$ and $\frac{1}{Re}\frac{L'^2}{T'^2}\partial_{t'}^2\vec{j}'$ for the AADE and momentum equations, respectively. Then the TRT scheme is conditionaly consistent provided that $\frac{\Delta_t^2}{\Delta_x^2} \to 0$ when $\Delta_x \to 0$ and $\Delta_t \to 0$, and the physical numbers are fixed. We stress that in principle this condition is weaker than the restriction $\Delta_t \propto \Delta_x^2$ set above for the consistency of the BGK model.

We recall that all spatial truncation errors, which are hidden in $(\mathcal{S}^{\pm}\cdot\mathbf{v}^{\pm})$, are controlled by physical numbers and Λ^{eo}. This property is shared by time dependent solutions only asymptotically, when $\frac{\Delta_t^2}{\Delta_x^2}\to 0.$.

2.8 Generic stability properties for AADE

We restrict ourselves here to mass conservation equation (AADE) without mass source or with time independent sources. The exact form of TRT mass conservation relation becomes:

$$T(\vec{r},t)+C(\vec{r},t) \;=\; \Lambda^{-}D(\vec{r},t)+(\Lambda^{eo}-\frac{1}{4})\sum_{q=1}^{Q-1}\Delta_q^2 g_q^{+}(\vec{r},t)\;. \tag{2.52}$$

The term T denotes the exact TRT mass term (2.51). The convective C and diffusion terms $\Lambda^{-}D$ are:

$$C(\vec{r},t) \;=\; \sum_{q=1}^{Q-1}\overline{\Delta}_q e_q^{-}(\vec{r},t)\;, \tag{2.53}$$

$$\Lambda^{-}D(\vec{r},t) \;=\; \Lambda^{-}\sum_{q=1}^{Q-1}\Delta_q^2 e_q^{+}(\vec{r},t)\;. \tag{2.54}$$

We take $\Lambda^{eo}=\frac{1}{4}$ and divide the conservation equation (2.52) by $(\Lambda^{-}+\frac{1}{2})=-1/\lambda^{-}$. An equivalent scheme is:

$$\begin{aligned} s(\vec{r},t+1) \;+\; & (1-p)(C(\vec{r},t)-2\Lambda^{-}(\frac{D(\vec{r},t)}{2}+s(\vec{r},t))+ps(\vec{r},t-1)=0\;,\\ \text{where } p \;=\; & \frac{\Lambda^{-}-\frac{1}{2}}{\Lambda^{-}+\frac{1}{2}}=1+\lambda^{-}\;. \end{aligned} \tag{2.55}$$

We substitute the Fourier modes $\mathbf{s}(\vec{r},t)=\Omega^{t}\mathbf{s}_0\exp(i\vec{r}\cdot\vec{k})$ into Eq. (2.55), and denote as A and iB the terms relating to Fourier transform of of the diffusion (symmetric) operator D and convective (anti-symmetric) operator C:

$$A \;=\; 1+\frac{1}{2}\exp(-i\vec{r}\cdot\vec{k})\sum_{q=1}^{Q-1}E_q^{+}\Delta_q^2\exp(i\vec{r}\cdot\vec{k})\;,\; A\in\Re\;, \tag{2.56}$$

$$iB \;=\; \exp(-i\vec{r}\cdot\vec{k})\sum_{q=1}^{Q-1}t_q^{\star}(\vec{U}\cdot\vec{c}_q)\overline{\Delta}_q\exp(i\vec{r}\cdot\vec{k})\;,\; B\in\Re\;. \tag{2.57}$$

Replacing $-2\Lambda^-(1-p)$ with $(1+p)$, the characteristic polynomial of the scheme (2.55) becomes:

$$\begin{aligned} \Omega^2 &- \Omega((1+p)A - i(1-p)B) + p = 0 \,, \\ &\text{where } |p| \le 1 \text{ if } -2 \le \lambda^- \le 0 \,. \end{aligned} \tag{2.58}$$

The stability bounds $||\Omega||^2 = 1$ of Eq. (2.58) are set by case $p = 0$, which is the BGK model with $\tau = 1$ in our case. This can be shown, e.g., following [155]. In the theory of the finite difference schemes, this type characteristic equations appear for their analysis of three-level time differences. Relations (2.55) tell us that the TRT-E model with $\Lambda^{eo} = \frac{1}{4}$ shares the properties of the LFCCDF scheme, which is leap-frog time difference, combined with the central-difference approximation of the convective term and Du Fort-Frankel approximation [47] of the diagonal diffusion term. The Du Fort-Frankel scheme for 1D diffusion equation reads

$$\begin{aligned} \bar{\Delta}_t \phi(x,t) &= \frac{H_{xx}}{\Delta_x^2}(\phi(x+\Delta_x,t) - [\phi(x,t+\Delta_t) + \phi(x,t-\Delta_t)] + \phi(x-\Delta_x,t)) \,, \\ \text{with} \quad & \bar{\Delta}_t \phi(t) = (\phi(t+\Delta_t) - \phi(t-\Delta_t))/2\Delta_t \,, \forall\, \phi \,, \end{aligned} \tag{2.59}$$

or, equivalently:

$$\bar{\Delta}_t \phi(t) + H_{xx}\frac{\Delta_t^2}{\Delta_x^2}\Delta_t^2\phi(x,t) = H_{xx}\Delta_x^2\phi(x,t) \,, \tag{2.60}$$

where $\Delta_x^2\phi(x,t)$ and $\Delta_t^2\phi(x,t)$ are central grid laplace operators. This scheme is distinctive in what it is both explicit and unconditionally stable, in the sense that Δ_t is not restricted by the values of the diffusion coefficient (see books[137, 155, 185, 194]). It is interesting that leap-frog central difference diffusion scheme is unstable. The Du Fort-Frankel scheme is however only conditionally consistent provided, as for that $\frac{\Delta_t^2}{\Delta_x^2} \to 0$ when $\Delta_x \to 0$ and $\Delta_t \to 0$. We derived above similar conditions for the TRT scheme (see (2.51)). However, the stability condition [122] of LFCCDF scheme depends on the diffusion coefficients for the anisotropic tensors:

$$[\sum_\alpha m_{\alpha\alpha}]\sum_\alpha \frac{U_\alpha^2}{m_{\alpha\alpha}} \le 1 \,,\; m_{\alpha\alpha} = 2\frac{H_{\alpha\alpha}\Delta_t}{\Delta_\alpha^2} \,,\; U_\alpha = \frac{u_\alpha \Delta_t}{\Delta_\alpha} \,. \tag{2.61}$$

This condition reduces to Courant-Friedrichs-Lewy (CFL) condition only for isotropic tensors. The conditions (2.61) is to be contrasted to stability conditions (1.77) and (1.78) of the FTCS and MFTCS schemes.

Let us come back to relation (2.55). The von Neumann stability analysis of the TRT model reduces then to inspection of the relation $A^2 + B^2 \le 1$. Hence, exact stability criteria depend on the selected equilibrium values (weights and characteristic

velocity), and the form of the involved finite-difference stencil in space (velocity set). The principal point is that the stability bounds can be established independently of the selected transport coefficients, provided that $\Lambda^{eo} = \frac{1}{4}$. For minimal anisotropic advection-diffusion schemes, the equation (2.55) is equivalent to FTCS scheme and its known stability bounds have been re-interpreted in Sections 1.6.6 and 1.6.7 for the whole sub-class of the TRT models given by $\Lambda^{eo} = \frac{1}{4}$. They are presented by relations (1.80) and (1.82). In 1D case, and taking $c_e = 1$, $E_q^{(u)} = 0$ then $E_0 \equiv 0$ and $d1Q3$ scheme without rest population becomes equivalent to Du Fort-Frankel scheme, combined with the central difference for convective term, with only CFL condition: $||U|| \leq 1$, for any diffusion coefficient. This property of two population scheme was first reported by Ancona [5].

Beyond the case $\Lambda^{eo} = \frac{1}{4}$, one needs to estimate the impact from the non-equilibrium term $(\Lambda^{eo} - \frac{1}{4}) \sum_{q=1}^{Q-1} \Delta_q^2 g_q^{\pm}$ in relation (2.50). Although several (very tedious) exact results were already obtained from Fourier analysis, they have not yet allowed to draw the detailed picture of the stability as a function of the selected values $\Lambda^{\pm}$.

2.9 Concluding remarks

When the second and higher-order variation of the non-equilibrium component is neglected in relations (2.17) and (2.18), or when $\Lambda^{eo} = \frac{1}{4}$, then the approximated macroscopic equations can be regarded as finite-difference type schemes where the macroscopic quantities are given by equilibrium moments. Their second-order approximation is governed by the physical numbers and their truncation errors scale with the physical parameters similar as for direct discretizations of the partial differential equations. However, the non-equilibrium contribution, proportional to $(\Lambda^{eo} - \frac{1}{4})$, keeps this property in general only for *steady* solutions provided that Λ^{eo} is set for any variation of the transport coefficients. In fact, the exact time difference relation (2.55) is not parametrized by Λ^{eo} and only conditionally consistent. It becomes second-order accurate in time for diffusion equation only when $\Lambda^{-} = \frac{1}{2}$. Hence, both mass and momentum conservation relations carry this property only for the BGK model with $\tau = 1$.

An interesting research path is to find the exact form of time-dependent non-equilibrium solutions as explicit functions of the eigenvalues and to investigate their most efficient parametrization. On the other side this could also give a way to assess the (infinite) multi-scale Chapman-Enskog time dependent approximations. Future works are needed to examine the most accurate choices for time dependent source terms. It would be also nice to explore the stability bounds of finite-difference equivalent system for hydrodynamic (Navier-Stokes) equations.

Chapter 3

Boundary schemes for the LBE

This topic is still one of the more fascinating in the LBE community! Far to be exhaustive, this list includes [7, 20, 33, 40, 44, 51, 55, 83, 87, 108, 111, 101, 112, 119, 128, 133, 139, 147, 151, 154, 170, 178, 181, 191, 204, 212, 218, 220] and the author's works in collaboration with P. Adler, D. d'Humières and F. Verhaeghe, [56, 57, 60, 66, 70, 74, 75].

The simple reflections of the populations at the solid walls were formulated as closure relations and examined for effective location of the no-slip and slip walls in the early works [40, 56, 57], giving exact solutions for effective channel width in simple (parallel to some lattice axis) Couette [40] and Poiseuille [56, 57] Stokes flow. Observed numerical artefacts of these schemes, such as the lack of precision and the appearing of Knudsen modes for inclined walls [60], stimulated the search of alternative boundary approaches. The node-based approaches of Skordos [178] and author's PhD work [57] prescribe the incoming populations with the finite-difference approximations of the Chapman-Enskog series. The *Local Second Order Boundary Method* [60] replaces the finite-difference approximations by a suitable local systems of the linearized equations, deriving all necessary (not only first, but also the second order) derivatives from the known populations. This idea takes later an elegant form of the *multi-reflection*, a link-based scheme for arbitrarily shaped boundaries.

Third-order accurate multi-reflection schemes were first formulated in [66], fitting the closure relation to the directional Taylor expansion of the Dirichlet velocity value. They were validated for static and moving boundaries, [44, 66, 112], and for porous media, [66, 151]. A generic form of the multi-reflection was established in [70] and turned as the Dirichlet boundary relation either for the symmetric equilibrium component (e.g., pressure or diffusion AADE's variable), or for the anti-symmetric one (velocity or advective-diffusive flux). Although the deficiency

of the simple reflections to prescribe the normal flux for the AADE was quantified and several corrections were proposed in [70], this problem is still open. Several new families of the multi-reflection hydrodynamic velocity schemes ($M_q^{(u)}$) and pressure ($M_q^{(u)}$) schemes have been recently developed in [74] and extended to corners. Then the "node" based mixed scheme combines the $M_q^{(u)}$ schemes for the tangential velocity and $M_q^{(p)}$ schemes for pressure. Both $M_q^{(u)}$ and $M_q^{(p)}$ schemes are accompanied with a formal estimate of their accuracy in time, which can be used to assign the most suitable boundary values in case of time dependent boundary conditions. All these findings are formulated in the algorithmic form and validated in [75].

Actually, there is an infinite number of multi-reflection schemes with equal, second or third order, formal accuracy. They are first built with one neighbor for the linear (second order accurate) schemes and with two neighbors for the parabolic (third order accurate) schemes. In both cases, they can be turned out as the one neighbor schemes, propagating the known populations *prior* the computing of the multi-reflection. With several arguments in hand, we built then their sub-classes which yield exact parametrization of the closure relations. We emphasize that the TRT model with the parametrized boundary schemes cure a main deficiency of the LBE hydrodynamic solutions: their unphysical dependency on the viscosity, recognized already by Skordos [178], confirmed by the analytical solutions and computations in porous media, [56, 66, 151], and discussed by Holdych et al [95] in connection with the convergence behavior of the BGK scheme. We propose explicit local correction which gets the parametrization property for all considered linear schemes, and, in particular, improve the popular Bouzidi-Firdaouss-Lallemand (BFL) rule [20] and the three population scheme [212]. These two schemes are called, respectively, ULI/DLI and YLI in [74, 75]. Exactly parametrized schemes keep the properties of the bulk operators on the numerical solution, then get viscosity independent permeability for any porous structure ! At the end of this chapter we summarize several techniques [66] for computations of the momentum transfer on the shaped boundaries and moving boundary algorithms, and give some remarks on the actual "state of art" for the boundary schemes in LBE.

3.1 Simple reflections

Borrowed from the Maxwell's idea, simple reflections of the particles on the solid walls were adapted to mimics the hydrodynamic boundary conditions in the Lattice Gas methods and later inherited by the Lattice Boltzmann schemes. The broadly used condition to implement no-slip velocity is the so-called *bounce-back* rule where the population leaving the fluid returns to the node of departure with the

opposite velocity (see sketch in Figure 3.1):

$$f_{\bar{q}}(\vec{r}_{\rm b},t+1) \;=\; \tilde{f}_q(\vec{r}_{\rm b},t)\;,\;\; \vec{c}_q=-\vec{c}_{\bar{q}}\;,\; \vec{r}_{\rm w}=\vec{r}_{\rm b}+\vec{c}_q\notin\Omega\;. \qquad (3.1)$$

This rule is not only very simple and available for any geometry, but also enforces the mass conservation in the computational domain. Unlike the bounce-back, the specular reflection is suitable only for flat walls, in general. The so-called *local specular reflection* (e.g., [67]) adapts it for complex geometries, both rules are equivalent for the flow invariant along the wall, but the local specular reflection may loss in accuracy for the AADE, [70].

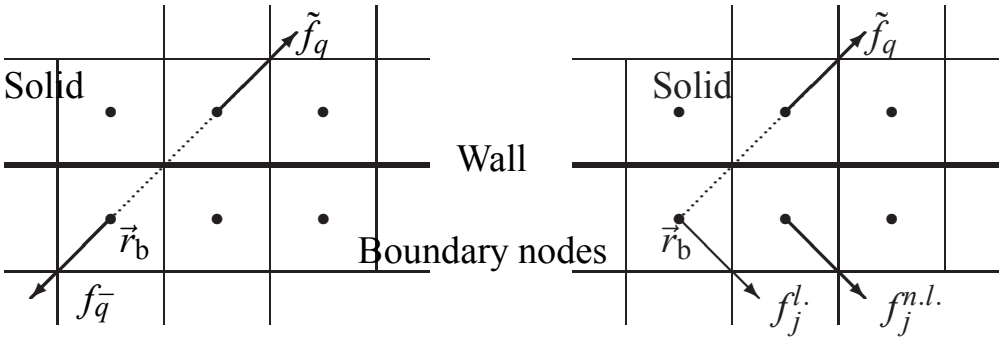

Figure 3.1: Sketch for the bounce-back on the left picture and specular reflection on the right picture: local ($f_j^{l.}=\tilde{f}_q$) and non-local ($f_j^{n.l.}=\tilde{f}_q$) specular reflections.

Intuitively suitable, the wall reflections raise however the question of the exact location of the no-slip and slip conditions. Exact solutions of the evolution equation with linear spatial velocity dependency, and invariant by the translation along the boundary parallel to one of the coordinate axes, were first constructed by Cornubert, d'Humières and Levermore [40]. They show that a mixture of the bounce-back (with a probability p) and the specular reflection (with a probability $1-p$) locates the no-slip condition at a distance equal to $\delta=\frac{1}{2}+\alpha\nu\frac{(1-p)}{p}$. Except for the bounce-back ($p=1$), which annihilates the velocity half-way between the row of the boundary fluid nodes $\vec{r}_{\rm b}$ and the outside row, the effective position of no-slip/slip velocity depends on the kinematic viscosity ν (α being lattice dependent constant). When $p=0$, the specular reflection mimics the free-slip condition. Performed in the terms of the mean distribution functions, the analysis [40] is valid not only for the Lattice Gaz method but also for the LBE.

Slightly different methodology was independently developed in the author's PhD thesis [57]. Motivated by finding an exact location of the boundaries in the parabolic (Poiseuille) flow, the first order Chapman-Enskog expansion was extended to include the second order equilibrium derivatives, in the presence of the

external force and in the frame of the FCHC (matrix) model (this is given in Appendices A and B of [56]). Substituting this expansion (which is exact for the Stokes Poiseuille flow) into the mixture of simple reflections, their closure relations were compared to the Taylor expansion of the boundary value. This gives the exact solutions for free eigenvalue $\lambda^-(\nu, p)$ or, inversely, for $p(\nu, \lambda^-)$ (formulas (2.31) in [57]) which yield slip velocity equal to zero midway the grid nodes.

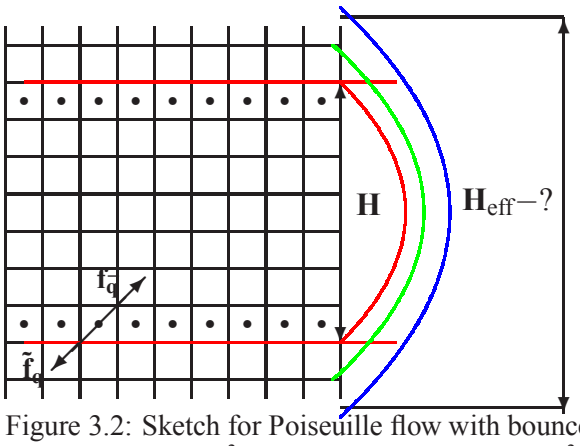

Figure 3.2: Sketch for Poiseuille flow with bounce-back: $H_{\rm eff} < H$ if $\Lambda^{eo} < \frac{3}{16}$ and $H_{\rm eff} > H$ if $\Lambda^{eo} > \frac{3}{16}$. Exact: $H_{\rm eff} = H$ if $\Lambda^{eo} = \frac{3}{16}$.

It was then understood that the effective width $H_{\rm eff}$ of the modeled with the bounce-back channel is controlled by the specific combination of viscous mode eigenvalues with free eigenvalues, associated with the third order polynomials. This combination is exactly what is called Λ^{eo}, then:

$$H_{\rm eff}^2 = H^2 + \frac{16}{3}\Lambda^{eo} - 1\,. \tag{3.2}$$

This solution is given by relation (47) in [56] (using $\lambda_{2c} \to \lambda^-$) and in terms of the Λ^{eo} by relation (43) in [66] (using $\lambda_2 \to -\lambda^-$, $\lambda_\nu \to -\lambda^+$) and formula (2.30) in [74]. The solution is valid for all commonly used hydrodynamic models, e.g., $d2Q9$, $d3Q15$ and $d3Q19$, provided that the velocity is redefined with the half forcing (relation (1.9)) and the force weights are set equal to velocity weights: $F_q^\star = t_q^\star(\vec{F}\cdot\vec{c}_q)$. If any one of these conditions is not respected, the same methodology applies but the exact solution for Λ^{eo} may differ from relations (3.3). The solution is also valid when the pressure gradient is modeled exactly, via the adequate inlet/outlet pressure conditions, then for any combination of the pressure

drop and forcing. Recently, the analytical solution [75] confirmed the validity of this solution in the presence of the non-linear term (see in Section 6.1.4).

It was rapidly recognized that the exact solutions $\lambda^-(\lambda^+)$, which equate $H_{\rm eff}$ to the assumed width H, differ for the parallel and diagonal (inclined at 45° with respect to coordinate axes) parabolic flow (relation (54b) of [56]):

$$\begin{aligned} H_{\rm eff} = H \qquad & \text{if} \\ \Lambda^{eo} &= \frac{3}{16} \text{ for parallel flow ,} \\ \Lambda^{eo} &= \frac{3}{8} \text{ for diagonal flow .} \end{aligned} \tag{3.3}$$

First relation defines $\lambda^-(\lambda^+) = -8\frac{(2+\lambda^+)}{(8+\lambda^+)}$, sometimes referred to as the "magic" rule, e.g., [2, 151], following our historical notations. Special (distance dependent) solutions for Λ^{eo} extend the relations (3.3) to arbitrary distance between the grid nodes and the flat walls, using the so-called "magic linear" schemes. These findings are summarized in Section 6.1.1.

The early analysis of the bounce-back was extended to 2D flow (Appendix C, [56]) and then worked out for stagnation flow. It was derived that the normal and tangential velocities do not vanish at the same distance with respect to the boundary fluid nodes. Altogether, these results indicated that there is no one universal "most accurate" dependency $\lambda^-(\lambda^+)$, even for flat walls and invariant flows. The alternative methods then were looked for.

3.2 "Node-based" schemes

The first approaches proposed by Ziegler [218] and Noble et al. [147] prescribe the velocity directly on solid grid nodes. More general schemes are based on the second-order [178] and third-order [57] accurate Chapman-Enskog expansions for $f_{\bar{q}}(\vec{r}_{\rm b}, t+1)$, where the derivatives are approximated with the help of the finite-differences. Three techniques were developed in [57] to locate velocity at any prescribed distance.

The first one, like the Skordos's "inverse mapping" method, computes the unknown populations directly in the form of series. The unknown pressure and velocity are then expressed with the help of a Taylor expansion, where prescribed Dirichlet velocity values are accounted for by a finite-difference approximation of the derivatives. In contrast, the (unknown) equilibrium variables are expressed via the moments of the known and unknown populations and the unknown populations themselves are looked for as a solution of the linearized equations, following the second approach. The third technique, called "réflexions generalisées", represent

the local set of the unknown populations as a linear combination of all outgoing populations; the local mass conservation was enforced, then the unknown coefficients form the "probability" matrix.

Using the finite-difference approximations, all these techniques require access to the populations of the neighboring lattice nodes, thus they are in general non-local. The main idea of the *local second-order boundary* (LSOB) method [60] is to split the hydrodynamic fields – momentum, its first- and second-order derivatives, and density – in two sets: the known fields given by the boundary conditions (or derived from them for sufficiently smooth walls) and the unknown fields. The linear system relating these unknown fields to the known populations is then written at each boundary node using two kinds of known populations: those arriving from neighboring liquid nodes, $\tilde{f}_q(\vec{r}_\mathrm{b}-\vec{c}_q,t)$ and those which should leave it and propagate into the solid: $\tilde{f}_q(\vec{r}_\mathrm{b},t)$. Then the number of known populations is equal to the number of the lattice velocities; this number was found to be larger than the number of unknown (non-derived from the boundary conditions) hydrodynamic fields. The LSOB method is exact for arbitrarily rotated Poiseuille Stokes flow and third-order accurate for flows invariant by translation along arbitrarily inclined 2D and 3D flat boundaries. A recent scheme by Hollis et al. [101] shares several common ideas but it is restricted to edge nodes and second-order expansion.

In order to avoid difficulties in sharp corners, the LSOB was reformulated in terms of the local (and not the wall's) derivatives (see Appendix A of [60]) and then successfully applied to different shaped pipes, [61] (several examples are reviewed in Section 6.1.2). It was observed that the independent closure relations should be established for each cut link, to avoid the loss of the uniqueness of the global system. This condition can be met naturally by the link-wise schemes, but in exchange of locality.

3.3 Generic multi-reflection scheme

Several link-wise boundary schemes are proposed in [20, 33, 51, 83, 128, 139, 212], bearing in mind the linear (directional) extrapolations and/or interpolations of the known populations or their non-equilibrium components. Our techniques [66, 69, 74] are thought more generally, based on the underlying third-order accurate expansion of the involved equilibrium components and the obtained closure relations. As above, we assume that $\vec{r}_\mathrm{b}$ is the grid boundary node, $\vec{r}_\mathrm{b}+\vec{c}_q \notin \Omega$ and that $\vec{r}_\mathrm{w}=\vec{r}_\mathrm{b}+\delta_q\vec{c}_q$, $0\le\delta_q\le 1$, is the point where "cut link" $\vec{c}_q$ intersects the wall (see Fig. 3.3).

Multi-reflection in its original form involves five known post-collision populations and two additional terms, $f_q^{\mathrm{p.c.}}(\vec{r}_\mathrm{b},t)$ and $w_q(\vec{r}_\mathrm{w},\tilde{t})$, for each unknown popula-

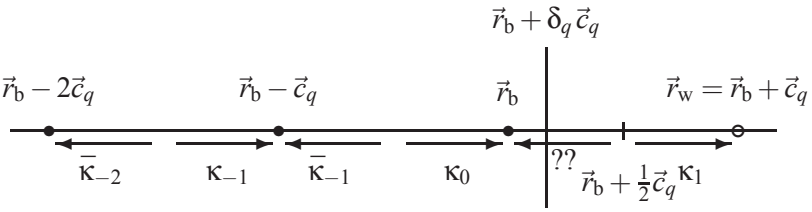

Figure 3.3: The velocity $\vec{c}_q$ cuts the boundary surface at $\vec{r}_b + \delta_q \vec{c}_q$, between the boundary node $\vec{r}_b$ and an outside node $\vec{r}_b + \vec{c}_q$. The figure is recalled from [66].

tion $f_{\bar{q}}(\vec{r}_b, t+1)$:

$$\begin{aligned} f_{\bar{q}}(\vec{r}_b, t+1) &= M_q(\vec{r}_b, t)\ ,\ M_q(\vec{r}_b, t) = R_q(\vec{r}_b, t) + f_q^{\text{p.c.}}(\vec{r}_b, t) + w_q(\vec{r}_w, \tilde{t})\ , \\ \text{where} & \\ R_q(\vec{r}_b, t) &= \kappa_1 \tilde{f}_q(\vec{r}_b, t) + \kappa_0 \tilde{f}_q(\vec{r}_b - \vec{c}_q, t) + \kappa_{-1} \tilde{f}_q(\vec{r}_b - 2\vec{c}_q, t) \\ &+ \bar{\kappa}_{-1} \tilde{f}_{\bar{q}}(\vec{r}_b, t) + \bar{\kappa}_{-2} \tilde{f}_{\bar{q}}(\vec{r}_b - \vec{c}_q, t)\ . \end{aligned} \tag{3.4}$$

Performing the propagation step from $\vec{r}_b - 2\vec{c}_q$ to $\vec{r}_b - \vec{c}_q$ *prior* the boundary rule, an equivalent *one neighbor* form for $R_q(\vec{r}_b, t)$ reads:

$$\begin{aligned} R_q(\vec{r}_b, t) &= \kappa_1 \tilde{f}_q(\vec{r}_b, t) + \kappa_0 f_q(\vec{r}_b, t+1) + \bar{\kappa}_{-1} \tilde{f}_{\bar{q}}(\vec{r}_b, t) \\ &+ \kappa_{-1} f_q(\vec{r}_b - \vec{c}_q, t+1) + \bar{\kappa}_{-2} \tilde{f}_{\bar{q}}(\vec{r}_b - \vec{c}_q, t)\ . \end{aligned} \tag{3.5}$$

The diagonal links in corners with no grid neighbors at $(\vec{r}_b \pm \vec{c}_q)$ reduce the rule (3.5) to $1-3$ population schemes (where $\kappa_{-1} = 0$, $\bar{\kappa}_{-2} = 0$) and replacing $\kappa_0 f_q(\vec{r}_b, t+1)$ with the previous step solution $\kappa_0 f_q(\vec{r}_b, t)$:

$$R_q(\vec{r}_b, t) = \kappa_1 \tilde{f}_q(\vec{r}_b, t) + \kappa_0 f_q(\vec{r}_b, t) + \bar{\kappa}_{-1} \tilde{f}_{\bar{q}}(\vec{r}_b, t)\ . \tag{3.6}$$

The third-order accuracy in corners can be maintained but compromising the link-wise implementation (see details in Section 5.2.4 in [74]). Indeed, different combinations of "node" based and "link" based approaches are possible and perhaps, they are most suitable in corners. One example is the "one point" method of Junk and Yang [112]. This scheme combines the LSOB method (restricting it to the second order expansion) and the link-wise fitting of the Taylor expansion to boundary values, but losses the simplicity, e.g., of the BFL rule for equal accuracy. We stress that the form (3.6) is local and can be adapted for all considered below linear schemes but the original forms (3.4) and (3.5) are preferable. A special care is required to avoid a decoupling of the diagonal corner link, $(\vec{r}_b \pm \vec{c}_q) \notin \Omega$, from the whole system. This case is considered in Section 5.5 of [74].

Exact closure relations of the multi-reflection are examined in terms of all relevant $e_q^{\pm}$ and $g_q^{\pm}$ components in the next section, for a sake of the analysis of their parametrization properties. The non-equilibrium components are then approximated with the third order expansion, involving suitable in accuracy directional derivatives between the neighbors. The idea behind this is to get the approximate closure relation in the form:

$$\begin{aligned} \alpha^{\pm}(e_q^{\pm} &+ \delta_q\partial_q e_q^{\pm} + \frac{1}{2}\delta_q^2\partial_q^2 e_q^{\pm} + \alpha^{(t)}\partial_t e_q^{\pm})(\vec{r}_{\rm b},t) = w_q(\vec{r}_{\rm w},\tilde{t}) + O(\Delta_x^3) + O(\Delta_t^2)\ , \\ w_q(\vec{r}_{\rm w},\tilde{t}) &= \alpha^{\pm}e_q^{\pm}(\vec{r}_{\rm w},\tilde{t})\ ,\ \alpha^{+}\neq 0\ ,\ \text{or}\ \alpha^{-}\neq 0\ . \end{aligned} \tag{3.7}$$

When the relation (3.7) is get exactly for $O(\partial_q^{(n-1)} j_q^{\star})$, $O(\partial_q^{(k-1)} \mathcal{P}_q^{\star})$ and $O(\partial_q^{(l-1)} F_q^{\star})$ components, in terms of the equilibrium components (1.42), we will say that the accuracy order of a given boundary scheme is represented by the triplet

$$j^{(n)}/\mathcal{P}^{(k)}/F^{(l)}\ . \tag{3.8}$$

The schemes with the triplet $j^{(2)}/\mathcal{P}^{(1)}/F^{(0)}$ are referred to as "linear" or "second-order" schemes and with the triplet $j^{(3)}/\mathcal{P}^{(2)}/F^{(1)}$ as "parabolic" or "third-order" schemes, respectively. The leading accuracy for time dependent boundary conditions is controlled by the parameter $\alpha^{(t)}$, via a proper selection of the boundary value $e_q^{\pm}(\vec{r}_{\rm w},\tilde{t})$. The linear schemes are exact for linear flows and uniform pressure (like Stokes Couette flow) and the parabolic schemes are exact for parabolic velocity profiles and linear pressure distributions (and/or uniform force distribution), as Poiseuille Stokes flow in arbitrarily inclined channels.

The coefficients κ_1 to $\overline{\kappa}_{-2}$ determine the coefficients of the obtained closure relations, e.g.,

$$\begin{aligned} \alpha^{-} &= \alpha^{(u)} = \kappa_1 + \kappa_0 + \kappa_{-1} - (\overline{\kappa}_{-1} + \overline{\kappa}_{-2}) + 1\ , \\ \alpha^{+} &= \alpha^{(p)} = \kappa_1 + \kappa_0 + \kappa_{-1} + (\overline{\kappa}_{-1} + \overline{\kappa}_{-2}) + 1\ . \end{aligned} \tag{3.9}$$

The solution for $\kappa_1 - \overline{\kappa}_{-2}$ is found such that the closure relations reduce to relations (3.7) up to prescribed triplet. The coefficients generally depend on δ_q. The solution for the coefficients of $M_q^{(u)}$ velocity schemes cancel the terms related to e_q^{+} and fit the relation (3.7) to Taylor expansion for $e_q^{-}(\vec{r}_{\rm w},\tilde{t})$. This is inverse for the $M_q^{(p)}$ pressure schemes. The correction $f_q^{\rm p.c.}(\vec{r}_{\rm b},t)$ is of special importance. In the original parabolic MR1 scheme [66] it removes the local post-collision component $\alpha^{(u)}\Lambda^{-}g_q^{-}(\vec{r}_{\rm b})$, which is incompatible with the relation (3.7) at the second order. In more recent schemes, the correction $f_q^{\rm p.c.}(\vec{r}_{\rm b},t)$ removes all undesired components, either from the parametrization point of view (typically, for the linear schemes), or for further improvement of the precision (typically, for the parabolic schemes), or both.

3.3.1 Parametrization of the boundary schemes

The dimensional analysis from Section 2.4 works *exactly* on the obtained numerical solution only when the *exact closure relations* keep the parametrization properties for all cut links. For steady solutions, it is simpler to elaborate on the two-point form (3.5). Substituting there $\tilde{f}_q(\vec{r},t) = f_q(\vec{r},t) + g_q(\vec{r},t) + S_q$ and dropping the time we get exact steady closure relations as:

$$\sum_{r=\{\vec{r}_\mathrm{b},\vec{r}_\mathrm{b}-\vec{c}_q\}} [A^{(u)} j_q^\star \quad + \quad A^{(p)} \mathcal{P}_q^\star + B^{(u)} g_q^+ + B^{(p)} m_q^{(F)} + A^{(u)} \Lambda^- F_q^\star](\vec{r})$$

$$= \quad -f_q^{\mathrm{p.c.}}(\vec{r}_\mathrm{b}) - w_q(\vec{r}_\mathrm{w}) \; , \; m_q^{(F)} = g_q^- + S_q^- \; , \qquad (3.10)$$

where all coefficients are linear combinations of the $\kappa_1 - \overline{\kappa}_{-2}$ and the collision eigenvalues, and $f_q^{\mathrm{p.c.}}(\vec{r}_\mathrm{b})$ is a given (selected) combination of the non-equilibrium components and/or finite-difference approximations. The subsequent analysis is similar as for the bounce-back condition above (see in Section 2.3.2). We multiply relation (3.10) by Λ^+. Bearing in mind the form (2.8)-(2.12) of the non-equilibrium components, the parity and dimensional arguments tell us that the proper parametrized closure relation should represent a linear combination of $\Lambda^+ j_q^\star$ and g_q^+, on the one side, with $m_q^{(F)}$ and $F_q^\star$, on the other side, where the coefficients of this combination depend on the eigenvalues only via Λ^{eo}. The numerical solutions obtained with the boundary schemes built along this rule keep the parametrization, at least for steady flow examples of [75].

Then we conjecture that the following conditions (the same as in [75]) are sufficient for proper parametrization of the hydrodynamic solutions:

$$\begin{aligned} A^{(u)}(\vec{r}) &= r_1(\Lambda^{eo},\vec{r},q) \; , \qquad B^{(u)}(\vec{r}) = r_2(\Lambda^{eo},\vec{r},q) \; , \\ A^{(p)}(\vec{r}) &= \Lambda^- r_3(\Lambda^{eo},\vec{r},q) \; , \; B^{(p)}(\vec{r}) = \Lambda^- r_4(\Lambda^{eo},\vec{r},q) \; . \end{aligned} \qquad (3.11)$$

Here, $r_i(\Lambda^{eo},\vec{r},q)$ abbreviates any function which depends on the eigenvalues only via Λ^{eo} or independent of them. It is noted that r_i may depend on δ_q and may differ for any two coefficients, from one point to another one, or from link to link. It should also be understood that if $A^{(u)}(\vec{r})$, $B^{(u)}(\vec{r})$, $B^{(f)}(\vec{r})$ vanish (e.g. pressure schemes below), the coefficients $A^{(p)}(\vec{r})$ and $B^{(p)}(\vec{r})$ can be reduced by a factor Λ^-. It is sufficient then to get them independently of the relaxation parameters or depending on them only via Λ^{eo}. All pressure and velocity schemes constructed in [74] satisfy these relations. Using the MRT models, Λ^{eo} in relations (3.11) should be replaced by a list of the relevant $\Lambda^{eo}(\lambda^-,\lambda^+)$ values. Then it may happen in principle that a particular boundary scheme (whose coefficients depend on the eigenvalues) will not inherit all parametrization properties of its TRT counterpart. We emphasize that the closure relations of any boundary scheme can be checked along these lines, but this is much more complicated for "node" based approach.

3.3.2 Summary of the Dirichlet velocity $M_q^{(u)}$ schemes

The $M_q^{(u)}$ schemes are developed in Section 5 of [74] and summarized in Section 2.3 of [75]. Two principal classes, the "linear" MGLI($\alpha^{(u)}$) family and the "parabolic" MGMR(C) family, are specified in Table 3.1. They yield $\alpha^{(u)}$ and C, respectively, as free parameters. The bounce-back is a particular instance of MGLI($\alpha^{(u)}$) family when $\alpha^{(u)} = 2$ ($\kappa_1 = 1$, all other coefficients vanish) and $\delta_q = \frac{1}{2}$. The $M_q^{(u)}$ schemes are computed with $w_q^{(u)} = -\alpha^{(u)} j_q^{\star b}(\vec{r}_w, \tilde{t})$, where for incompressible flow $j_q^{\star b}(\vec{r}_w, \tilde{t}) = t_q^{\star} \rho_0 u_q^b(\vec{r}_w, \tilde{t})$. The theoretical estimates for $\tilde{t} = t + \alpha^{(t)}$ are given in Table 8 of [74]. We suggest that these estimates are efficient for linear schemes only when their second-order spatial error is reduced with a proper choice of Λ^{eo}. In such a case, $\alpha^{(t)}$ has the same value for parabolic and linear schemes.

The idea behind the MGLI($\alpha^{(u)}$) family is as follows. An infinite number of second order accurate, "linear" schemes was first defined with $1-3$ neighbor populations ($\overline{\kappa}_{-2} = \kappa_{-1} = 0$). Their coefficients are governed by a choice of the coefficient $\alpha^{(u)}$ and their parametrization properties are related to the value of the coefficient $B^{(p)}$ in relation (3.10), such that the condition $B^{(p)} = -\alpha^{(u)} \Lambda^-$ yields: $\alpha^{(u)} = 2(1 + \kappa_0)$. This choice fixes one particular scheme, called (central linear scheme) CLI scheme ($\alpha^{(u)} = \frac{4}{1+2\delta_q}$, $\kappa_1 = 1$, $\kappa_0 = -\overline{\kappa}_{-1} = \frac{1-2\delta_q}{1+2\delta_q}$). It seems that this scheme is less robust than the BFL rule. The BFL rule selects the solution with $\alpha^{(u)} = 2$, $\kappa_1 = 2\delta_q$, $\kappa_0 = 1 - 2\delta_q$ when $\delta_q \leq \frac{1}{2}$ and, otherwise, $\alpha^{(u)} = \frac{1}{\delta_q}$, $\kappa_1 = \frac{1}{2\delta_q}$, $\overline{\kappa}_{-1} = \frac{2\delta_q - 1}{2\delta_q}$. The key point is that all BFL coefficients belong to interval $[0\ ,1]$. The ULI/DLI and CLI all reduce to the bounce-back for $\delta_q = \frac{1}{2}$.

However, in contrast with the bounce-back and CLI scheme, the BFL rule is not parametrized correctly. With a purpose to get a correct parametrization for all linear schemes, we introduce a local $f_q^{\text{p.c.}(u)}$ correction, which is given in Table 3.1. The resulting "magic linear" schemes form the MGLI($\alpha^{(u)}$) family. The ULI/DLI schemes with the $f_q^{\text{p.c.}(u)}$ correction are then called MGULI/MGDLI. The correction vanishes for the bounce-back and CLI schemes. It is important that all schemes from MGLI($\alpha^{(u)}$) family have equivalent exact steady closure relations (3.10). There steady solutions are then identical but the stability properties may differ. So called parabolic MLI($\alpha^{(u)}$)$-$family have the same coefficients as their MGLI($\alpha^{(u)}$) counterparts but they make them third-order accurate with the help of the following correction:

$$f_q^{\text{p.c.}(u)} = -(B^{(p)} m_q^{(F)} + \alpha^{(u)} \Lambda^- F_q^{\star}) + \alpha^{(u)} \frac{\delta_q^2}{2} \partial_q^{2f.d} j_q^{\star}\,, \tag{3.12}$$

where $\partial_q^{2f.d} j_q^{\star}$ is computed using three-point directional finite-differences, involv-

ing the boundary and link neighbor velocity values. The ULI/DLI schemes with either linear or parabolic corrections are robust in numerical computations.

The five populations based "parabolic" family MGMR(C) extends the original MR1 scheme [66]. The MGMR(C) family yields $\alpha^{(u)} = \frac{2}{k+1}$, $k = k(\delta_q) - C\Lambda^-$, $k(\delta_q) = \frac{1}{2}(1+\delta_q)^2 - 1$ and $C^{min} \leq C\Lambda^- \leq 0$. This family holds the exact parametrization properties owing to a choice of its coefficients and reduces to MR1 scheme for $C = 0$, then $\kappa_1 = 1$, $\kappa_0 = -\overline{\kappa}_{-1} = \frac{1-2\delta_q-2\delta_q^2}{(1+\delta_q)^2}$, $\kappa_{-1} = -\overline{\kappa}_{-2} = \frac{\delta_q^2}{(1+\delta_q)^2}$, $\alpha^{(u)} = \frac{2}{k(\delta_q)+1}$. The heuristic stability bounds for C^{min} are formulated in Section 5.2.3 of [74]. We suggest (based on preliminary numerical tests) that proper selection of C value may improve the stability of the MR1 scheme. Other exactly parametrized schemes may be build when C takes a form of the polynomials of Λ^{eo}. These possibilities have not yet been explored.

$M_q^{(u)}$	MGLI($\alpha^{(u)}$)	MGMR(C)
κ_0	$-1-\alpha^{(u)}\delta_q$	$\frac{1-2\delta_q-2\delta_q^2-4C\Lambda^-}{(1+\delta_q)^2-2C\Lambda^-}$
κ_{-1}	0	$\frac{2C\Lambda^-+\delta_q^2}{(1+\delta_q)^2-2C\Lambda^-}$
$\overline{\kappa}_{-1}$	$1-\frac{1}{2}\alpha^{(u)}$	$\frac{-1+2\delta_q+2\delta_q^2-4C\Lambda^-}{(1+\delta_q)^2-2C\Lambda^-}$
$\overline{\kappa}_{-2}$	0	$\frac{2C\Lambda^--\delta_q^2}{(1+\delta_q)^2-2C\Lambda^-}$
$f_q^{\text{p.c.}(u)}$	$-(B^{(p)}+\alpha^{(u)}\Lambda^-)m_q^{(F)}$	$\alpha^{(u)}\Lambda^-(m_q^{(F)}-F_q^\star)$
order	$j^{(2)}/\mathcal{P}^{(1)}/F^{(0)}$	$j^{(3)}/\mathcal{P}^{(2)}/F^{(1)}$

Table 3.1: The coefficients κ_0, κ_{-1}, $\overline{\kappa}_{-1}$, $\overline{\kappa}_{-2}$ and $f_q^{\text{p.c.}(u)}$ correction for "linear" MGLI($\alpha^{(u)}$) and "parabolic" MGMR(C) schemes. The missing coefficient is $\kappa_1 = 1-\kappa_0-\kappa_{-1}-\overline{\kappa}_{-1}-\overline{\kappa}_{-2}$. Other parameters are: $B^{(p)} = -(\kappa_0+2\kappa_{-1}+\overline{\kappa}_{-2}+1)+\alpha^{(u)}(\frac{1}{2}-\Lambda^-)$ and $m_q^{(F)} = g_q^- + S_q^-$. Free parameters $\alpha^{(u)}$ and $C < 0$ are discussed in text.

3.3.3 Staggered invariants

Spurious conserved quantities have already been recognized for Lattice Gas by Zanetti [213] and then studied for the LBE (see review in [12] and [162]). They obey the relation

$$S(t) = -S(t+1) \text{ then } S(t)+S(t+1) = 0\ ,\ \forall t\ . \tag{3.13}$$

Their exact solution in an open channel consisting of $N_\perp$ lines parallel to the solid walls is derived in Section 5.4.2 of [74]. Indeed, owing to the momentum conser-

vation by the collision operator, the vertical momentum $\vec{J}_n(\vec{r},t)$ is exchanged (no forcing) between even and odd numbered grid lines, excepted at the boundary lines. Then, for several boundary schemes (which are precised below), the staggered invariants represent the specific linear combinations of the total vertical momentum, $\vec{J}_n^{(2l)}$ and $\vec{J}_n^{(2l-1)}$ which are computed for even and odd numbered lines. The solutions differ when the channel contains odd ($N_\perp = 2K+1$) or even ($N_\perp = 2K$) number of lines:

$$\begin{array}{rcl} N_\perp & = & 2K+1: \\ S(t) & = & [(\sum_{l=1}^{K}\vec{J}_n^{(2l)} - \sum_{l=1}^{K+1}\vec{J}_n^{(2l-1)}) \quad - \quad \kappa_0(\sum_{l=1}^{K}\vec{J}_n^{(2l)} - \sum_{l=2}^{K}\vec{J}_n^{(2l-1)}) \\ & & \qquad\qquad\qquad\qquad\qquad + \quad \kappa_{-1}(\sum_{l=2}^{K-1}\vec{J}_n^{(2l)} - \sum_{l=2}^{K}\vec{J}_n^{(2l-1)})](t) \\ N_\perp & = & 2K: \\ S(t) & = & [(\sum_{l=1}^{K}\vec{J}_n^{(2l)} - \sum_{l=1}^{K}\vec{J}_n^{(2l-1)}) \quad - \quad \kappa_0(\sum_{l=1}^{K-1}\vec{J}_n^{(2l)} - \sum_{l=2}^{K}\vec{J}_n^{(2l-1)}) \\ & & \qquad\qquad\qquad\qquad\qquad + \quad \kappa_{-1}(\sum_{l=2}^{K-1}\vec{J}_n^{(2l)} - \sum_{l=2}^{K-1}\vec{J}_n^{(2l-1)})](t)\ . \end{array} \tag{3.14}$$

The multi-reflection supports the uniform in space and oscillating in time vertical velocity when:

$$\kappa_0 + \overline{\kappa}_{-1} = 0\ ,\ \kappa_1 + \kappa_{-1} + \overline{\kappa}_{-2} = 1\ . \tag{3.15}$$

These conditions are satisfied by the bounce-back and CLI scheme where $\kappa_1 = 1$ (and $\kappa_{-1} = \overline{\kappa}_{-2} = 0$ for all linear schemes). Then the parametrization condition and "staggered" condition (3.15) coincide. Selecting $\kappa_1 = 1$ for five populations schemes, we get the MR1 scheme: $\kappa_0 = -\overline{\kappa}_{-1}$ and $\kappa_{-1} = -\overline{\kappa}_{-2}$. It follows that three naturally parametrized multi-reflections, all with the coefficient $\kappa_1 = 1$ for the outgoing population $\tilde{f}_q(\vec{r}_\mathrm{b},t)$: the first-order (bounce-back), the second-order (CLI) and the third-order (MR1) schemes support the spurious invariants ! However, as was early known [12], the staggered invariants are induced by the initialization and not self-generated. Consistent initialization routines are discussed in [140].

3.3.4 Summary of the Dirichlet pressure $M_q^{(p)}$ schemes

Known pressure boundary conditions mainly locate the solid walls at grid nodes, either prescribing the equilibrium distribution for the incoming populations or by deriving their solution from a local system of mass/momentum constraints, e.g., in [220]. So far a simple link-wise approach is the first-order accurate *anti-bounce-back* rule:

$$f_q(\vec{r}_\mathrm{b} + \vec{c}_q, t+1) = -\tilde{f}_{\overline{q}}(\vec{r}_\mathrm{b},t) + 2e_q^+(\vec{r}_\mathrm{w},\tilde{t})\ . \tag{3.16}$$

The equivalent scheme is used as a pressure condition on a free interface, [121, 197] and as an inlet/outlet pressure scheme in [2]. In our studies it first appears in [70], as a Dirichlet scheme for the diffusion equation (see also in Section 6.3.1). The pressure schemes developed in [74] fit their closure relations (3.7) to the link-wise Taylor expansion for $\mathcal{P}_q^\star$:

$$\begin{aligned}\alpha^{(p)}(\mathcal{P}_q^\star &+ \delta_q\partial_q\mathcal{P}_q^\star+\frac{1}{2}\delta_q^2\partial_q^2\mathcal{P}_q^\star+\alpha^{(t)}\partial_t\mathcal{P}_q^\star)(\vec{r}_{\rm b},t)=\alpha^{(p)}\mathcal{P}_q^\star(\vec{r}_{\rm w},\tilde{t})+Err^{(p)}\,,\\ \alpha^{(t)} &= -\frac{1+B^-}{\alpha^{(p)}}\,,\ B^-=-(\kappa_0+2\kappa_{-1}-\overline{\kappa}_{-2})\,.\end{aligned}\tag{3.17}$$

$M_q^{(p)}$	PAB	PLI	PMR(k)
κ_1	-1	$\frac{1}{2}-\delta_q$	$1+\lambda^+$
κ_0	0	δ_q-1	$-1+\frac{3\lambda^+(k-2)+\delta_q k(2+3\lambda^+)}{4}$
κ_{-1}	0	0	$-\frac{k\delta_q}{2}+\lambda^+\frac{1-3\delta_q k}{4}$
$\overline{\kappa}_{-1}$	0	$\frac{1}{2}$	$1+\frac{\delta_q k(\lambda^+-2)+\lambda^+(3k-2)}{4}$
$\overline{\kappa}_{-2}$	0	0	$\frac{-k\delta_q(\lambda^+-2)-\lambda^+(k-2)}{4}$
δ_q	$\frac{1}{2}$	$0\le\delta_q\le 1$	$0\le\delta_q\le 1$
order	$j^{(2)}/\mathcal{P}^{(2)}/F^{(2)}$	$j^{(2)}/\mathcal{P}^{(2)}/F^{(2)}$	$j^{(3)}/\mathcal{P}^{(2)}/F^{(2)}$

Table 3.2: The coefficients κ_1, κ_0, κ_{-1}, $\overline{\kappa}_{-1}$, $\overline{\kappa}_{-2}$ for the Dirichlet pressure $M_q^{(p)}$ schemes. The coefficients $\kappa_1-\overline{\kappa}_{-2}$ are found inside the heuristic stability interval $[-1,1]$ when $\frac{2}{3}\le k\le\frac{6}{5}$; we mostly use PMR1 scheme with $k=1$.

Table 3.2 summarizes the principal $M_q^{(p)}$ schemes: (*pressure anti-bounce-back*) PAB, (*pressure linear interpolation*) PLI and the five-populations based PMR(k) family, where k is a free parameter. All $M_q^{(p)}$ schemes use $f_q^{\text{p.c.}(p)}=-\beta^{(u)}g_q^+(\vec{r}_{\rm b},t)$, with $\beta^{(u)}=-(\kappa_0+2\kappa_{-1}-\overline{\kappa}_{-2}-1)+\alpha^{(p)}(\frac{1}{2}-\Lambda^+)$. This correction removes the first-order derivatives of velocity and forcing from the closure relation and differs the PAB and PLI schemes from their diffusion analogs [70]. The PMR(k)−family also cancels the second order velocity gradients, owing to selection of its coefficients. The particular choice, PMR2 = PMR($k=\frac{2}{(1+\delta_q)^2}$) yields a triplet $j^{(3)}/\mathcal{P}^{(3)}/F^{(2)}$: it is exact when both pressure and velocity fields are parabolic in space. The PMR2 yields exact closure relation $\mathcal{P}_q^\star(\vec{r}_{\rm b})\equiv\mathcal{P}_q^b(\vec{r}_{\rm w})$ when $\delta_q=0$, but it may loss the uniqueness of the solutions in such a situation, because of the insufficient number of restrictions on the non-equilibrium components. We emphasize that $\delta_q=0$ can be avoided and replaced by $\delta_q=1$, in a (possible) exchange of accuracy.

The pressure boundary values are carried out with $w_q^{(p)} = -\alpha^{(p)} e_q^+(\vec{r}_\mathrm{w}, \tilde{t})$. Then the pressure and the non-linear equilibrium term $E_q^{(u)}(\vec{r}_\mathrm{w}, \tilde{t})$ should be prescribed on the wall. Assuming the pressure and tangential velocity to be known on the boundary (see conditions (3.18) below), the normal velocity component, $u_n(\vec{r}_\mathrm{w}, \tilde{t})$, was extrapolated from the bulk using suitable directional approximations. In author's opinion the highly precise pressure conditions are meaningful only when the boundary pressure values are accurately prescribed. This is not usually the case of far field conditions where either alternative methods should be found, e.g., [113], or the velocity and pressure values should be first derived, e.g., with the help of approximate solutions [131, 111]. In this last work, the PAB scheme is successfully combined with the characteristics method to prescribe pressure values. One can then prescribe these values with one of the proposed pressure schemes.

3.3.5 Summary of the mixed $M_q^{(m)}$ schemes

A Dirichlet pressure condition is not sufficient to set the unique solution of the Navier-Stokes equations. As an example, we extend the MR approach to a mixed condition which prescribes the pressure and the tangential velocity, and actually combines the node based and link based approaches.

Let $\{\vec{n}, \vec{\tau}_1, \vec{\tau}_2\}$ be a local coordinate system built on the normal vector $\vec{n}$, perpendicular to the solid wall at $\vec{r}_\mathrm{w}$, and the tangential vectors $\vec{\tau} = \{\vec{\tau}_1, \vec{\tau}_2\}$. The mixed scheme prescribes the pressure $P^b = P(\vec{r}_\mathrm{w}, \tilde{t})$ (as a normal condition) and the tangential velocity $\vec{u}_\tau^b(\vec{r}_\mathrm{w}, \tilde{t})$ (as a tangential condition) at a smooth part $\Gamma^{(p)}$ of the solid boundary. Mixed condition can be viewed as a particular form of the third kind condition [80]:

$$\begin{aligned} -P + 2\mu\partial_n u_n|_{\Gamma^{(p)}} &= -P^b(\vec{r}_\mathrm{w}, t)\ ,\ \vec{r}_\mathrm{w} \in \Gamma^{(p)}\ , \\ \vec{u}_\tau - \beta\nu\partial_n \vec{u}_\tau|_{\Gamma^{(p)}} &= \vec{u}_\tau^b(\vec{r}_\mathrm{w}, t)\ ,\ \vec{u}_\tau = \{u_{\tau_1}, u_{\tau_2}\}\ , \end{aligned} \tag{3.18}$$

when the free parameter β is set equal to zero and the viscous stress component $\mu\partial_n u_n$ is neglected, e.g., when the normal velocity components are nearly invariant along the normal direction at the inlet/outlet, as in a straight long channel.

Actually, the closure relations of $M_q^{(u)}$ and $M_q^{(p)}$ schemes represent two independent Taylor directional expansions for $e_q^-(\vec{r}_\mathrm{w})$ and $e_q^+(\vec{r}_\mathrm{w})$, respectively. They cannot prescribe both equilibrium components *for each link* separately. The idea behind the $M_q^{(m)}$ scheme is (i) to equate the tangential projections on $c_{q\tau_1}$ and $c_{q\tau_2}$ vectors of the whole set of obtained closure relations to those projections of $M_q^{(u)}$ schemes and, (ii), to equate the total set of the normal projections (on the c_{qn}, $c_{q\tau_1}^2$, $c_{q\tau_2}^2$ and $c_{q\tau_1} c_{q\tau_2} c_{qn}$ vectors) to those of the $M_q^{(p)}$ scheme. These constraints are formulated in a generic way by relations (7.2)-(7.4) in [74]. Further works is needed

to evaluate this system in complex geometries. Actually, the details are worked out for $d2Q9$, $d3Q15$ and $d3Q19$ velocity sets but only for simple (parallel) orientation of the boundary, then adapted for corners. As an example, the $d2Q9$ scheme yields the incoming populations on the planar inlet as (see sketch 1.1 for velocity numbering):

$$\begin{aligned} f_1 &= M_3^{(p)}\,, \\ f_5 &= \frac{1}{2}(M_6^{(p)}+M_7^{(p)})-\frac{1}{2}(M_6^{(u)}-M_7^{(u)})\,. \\ f_8 &= \frac{1}{2}(M_6^{(p)}+M_7^{(p)})+\frac{1}{2}(M_6^{(u)}-M_7^{(u)})\,. \end{aligned} \tag{3.19}$$

Any $M_q^{(u)}$ and $M_q^{(p)}$ schemes can be substituted here. The results [75] show that the combinations of MGMR(C) (and especially MR1) and MLI($\alpha^{(u)}$) velocity families with the PMR1/PMR2 pressure schemes are superior in overall accuracy for steady and pulsatile flow.

3.3.6 Link-wise boundary schemes for the AADE

The coefficients of the multi-reflection scheme were tuned to meet second and third order accurate Dirichlet boundary conditions for the diffusion variable $\bar{\mathcal{D}}(s)$ in [70], *prior* to $M_q^{(p)}$ schemes. Second-order accurate AADE schemes (relation (32) of [70]) have the same coefficients as the PAB pressure scheme (see Table 3.2), but, without using the correction $f_q^{\mathrm{p.c.}(p)} = -\beta^{(u)} g_q^+(\vec{r}_\mathrm{b},t)$, they neglect the leading order variation of the advective term $\vec{J}\cdot\vec{c}_q$. Also, in contrast with the PMR(k)family, third order accurate schemes [70] (relations (27), (35)-(36) there) do not remove the second order derivatives of this term from the closure relations. Then we conjecture that the $M_q^{(p)}$ schemes are more accurate for advective-diffusion equations than the previously developed diffusion schemes.

Neumann, or specified flux boundary conditions, present a difficult problem for link-wise schemes. These schemes restrict the flux projection on each cut link, then they prescribe both the normal and tangential flux by the ensemble of the separate closure relations. The effective normal and tangential constraints were analysed in [70] for the bounce-back and specular reflection. It was confirmed that they specify the normal advective-diffusion flux for both, equilibrium-type and link-type approaches. The specular reflection releases the tangential velocity, at least when the advection velocity is constant. In contrast, the bounce-back restricts the tangential advective-diffusive flux to zero. This presents an additional condition, not compatible in general with the solutions of the AADE. Such a deficiency of the bounce-back was also numerically recognized in [48, 215].

Several correction terms for release of the tangential constraints, at least at leading orders, were proposed in [70] (Eqs. (56) and (57) there). This type correction was successfully adapted in [73] to prescribe the boundary value of the normal derivative $\partial_n \bar{\mathcal{D}}(\vec{r}_{\rm w},t)$ in the presence of the cross-diffusion components. Let us here include the advection velocity $s\vec{U}$ into the modified bounce-back scheme which is proposed in [73]. We write it down in the local coordinate system associated with the wall:

$$f_{\bar{q}}(\vec{r}_{\rm b},t+1) = \tilde{f}_q(\vec{r}_{\rm b},t) + w_q(\vec{r}_{\rm w},t) + f_q^{\rm p.c.}(\vec{r}_{\rm b},t)\ , \tag{3.20}$$

$$w_q(\vec{r}_{\rm w},t) = 2\Lambda_q^- E_q \partial_n \bar{\mathcal{D}}(\vec{r}_{\rm w},t) c_{qn}\ , \tag{3.21}$$

$$f_q^{\rm p.c.}(\vec{r}_{\rm b},t) = -2 \sum_{\tau=\{\tau_1,\tau_2\}} [sU_\tau - \Lambda_q^- E_q \partial_\tau \bar{\mathcal{D}}(\vec{r}_{\rm b},t)] c_{q\tau}\ . \tag{3.22}$$

The terms $\partial_\tau \bar{\mathcal{D}}(\vec{r}_{\rm b},t)$ can be derived from the g_q^- components moving along the wall, $\partial_\tau \bar{\mathcal{D}} \approx g_q^- / (E_q c_{q\tau})$. In complex geometries, they can be derived from the local gradient $\nabla \mathcal{D}$, using the rotational invariance of g_q^- at the first order (similar as in Section 5.4). Based on the bounce-back closure relation, the normal flux or normal gradient are prescribed only at the leading-order, and exactly for linear or piece-wise linear solutions taking $\delta_q = 1/2$. The error dependency on Λ^{eo} for non-linear solutions is examined in Section 6.3.1 of [73].

Another observed problem is that the separate closure relations may differ from the global condition, giving rise to accommodation (Knudsen) layers near the wall, especially when the diffusive flux components and the advective/injection flux components have different equilibrium weights, e.g., isotropic weights $t_q^\star$ for e_q^- and anisotropic weights E_q for e_q^+. The amplitude of the accommodation correction exponentially decreases towards the center of the channel and linearly decreases with grid refining. Similar behaviour was observed for the flux condition using the L-model with the anisotropic set of eigenvalues $\{\lambda_q^-\}$. This problem is illustrated in Section 8.2.1.2 of [75].

3.4 Momentum transfer on the boundary

Two definitions of momentum transfer were examined in [66], Section IV. The classical definition follows Ladd [123] and computes the momentum transfer as a difference between the local momentum of the outgoing and incoming populations:

$$\vec{M}^{(c)} = \sum_{q\in C} \tilde{f}_q(\vec{r}_{\rm b})\vec{c}_q - \tilde{f}_{\bar{q}}(\vec{r}_{\rm b})\vec{c}_{\bar{q}} = \sum_{q\in C} M_q \vec{c}_q\ ,\ M_q = \tilde{f}_q(\vec{r}_{\rm b}) + \tilde{f}_{\bar{q}}(\vec{r}_{\rm b})\ . \tag{3.23}$$

Hereafter in this section, the summation goes through the cut links. With the help of the Chapman-Enskog expansion, we show in [66] that, for incompressible steady

Navier-Stokes flows near flat boundaries, this definition is equivalent to the classical definition (at least up to the third order errors in the population expansion):

$$\vec{M}^{(c)} = A_s(P\vec{n} + \frac{j_n\vec{j}}{\rho_0} - \nu(\partial_n\vec{j} + \nabla j_n)) \,, \tag{3.24}$$

where A_s is the area of the plane solid surface discretized in a staircase manner on the grid. Then the conservation of the momentum yields (for total quantity of the momentum transfer in stationary flow under constant forcing)

$$\vec{M}^{(c)} = \vec{F}V^l \,, \tag{3.25}$$

where V^l is the number of nodes where the outgoing populations get the constant force quantities $t_q^\star(\vec{F}\cdot\vec{c}_q)$. By this means, $\vec{M}^{(c)}$ is both independent of the obtained solution and of the form of the boundary when the force is applied. Recently, the definition (3.23) has been analysed with the tools of the asymptotic analysis in [26]. The recent work by Peng and L.-S. Luo [154] discusses fluid-boundary interactions along similar ideas.

An alternative, "boundary" fitted definition was proposed by relation (66) in [66]:

$$\begin{aligned} \vec{M}^{(n)}(\vec{r}_\mathrm{b}) &= \sum_{q\in C} M_q^{(b)}(\vec{r}_\mathrm{b} + \delta_q\vec{c}_q)\vec{c}_q \,, \text{ where} \\ M_q^{(b)}(\vec{r}_\mathrm{b} + \delta_q\vec{c}_q) &= (\frac{1}{2} + \delta_q)M_q(\vec{r}_\mathrm{b}) + (\frac{1}{2} - \delta_q)M_q(\vec{r}_\mathrm{b} - \vec{c}_q) \,. \end{aligned} \tag{3.26}$$

Using exact populations for Couette and Poiseuille flows in the inclined channel, and Poiseuille-type flow in a circular pipe, we show that $\vec{M}^{(n)}(\vec{r}_\mathrm{b}) = \vec{F}V^{eff}$ (see Appendix B of [66]), where V^{eff} is *an effective grid volume* where the force is applied. Then the definition (3.26) equates the moment exchange to the effective volume forcing, to be contrasted with the "computational" volume V^l, which is independent of the actual position of the solid boundary on the grid.

3.5 Moving obstacles

Our motivation for the development of the LBE schemes [66] for the moving obstacles was two-fold. First, this allowed us to validate the multi-reflection approach in difficult situations, when the respective location of the wall and grid boundary nodes varies. Second, this required us to extend the method for the dynamical change of a status of the given grid node: from fluid to solid and from solid to fluid. An example is demonstrated in Fig. 3.4: here, three cylinders follow the imposed trajectories and the fluid fields are computed around them.

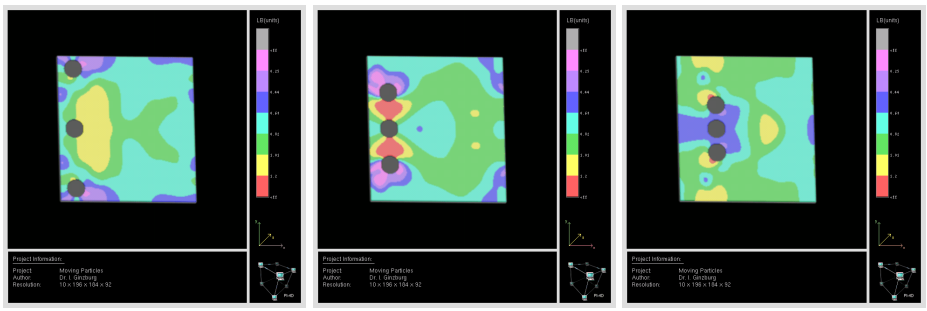

Figure 3.4: ParPac code computations for pressure distribution around three cylindres moving in periodic channel.

Using so-called “LB in fluid” algorithm, the collision operator was applied only in fluid points, like in works [4, 128]. A delicate point of this approach is the reconstruction of all the populations in new boundary points. The equilibrium distribution with the mean density of the surrounding fluid and a velocity equal to that of the solid body is imposed for all them in [4]. Alternatively, all populations are extrapolated from bulk with the second order accuracy in [128]. In our approach, the populations pointing to the solid were first propagated from the fluid neighbors. The opposite ones were then reconstructed with the static boundary techniques, with the help of the extrapolations of missing (post-collision) multi-reflection components. The immobile population and the ”tangential” populations, having both link neighbors in solids, were computed in a form of explicit (equilibrium) solution where the equilibrium density value is treated as a local (mass) variable (see Eq.(85) in [66]). Smaller oscillations were observed for this approach to be contrasted with the averaged density values.

As an alternative approach, ”LB in solid” algorithm computes the collision for all, solid and fluid, points. The fluid boundary nodes are treated with the static boundary techniques. The propagation takes place from the fluid nodes into the solid. The immobile and tangential populations keep their values obtained in solid. All other boundary links are computed equally for both moving algorithms. This approach differs from the methods [105, 124] where the boundary schemes are applied on both (concave and convex) sides of the solid wall.

The two techniques were confronted to the same benchmark simulations: a periodic flow past a cylinder between flat walls (the analytical solution of the problem was built by D.d’Humières and discussed in Section V.A.6 of [66]) and a sphere in a cylinder. Both tests were run in two frames, once with the moving outer boundary and once with the moving obstacle. The results were compared for the Galilean invariance and accuracy of the obtained drag values. The momentum exchange was

computed with two techniques (3.23) and (3.26). It was observed that the second definition suppresses the fluctuations owing to discretization errors, at least when the parabolic boundary schemes are used. They were found twice more accurate than the linear interpolations given by the BFL rule for moving obstacle. Altogether, the "LB in fluid" algorithm was found as the most accurate, especially for new points.

Recent work [27] investigates the initialization of new nodes with the help of asymptotic analysis techniques. The "refill" algorithms considered there are based on the equilibrium reconstruction with and without extrapolation of the non-equilibrium component.

3.6 Concluding remarks

Let us finish this Chapter with the following remarks. Modeling hydrodynamic boundary conditions, the observed mismatch between the effective and assumed closure relations was first interpreted as an error in the location of the Dirichlet boundary values at the wall. In contrast, this numerical artefact is fitted more recently, e.g, in [9, 119, 191, 181, 170] to boundary layer continuum solutions [30, 115] where the coefficients associated with the first and second derivatives are proportionally to Kn and Kn^2, the Knudsen number Kn is proportional to the kinematic viscosity and to the inverse of the channel width. In author's belief, such interpretation should be used with a care. First, the closure relation actually depends on the free collision eigenvalues, beyond the BGK collision, where the coefficient Λ^{eo} becomes proportional to the square of the viscosity (then, to Kn^2). Second, the solutions obtained for simple orientations are not applicable in complex geometries: Poiseuille flow in straight and rotated channels based on the non-linear equilibrium gives one example (see sections 6.1.4 and 6.1.5).

Among important open questions let us mention the sufficiency of the closure conditions, practically not yet raised in the LBE literature. We have first met the loss of uniqueness of the steady solutions in sharp corner geometries for the LSOB. The system may degenerate in closed geometries with the parabolic multi-reflections, e.g., when the grid nodes are located on the wall. We find that the parabolic schemes enforce then the exact equilibrium boundary values but do not have a sufficient number of the non-equilibrium constraints and should avoid this location. Linear schemes may meet this difficulty in grid corners.

The rigorous stability analysis of the LBE schemes in the presence of closure relations is not yet established. Linear stability modes are computed in Appendix B of [60] for the minimal system of two nodes. The heuristic stability conditions on the multi-reflection coefficients of the velocity schemes: keep them inside interval

$[-1,1]$, or better $[0,1]$, were suggested in [66] and confirmed to some extent by our numerical observations. Quite likely, the necessary stability conditions may differ for symmetric and anti-symmetric equilibrium components.

Finally, we emphasize that the accurate boundary approaches for complex geometries do not guarantee either local or global mass conservations. One interesting, mass conserving "finite-volume" scheme by Dubois and Lallemand [44] is restricted to the parallel walls. Another very recent approach in LBE is the immersed boundary method by Peng and Luo, which is however actually less accurate than the BFL rule. The multi-reflection approach tries to minimize the discrepancy with the bulk solution, and mass fluctuations for transient flow, with the help of advanced accuracy for incoming populations. The parabolic multi-reflection schemes are perhaps the most accurate ones for arbitrarily shaped boundaries, owing to their accurate handling of the velocity curvature and pressure gradients. Hence, their solutions do not depend on the choice of Λ^{eo} at the second order in population expansion and the obtained solutions are fairly independent of their actual values, when Λ^{eo} is found in reasonable intervals, $\Lambda^{eo} \leq 1$, at least. Altogether, a way to combine the versatility of the multi-reflections with the desired conserving and stability properties is still to be found !

Chapter 4

Analysis of planar interface

The question is what conditions are set when the populations traverse the interface between the nodes with discontinuous components: equilibrium functions and/or relaxation parameters. This problem was first raised in the author's PhD thesis [57] for the continuity conditions on flat interface between two immiscible fluids. Working last years on the link-wise discontinuous collision operators, it was recognized and reported in [72] that the microscopic interface continuity conditions can be first established independently of the nature of the modeled conservation laws. The results are validated for flow modeling in variably saturated (described by Richard's equation) layered soils [71, 72] and for immiscible fluids with different densities and viscosities on the flat interface, using the "color gradient" model described in Section 5.3.

An important question of the choice between discontinuous equilibrium functions (TRT-E model) and discontinuous sets of eigenvalues (L-model) was then revealed and elaborated in a common work [73] with D. d'Humières on the anisotropy and heterogeneity (in stratified sub-domains) of the *full* diffusion tensors. In this general situation, the analysis shows the necessity of the explicit interface corrections, which are presented in Section 4.3.3. They have been validated in two and three dimensions by the established exact analytical solution which we discuss in Section 4.3.4.

4.1 Generic interface link conditions

Using the symmetry properties, the populations and their post-collision values in relations (1.2) can be written as:

$$f_q = e_q^+ + e_q^- - \left(\frac{1}{2}+\Lambda^+\right) g_q^+ - \left(\frac{1}{2}+\Lambda_q^-\right) g_q^- = \mathcal{S}_{\bar{q}}^- - \mathcal{G}_{\bar{q}}^-, \tag{4.1}$$

$$\tilde{f}_q = e_q^+ + e_q^- + \left(\frac{1}{2} - \Lambda^+\right) g_q^+ + \left(\frac{1}{2} - \Lambda_q^-\right) g_q^- = \mathcal{S}_q + \mathcal{G}_q \,, \tag{4.2}$$

$$\mathcal{S}_q = e_q^+ + \frac{1}{2} g_q^- - \Lambda^+ g_q^+ \,, \qquad \mathcal{G}_q = e_q^- - \Lambda^- g_q^- + \frac{1}{2} g_q^+ \,. \tag{4.3}$$

Then the solution of the evolution equation (1.1) at steady state obeys for each link:

$$f_q(\vec{r} + \vec{c}_q) = \tilde{f}_q(\vec{r}) \;=\; \mathcal{S}_q(\vec{r}) + \mathcal{G}_q(\vec{r}) = \mathcal{S}_{\bar{q}}(\vec{r} + \vec{c}_q) - \mathcal{G}_{\bar{q}}(\vec{r} + \vec{c}_q) \,, \tag{4.4}$$

and

$$f_{\bar{q}}(\vec{r}) = \tilde{f}_{\bar{q}}(\vec{r} + \vec{c}_q) \;=\; \mathcal{S}_q(\vec{r}) - \mathcal{G}_q(\vec{r}) = \mathcal{S}_{\bar{q}}(\vec{r} + \vec{c}_q) + \mathcal{G}_{\bar{q}}(\vec{r} + \vec{c}_q) \,. \tag{4.5}$$

We consider two nodes from two adjacent layers, $\vec{r}^{(i)} = \vec{r}^{(j)} + \vec{c}_{\bar{q}}$ and $\vec{r}^{(j)} = \vec{r}^{(i)} + \vec{c}_q$, linked by a pair of anti-parallel velocities (see Fig. 4.1). The sum and the difference of these relations yield two conditions per interface link q

$$\mathcal{S}_q(\vec{r}) = \mathcal{S}_{\bar{q}}(\vec{r} + \vec{c}_q) \text{ , and } \mathcal{G}_q(\vec{r}) = -\mathcal{G}_{\bar{q}}(\vec{r} + \vec{c}_q) \,, \quad q \in I \,,\, \bar{q} \in \bar{I} \,. \tag{4.6}$$

Relations (4.6) only rely on the link-based form of the evolution equation and are exact for any equilibrium function. They are explored with the second-order Chapman-Enskog expansion of the non-equilibrium part, using relations (1.41) or dropping the time derivatives in relations (1.40).

$$\begin{aligned} NS: \quad & g_q^{-[1]} = \partial_q e_q^+ \,,\, g_q^{+[1]} = \partial_q e_q^- \,, \\ & g_q^{-[2]} = -\partial_q \Lambda^+ g_q^{+[1]} - S_q^- \,,\, g_q^{+[2]} = O(\varepsilon^3) \,. \end{aligned} \tag{4.7}$$

$$\begin{aligned} AADE: \quad & g_q^{+[1]} = \partial_q e_q^- \,,\, g_q^{-[1]} = \partial_q e_q^+ \,, \\ & g_q^{+[2]} = -\partial_q \Lambda_q^- g_q^{-[1]} - S_q^+ \,,\, g_q^{-[2]} = O(\varepsilon^3) \,. \end{aligned} \tag{4.8}$$

4.2 Immiscible fluids: continuity relations

We assume continuous velocities and normal shear stress tensor components for two immiscible incompressible fluids separated by a flat interface at $z = z^{(int)}$:

$$\left\{ \begin{array}{lcl} \vec{u}^{(i)} & = & \vec{u}^{(j)} \,,\, P^{(i)} - 2\mu^{(i)} \partial_z u_z^{(i)} = P^{(j)} - 2\mu^{(j)} \partial_z u_z^{(j)} \,, \\ \mu^{(i)} D_{\alpha z}^{(i)} & = & \mu^{(j)} D_{\alpha z}^{(j)} \,,\, D_{\alpha z} = (\partial_\alpha u_z + \partial_z u_\alpha) \,. \end{array} \right. \tag{4.9}$$

Relations (4.6) yield effective continuity conditions for *implicit* interface tracking. Any two phase sharp-interface algorithm can be assumed at this stage, combined

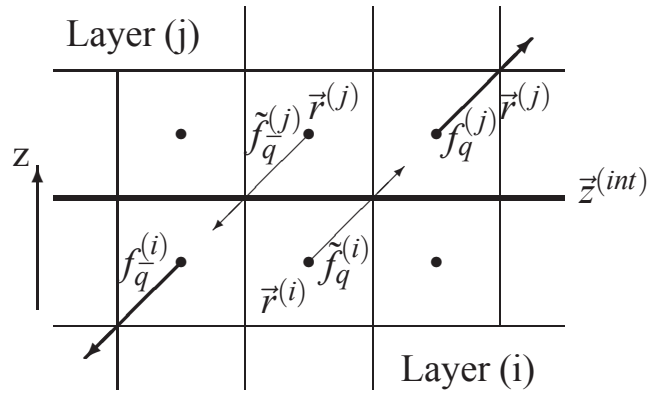

Figure 4.1: Sketch for interface sub-layers ($\vec{r}^{(j)}$ is moved one node to the left for clarity).

with the TRT hydrodynamic model. The extreme situation is addressed in [57, 58, 72], when the collision operator assigned to one of the two phases is applied to the grid nodes below an imaginary interface and another operator is applied to the grid nodes above, regardless of the effective phase distribution in these interface boundary nodes. For example, the choice of the collision operator with a *majority* rule results in a simplified interface handling. The question is what are the interface continuity relations for the pressure, velocity and strain stress tensor components ? And where are they satisfied ? Altogether, we show that the implicit interface tracking enforces stress continuity conditions, at least for immobile interface or when j_z is constant, but the continuity of the velocity is replaced by the continuity of the momentum: $\vec{j}^{(i)} = \vec{j}^{(j)}$. Actually, if the velocity is defined as $\vec{u}^{(i)} = \vec{j}^{(i)}/\rho^{(i)}$ then it is discontinuous on the interface when two densities differ. We return to this unexpected situation in Section 5.3.

Semi-explicit interface tracking applies a special *interface* collision operator in grid nodes where the two fluid coexist. We built it from the continuity conditions in [57, 72]. Exact piece-wise linear and piece-wise parabolic solutions, derived from the interface analysis, are illustrated in Section 6.1.3, both for the implicit and semi-explicit interface tracking.

4.2.1 Continuity of stress tensor components

At the leading order, the first interface condition (4.6) is:

$$[e_q^{+(i)} - \Lambda^{+(i)} g_q^{+(i)}](\vec{z}^{(int)}) = [e_{\bar{q}}^{+(j)} - \Lambda^{-(j)} g_{\bar{q}}^{+(j)}](\vec{z}^{(int)}) + O(\varepsilon^2) \,. \qquad (4.10)$$

Let $q_\perp$ denotes the *vertical (normal)* interface links. Assuming $\partial_z j_z(\vec{z}^{(int)}) = 0$ and using relations (4.8) one gets $g^+_{q_\perp} = 0$. Then using the Stokes equilibrium function ($E^{(u)}_q = 0$), the pressure continuity condition follows from the continuity of the normal equilibrium component in relation (4.10): $e^{+(i)}_{q_\perp} = e^{+(j)}_{q_\perp}$, hence

$$P^{(i)}(\vec{z}^{(int)}) \;\; = \;\; P^{(j)}(\vec{z}^{(int)}) + O(\varepsilon^2)\,. \tag{4.11}$$

The restriction to Stokes equilibrium is not necessary when the equilibrium non-linear term $E^{(u)}_q(\vec{j},\tilde{\rho})$ is continuous on the interface. The continuity of the momentum $\vec{j}$ is established in the next section. However, equal densities $\tilde{\rho}$ are again required, likely as for the continuity of the velocity.

When the symmetric equilibrium components are continuous, the continuity of the tangential shear stress components in incompressible flow: $\nu\mathcal{D}_{\alpha z} = \frac{2}{3}\Lambda^+ \sum_{q\in I} g^+_q c_{q\alpha}$, $\nu\mathcal{D}_{\alpha z} \approx \mu D_{\alpha z}$, follows from the sum of relations (4.10) over all cut links:

$$\nu^{(i)}\mathcal{D}^{(i)}_{\alpha z} = \nu^{(j)}\mathcal{D}^{(j)}_{\alpha z} + O(\varepsilon^2)\,,\; \mathcal{D}_{\alpha z} = (\partial_\alpha j_z + \partial_z j_\alpha)\,. \tag{4.12}$$

This analysis is also valid for the incompressible MRT models.

4.2.2 Momentum and velocity

Including only the first derivative: $\mathcal{G}_q = e^-_q + \frac{1}{2}g^+_q$, the second interface condition (4.6) means the continuity of the link momentum component j_q *midway* the interface link:

$$j^{(i)}_q(\vec{z}^{(int)}) = j^{(j)}_q(\vec{z}^{(int)}) + O(\varepsilon^2)\,,\; \vec{z}^{(int)} = \vec{r}^{(i)} + \vec{c}_q/2 = \vec{r}^{(j)} + \vec{c}_{\bar{q}}/2\,, q \in I\,. \tag{4.13}$$

Taking the sum over the interface links going through a given point $\vec{z}^{(int)}$, one obtains the continuity condition for the normal component $j_z(\vec{z}^{(int)})$. Substituting condition $j^{(i)}_z = j^{(j)}_z$ into relation (4.13), or in the case of immobile interface, one derives the continuity condition for the tangential momentum components. Then,

$$j^{(i)}_\alpha(\vec{z}^{(int)}) = j^{(j)}_\alpha(\vec{z}^{(int)}) + O(\varepsilon^2)\,,\; \alpha = \{x,y,z\}\,. \tag{4.14}$$

We emphasize that condition (4.14) is equivalent to the continuity of the tangential velocity, Eq. (4.9), only when the two densities are equal.

4.3 Diffusion equation in stratified media

The analysis of the effective continuity relations set by implicit tracking of the boundaries between two different soils appears in author's work on the Richard's

equation, [71]. It was then understood that the method enforces, at the leading order, the link-wise continuity of the symmetric and anti-symmetric equilibrium components, relations (4.6) above. It became hence mandatory to redesign the Richard's schemes, originally based on the water content or Kirchhoff transform *diffusion equilibrium variables*. Both these variables should become discontinuous on the interlayer boundary. The coupling between heterogeneity and the anisotropy was examined in 2D by using the distinct space steps in two neighboring layers and tested against uniform grid solutions, [71]. The existing LBE schemes for anisotropic advection-dispersion equations were then formulated in a more general framework [73], in which the leading-order interface corrections are constructed and analyzed for linear and highly nonlinear exact solutions. Particular piece-wise linear and parabolic solutions, similar to those constructed for immiscible fluids, are set exactly by this analysis for implicit and semi-explicit interface tracking and described in Section 6.3.2. The benefit of interface corrections for highly non-linear pressure solution is discussed in Section 4.3.4.

4.3.1 Continuity of the symmetric equilibrium component

For pure diffusion equations, g_q^+ is related to the second order gradients of e_q^+ (cf. relation (1.41)) and can be neglected for the first order analysis. It follows then from the first interface condition (4.6) that e_q^+ is continuous at the "interface point" $\vec{z}^{(int)} = \vec{r}^{(i)} + \vec{c}_q/2 = \vec{r}^{(j)} + \vec{c}_{\bar{q}}/2$ (midway between $\vec{r}^{(j)}$ and $\vec{r}^{(i)}$):

$$(e_q^{+(i)} + \frac{1}{2}\partial_q e_q^{+(i)})(\vec{z}^{(int)}) = (e_{\bar{q}}^{+(j)} + \frac{1}{2}\partial_{\bar{q}} e_{\bar{q}}^{+(j)})(\vec{z}^{(int)}) + O(\varepsilon^2)\ . \qquad (4.15)$$

This continuity condition is exact for piece-wise linear equilibrium distributions, then for all the links cut by the interface:

$$\left[E_q^{(i)}\bar{\mathcal{D}}^{(i)}\right](\vec{z}^{(int)}) \quad = \quad \left[E_q^{(j)}\bar{\mathcal{D}}^{(j)}\right](\vec{z}^{(int)})\ ,\ q \in I\ . \qquad (4.16)$$

Then the diffusion function (e.g., pressure in saturated flow) is continuous: $\bar{\mathcal{D}}^{(i)}(\vec{z}^{(int)}) = \bar{\mathcal{D}}^{(j)}(\vec{z}^{(int)})$, if, necessary:

$$\sum_{q\in I} E_q^{(i)} = \sum_{q\in I} E_q^{(j)}\ . \qquad (4.17)$$

Let us elaborate these relations for the L and TRT-E models introduced in Section 1.6.4. The L-model holds continuous E_q for equal coefficients c_e. The TRT-E model holds the necessary condition (4.17) if the ratio of Λ_q^- is set equal to ratio of the vertical diffusion coefficients:

$$\text{L} \quad : \quad c_e^{(i)} = c_e^{(j)}\ ,\ \text{then}\ \bar{\mathcal{D}}^{(i)}(\vec{z}^{(int)}) = \bar{\mathcal{D}}^{(j)}(\vec{z}^{(int)}) \qquad (4.18)$$

$$\text{TRT-E} \quad : \quad \Lambda^{-(i)}/\Lambda^{-(j)} = K_{zz}^{'(i)}/K_{zz}^{'(j)} \ , \ \text{then} \ \sum_{q\in I} E_q^{(i)} = \sum_{q\in I} E_q^{(j)} \ . \qquad (4.19)$$

After including the second-order term g_q^+, the Taylor expansion is accurate provided that $\Lambda_q^{e\,(j)} = \Lambda_q^{e\,(i)} = 1/8$. Since all symmetric eigenvalues are equal, this condition can be only satisfied by the TRT model for all cut links, with the proper choice of the eigenvalue λ^+. This analysis is illustrated for piece-wise parabolic solution in Section 6.3.2.

4.3.2 Continuity of the normal diffusive flux and tangential pressure derivatives

The second interface condition (4.6) is related to the continuity of the link component of the advective-diffusive flux. At leading-order, and for pure diffusion problem,

$$[\Lambda_q^- g_q^-]^{(i)} = -[\Lambda_q^- g_{\bar{q}}^-]^{(j)} \ , \ \text{i.e.} \ , \ \Phi_q^{(i)}(\vec{z}^{(int)}) = -\Phi_{\bar{q}}^{(j)}(\vec{z}^{(int)}) \ . \qquad (4.20)$$

In fact, due to the exact mass conservation, the total diffusive flux across the infinite flat interface is constant:

$$\sum_{\vec{r}^{(i)}} \Phi_z^{(i)} = -\sum_{\vec{r}^{(j)}} \Phi_z^{(j)} \ , \ \Phi_z^{(i)} = 2\sum_{q\in I} \Phi_q^{(i)} \ , \ \Phi_z^{(j)} = 2\sum_{\bar{q}\in \bar{I}} \Phi_{\bar{q}}^{(j)} \ . \qquad (4.21)$$

The physical conditions prescribe the continuity of the vertical flux and the continuity of the tangential derivatives. Then the following ratios, $\mathbf{r}_z^{(i)}$ and $\mathbf{r}_\alpha{}^{(i)}$, are set on the physical grid:

$$\begin{aligned} \mathbf{r}_z^{(i)} &= \frac{\partial_z \bar{\mathcal{D}}^{(j)}}{\partial_z \mathcal{D}^{(i)}} = \frac{K_{zz}^{(i)}}{K_{zz}^{(j)}} \ , \ \text{if} \ \ K_{\alpha z} = 0 \ , \ \ \text{and} \\ \mathbf{r}_\alpha{}^{(i)} &= \frac{\partial_\alpha \bar{\mathcal{D}}^{(j)}}{\partial_\alpha \mathcal{D}^{(i)}} = 1 \ , \ \alpha = \{x,y\}. \end{aligned} \qquad (4.22)$$

On the computational grid, assuming possible different coordinate space scaling: $\vec{r}' = \mathcal{L}\mathbf{L}\vec{r}$ (cf. relations (1.47)) the interface conditions should then obey:

$$[\partial_{\alpha'} \bar{\mathcal{D}}^{(j)}/\partial_{\alpha'} \bar{\mathcal{D}}^{(i)}](\vec{z}^{(int)}) = r_\alpha^{(i)}/r_{L_\alpha}^{(i)} = r_\alpha^{'(i)} \ , \ r_{L_\alpha}^{(i)} = \frac{L_\alpha^{(j)}}{L_\alpha^{(i)}} \ . \qquad (4.23)$$

Combining conditions (4.20) and (4.23), one needs to set:

$$\mathcal{T}_q^{(i)}/\mathcal{T}_q^{(j)} = r_\alpha^{'(i)} \ , \ \mathcal{T}_q = \Lambda_q^- E_q \ , \quad q \in I \ , \ \alpha = \{x,y,z\} \ . \qquad (4.24)$$

Clearly, the horizontal and vertical constraints cannot be, in general, simultaneously satisfied by the diagonal links with continuous equilibrium weights (L-model: $E_q^{(i)} = E_q^{(j)}$). This analysis was confirmed with the help of special "vertical" and "horizontal" eigenvalue strategies developed in [72, 73]. They set the eigenvalue functions Λ_q^- such that either the vertical or the horizontal flow become exact solutions of the L and TRT-E models. It was then understood that when the equilibrium weights are continuous, the principal "risk" in violation of the condition (4.24) *for the vertical flow* only consists in a possible shift of the effective interface position. In contrast, working with a discontinuous equilibrium function, one enforces, in general, the discontinuity of the diffusion variable if the condition (4.19) is violated. The condition (4.24) is more strong than the condition (4.19) but the latter appear to be sufficient *for the vertical flow*. These situations are illustrated in Figure 4.2.

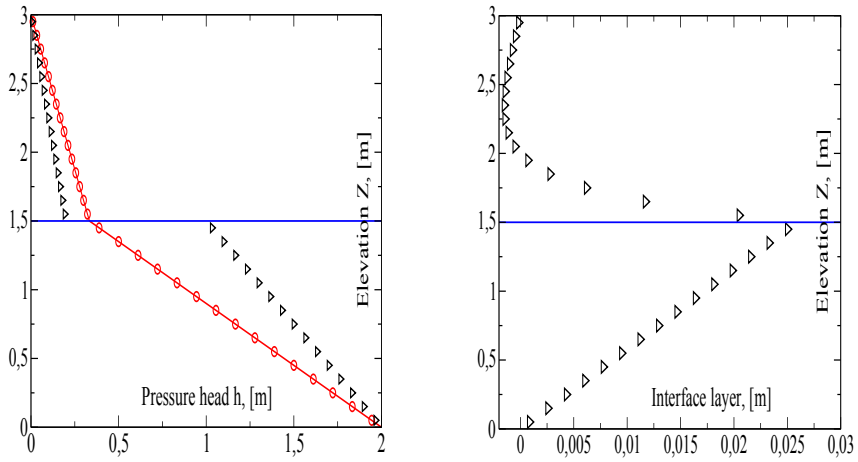

Figure 4.2: This picture illustrates the necessity of the continuity condition (4.24) for the vertical flow. When it is satisfied, then $\Lambda^{-(j)}/\Lambda^{-(i)} = K_{zz}{}^{(j)}/K_{zz}{}^{(i)} = 5$ and the solution is exact (red line in the left picture). If $\Lambda^{-(j)} = \Lambda^{-(i)}$, then the solution is discontinuous for the TRT-E model (left picture): $h^{(i)}/h^{(j)} = 5$. The L model (right picture) develops the interface layer if $\mathcal{T}_q$ are not all proportional, e.g.: $\mathcal{T}_q^{(j)} = \mathcal{T}_q^{(i)} = \mathcal{T}_\perp^{(i)}$ and $\mathcal{T}_\perp^{(j)}/\mathcal{T}_\perp^{(i)} = 7$. Here, the interface layer presents a difference between the exact piece-wise linear solution and numerical solution.

4.3.3 Explicit interface corrections

The main advantage of the implicit interface tracking is that it does not modify the evolution equation and keeps the mass balance exactly. However, interface continuity conditions are not guaranteed for all collision configurations. This deficiency can be amended by some interface corrections $\delta_q^{(i)}(\vec{r}^{(i)},t)$ and $\delta_{\bar{q}}^{(j)}(\vec{r}^{(j)},t)$ such that

$$\begin{aligned} f_q(\vec{r}^{(j)},t+1) &= \tilde{f}_q(\vec{r}^{(i)},t)+\delta_q^{(i)}(\vec{r}^{(i)},t)\,, \\ \tilde{f}_{\bar{q}}(\vec{r}^{(j)},t)+\delta_{\bar{q}}^{(j)}(\vec{r}^{(j)},t) &= f_{\bar{q}}(\vec{r}^{(i)},t+1)\,, \end{aligned} \tag{4.25}$$

where each interface correction $\delta_q^{(i)}$ is split into two parts: $\delta_q^{(i)} = \delta_q^{+\,(i)} + \delta_q^{-\,(i)}$. The symmetric component enforces the continuity of the diffusion variable for discontinuous equilibrium weights:

$$\delta_q^{+\,(i)} = \mathcal{S}_q^{(i)}(r_E^{(i)}-1)\,, \qquad r_E^{(i)} = \frac{E_q^{(j)}}{E_q^{(i)}}\,, \tag{4.26}$$

where the terms $\mathcal{S}_q^{(i)}$ and $\mathcal{S}_{\bar{q}}^{(j)}$ are given by relations (4.3). The anti-symmetric component enforces the relations (4.23) for prescribed ratios $r_\alpha^{\prime(i)}$:

$$\begin{aligned} \delta_q^{-\,(i)} &= \sum_{\alpha=\{x,y,z\}} \delta_{q\,\alpha}^{-\,(i)}\,, & \delta_{q\,\alpha}^{-\,(i)} &= \Phi_{q\alpha}^{(i)}(r_E^{(i)} r_\Lambda^{(i)} r_\alpha^{\prime(i)} - 1)\,, \\ \Phi_{q\alpha}^{(i)} &= -\Lambda_q^{-\,(i)} E_q^{(i)} \partial_\alpha \bar{\mathcal{D}}(s) c_{q\alpha}\,, & r_\Lambda^{(i)} &= \Lambda_q^{-\,(j)}/\Lambda_q^{-\,(i)}\,. \end{aligned} \tag{4.27}$$

These corrections can be computed with the approximations used to compute normal flux condition (3.20). The corrections $\{\delta_{\bar{q}}^{+\,(j)}, \delta_{\bar{q}}^{-\,(j)}\}$ are obtained by exchanging (i) with (j) and q with $\bar{q}$ in the above formulae.

The proposed corrections are exact for piece-wise linear solutions, e.g., the vertical flow, *for any collision configuration and any heterogeneity ratios*. We conjecture that a perturbation of the mass balance may play a crucial role for robustness of any explicit interface tracking routines. An attempt to quantify this problem is proposed in Appendix C of [73].

4.3.4 Saturated flow in stratified anisotropic aquifer

The exact solution for the saturated flow in three-dimensional aquifer made of the horizontal layers is presented by Sections 6.1 and 6.2 of [73]. Following configuration proposed by M. Bakker and K. Hemker in [15], the vertical axis represents the principal direction for all permeability tensors: $K_{zx}^{(i)} = K_{zy}^{(i)} = 0$, for each layer (i).

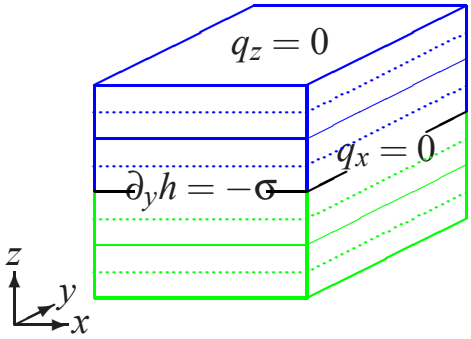

Figure 4.3: Sketch of a two-layer aquifer with two sublayers borrowed from [73]. The dotted lines locate the planes in which the pressure head h is computed. The boundary conditions are given for each visible face and are the same for the opposite faces.

The two principal tangential axes (x,y) may be rotated with respect to the Cartesian coordinate system so that the off-diagonal element $K_{xy}^{(i)}$ may differ from zero. The solution satisfies the mass conservation equation in saturated soil written with respect to pressure (diffusion) variable $\mathcal{D}(s) = h(x,y,z)$:

$$\sum_{\alpha,\beta} \partial_\alpha K_{\alpha\beta}^{(i)} \partial_\beta h = 0 \,, \tag{4.28}$$

with

$$\mathbf{K}^{(i)} = \begin{pmatrix} K_{xx}^{(i)} & K_{xy}^{(i)} & 0 \\ K_{xy}^{(i)} & K_{yy}^{(i)} & 0 \\ 0 & 0 & K_{zz}^{(i)} \end{pmatrix} . \tag{4.29}$$

The solution of this problem is looked for in box-shaped aquifer, impermeable at the east/west ($x = \pm X$) and at the top/bottom ($z = \pm H$). A constant value of the pressure head gradient $\partial_y h = -\sigma$ is set along the $y-$axis. Then the impermeability condition at the east/west boundaries reads:

$$u_x^{(i)} = -\left[K_{xx}^{(i)} \frac{\partial h}{\partial x} - K_{xy}^{(i)} \sigma \right] \Big|_{\pm X} = 0 \,, \tag{4.30}$$

A particular feature of this set-up consists in discontinuity of the boundary value of the tangential derivative $\partial_x h^{(i)}(\pm X)$ along with the ratio $K_{xx}^{(i)}/K_{xy}^{(i)}$.

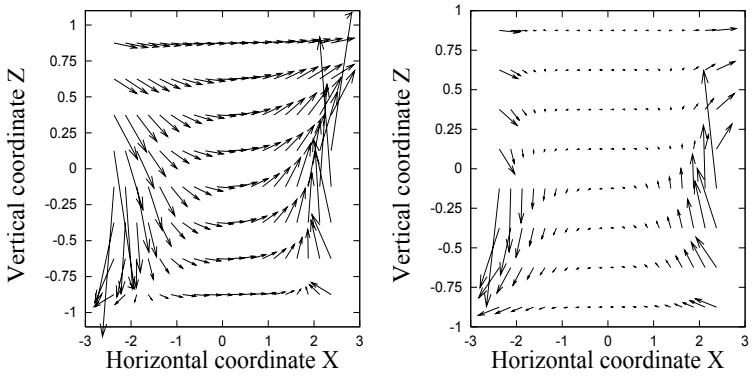

Figure 4.4: Vector fields $\{\partial_x\phi^\star, \partial_z\phi^\star\}$ obtained from the analytical solution for two heterogenous layers: top (1) and bottom (2). Left picture: $K_{xx}^{(1)} = 5$, $K_{xx}^{(2)} = K_{zz}^{(1)} = K_{zz}^{(2)} = 1$, Right picture: $K_{zz}^{(1)} = 5$, $K_{zz}^{(2)} = K_{xx}^{(1)} = K_{xx}^{(2)} = 1$. The pictures are extracted from figure 4 of [73].

The two-layered solution of this problem takes a form

$$h(x,y,z) \quad = \quad \phi(x,z) - \sigma y + h_r \ , \ h_r = h(0,0,0) \ , \tag{4.31}$$

where $\phi(x,z)$ is looked for in the form:

$$\phi(x,z) \quad = \quad \sigma(b_{xy}x + 2d_{xy}\phi^\star(x,z)) \ , \tag{4.32}$$

and $\phi^\star(x,z)$ satisfies the 2D diffusion equation in two layers:

$$\partial_{xx}\phi^\star + {a^{(i)}}^2\partial_{zz}\phi^\star = 0 \ , \ a^{(i)} \equiv \sqrt{\frac{K_{zz}^{(i)}}{K_{xx}^{(i)}}} \ , \tag{4.33}$$

with the following boundary and interface (at $z = 0^{\pm}$) conditions:

$$\begin{aligned} \partial_x\phi^\star(\pm X,z) &= \frac{1}{2}\mathrm{sign}(z) \ , \qquad \partial_z\phi^\star(x,\pm H) = 0 \ , \\ \partial_x\phi^\star(x,0^+) &= \partial_x\phi^\star(x,0^-) \ , \\ K_{zz}^{(1)}\partial_z\phi^\star(x,0^+) &= K_{zz}^{(2)}\partial_z\phi^\star(x,0^-) \ . \end{aligned} \tag{4.34}$$

The parameters b_{xy} and d_{xy} are, respectively, symmetric and anti-symmetric components of the prescribed boundary values for the horizontal derivative:

$$\partial_x\phi(\pm X,z) = \sigma(b_{xy} + d_{xy}\mathrm{sign}(z)) \ . \tag{4.35}$$

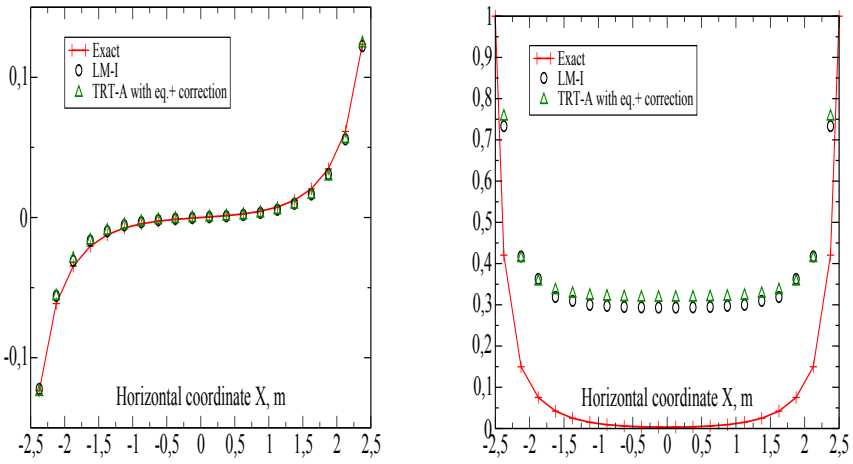

Figure 4.5: This figure illustrates the solutions obtained for $\phi^\star(x)$ and its derivative $\partial_x\phi^\star(x)$ with the L and TRT-E models without anti-symmetric interface correction (4.27), when $K_{zz}^{(1)}/K_{zz}^{(2)} = 5$ and $K_{xy}^{(i)} = \frac{1}{8}K_{xx}^{(i)}\mathrm{sign}(z)$. The pictures plot the difference between interface solution in two layers: $\phi^\star(x)$ (on the left) and $\partial_x\phi^\star(x)$ $\phi^\star(x)$ (on the right), following Fig. 14 of [73].

Taking $b_{xy} = 0$ the impermeable condition $u_x = 0$ is yield with the heterogeneous cross-diffusion components: $K_{xy}^{(i)} = d_{xy}K_{xx}^{(i)}\mathrm{sign}(z)$.

The analytical solution of the problem (4.33) with the interface and boundary conditions (4.34) is built in a form of Fourier series and described by relations (87)-(88) in [73]. This solution is valid for any anisotropy of the diagonal diffusion components. Two examples are plotted in Figure 4.4. Then the three-dimensional Darcy velocity field $\vec{u}$ follows the spiral-shaped streamlines when $d_{xy} \neq 0$, i.e., when the ratio $K_{xy}^{(i)}/K_{xx}^{(i)}$ is not continuous on the interface.

This solution was used for evaluation of the anisotropic techniques both in the original (three-dimensional) configuration and its reduced (two-dimensional) form, and investigated up to heterogenity ratio equal 500 for K_{xx} and K_{zz} and in the presence of highly discontinuous off-diagonal elements. The TRT-E, L and mixed M models (which are described in Section 1.6), in combinations with the boundary flux scheme (3.20), were validated using $d3Q15$ velocity set. We observed a drastical amelioration of the precision with the help of the interface corrections (4.25), especially for the tangential pressure derivative, when is derived (as usually) from the non-equilibrium flux. This is illustrated in Figures 4.5 and 4.6. The left picture in figure 4.5 confirms that the pressure distribution becomes continuous when

the symmetric correction (4.27) is included for the TRT-E model. In contrast, its $x-$derivative, which is derived from the tangential population flux and compared to the analytical solution for $\partial_x \phi^\star(x)$ on the right picture, is clearly discontinuous for both models. The next picture shows an improvement of this behaviour for very high ratio of the heterogenity and anisotropy, due to anti-symmetric interface correction (4.27). As one example, the ratio of anisotropic eigenvalue functions Λ_q^- for the solution on the right picture 4.6 is: $\Lambda_q^{(1)}/\Lambda_q^{(2)} = 100$ (tangential and diagonal links), and $\Lambda_q^{(1)}/\Lambda_q^{(2)} = 1300$ (vertical links). Altogether, the L model with the local eigenvalue strategy has demonstrated a reasonable robustness and accuracy on extremely coarse grids for high anisotropy ratios in these simulations.

4.4 Concluding remarks

It might be suggested that the evaluation of the effective continuity relations should accompany LBE schemes with the discontinuous collision components. In situations when the interface cuts the links at different distances, a case of arbitrarily shaped interface, we believe that the interface corrections could be developed to account for this in the spirit of the multi-reflection boundary schemes. The proposed interface corrections decrease the accommodation layers commonly appearing near the interfaces, as for inexact boundary closure relations. Finally we would like to emphasize that the questions raised in this Chapter for heterogeneous rotating anisotropy are not specific to Lattice Boltzmann approach. They reflect the actual problems in "state of the art" numerical methods for water modeling, e.g., with finite-volume schemes, [6, 77] or finite-element codes, [90].

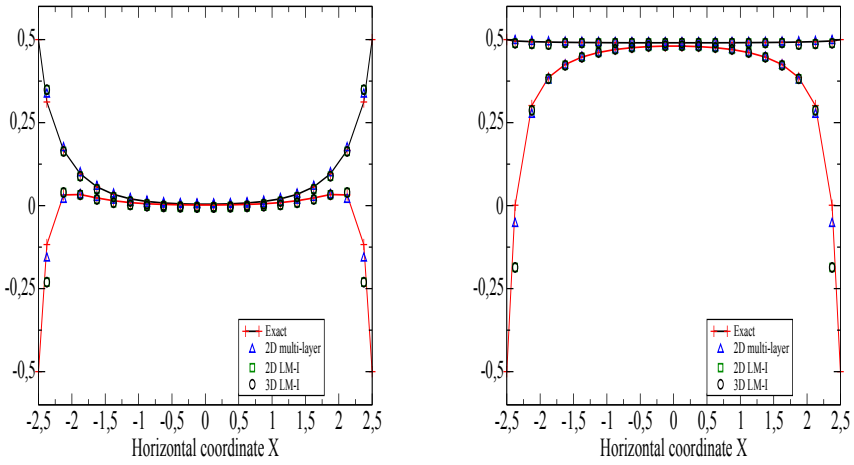

Figure 4.6: Semi-analytical solution (following Bakker & Hemker, [15]) and the L model (in two and three dimensions) with the interface correction (4.27) are compared to the constructed analytical solution for $\partial_x \phi^\star(x, 0^\pm)$, when the ratio of the vertical permeabilities is 500 (on the left picture) and, in addition, the ratio of the horizontal permeabilities is 100 (on the right picture); and $K_{xy}^{(i)} = \frac{1}{2} K_{xx}^{(i)} \operatorname{sign}(z)$ in both cases.

Chapter 5

Several applications of the LBE

5.1 Magic recipe for porous medium

Pioneered by D. Rothman [168] for the LGA and S. Succi et al [186] for the LBE, the Lattice Boltzmann equation in combination with the bounce-back rapidly gained popularity to measure permeability in *staircase* reconstructions of porous samples (a far to be exhaustive but a long list of works includes [18, 28, 35, 38, 41, 43, 109, 116, 120, 125, 134, 149, 156, 172, 182, 202, 203, 208]). However, the measured permeability values depend on the viscosity of the modeled fluid ! The author proposes to avoid this unphysical result with the help of collision numbers and suitable boundary schemes, for any porous structure. These "magic" properties have been discovered in winter 1994-1995 while working with L. Giraud, D. d'Humières and P. Lallemand at the ASCI laboratory (CNRS). They were summarized in (unpublished) work [59] and in the PhD thesis of L. Giraud. Later, the "magic" properties have been confirmed by intensive computations in porous media, e.g., [2, 66, 151] but finally understood very recently, owing to derivation of the recurrence equations, and proved in common work [103] with D. d'Humières.

5.1.1 Permeability dependency on the viscosity

The geometric structure and the effective hydrodynamic properties of porous media are characterized by a series of effective parameters. Among them the permeability tensor **K**, a measure of the fluid conduction, relates the averaged mass flux $\overline{\vec{j}}$ to the driving pressure drop: $\overline{\nabla P}$, and forcing: $\overline{\vec{F}}$, via Darcy's law:

$$\overline{\vec{j}} = \mathbf{K}\frac{\overline{(\vec{F}-\nabla P)}}{\nu}\,, \tag{5.1}$$

assuming a slow steady and incompressible creeping flow governed by the Stokes equation:

$$\nabla \cdot \vec{u} = 0 \ , \ \nu \Delta \vec{u} = \frac{1}{\rho_0} (\nabla P - \vec{F}) \ . \tag{5.2}$$

This equation represents the second-order approximation of the exact LBE conservation equations (2.17), using equilibrium function (1.42) with $g_S = 0$ and $M = 0$, and defining $\vec{u}$ as $\vec{j}/\rho_0$. Then flow rate $\overline{\vec{j}}$ is computed as a volume mean value of the momentum $\vec{j}$:

$$\overline{\vec{j}} = \frac{1}{V_s} \sum_{\vec{r}} \vec{j}(\vec{r}) \ , \tag{5.3}$$

where the summation goes through all fluid grid points and V_s is equal to the volume of the sample. It can be shown that when the momentum is redefined with half forcing, $\vec{j}(\vec{r}) = \sum_{q=1}^{Q-1} f_q(\vec{r}) \vec{c}_q + \frac{\vec{F}}{2}$, this definition is equivalent to averaging of the centered population flux values, $\frac{1}{2} \sum_{q=1}^{Q-1} (f_q + \tilde{f}_q) \vec{c}_q$. Alternatively, the permeability can be derived from the measurements of the drag on the solid, with the help of relations (3.23) or (3.26).

However, performing LBE computations with the MRT, TRT or BGK operators, and prescribing the same forcing, e.g., across a periodic sample of the porous media (hence $\overline{(\vec{F} - \nabla P)} = \vec{F}$), but using different values of ν, the solutions obtained for $\nu\vec{u}$ differ. The dependency of the derived permeability values on the viscosity is quite unexpected from the linearity of the Stokes equation. Moreover, this unphysical error increases with the kinematic viscosity ν. At the same time, the convergence rate toward the steady state can be improved by using rather large values for ν.

5.1.2 The TRT against the BGK

In the same time, it was first observed using the *FCHC* and $d3Q19$ velocity sets with the bounce-back boundary rule for flows around square arrays of cylinders and for differently shaped pipe flows that the permeability values do not change any more when the viscosity varies provided that all magic combinations $\Lambda^{eo\,(k,j)}$ of the MRT model are kept constant, [59, 78]. Then this appears to be valid, e.g., for cubic arrays of spheres and reconstructed fiber materials (illustrated in Figure 5.1), using the $d3Q15$ MRT model in [66], and for body-centered cubic arrays of spheres and random-size sphere-packed porous media, using $d3Q19$ MRT model in [151]. In fact, the MRT model (1.15) was used in its TRT configuration in these two last studies, taking all equal "symmetric" eigenvalues.

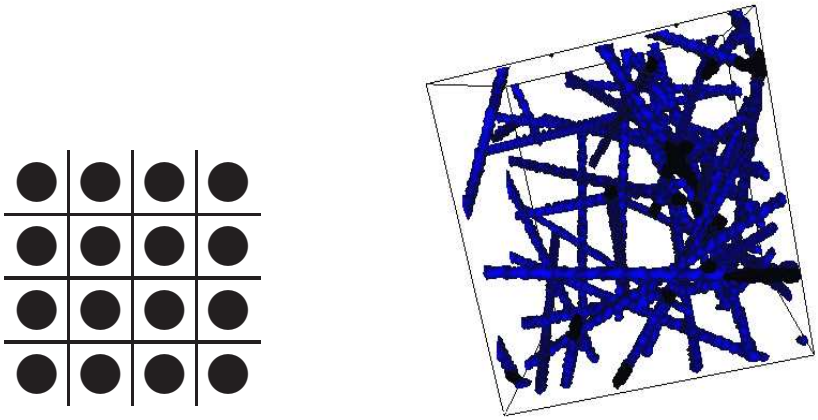

Figure 5.1: Regular array of cylindres and reconstructed fiber material.

Moreover, the results [66, 151] were obtained not only with the bounce-back rule but also with the parabolic (third-order accurate) MR1 scheme [66]. At the same time, using the linear BFL rule [20] for permeability measurements of a cubic array of spheres, it was observed that decreasing the viscosity by a factor 15 increases both the accuracy and the convergence time by almost the same factor (see Table V of [66]). The results in Table 1 and Figures 5 and 6 in [151] for linear and quadratic BFL rules confirm this analysis. Surely, replacing of the bounce-back with precise boundary schemes is worthwhile only when the boundary surface (and a distance to it) is described in sufficient details. A triangulation of X-ray scan of the porous media is adapted for the LBE computations in a recent work [2]. With this technique, it is possible to decouple the computational grid from the binary image resolution and substantially save the computational time. However, using the BFL rule with the fixed magic combination, the permeability again depends on the viscosity, even if this effect is considerably reduced.

Then it was believed that the dependency of the permeability measurements on the viscosity and free collision eigenvalues is (uniquely) caused by unknown dependency on them in location of the solid walls, keeping in mind that the permeability of the straight channel is controlled by Λ^{eo} using the bounce-back:

$$\frac{k-k^{th}}{k^{th}} = \frac{(\frac{16}{3}\Lambda^{eo} - 4\delta^2)}{H^2}\,,\; k^{th} = \frac{H^2}{12}\,. \tag{5.4}$$

This solution immediately follows from the exact solution (3.3). The error of the BGK model rapidly increases, as $(48\nu^2 - 1)$ in a straight channel, and as something between ν and ν^2 in porous media. The benefit of using a constant value of Λ^{eo}

over the BGK model is illustrated for the permeability measurements of fibrous materials (Table 3 in [66]), a body-centered cubic array of spheres and a random-sized sphere-pack (Table 3 and Figs. 4 and 8 in [151]).

Contrary to what we might expect, and owing to derivation of the recurrence equations and subsequent parametrisation of the truncation errors of the TRT Stokes equation in bulk (see in Section 2.4.2) it became clear that: first, the observed numerical artifacts are not restricted to wall location but they concern all truncation errors of bulk solutions; second, the TRT model may maintain the linearity of the Stokes equation for all orders provided that Λ^{eo} is set; third, the MRT may share the same property provided that all $\Lambda^{eo(k)}$ combinations are set, hence all combinations Λ^{+k} vary linearly with the kinematic viscosity; and finally, that the BGK model is not able to get either viscosity independent permeability or the consistent numerical behaviour.

The derived condition: to keep constant Λ^{eo} value, is a necessary but not a sufficient condition for achieving the linearity of Stokes flow on the numerical solution. This condition becomes sufficient provided that the exact closure condition of the boundary scheme is parametrized with Λ^{eo}, as well. The analysis of the closure relations from this point of view is developped in [74] and summarized in Section 3.3.1. It confirms the previously observed, suitable parametrization properties of the bounce-back and MR1 boundary rules, and their insufficiency for the BFL rule and linear interpolation scheme [212] (see also in Section 3). Using them, the results in Table 5.1 illustrate very significant increasing of the error with ν, obtained for fixed Λ^{eo} value. At the same time, using the BFL coefficients but including the correction $f_q^{\mathrm{p.c.}(u)}$ from Table 3.1, the MGULI/MGDLI and all other linear schemes from the MGLI ("magic linear") family get equal, viscosity independent permeability values. It is noted that the results obtained with MGLI are much more accurate even for small viscosity value: $\nu = \frac{1}{30}$. When the pressure drop across the medium is modeled with the inlet/outlet boundary conditions, their exact closure relations have to share the parametrization properties, as well. The simplest parametrized pressure boundary condition is the anti-bounce-back rule (3.16).

On the whole, there is no one best Λ^{eo} value suitable for any flow. The dependency of the permeability errors on the selected Λ^{eo} values is examined for a cubic arrays of spheres versus relative solid concentration in Table 6 of [74]. These results show that the error remains below 2% for all concentrations keeping Λ^{eo} below $\frac{1}{2}$, for the bounce-back and MGLI family. However, it rapidly increases and reaches 13% for most dense solid matrix $c/c^{\max} = 0.95$ when $\Lambda^{eo} = \frac{3}{4}$. Very small Λ^{eo} values are often more accurate but have to be avoided, at least for non-linear flows, by stability reasons. The Λ^{eo} may take larger values, say up to $\Lambda^{eo} = 1$, for the parabolic schemes, MGMR(C) and MLI($\alpha^{(u)}$), which are presented in Sec-

$c/c^{\max}$	$\forall\nu$	$\nu=\frac{1}{30}$		$\nu=\frac{1}{6}$		$\nu=\frac{1}{2}$		$\nu=\frac{3}{2}$	
	MGLI	BFL	YLI	BFL	YLI	BFL	YLI	BFL	YLI
0.5	0.57	0.9	1.2	2	3.5	4.3	8.0	8.8	16
0.6	0.05	0.3	0.6	1.3	2.8	3.3	7.1	7.8	16
0.7	0.1	0.4	0.8	1.4	3.2	3.6	8.1	8.4	18
0.85	1.1	1.7	2.3	3.6	6.6	7.7	15.5	17	34
0.95	0.28	1.0	1.9	4.0	8.1	10.3	21.3	24.2	50.4

Table 5.1: Comparison of the relative permeability errors $E^{(r)}(k)[\%]$ for a cubic array of spheres in a 25^3 box using the TRT model with $\Lambda^{eo}=\frac{3}{16}$ and the linear schemes, MGLI($\alpha^{(u)}$) from [74], BFL rule [20] and YLI scheme [212]. The permeability is independent of the kinematic viscosity ν only for MGLI($\alpha^{(u)}$) family. These results are taken from Table 7 in [74].

c/c^{max}	Edwards [49]	Bounce-back	BFL	MR1	Ghaddar [54]
0.2	2.54	-1.63	5.5×10^{-2}	-6.5×10^{-2}	-2.4×10^{-2}
0.3	0.53	0.78	0.51	2.8×10^{-2}	9.8×10^{-3}
0.4	-0.64	-4.86	0.13	-9.2×10^{-2}	-2.2×10^{-2}
0.5	-2.54	-1.1	-0.95	-8.9×10^{-3}	3.4×10^{-2}
0.6	-8.36	-6.9	0.55	-2.1×10^{-1}	1.3×10^{-2}

Table 5.2: Comparison of the relative permeability errors $E^{(r)}(k)[\%]$ versus relative solid concentration with respect to quasi-analytical solution and two finite-element based reference methods for a square array of spheres in a 66^3 box, using the MRT/TRT model with the bounce-back, BFL rule and multi-reflection MR1, for $\Lambda^{eo}=\frac{3}{16}$. The results are partially taken from Table XI in [66].

tion 3.3.2. These schemes may achieve quasi-analytical accuracy in permeability measurements, as illustrated in Table 5.2. In contrast to MLI($\alpha^{(u)}$) family, the MGMR(C) family (with the MR1 scheme as one particular element) does not use any finite-difference directional approximations to achieve its accuracy. The MGMR(C) family occurs to behave less robustly than the MGULI/MGDLI linear schemes. Worthwhile to mention that all the schemes from MGLI($\alpha^{(u)}$) yield exact parabolic (Poiseuille) solutions in a straight channel when $\Lambda^{eo}\in]0\,,\frac{3}{4}]$ (see relations (6.6)). Altogether, we suggest that a reliable estimate of the permeability should lie (roughly) in interval $\Lambda^{eo}\in[\frac{1}{8},\frac{1}{4}]$ for "magic" linear and parabolic schemes. Then one can significantly accelerate the convergence towards a steady

state, taking, roughly, $\frac{1}{2} \leq \Lambda^+ \leq 2$.

5.2 Brinkman model of porous medium

A uniform numerical scheme can be designed for solving the microscopic and macroscopic porous flow in the frame of the LBE method. The BGK Brinkman models [52, 84, 114, 136, 146, 182] incorporate Darcy or Forchheimer resistance force into the single-relaxation-time (BGK) hydrodynamic model [161]. Then Nie and Martys [146] interpret the angular-dependent deviation of the apparent viscosity coefficient from the predicted one in simply oriented channels as a "breakdown" of the Chapman-Enskog expansion.

Our works show that if the bulk solution exists as a *full* (infinite) Chapman-Enskog series, it satisfies the reference equations [103] and their macroscopic relations (see Section 2.2). The full series then yield the exact solution for the apparent viscosity for the Brinkman flow, provided that the force variation is properly accounted. The exact TRT Stokes equation with the resistance forcing is analysed in recent author's work [76]. Exact and approximate solutions for apparent viscosity coefficient are obtained, respectively, for simply and arbitrarily-oriented channels. They confirm that one needs at least one free collision relaxation rate to avoid the non-linear dependency of the apparent corrections on the viscosity.

5.2.1 Brinkman equation

The Brinkman equation [22], a semi-empirical viscous modification of Darcy's law for the volume-averaged pressure $\overline{P}$ and velocity $\vec{u}$

$$\nabla \cdot \vec{u} \;=\; 0\,,\; \nu \mathbf{K}^{-1}\vec{u} + \frac{1}{\rho_0}\nabla \overline{P} - \vec{g} = \frac{\nu_e}{\phi}\Delta \vec{u}\,, \tag{5.5}$$

aims to account for the presence of the solid boundaries in Darcy (small-pore) flows, combined with a Stokes description for free (large-pore) fluid. Darcy's law is recovered when the velocity derivatives are sufficiently small, i.e., the scale of velocity variation is much larger than $O(\sqrt{||K||})$. The effective value of the Brinkman viscosity coefficient, hereafter $\frac{\nu_e}{\phi}$ with ϕ as the porosity of the medium, is still a subject of theoretical and numerical investigations.

5.2.2 Apparent viscosity for parallel and diagonal channel flows

Assuming $\overline{P} = const$, the Brinkman equation (5.5) becomes for the "parallel" ("non-inclined", $\alpha = 0°$) and "diagonal" ($\alpha = 45°$) channel flow:

$$-F_{x'} \;=\; \rho_0 \nu_e \partial^2_{y'} u_{x'}\,,\; \vec{F} = -F_c \vec{j}\,,\; F_c = \frac{\phi \nu}{k}\,, \tag{5.6}$$

where $\vec{u}$, $\vec{j}$ and $\vec{J}$ are related as:

$$u_{x'} = \frac{j_{x'}}{\rho_0} \text{ , and } \vec{j} = \frac{2\vec{J}}{2+F_c} . \tag{5.7}$$

Let $\nu_a = \nu_e + \delta\nu_e = \nu_e(1+\bar{\delta}\nu_e)$ and $\delta\nu_e = \nu_e\bar{\delta}\nu_e$ denote the apparent viscosity coefficient and its difference from the predicted value ν_e, respectively. Because of the translation invariance, momentum conservation relation and weight property $3\sum_{q=1}^{Q-1} c_{q\,x'}^2 c_{q\,y'}^2 = 1$, the solution for post-collision correction $g_q^-(y')$ takes a form:

$$g_q^-(y') = 3c_{q\,y'}^2 F_q^\star(y') \text{ , } \forall q . \tag{5.8}$$

Substituting this solution into exact conservation equation (2.17), it comes that the TRT scheme with the equilibrium (1.42) and the resistance forcing (5.6) solves the *anisotropic* finite-difference equation:

$$\begin{aligned} \Delta^2_{y',\Theta} j_{x'}(y') &= 4b^2 j_{x'}(y') , \\ \text{with } b^2 = \frac{F_0}{4(1+\delta\nu_e)} \text{ , } F_0 &= \frac{F_c}{\nu_e} \text{ , with} \\ \nu_e = \frac{1}{3}\Lambda^+ \text{ , and } \bar{\delta}\nu_e &= (\Theta^2(\Lambda^{eo} - \frac{1}{4}) - \frac{\Lambda^{eo}}{3})F_0 . \end{aligned} \tag{5.9}$$

This form is based on the finite-difference type operators $\bar{\Delta}_{y',q}$ and $\Delta^2_{y',q}$ along the link $(\vec{c}_q, \vec{c}_{\bar{q}})$, with $|\Theta_q|$ being the distance along the $y'-$axis between a grid node $\vec{r}$ and its grid neighbors $\vec{r} \pm \vec{c}_q$. Let their $y'-$coordinates be respectively denoted $y'^{\pm}_q$, then:

$$\bar{\Delta}_{y',q}\psi(y') = \frac{\psi(y'^{+}_q) - \psi(y'^{-}_q)}{2\Theta_q} , \tag{5.10}$$

$$\Delta^2_{y',q}\psi(y') = \frac{\psi(y'^{+}_q) - 2\psi(y') + \psi(y'^{-}_q)}{\Theta_q^2} \text{ , } \Theta_q = c_{q\,y'} \text{ , } c_{q\,y'} \neq 0 . \tag{5.11}$$

These operators are all equivalent for links $c_{q\,y'} \neq 0$ in simple channels: $\Theta_q^2 = \Theta^2 = c_{q\,y'}^2 = 1$ for all the non-horizontal links in "parallel" channel; and $\Theta_q^2 = \Theta^2 = \frac{1}{2}$ for all the links with $c_{q\,x'}c_{q\,y'} \neq 0$ in "diagonal" channel. Indeed, the apparent correction (implicitly) accounts for the infinite series of the coefficients associated with even-orders force gradients, each of them being proportional to the laplacian of the velocity. The isotropic component of this correction, $-\frac{\Lambda^{eo}}{3}F_0$ appears already in Chapman-Enskog analysis, via the term $err(\vec{F}) = \nabla \cdot \frac{\Lambda^+}{3}\nabla\Lambda^-\vec{F}$ in derived momentum equation (1.45). The remaining (anisotropic) correction results from the

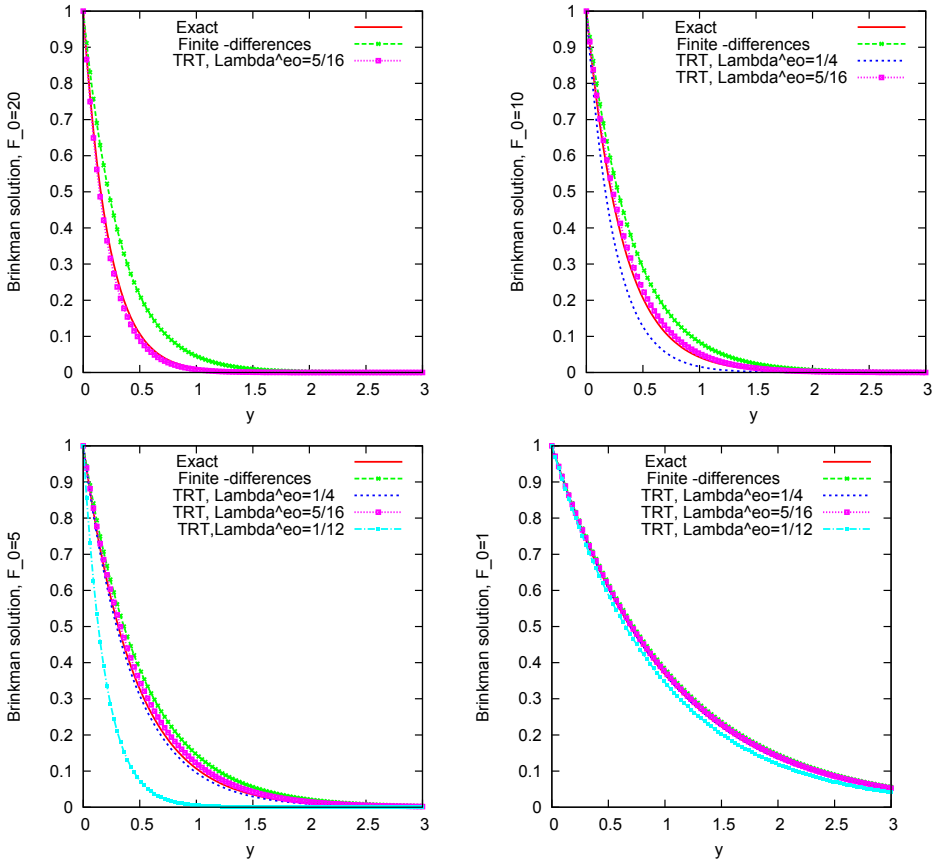

Figure 5.2: Exact exponential solution of Brinkman flow in straight channel $u(y)/u(0)$ is plotted against the finite-difference and TRT solution. The finite-difference and TRT solutions coincide when $\Lambda^{eo} = \frac{3}{8}$. The TRT and exact solution coincide when $\Lambda^{eo} = \{0.3175(3), 0.293241, 0.275982, 0.25601\}$ for $F_0 = \{20, 10, 5, 1\}$, following solution (6.30).

truncated term $-(\Lambda^{eo} - \frac{1}{4}) \sum_{q=1}^{Q-1} \Delta_q^2 g_q^- \vec{c}_q$ in momentum conservation equation (cf. relation (2.33)). Then the TRT numerical solution and its apparent viscosity are controlled by two parameters: F_0 and Λ^{eo}. The correction $\delta\nu_e$ vanishes if

$$\Lambda^{eo} = \frac{3\Theta^2}{4(3\Theta^2 - 1)} \,. \tag{5.12}$$

The BGK scheme yields $\Lambda^{eo} = 9\nu^2$, hence:

$$\bar{\delta\nu}_e \;=\; (3\nu^2(3\Theta^2 - 1) - \frac{\Theta^2}{4})F_0 \,. \tag{5.13}$$

This solutions correspond to the formulas (11) and (12) of Nie and Martys [146], if we take there $c_s^2 = \frac{1}{3}$, $\delta t = 1$ and replace $\frac{\varepsilon\nu}{k}$ with F_c. Their solutions are obtained by solving the BGK evolution equation with respect to velocity, with the help of the methodology [87]. The relation (5.13) shows that the numerical solution of the BGK scheme is not controlled by the governing parameter F_0 because of the dependency of the relative viscosity error $\delta\nu_e$ on the viscosity. It is noted that the non-linear function (5.13) increases rapidly with ν, with a prefactor equal to $(6\nu^2 - \frac{1}{4})$ in the straight channel.

The analytical solutions for channel flows confirm that, when the forcing factor F_c and the parameter of effective viscosity ν_e vary but their ratio is kept at a fixed value F_0, the TRT Brinkman scheme obtains the same velocity solutions, provided that the eigenvalue combination Λ^{eo} is fixed to some value. The exact solution $u_{\underline{x}}(y)/u_0 = e^{-2By}$ in the parallel channel is compared in Fig. 5.2 to finite-difference ($\delta\nu_e = 0$) and TRT solutions to Eq. (5.9) when $\Lambda^{eo} < \frac{3}{8}$. Two last solutions are described by relations (6.27) and (6.28). It may occur that the TRT solution is more accurate than the finite-difference one, owing to $\overline{\delta\nu}_e$. When $\Lambda^{eo} = \frac{3}{8}$, then $\overline{\delta\nu}_e = 0$ and the finite-difference and TRT solutions coincide. However, the apparent correction restricts the range of available positive values F_0. The available values satisfy the condition: $1 + \delta\nu_e > 0$. Then, $F_0 < \frac{12}{3-8\Lambda^{eo}}$ in the parallel channel when $\Lambda^{eo} < \frac{3}{8}$. A special dependency $\Lambda^{eo}(B,\Theta)$ given by relations (6.30) equates the solution of the TRT model to exact solution of equation (5.6). It is interesting that $\Lambda^{eo}(B,\Theta) \to \frac{1}{4}$ when $F_0 \to 0$ and $\Lambda^{eo}(B,\Theta) \to \frac{3}{8}$ when $F_0 \to \infty$. Therefore, Λ^{eo} should belong to the interval $[\frac{1}{4}, \frac{3}{8}]$ for Brinkman flow in parallel channel. These limits are however $\frac{1}{2}$ and $\frac{3}{4}$ for the diagonal flow.

5.2.3 Approximate of the apparent viscosity for rotated flow

Except for the linear and parabolic flows, the values $\Delta^2_{y',q} j_{x'}(y')$ differ for all non-parallel links. We conjecture, that the translation invariant Brinkman channel solution, $j_{x'}(y') = k_1 r^{y'} + k_2 r^{-y'}$, cannot satisfy the reference equations (2.5) in arbitrarily-rotated channel, at least using the isotropic force weights. Let us limit then ourselves to the second-order (isotropic) approximation:

$$\Delta^2_{y',q} j_{x'}(y') \approx \partial^2_{y'} j_{x'}(y') \ , \ \text{when } c_{q\,x'} c_{q\,y'} \neq 0 \ . \tag{5.14}$$

The approximated momentum equation then becomes:

$$\begin{aligned} -F_{x'}(y') &\approx \nu_a{}^{(2)} \partial^2_{y'} j_{x'}(y') \ , \ \nu_a{}^{(2)} = \nu_e(1 + \overline{\delta}^{(2)}\nu_e) \ , \\ \delta^{(2)}\nu_e &= (\overline{\nu}_\alpha(\Lambda^{eo} - \frac{1}{4}) - \frac{\Lambda^{eo}}{3})F_0 \ , \ \overline{\nu}_\alpha = 3\sum_{q=1}^{Q-1} t^\star_q c^2_{q\,\alpha'} c^4_{q\,\beta'} = \frac{1}{4}(3 + \cos 4\alpha) \ . \end{aligned} \tag{5.15}$$

These relations are valid for the $d2Q9$, $d3Q15$ and $d3Q19$ velocity sets. For simple orientations, $\bar{\nu}_{\underline{\alpha}} = \Theta^2$ and $\bar{\delta}^{(2)}\nu_e$ reduces to $\delta\nu_e$, given by relation (5.9) One can remove again $\bar{\delta}^{(2)}\nu_e$ with the help of $\Lambda^{eo}(\alpha)$ but only for each particular orientation. The solution (5.15) shows that *the second-order isotropic* estimate of the difference between the apparent and predicted values, ${\nu_a}^{(2)} - \nu_e$, is equal to $-\frac{\Lambda^{eo}F_c}{3}$ when $\Lambda^{eo} = \frac{1}{4}$, in agreement with the truncated Chapman-Enskog analysis mentioned above.

5.2.4 Concluding remarks

We suggest keeping Λ^{eo} close to $\frac{1}{4}$ when one expects any significant corrections from the variation of the source terms. Hence, one can consider

$$\nu_a = \nu_e(1 - \frac{\Lambda^{eo}}{3}F_0) \tag{5.16}$$

as the apparent (isotropic) viscosity coefficient for Brinkman flow. Then the truncation errors are similar to those of the finite-difference scheme. According to exact solution (6.30), $\Lambda^{eo} = \frac{1}{4}$ is most accurate in a parallel channel when $F_0 \to 0$. Further numerical work is required for evaluation of these predictions in realistic computations. Besides that, a rapid inspection of the closure relations in the presence of apparent viscosity corrections suggests their revision already at the first order. Let us also mention a curious example inspired by channel Brinkman solution and reported in Section 6.3.6: exact 1D Brinkman solution in arbitrarily rotated channel can be obtained using the diffusion scheme with variable mass source, owing to the anisotropic choice of the anti-symmetric eigenvalues of the L operator.

5.3 Immiscible Lattice Boltzmann model

One early lattice Boltzmann model for immiscible fluids (ILB) has been proposed by Gunstensen and Rothman [82, 85], based on the idea of multi-species lattice-gas cellular automaton (see exhaustive review on the ILGA by Rothman and Zaleski [169], Pot and Genty [159, 160]). The ILB model was extended for different densities and kinematic viscosities of two (or three) immiscible fluids in [81, 145] and in early author's works [57, 58]. Later the ILB MRT model was reformulated and adapted for the measurements of the relative permeability and capillary pressure in oil-gas system in porous media, then compared to the experimental data, in a common work on the ParPac project [63] with P. Klein, D. Reinel-Bitzer and K. Steiner. The recent work [172] applies this model for computations of oil and air in glass fiber papers which are used in oil filtration. The mathematical analysis of the BGK version of the model is developed in PhD thesis of D. Kehrwald [117].

The optimized version of the MRT algorithm [200] is extended to describe the rising bubles with adaptively refined hierarchical grids, and further intensively validated in [3]. The works [3, 206] also investigate the properties of the hysteresis loop, and compare the obtained results with the experiment and a morphological pore network model. Resulting pressure-saturation capillary curves can be applied for macroscopic water modeling, e.g., using the Richard's equation described in Section 5.6.

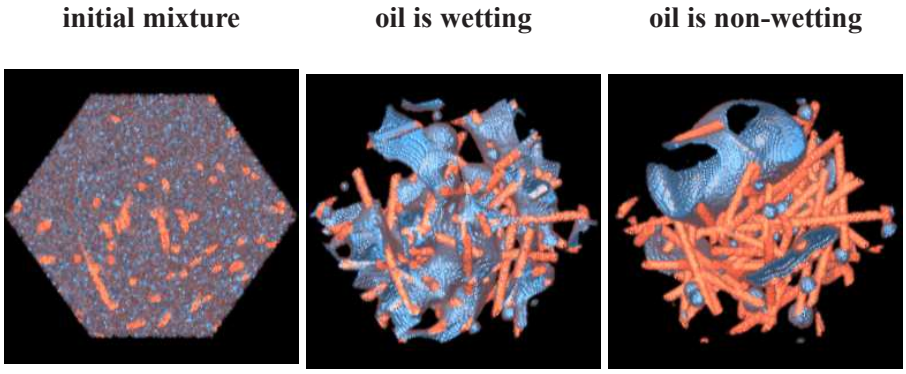

Figure 5.3: The pictures show the initial and steady state distributions of viscous phase in reconstructed fibrous material, computed with two phase ParPac code.

Two principal alternative approaches, as free energy formulation originated by Swift et al., [190], and intermolecular interactions model, Shan-Chen model [175, 176], are analyzed with respect to kinetic based non-ideal gas model by L.-S. Luo [132] and exhaustively reviewed in [96, 34, 150, 163]. Hysteresis effects are investigated with Shan-Chen type model in [150].

5.3.1 Re-formulated ILB

The original ILB model uses two type (color) populations: $\{R_q(\vec{r},t)\}$ and $\{B_q(\vec{r},t)\}$ but the actually the ILB only operates on their sums: $\sum_{q=0}^{Q-1} R_q(\vec{r},t)$ and $\sum_{q=0}^{Q-1} B_q(\vec{r},t)$. The re-formulated ILB model (summarized in [65, 67, 72]) has an equivalent but more convenient form. It operates with two independent families of the variables: the populations $\{f_i(\vec{r},t)\}$ and the mass fraction of one of two fluids, say $\rho^{(\mathrm{R})}(\vec{r},t)$, which plays a role of phase indicator. The algorithm reduces the ILB memory expenses by a factor two and can be easily divided into two independent steps: the ILB Navier-Stokes solver and the interface advection. Then one needs to define the collision operators for each phase and interface, e.g., by the majority of the occupying fluid or using some kind of the weighted mean values. When this choice is done, the ILB Navier-Stokes solver reduces to single phase LBE scheme except for

the surface tension correction. The original ILB model advects the interface with so-called "recoloring step" algorithm but any other interface tracking method, e.g., free interface [67], the volume of fluid [117] or level set techniques [11, 195] can be adapted.

5.3.2 Different densities and different viscosities

The ILGA approach handles the density ratio via the different numbers of the immobile particles in two phases. In ILB models [57, 145] this condition is inherited via different values assigned for the equilibrium density weights $c_s^2 t_q^\star$ (cf. relation (1.42)). It was then recognized that the propagation of the populations from the one phase into another (implicit interface tracking) necessary enforces the continuity of the equilibrium pressure and momentum variables:

$$c_s^{2\,(R)}\rho^{(R)} = c_s^{2\,(B)}\rho^{(B)}\,,\ \vec{j}^{(R)} = \vec{j}^{(B)}\,, \tag{5.17}$$

hence, the discontinuity of the velocity when $\rho^{(R)} \neq \rho^{(B)}$:

$$\vec{u}^{(R)} = \frac{\vec{j}^{(R)}}{\rho^{(R)}} \neq \frac{\vec{j}^{(B)}}{\rho^{(B)}} = \vec{u}^{(B)}\,. \tag{5.18}$$

This undesirable property, first reported in [57], is later confirmed by the link-wise interface analysis (see relations (4.11), (4.13)). Due to these reasons, and also because of the instabilities observed for sharp interfaces, the ILB model should be preferred (in author's opinion) with the continuous mass weights. Then, at least for steady creeping flow, the prescribed ratio of the dynamic viscosities can be numerically interpreted as a ratio of the kinematic viscosities, i.e.: $\frac{\Lambda^{+(R)}}{\Lambda^{+(B)}} = \frac{\nu^{(R)}}{\nu^{(B)}}$, with two different acceleration values $g^{(i)}$: $\vec{F}^{(i)} = \rho_0 g^{(i)}\mathbf{1}_z$ and $\frac{g^{(R)}}{g^{(B)}} = \frac{\rho^{(R)}}{\rho^{(B)}}$. Then the velocity is defined as $\vec{u} = \vec{j}/\rho_0$, for both phases. This approach is pursued in modeling [63, 172] and [3, 206].

As a positive property, the implicit interface tracking implies the continuity of the shear stress components (cf. relations (4.14)). The piece-wise linear and parabolic exact solutions described in Section 6.1.3 confirm this analysis for two-phase Couette and Poiseuille flows, for any disparity in viscosity and forcing values.

5.3.3 Surface tension

The surface tension can be incorporated into two-phase Navier-Stokes equation in a form of the bulk forcing term $\vec{F}_s$:

$$\vec{F}_s = -\sigma\nabla\cdot(\mathbf{I} - \mathbf{n}\otimes\mathbf{n})\delta_s\,, \tag{5.19}$$

which acts in the neighborhood of interface ($\delta_s \approx 1$). This approach follows the idea of Lafaurie and co-workers, [126].

In our model [63] this term appears with the help of mass and momentum conserving modification of the outgoing populations, $g_q^+ \rightarrow g_q^+ + \delta S_q^+$:

$$\delta S_q^+(\vec{r},t) = A \parallel \vec{n} \parallel Q_{qnn} \ , \ Q_{qnn} = t_q^\star (c_{q\,n}^2 - \frac{c_q^2}{d}) \ , \ c_{q\,n} = (\vec{c}_q \cdot \vec{n}) \ . \tag{5.20}$$

This form is isotropic with respect to the position of the interface on the grid. Then the surface tension coefficient σ is controlled by selection of the parameter A. The normal vector $\vec{n} \approx \nabla \rho^{(\mathrm{R})}$ is approximated with the help of the central difference stencil (see Section 3.2 in [67]). The possibility to have wetting/non-wetting condition at solid boundary is controlled with the assignment of the positive (negative, respectively) mass quantity to solid cites. A recent work [42] investigates the properties of the contact angles.

An approximate of the surface tension coefficient can be derived from the mechanical test, e.g., assuming the form [58] for steady solution on the planar interface perpendicular to arbitrarily inclined $z'-$axis:

$$f_q^+(z') = t_q^\star c_s^2 \rho - \frac{A}{\lambda^+} \parallel \vec{n} \parallel Q_{qnn} + O(\varepsilon^2) \ldots , \tag{5.21}$$

hence,

$$\sigma = \sum_{q=0}^{Q-1} f_q^+(z')(Q_{qnn} - Q_{q\tau\tau}) \approx -\frac{2A}{3} \int_{-\infty}^{\infty} \frac{\parallel \vec{n}(z') \parallel}{\lambda^+} dz' \approx A^\star (\nu^{(\mathrm{R})} + \nu^{(\mathrm{B})} + \frac{1}{3}) \tag{5.22}$$

The coefficient $A^\star$ is model dependent, e.g., $A^\star = \frac{8A}{3}$ for $d2Q9$ and $A^\star = \frac{16A}{3}$ for $d3Q15$. We find that the leading order corrections of this estimate is reduced for flat interface when the interface viscosity $\nu^{(int)}$ is computed as weighted mean value (see also Appendix A of [65]) :

$$\nu^{(int)} = \rho^{(\mathrm{R})}(z^{(int)}) \nu^{(\mathrm{R})} + (1 - \rho^{(\mathrm{R})}(z^{(int)})) \nu^{(\mathrm{B})} \ . \tag{5.23}$$

This estimate reduces to arithmetic mean value of bulk viscosities for half to half interface mixture, to be contrasted with the harmonic mean value obtained for the continuity of the shear stress (cf. relation (6.12) below).

The mathematical analysis of the consistency of the ILB surface tension models is developed in Section 2.4 of [117]. Two surface tension forms are analysed, one is similar to relation (5.20); another one is proposed by Nie at all [145]. It was concluded that the first variant fits better the surface tension term (5.19) in derived Navier-Stokes equation.

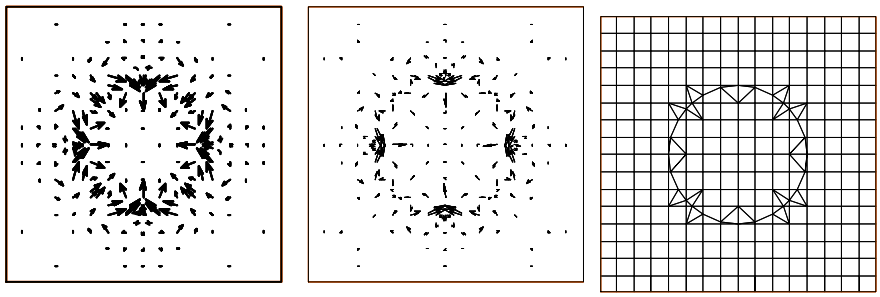

Figure 5.4: Anomalous currents on the collocated (left picture) and staggered (middle picture) grids when the surface tension force is computed in conservative form (5.19). They dissapear computing surface tension force on the interface aligned grid (right picture) with Frenet formulas (5.24).

It is well known that the perturbative terms provoke the anomalous density variation and the associated spurious currents. They are examined in details for planar interfaces when they are inclined with respect to the lattice, [57, 58]. In the presence of strong surface tension effects, the currents can progressively grow and destabilize the solution. Using *direct discretization methods*, the problem was cured modeling a surface tension force on the cubic spline interpolants and taking into account the interface position for discretization of pressure gradients, [158, 171]. This was automatically achieved on the interface fitted, spline aligned staggered grids in author's work with G. Wittum [62], when the surface tension force over the interface segment (AB), lying inside the control volume (see sketch for Frenet formulas in Fig. 5.5) can be computed as:

$$\int_{CV_u} \vec{F}_s = \oint_A^B \sigma k \vec{n} = \sigma(\vec{t}_B - \vec{t}_A) \ , \ \vec{t} = \frac{(x'(s), y'(s))}{\sqrt{x'^2(s) + y'^2(s)}} \ . \tag{5.24}$$

The anomalous currents and spline aligned grid are illustrated in Fig. 5.4. The problem of anomalous currents is still open in LBE modeling, e.g., [117, 154].

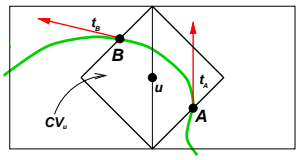

Figure 5.5: Sketch of bisection of spline with control volume CV_u (recalled from Ginzburg and Wittum, 2001).

5.3.4 Recoloring step

The recoloring step advects the interface but prevent its diffusion and smearing. For this, one looks for the interface distribution $\{f_i^{(\mathrm{R})}(\vec{r},t)\}$ which maximizes the post-collision fluid flux $\tilde{F}$ along the normal to the interface $\vec{n}$ and constrained to mass conservation:

$$\tilde{F} = \sum_{q=0}^{Q-1} f_q^{(\mathrm{R})} c_{qn} \; , \; \sum_{i=0}^{Q-1} f_q^{(\mathrm{R})} = \rho^{(\mathrm{R})} \; , \; 0 \leq f_q^{(\mathrm{R})} \leq \tilde{f}_q(\vec{r},t) \; . \tag{5.25}$$

Updated mass value $\rho^{(\mathrm{R})}(\vec{r},t+1)$ accumulates the sum of all incoming fluid quantities: $\rho^{(\mathrm{R})}(\vec{r},t+1) = \sum_{i=0}^{Q-1} f_i^{(\mathrm{R})}(\vec{r}-\vec{c}_q,t)$.

In summary, main advantages of the recoloring step rely in its intrinsic conservative properties, anti-diffusive interface behaviour and natural fitting of the LB evolution equation. Its main drawbacks are the reverse of its advantages. First, the recoloring step may not keep the symmetry of the solution and the regularity of the interface. Second, its expression (5.25) is restricted to positive populations. Indeed, the negative populations appear in LBE simulations and, especially, when the non-equilibrium solution undergoes stiff variations, but they do not necessary trigger the instabilities. When the negative populations are present, the procedure (5.25) can be restricted to the sub-set of local positive values, unless all populations become negative in a given (interface) node. Another approach consists in recoloring of the equilibrium distributions (replacing $\tilde{f}_q(\vec{r},t)$ with $e_q(\vec{r},t)$ in relation (5.25)), inspired by the LBE-based advection schemes. Actually, the positivity of the equilibrium is controlled more simply.

Actually, the recoloring yields very sharp interfaces between two lattice nodes. Several smoothing techniques were developed by Tölke et co-workers [198, 199] and recently, by M. Latva-Kokko and D. H. Rothman in [130], following the original approach by Ortona et al. [148]. They allow the interface to smear out over a few lattice points or to diffuse along itself, but reduce solution irregularities and attenuate the anomalous currents. In his PhD work, D. Kerhwald [117] tries to establish the mathematical form of the underlying anti-diffusion mechanism for the equilibrium based recoloring step, in the frame of the BGK model. The numerical analysis shows (Section 2.3 of [117]) that this step may have the negative side effects of disturbing the interface, keeping however better the sharp interfaces than a Riemann solver. It was suggested that the interface irregularities are provoked by a lack of the diffusion along the interface and an attempt to replace the recoloring step with the anisotropic diffusion finite-difference type scheme was under-taken (Section 3 of [117]). This approach was able to regularize the interface shape but the mass conservation was lost. Finally, a coupling of the ILB Navier-Stokes

solver with the conserving, volume of fluid based interface advection scheme has shown several important improvement. It should be remembered that all the studies [117] are restricted to the simplest case of equal densities and viscosities, when the non-equilibrium effects are not very significant, and they need a validation in more realistic situations.

5.3.5 Concluding remarks

In author's believe, a using of the TRT (at least) or MRT models becomes mandatory when the ratio of two kinematic viscosities is large, for any two phase model. Using the BGK operator for each phase, a large disparity of the collision values Λ^{eo} results in very high bulk and boundary errors for more viscous fluid, and increases the interface errors. Using of relatively small LBE viscosities for both fluids slows crucially the convergence to steady state, [3, 63].

It might be conjectured that the interface analysis for flat interface remains suitable for any equilibrium function and sources, provided that the sharp interface can be handled by the underlying interface tracking algorithm. The semi-explicit interface tracking proposed in author's works [57, 72] presents the examples how to construct the interface operators from the prescribed continuity relations. The harmonic mean value of the kinematic viscosities holds the continuity of shear stress across the planar (half red/half blue) interface. Explicit interface tracking is developed in recent works [11, 195]. They describe the interface dynamics with the level set approach and impose interface continuity relations as the boundary conditions on the reconstructed interface. This approach might introduce density ratios for continuous velocities but actually is very expensive. We suggest that suitable (link-wise) interface corrections could improve the interface continuity conditions along the same lines as for pressure and diffusive fluxes in anisotropic stratified heterogeneous soils, [73].

5.4 Free Interface method

Free interface Lattice Boltzmann approach for Newtonian [63, 64, 67] and Bingham fluid [65] is developed in parallel with the ILB model in ITWM (Kaiserslautern), in collaboration with K. Steiner, P. Klein and C. Lojewski. A distinctive feature of the model is that the collision is carried out only on the points occupied partially or fully by the fluid. The unknown (interface) distribution functions incorporate directly the free-surface boundary conditions into their non-equilibrium components, by construct of their first order Chapman-Enskog expansion. The necessary hydrodynamic information is derived locally from the *arriving fluid pop-*

ulations, following the basic philosophy of the LSOB methods [60, 61]. The free interface numerical algorithm is summarized in Section 3.4 of [67]. Intended to solve high Reynolds number filling flow, it neglects the surface tension effects.

5.4.1 Ideas and algorithm

One striking difference between free interface and multi-phase models is that the collision only occurs on the "active" cells, indicated by non-zero values of fluid mass. A "recoloring operator", similar to that in the ILB models, determines the redistribution of fluid mass carried by each population. The populations at the front of free-surfaces, which cannot be obtained by the propagation step from inactive nodes, are re-constructed by using the first order Chapman-Enskog expansion. Due to the rotational invariance, the first-order non-equilibrium spatial component is naturally expressed in local coordinates $\{x',y',z'\} = (n,\tau_1,\tau_2)$ (which are here normal and tangent to the free-surface):

$$\begin{aligned} n_q^+ &\approx \sum_{\tau=\{\tau_1,\tau_2\}} \frac{1}{\lambda^+}\left(\frac{\partial j_\tau}{\partial n}+\frac{\partial j_n}{\partial \tau}\right)Q_{q\,n\tau}+\frac{1}{\lambda^+}\left(\frac{\partial j_n}{\partial n}Q_{q\,nn}+\frac{\partial j_\tau}{\partial \tau}Q_{q\,\tau\tau}\right)+\frac{\nabla\cdot\vec{j}}{\lambda_e^{im}}v_q^{\rm im}\,, \\ Q_{q\alpha'\beta'} &= t_q^\star\left(c_{q\alpha'}c_{q\beta'}-\frac{c_q^2}{d}\delta_{\alpha'\beta'}\right) \text{ and} \\ v_q^{\rm im} &= t_q^\star\frac{c_q^2}{d}-r_q^\star\,,\; r_q^\star = c_s^2 t_q^\star\,,\; q\neq 0\,,\; r_0^\star = 1-\sum_{q\neq 0} r_q^\star\,. \end{aligned} \tag{5.26}$$

The projection $(\mathbf{f}\cdot v_q^{\rm im})$ on the isotropic second-order vector $\mathbf{v}^{\rm im}$ gives a simple local estimation of the compressible effect, $\nabla\cdot\vec{j}$. The basis vectors used in [65, 67] are equivalent to MRT basis [98, 100, 127], except for two symmetric vectors, one is $\mathbf{v}^{\rm im}$ and another one is orthogonal fourth-order polynomial vector. Two basis systems are interconnected by relations (A.3) and (A.4) in [67].

By this means, free interface populations are looked for in the form:

$$f_q = e_q+\frac{(P-P_0)}{\nu\lambda^+}Q_{q\,nn}+O(\varepsilon^2)\,, \tag{5.27}$$

in two-dimensions, and

$$\begin{aligned} f_q &= e_q+\frac{3(P-P_0)}{4\lambda^+\nu}Q_{qnn}+\frac{1}{2\lambda^+}(Q_{q\tau_1\tau_1}-Q_{q\tau_2\tau_2})\left(\frac{\partial j_{\tau_1}}{\partial\tau_1}-\frac{\partial j_{\tau_2}}{\partial\tau_2}\right) \\ &\quad+\frac{1}{\lambda^+}Q_{q\tau_1\tau_2}\left(\frac{\partial j_{\tau_1}}{\partial\tau_2}+\frac{\partial j_{\tau_2}}{\partial\tau_1}\right)+O(\varepsilon^2)\,, \end{aligned} \tag{5.28}$$

in three-dimensions. This solution follows from the Chapman-Enskog expansion (5.26), where, first, $\sum_\tau \partial_\tau j_\tau$ was replaced here by $\nabla \cdot \vec{j} - \frac{\partial j_n}{\partial n}$, then $\frac{\partial j_n}{\partial n}$ is expressed through the pressure jump, $P - 2\nu\frac{\partial j_n}{\partial n} = P_0$. Also, the component $\frac{\partial j_\tau}{\partial n} + \frac{\partial j_n}{\partial \tau}$ was set to zero. Two last relations follow from the continuity of the normal stress component on the heavy/light interface ($\mu(gas) \to 0$). The projection $\nabla \cdot \vec{j}$ is either kept as one more variable or omitted, when the fluid can be regarded as incompressible. With the help of several linearizations, e.g., $\rho U_\alpha U_\beta(t+1) \approx j_\alpha(t+1)U_\beta(t)$, the known populations (the RHS here, **f**) are written in a form of linear system:

$$\mathbf{BX} + \mathbf{b} = \mathbf{f}\,,\ \mathbf{X} = \begin{cases} \{\rho, j_x, j_y\}\,,\ 2d\,; \\ \{\rho, j_x, j_y, j_z, \frac{\partial j_{\tau_1}}{\partial \tau_1} - \frac{\partial j_{\tau_2}}{\partial \tau_2}, \frac{\partial j_{\tau_1}}{\partial \tau_2} + \frac{\partial j_{\tau_2}}{\partial \tau_1}\}\,,\ 3d\,. \end{cases} \tag{5.29}$$

Vector **X** contains $s^{un} = 3$ unknowns in $2d$ and $s^{un} = 6$ unknowns in $3d$. The mass constraint completes the linear system:

$$\rho - \sum_{i \in Q^{un}} f_i = \sum_{i \in Q^{kn}} f_i\,, \tag{5.30}$$

where $\sum_{i \in Q^{kn}} f_i$ is the sum of s^{kn} known (obtained by propagation step) and $\sum_{i \in Q^{un}} f_i$ is the sum of unknown populations (expressed in terms of **X** variables, with relations (5.27) and (5.28)). Hence, obtained linearized system of equations contains $m = s^{kn} + 1$ equations: $2 \le m \le Q$. When $s^{un} \le m$, the linear system is solved using fast least-square method with permutations. In singular cases, the unknown populations are extrapolated from the fluid side.

5.4.2 Filling process

The proposed free interface method was developed for filling process in casting, with conceptual and technical input by Magma GmbH, and validated for characteristic flow behavior by known benchmarks tests in "Modeling of Casting Welding and Advanced Solidification Processes", as Hammer box, Cambell box, Sheffield box and Motorblock in three dimensions, using $d3Q15$ model. The filling of Hammer Box is illustrated in Figure 5.6. The results agree with the numerical simulations of Hirt and Harper [94]. The solidification during the filling was computed by coupling with the finite-difference scheme. Reducing of the artificial compressibility of the velocity field was found as a most difficult problem for the whole efficiency of the method in this application.

A special attention was paid to inlet (constant flux) boundary condition, $\vec{j}^{in} = \rho_0 \vec{U}^{in}$. In the context of the filling applications, applying of constant ρ_0 value was detected as quite inaccurate, because of the dynamic pressure variation. The

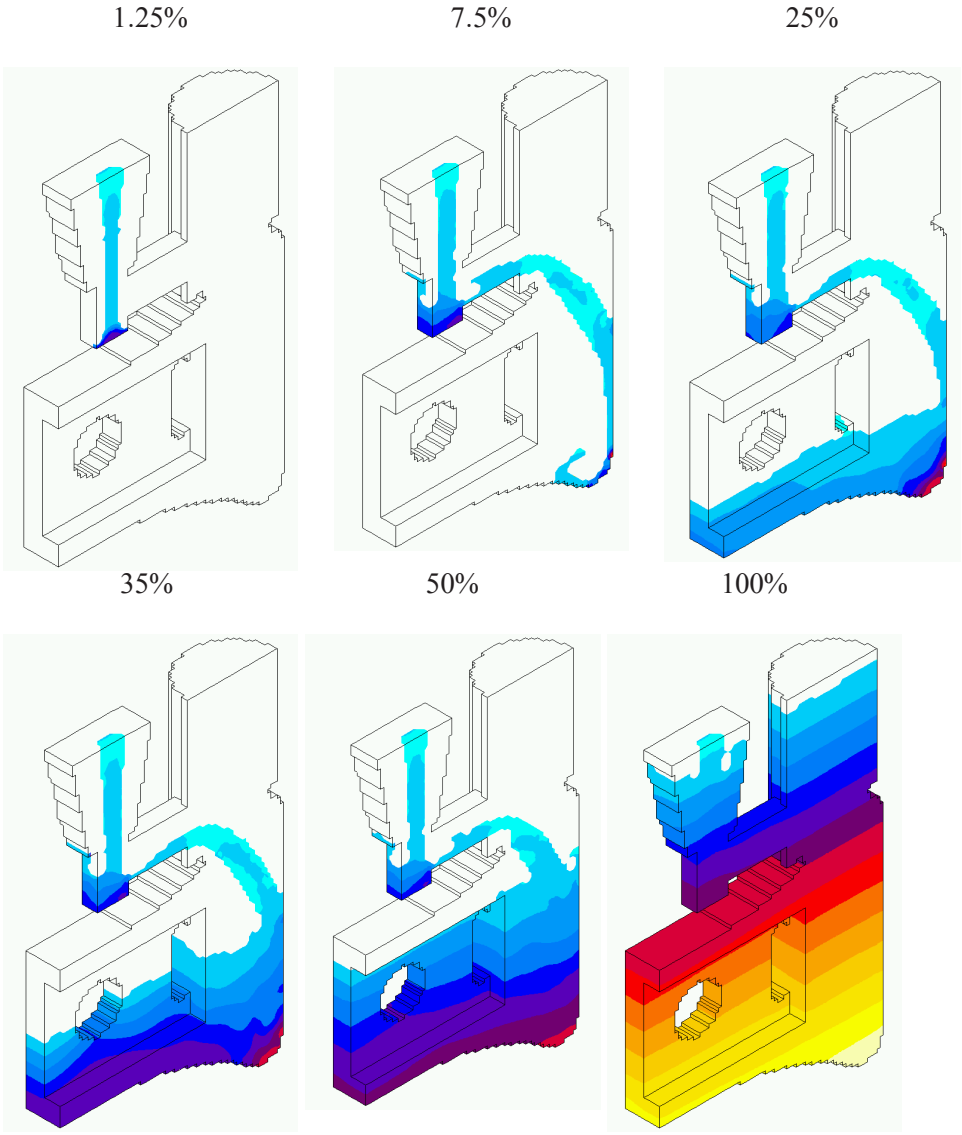

Figure 5.6: Filling sequence of pressure distribution in Hammer box, close to symmetry plane, at $Fr = 5.1$ and $Re = 53,417$. Expected time of filling 15 s for infiltration velocity $u_z = 123$ cm/s. Data: $\tau = -\frac{1}{\lambda^+} = 0.500034$, $U' = 0.1$, $T' = 36,858$, $L' = 6$, $\nu = 6.9 \times 10^{-7}$ m^2/s. Grid: 110,573 liquid cells. Colors: yellow (1339 – 1366 mbar), red (1203 – 1230 mbar), and blue ($<$ 1122 mbar). The picture corresponds to Figure 10 in [67].

satisfactory results were found keeping again ρ as a variable (cf. relation (5.30)), then:

$$\rho = \frac{\sum_{q\in Q^{kn}} f_q + \sum_{q\in Q^{un}} b_q}{1-\sum_{q\in Q^{un}} e_q}\ ,\ b_q = \frac{\rho_0 g}{c_s^2}\frac{U_\alpha^{in}}{\lambda^+}Q_{q\alpha z} - \frac{\rho_0 g}{2}c_{q\,z}\ . \qquad (5.31)$$

Here, the known populations are those arriving from the bulk, and the incoming populations are approximated with the first order expansion based on the constant (inlet) velocity and the hydrostatic pressure distribution, $f_q = \rho e_q + b_q$, $e_q = e_q(\rho = 1, \vec{J} = \vec{U}^{in})$. This technique for computation of the incoming fluxes could be suitable for other applications were the compressible effects are not negligible.

The numerical assessment of the compressibility effects and robustness of the algorithm is resumed in Section 5 of [67], along with the overview of the possible improvement which can be get either using the grid refining or altering the characteristic scaling. Some very preliminary LBE models with upwinding were constructed in [64]. In free interface filling applications, a naive explicit upwind rule was found as most efficient. The local quantity of the numerical diffusion was estimated with the "optimal rule", reviewed in Section 6.3.3. Recently, upwind scheme for the finite-volume LBE is proposed by Stiebler et all, [183].

5.4.3 Concluding remarks

Very intensively developed during last five years, free interface models [121, 193, 196, 197] keep the same conceptual idea but differs from the proposed scheme in technical details. Actually, they avoid the node-based reconstruction of the unknown interface populations, computing them with the link-wise "anti-bounce back" boundary rule (3.16), which (approximately) sets gas pressure value outside the interface. A possibility to include the surface tension is considered by Thürey [196], with the help of a local and curvature depending correction of the imposed pressure value. Quite likely, the effective continuity conditions on the components of shear stress are implicitly prescribed by the ensemble of the closure interface relations. These models also replace the recoloring step with the mass-exchange population-based advection algorithm (see discussion on the ILB). Unlike the free interface recoloring step, this algorithm is not guaranteed to yield the mass fractions between 0 and 1 but perhaps has a better control of the regularity of the interface.

Despite some natural difficulties, being recognized in different degrees by all multi-phase algorithms, very good results are obtained for a wide range of problems with free-interface LBE schemes: they include the filling of cavities [65, 67], modeling of metal foams [121], rising bubbles, broken damps and jets [196, 197].

In the future, we hope to adapt this method for simulations of overland flow on hillslope topography with furrows and to incorporate the rainfall episodes.

5.5 Extension for the Bingham Fluids

A coupling of the free interface method with the non-newtonian Bingham fluid model is proposed in [65]. According to Bingham model, the fluid behaves as a rigid solid when the norm of the extra stress tensor τ, $\tau = \nu\mathbf{D}$, $\mathbf{D} = (\nabla\vec{u} + \nabla^t\vec{u})/2$, is less than yield stress value τ_0. In liquid state, effective (apparent) viscosity of the material depends on the magnitude of the rate strain tensor: when $\|\tau\| > \tau_0$, the fluid has an effective viscosity $\nu^{\text{eff.}}$, $\nu^{\text{eff.}} = \nu + \tau_0/\|\mathbf{D}\|$. The so called "yield surface" $\|\tau\| = \tau_0$ separates two regions:

$$\begin{aligned} \|\mathbf{D}\| = 0 \quad &\text{if} \quad \|\tau\| < \tau_0 \quad , \\ \tau = (\nu + \frac{\tau_0}{\|\mathbf{D}\|})\mathbf{D} \quad &\text{if} \quad \|\tau\| > \tau_0 \quad . \end{aligned} \tag{5.32}$$

Here, $\|\mathbf{D}\| = \sqrt{2\mathbf{D}_{ij}\mathbf{D}_{ij}}$ and $\|\tau\| = \sqrt{2\tau_{ij}\tau_{ij}}$ are respectively the second tensor invariants.

Numerical difficulties of this model come from the singularity at yield surface. The regularized model [153] is used with the LBE simulations:

$$\tau = \left[\nu + \frac{\tau_0(1 - \exp\{-m\|\mathbf{D}\|\})}{\|\mathbf{D}\|}\right]\mathbf{D} \, . \tag{5.33}$$

Its applicability to predict viscoplastic behaviour in the limit $m \to \infty$ is studied in [14]. If $\|\tau\| < \tau_0$, the current viscosity value $\nu^{\text{eff.}}(t)$ is set equal to its limit value $\nu + \tau_0 m$. An additional non-dimensional parameter, the Bingham number B_n, controls the viscoplastic effects:

$$B_n = \frac{\tau_0 L}{\nu U} \, , \; m' = \frac{mU}{L} \, , \quad \nu^{\text{eff.}} = \nu[1 + \frac{B_n(1 - \exp\{-m'\|\mathbf{D}\|\})}{\|\mathbf{D}\|}] \, . \tag{5.34}$$

Like for large eddy turbulent modeling, the LBE may locally compute the components of strain-rate tensor $\mathbf{D}$. They appear as the prefactors in relations (5.26) and can be computed from the non-equilibrium projections on the orthogonal symmetric MRT basis vectors of the viscous modes (the details are given in Appendix A of [67] and relations (3.11) of [65]).

Very interesting theoretical and numerical study of injection moulding in 2D cavity with Bingham fluids is presented by A. N. Alexandrou, E. Duc and V. Entov, [8]. Our preliminary results of filling of 2D cavities with and without plastic

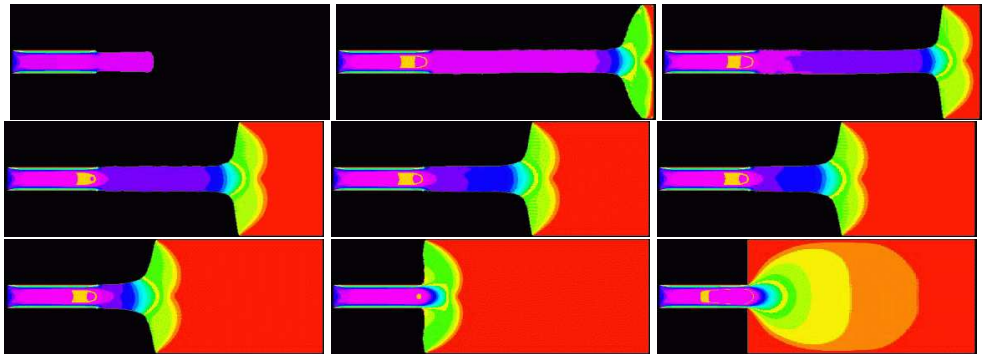

Figure 5.7: Velocity magnitude during the filling in 2D horizontal cavity at $Re = 5O$ and $Bi = 10$, $m' = 200$ for $t(\text{ s}) = \{0.11, 0.27, 0.32, 0.43, 0.54, 0.59, 0.75, 0.92, 1.02\}$. Infiltration velocity $u_x = 100$ cm/s and filling time 1.08 s. Data LBE: $U' = 0.1$, $\nu = 0.08$, $L' = 40$. No-slip boundary conditions. Colors (cm/s): red$(0-15)$, yellow$(15-25)$, green $(25-55)$ and blue $(60-115)$. The figure is recalled from [65].

effects were found in good (qualitative) agreement with these investigations. They are illustrated in Fig. 5.7. Simple, explicit in time coupling of the free interface method with the regularized Bingham model is robust at very low Reynolds numbers. An alternative and more conceptual approach is proposed in PhD work by L. Giraud, [78, 79] and further extended by P. Lallemand et al, [102]. In these works, the Generalized Lattice Boltzmann equation is extended for viscoelastic (Jeffreys) fluids in two and three dimensions, based on more large sets of velocities. The dispersion analysis is involved to get the isotropy and Galilean invariance and optimize the stability of new models.

5.6 Richard's equation for variably saturated flow

5.6.1 Overview

Richards' equation [166] describes water flow in variably saturated soils under the assumptions that the air phase is both continuous and at atmospheric pressure, and that the velocity and pressure are linked through Darcy's law. Nonlinear retention functions relate the pressure head (capillary pressure) and the moisture content values for unsaturated flow. The pressure head reaches its air entry value on the unsaturated/saturated interface and the moisture content (under incompressibility assumption) keeps its saturated value within the saturated zone. The numerical method should couple a highly non-linear parabolic type equation with a linear

elliptic one at the unsaturated-saturated interface. Despite significant advances [29, 141, 167, 209] Richard's equation still represents a difficult numerical task [142].

In the stratified media, we assume the flow velocity $\vec{u}^{(i)}$ inside the i^{th} layer be related to the capillary pressure $\psi^{(i)}(\theta)$ via Darcy's law:

$$\partial_t \theta^{(i)} + \nabla \cdot \vec{u}^{(i)} = q_s^{(i)} \ , \ \vec{u}^{(i)} = -\mathbf{K}^{(i)}(\nabla h^{(i)}(\theta) + \vec{1}_z) \ , \ h^{(i)}(\theta) = -\frac{\psi^{(i)}(\theta)}{\rho_0 g} \ . \quad (5.35)$$

Pressure head distribution $h^{(i)}(\theta)$ is a given function of the moisture content variable $\theta^{(i)}(\vec{x},t)$, a relative volumetric part of a soil occupied by water. The medium is saturated when $\theta^{(i)} = \theta_s^{(i)}$, $h^{(i)} \geq h_s^{(i)}$ and it is dry when $\theta^{(i)} = \theta_r^{(i)}$, $h^{(i)} = h_r^{(i)}$. In Eq. (5.35), $q_s^{(i)}$ is a mass source, $\vec{1}_z$ is an upward unit vector, $K_{\alpha\beta}^{(i)} = K(h)K_{\alpha\beta}^{a(i)}$ where $K^{(i)}(h) = k^{(i)}\rho_0 g/\mu$ is the hydraulic conductivity function and $k^{(i)}\mathbf{K}^{a(i)}$ is the permeability tensor. The conductivity function is set as $K(h) = K_s K_r(h)$, $K_r(h_r) \leq K_r(h) \leq 1$ where K_s is the saturated conductivity value: $K_r(h_s) = 1$.

Using the scaling procedure (1.47) the Richard's equation (5.35) becomes on the LBE computational grid (layer's number (i) is omitted):

$$\begin{aligned} \partial_{t'}\theta &+ \nabla' \cdot \vec{J} = \nabla' \cdot \mathbf{K}' \cdot \nabla h' + M \ , \ h' = \mathcal{L}h \ , \ \vec{J} = -\mathbf{K}'(h)\mathbf{L} \cdot \vec{1}_z \ , \\ \mathbf{K}' &= K'(h)\mathbf{K}^{\mathbf{a}'} \ , \ K'(h) = \mathcal{U}K(h) \ , \ \mathbf{K}^{\mathbf{a}'} = \mathbf{L}\mathbf{K}^{\mathbf{a}}\mathbf{L} \ , \ M = q_s/\mathcal{T} \ . \end{aligned} \quad (5.36)$$

Our first approach considers the Richard's equation (5.36) in unsaturated soil as a non-linear advection-diffusion equation for the conserved quantity $s = \theta$ based on the equilibrium distribution (1.48), where the "convection" function $\vec{J}(\theta)$ and the "diffusion" coefficients, $\mathbf{K}'\partial_\theta h(\theta)$ are prescribed (non-linear) functions of the conserved quantity. The eigenvalue functions $\Lambda^-(\theta)$ are then proportional to the slope of the modeled retention relation, $\partial_\theta h(\theta)$. However, several models of soil have a very rapid variation (or even, unboundness) of the retention curves $h(\theta)$ near the saturation front, as for example (Van-Genuchten-Mualem) VGM-model [201] of the coarse-textured SAND soils. With a purpose of avoiding the very sharp variation of the eigenvalues, the Kirchhoff-transform based selection of the diffusion function $\bar{\mathcal{D}}(s)$ was proposed: $\bar{\mathcal{D}}(s) = \int_{-\infty}^{h'(\theta)} K'(h)dh$. These two first LBE formulations for Richard's equation were examined in [68] for homogeneous isotropic soil. It becomes possible to easily vary the sharpness of the infiltration fronts before ponding with the versatile model [23, 207]. We derived the uniform analytical solution for several types of the constitutive relations based on these ideas. These solutions are summarized in Section 5.6.8 and applied to validate the LBE results in Figure 5.16.

The coupling between the unsaturated and saturated zones is built with no change of the primary variables, solving the Poisson equation which yields the

Darcy's law in saturated zone as a local steady state: $\partial_{t'} h \to 0$ (more details are given in Section 5.6.3). Steady state profiles of capillary tension under constant rainfall episode, $\vec{u_r}(z = H) = -i_r \vec{1}_z$, were validated using direct integration of Richards' equation in 1D:

$$-i_r^\star \quad = \quad -K_r(h)(\partial_z h + 1)\ ,\ i_r^\star = i_r / K_s\ , i_r^\star < 1\ ,\ z > 0\ , \tag{5.37}$$

either with the help of the analytical solutions [219] for Brooks-Corey-Mualem (BCM) model [24, 143] or by means of the numerical integration for the VGM model. When the bottom pressure is fixed, $h(z_L) = h_L$, the solution has a following form:

$$z = z_L + \int_h^{h_L} \frac{K_r(h')}{K_r(h') - i_r^\star} dh'\ , \quad \text{then:} \quad z - z_L = \frac{h_L - h}{1 - i_r^\star} \ \text{ when } \quad K_r \equiv 1. \tag{5.38}$$

Unsteady infiltration columns were efficiently validated using the class of the analytical solutions proposed by Barry et al. [10]. Valid for both, saturated and unsaturated zones, these models were extended in our work for Brooks and Corey conductivity function: this is described in Section 5.6.8 and demonstrated in Fig. 5.17. These simulations indicate that the accuracy of the whole developed method for the variably saturated flow depends on the precision which is reached for local steady state in the saturated zone.

It was earlier recognized that the numerical difficulties of solving Richard's equation depend on the specific mathematical properties of the retention curves and conductivity functions, [205]. We elaborate this point for the stability aspects of our method in the next section. Direct discretization methods based on the pressure formulation, e.g., [17, 205], meet the numerical difficulties (bad convergence) when the conductivity function $K_r(h)$ and water capacity function, $C(h) = \frac{\partial \theta}{\partial h}$ have very sharp or unbounded slopes on the saturation. This typically occurs for fine-textured soils, as the SCL soil for example, and more generally, when the VGM parameter n is smaller than 2. So-called modified VGM functions [205] were introduced to solve this problem: they smooth the shape of the water capacity function near the saturation front for the fine-textured soils, then the shape of the retention curves $h(\theta)$ for the coarse-textured soils, allowing small negative values for open pressure h_s (instead of commonly used zero value). However, it was realized that even a relatively small altering of $C(h)$ affects noticeably the dynamic behaviour of the saturated front [16, 205] and water tables [17], for fine-textured soils. Infiltration into clay soil in Fig. 5.8 with $h_s = -2\ cm$ (left picture) and $h_s = 10^{-2}\ cm$ (right picture) illustrates this point. We observe that the simulations with $h_s \to 0$ encounter the convergence problems for the broadly used commercial software, HYDRUS 2D code [107]. At the same time, the $\theta-$based LBE solution, obtained

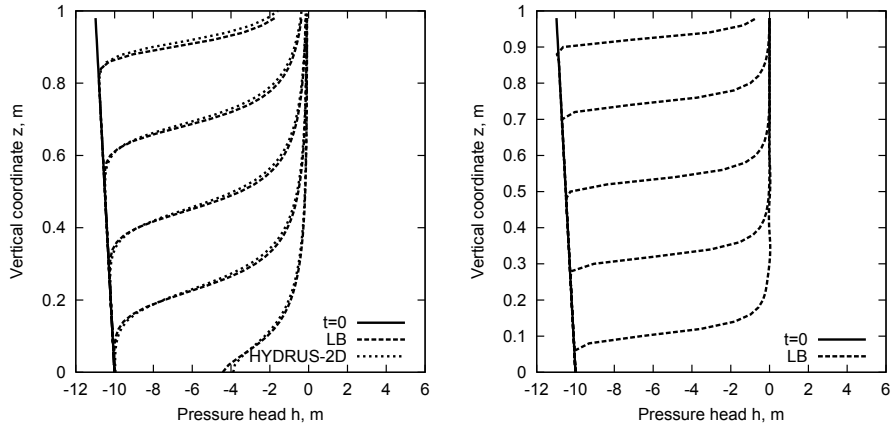

Figure 5.8: Two pictures show profiles for downward infiltration into $1m$ long clay soil box subject to constant flux $\vec{u_r} = -i_r\vec{1}_z$, $i_r = K_s/2$ at time $t = 2.4, 12, 24, 36, 48\ h$. Modified VGM relations with $h_s = -2\ cm$ is used on the left picture and with $h_s = 10^{-2} cm$ on the right picture. The initial condition corresponds to an hydrostatic distribution with a total head $h + z = -10\ m$. The box contains 50 grid cells. The $\theta-$form is used for LBE with $\mathcal{U} = 1$.

for $h_s = 10^{-2}\ cm$, compares well with the benchmark solution of [205] (right picture in Figure 8). By this means, the $\theta-$based LBE method and pressure-based direct discretization methods complement each other. Moreover, no significant impact of the negative h_s values ($\approx -10\ cm < h_s \leq 0$ was detected for the front dynamics in coarse-textured soils. This advocates using of the regularized VGM functions for the LBE approach. This enables us to extend the method for the interaction of shallow water tables with the ground surface for a large range of soils, and to apply it in virtual hillslopes under constant rainfall conditions. The results are described in section 5.6.4 and compared with the finite-element model [17].

At the same time the LBE method was extended for the heterogeneous soils. The continuity analysis from Section 4.3 tells us that neither a moisture content based nor a Kirchhoff transform based formulations are able to handle the interlayer continuity of pressure with the implicit interface tracking. This simplest (and conservative) approach ensures the continuity of Darcy's flux but also enforces the continuity of the equilibrium diffusion variable. That means that the transition of the populations across the interface forces both θ and Kirchhoff transform variables be continuous on the interlayer boundary. This is in contradiction to the continuity of pressure for two different soils. The "mixed" θ/h equilibrium distribution

was introduced to solve this difficulty, keeping moisture content as the conserved variable and the pressure as the diffusion equilibrium variable for transient flow, or using the pressure based formulation for steady flow. Next the anisotropic heterogeneous situations were examined with the help of the non-uniform grid transformations. These results are discussed in Section 5.6.5.

5.6.2 Equilibrium and primary variables

Let us consider the modeling of the Richard's equation (5.36) in the form:

$$\partial_{t'} s \quad + \quad \nabla' \cdot \vec{J} = \nabla' \cdot \vec{D} + q'_s \; , \; \vec{J} = -K'(s)\vec{1}'_z \; , \; \vec{1}'_z = \mathbf{K}' \cdot \vec{1}_z \; . \tag{5.39}$$

The Darcy velocity $\vec{u}'$ is the local sum of the advective and diffusive fluxes (with $\vec{D} = -\vec{\Phi}$, cf. (1.50))

$$\vec{u}' = \vec{J} + \vec{\Phi} \; , \; \text{where } \vec{\Phi} = \{\Phi_\alpha = (\Phi \cdot \mathbf{c}_\alpha)\} \; , \; \Phi = \{\Phi_q = -\Lambda_q^- g_q^-\} \; . \tag{5.40}$$

Using the MRT, L and TRT-E models the diffusive flux takes the following forms:

$$\begin{aligned} \text{MRT:} \quad \Phi_\alpha &= \mathbf{D}_{\alpha\alpha} \cdot \partial_{\alpha'} \bar{\mathcal{D}}(s) \; , \; \mathbf{D}_{\alpha\alpha} = k(s) K^{a'}_{\alpha\alpha} \quad , \\ \text{L:} \quad \Phi_\alpha &= \mathbf{D}_{\alpha\beta} \cdot \partial_{\beta'} \bar{\mathcal{D}}(s) \; , \; \mathbf{D}_{\alpha\beta} = k(s) K^{a'}_{\alpha\beta} \quad , \\ \text{TRT-E:} \quad \Phi_\alpha &= k(s) \partial_{\beta'} \mathcal{D}_{\alpha\beta} \bar{\mathcal{D}}(s) \; , \; \mathcal{D}_{\alpha\beta} = K^{a'}_{\alpha\beta} \; . \end{aligned} \tag{5.41}$$

We assume the isotropic equilibrium function for the MRT and L models: hence, the MRT model is restricted to modeling of anisotropic diagonal diffusion tensors (see discussion in section 1.6.1). Different equilibrium formulations for Richard's equation (5.35) are guided by the physical meanings assigned to the equilibrium diffusion variable $\bar{\mathcal{D}}(s)$. When the diffusion function $\bar{\mathcal{D}}(s)$ and the conserved quantity s differ, we assume that the condition $0 < c_e \leq c_e^{\max}$ (which is obtained for linear diffusion equation, see relation (1.66)) can be used in the *approximate linearized* form:

$$0 < c_e \frac{\partial_s \bar{\mathcal{D}}(s)}{s} \leq c_e^{\max} \; . \tag{5.42}$$

Based upon, let us introduce several equilibrium formulations, defined by their choice of the diffusion variable $\bar{\mathcal{D}}(s)$, then the diffusion function $k(s)$:

- The moisture content, $\theta-$form:

$$s = \theta \; , \; \bar{\mathcal{D}}(s) = \theta \; , \; k(s) = K'(\theta)\partial_\theta h' \; , \; \partial_s \bar{\mathcal{D}}(s) = 1 \; . \tag{5.43}$$

One of the main advantages of the $\theta-$form is that the stability restriction (5.42) is independent of the soil properties. The $\theta-$form has no difficulties in dealing with dry soil when the diffusion coefficient $K'(\theta)\partial_\theta h'$ is bounded. This is illustrated for sharp infiltration into sec soil in Fig. 5.16. However, this formulation may loss the accuracy on the saturated/unsaturated interface for very sharp retention curve, because of a much too rapid variation of $\Lambda^-(\theta)$, as we discussed above. Figure 5 in [68] shows one example.

- The Kirchhoff transform [118], $\theta/K-$form is

$$s=\theta\ ,\ \bar{\mathcal{D}}(s)=\int_{-\infty}^{h'(\theta)}K'(h)dh\ ,\ k(s)=1\ ,\ \partial_s\bar{\mathcal{D}}(s)=K'(\theta)\partial_\theta h'(\theta)\ . \quad (5.44)$$

The distinguished property of this formulation is that the eigenvalue functions Λ^- are independent of θ. This enabled us, as one example, to compute SAND soil with the original VGM functions and $h_s=0$ (this yields extremely sharp retention curves): see unconfined flow in rectangular embankment in the presence of seepage face in [39, 68]. It is noted however that (semi-analytical) expression of the Kirchhoff transform of the used there VGM retention function (which we derive in [68]) is difficult to compute numerically.

- The mixed, $\theta/h-$form follows the original form of Richard's equation (5.36):

$$s=\theta\ ,\ \bar{\mathcal{D}}(s)=h'\ ,\ k(s)=K'(\theta)\ ,\ \partial_s\bar{\mathcal{D}}(s)=\partial_\theta h'\ . \quad (5.45)$$

The mixed form enforces a continuity of pressure on the interfaces, provided that the equilibrium weights are homogeneous. This condition is satisfied only by the L model when the anisotropic properties of two soils differ. The stability criterion (5.42) becomes quite restrictive for mixed equilibrium formulation when the retention curves are sharp: if $\partial_\theta h'\to\infty$ then $c_e\to 0$. Again, the modified VGM relations help here to improve the robustness of the method.

- Pressure head, $h-$form with an equilibrium parameter $H^{\rm eq}$:

$$s=\frac{h'}{H^{\rm eq}}\ ,\ \bar{\mathcal{D}}(s)=h'\ ,\ k(s)=K'(h)\ ,\ \partial_s\bar{\mathcal{D}}(s)=H^{\rm eq}\ . \quad (5.46)$$

This form is restricted to steady problems because of the inconsistency of its mass variable $\frac{h'}{H^{\rm eq}}$, then the transition mass term $\partial_{t'}h'/H^{\rm eq}$, with respect to the mass term $\partial_{t'}\theta$ of the Richard's equation. The convergence to steady state improves when $H^{\rm eq}\to\infty$, but the stability condition restricts then c_e to the

interval $]0; c_e^{\max}/H^{\text{eq}}]$. Main advantage of the $h-$form is in its independence of the retention curves. Like the mixed form, $h-$form maintains the pressure continuity in vertical columns.

5.6.3 Saturated zone

The water content reduces to its saturated value $\theta^{(i)} \equiv \theta_s^{(i)}$ and Richard's equation (5.35) reduces to Poisson equation in saturated zone:

$$\nabla \cdot K^{(i)}(\nabla h^{(i)} + \vec{1}_z) = 0 \ , \ K^{(i)}(h) \equiv K_s^{(i)} \ , \ h^{(i)} \geq h_s^{(i)} = h^{(i)}(\theta_s^{(i)}) \ . \tag{5.47}$$

The coupling with the saturated zone relies on the idea of pseudo-compressible pressure equilibrium formulation, which is described by the $h-$form (5.46). This is achieved with the help of the linear extrapolation of the retention curves beyond the air entry value (for each layer, $H^{\text{eq}} \rightarrow P^{(i)}$):

$$h'(\theta) = P(\theta - \theta_s) + h'_s \ , \ P = \partial_\theta h(\theta_s) \ , \ h \geq h_s \ , \ \theta \geq \theta_s \ . \tag{5.48}$$

The macroscopic law is modeled in a form of pseudo-compressible Darcy's law:

$$\frac{1}{P^{(i)}} \partial_t h'^{(i)} + \nabla \cdot K_s^{(i)}(\nabla h'^{(i)} + \vec{1}_z) = q_s^{(i)} \ , \ h^{(i)} \geq h_s^{(i)} \ . \tag{5.49}$$

The temporal derivative vanishes for both the local steady state and stationary flow. Usually, the convergence to steady state improves when $P^{(i)}$ increases. It was mainly observed that the results are not sensitive to using of discontinuous slopes, i.e. taking $P > \partial_\theta h(\theta_s)$, provided that the local steady state is reached with a good accuracy. We emphasize that the acceleration of the saturation step is mandatory for the efficiency of the whole method. Similar acceleration techniques to reach the steady state is recently proposed in [110].

5.6.4 Dynamics of shallow water tables

Variably saturated subsurface flow in isotropic homogeneous soils was modeled with the continuous linear finite-element 2D method [17] (at the metric and hectometric scales), and with the 3D LBE method (at the metric scale). The finite-element solutions were also compared with a more detailed coupling of subsurface and shallow water flow, the latter being restricted to diffusive wave approximation. Their results have not show any significant difference, at least neglecting the feedback of surface runoff. The pressure based finite-element method and all developed LBE techniques were validated by the same analytical solutions, [16, 68]. The simulations in hillslopes were compared for two methods and presented on

the Dynas Workshop 2004 (see [46]). In whole, the results are found in very good agreement for two methods. Let us discuss here several numerical aspects of the LBE model.

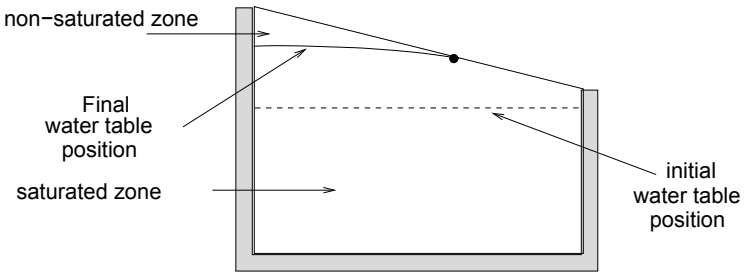

Figure 5.9: Sketch for steady state in virtual hillslope. The picture is recalled from [17].

The two-dimensional configuration modeled at the metric scale is borrowed from Abdul and Gillham [1] and sketched in Fig. 5.9. The domain dimensions are 1.4 m in length and $1-0.8$ m high; the box is impermeable for all boundaries except for open surface. The initial condition is horizontal water table located at 0.7 m and the hydrostatic pressure profile. The simulations were run using a constant rainfall intensity i_r, $\vec{u}_r(z=H) = -i_r\vec{1}_z$, for three different soils (SCL, YLC and SAND), with a focus on the impact of their hydraulic properties on the dynamic response of water tables.

The TRT $d3Q15$ isotropic model with $\theta-$based and $\theta/h-$based equilibrium forms was applied on the cuboid grid. Two types of the discretization were examined: the first one corresponds to Figure 5.9 and the second one to Figure 5.10. In later case, the modeled Richard's equation is described in rotated coordinate system. This enables the LBE scheme to locate grid boundary nodes on the open surface, hence simplifies the comparison with the finite-element method.

A particularity of underground modeling is a presence of so-called boundary seepage face, when the water table rises so much that some portion of the ground is saturated. When the overland flow is not modeled, a common numerical technique for treating this situation consists in a "switch" from the rain flux (Neumann) condition $\vec{u}(\vec{r}_{\rm w}) = \vec{u}_r$ to Dirichlet condition, $h(\vec{r}_{\rm w}) = h_s$. In addition to saturation event, the flux control criteria: $(\vec{u},\vec{n}) > (\vec{u}_r,\vec{n})$, where $\vec{n}$ is outward normal, is involved by several modeling approaches to decide if the altering of the boundary condition takes a place. Based upon, the obstacle-type dynamical formulation is proposed in [17]. The method involves the fixed-point iterative scheme to localize the water table and seepage face for each time step of the implicit-Euler solver of the Richard's equation. The LBE approach,in contrast, locally controls the seepage

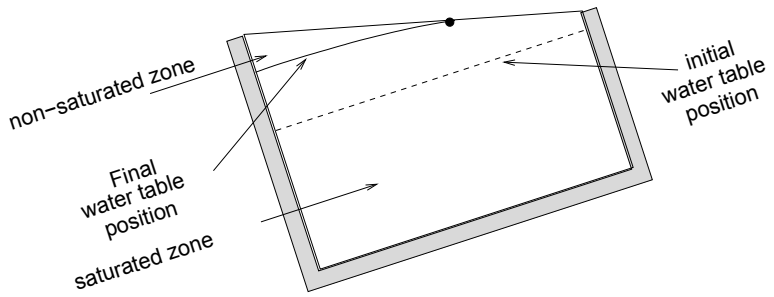

Figure 5.10: Sketch for steady state in rotated hillslope: open surface is aligned to rows of the regular grid.

face boundary conditions, based only on the obtained pressure distribution. This performs more accurately on the surface aligned grid, where no The evolution of water tables is most slow SCL soil is illustrated in Fig. 5.11.

It was observed that steady state solutions do not depend on the soil properties when the rain intensity i_r is proportional to prescribed soil saturated conductivity K_s. The Fig. 5.12 demonstrates the steady (fairly independent of soil nature) distribution of the reduced normal velocity u_n/K_s on the open surface. They are obtained by the LBE on the surface aligned grid using the $\theta-$form for the SCL and YLC soils, and the $\theta/h-$form for the SAND soil. The temporal evolution of their relative exfiltration fluxes is plotted in Fig. 5.13. On the whole, the results of the finite-elements and the LBE agree very well. They confirm that there is no any noticeable impact of the using negative h_s values in modified VGM relations for the SAND. We provoke a difference between the finite-element and LBE solution when the local steady state is not reached in the saturated sub-domain (cf., the solutions with 80 and 20 sub-steps in the SCL soil on the left picture, and with 40 and 20 sub-steps in the SAND soil on the right picture). The SCL soil is more simple for the LBE than the YLC and SAND, but it needs more sub-steps in saturated zone, as the converse of the smoothness of its retention shape (see relations (5.48) and (5.49)). More complicated dynamics of water tables in heterogeneous soils would allow further access the weak and strong points of two developed approaches.

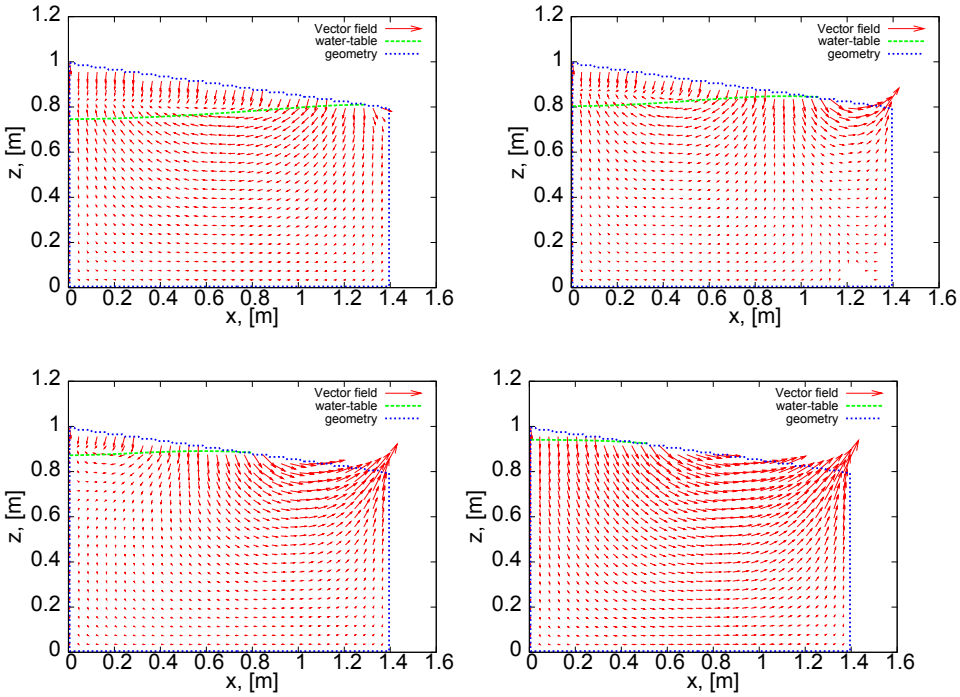

Figure 5.11: Temporal evolution of the water table in the SCL soil after 4, 6, 8 and 10 hours of the rainfall event with $i_r = 10\%K_s$.

5.6.5 Heterogeneous soils

We verify first the analysis from Section 4. In accordance with them, both mixed and pressure based formulations yield exact piece-wise linear solutions for saturated steady vertical flow in a stratified column, when the interlayer interfaces are located in the middle between the lattice nodes. Although the vertical strategies were developed for heterogeneous diffusion coefficients, they also work in the presence of the discontinuous advection components, $K_s^{(i)}\vec{1}_z$, as was reported in [72]. We then verify that this remains valid for the non-uniform refining, using not equal scaling factors $L_z^{(i)}$ for different sub-domains. This technique was validated for variably saturated flow subject constant rainfall, against the direct integration of the Darcy's law (5.37). These results are illustrated in Figures 2 and 4 in [71]. It was observed that both TRT-E and the L models equally improve the resolution of the discontinuous pressure head gradient with the additional grid points within the middle layer. The reader can observe the difference between the uniform and non-uniform grid transformations in Figure 5.14.

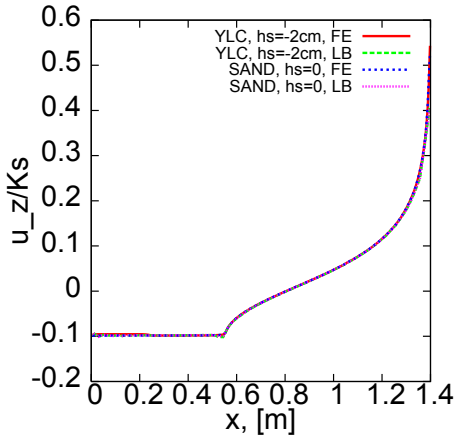

Figure 5.12: Steady state distribution of the reduced vertical velocity u_z/K_s on the open surface is ploted for YLC ($h_s = -2$ cm) and SAND ($h_s = 0$ cm). The solutions are obtained with FE method (280 nodes on the open surface) and LBE method (70 surface nodes on the aligned grid).

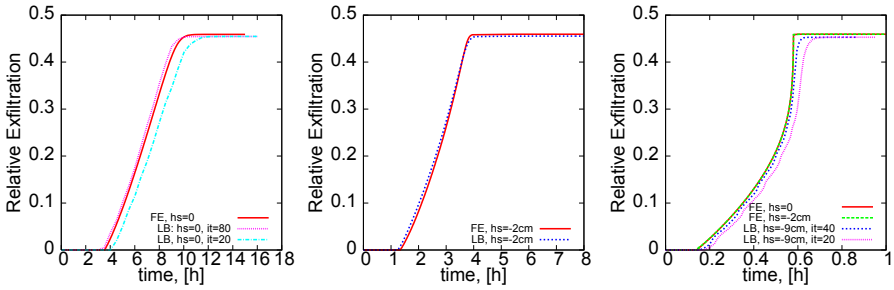

Figure 5.13: Temporal evolution of the relative exfiltration flux is ploted for SCL, YLC and SAND soils when $i_r = 10\%K_s$ for each of them. Number of iterations in saturated zone controls the accuracy of local steady state (Darcy law). The esults are compared for the LBE and the finite-element model [17].

A comparison with "semi-analytical" (Runge-Kutta based) implicit RK method [135] allowed us to make two curious observations: first, without any adaptive space stepping, the RK method required in a factor of $200 - 300$ more grid points for a correct capturing of the the sharp jump of the pressure gradients; second, the smallest size of the adaptive RKA method is in a factor of $10^5 - 10^6$ smaller than the uniform spacing of the LBE method, for similar accuracy. These results are illustrated in Figure 3 of [71]. The progression at time of the vertical drainage in

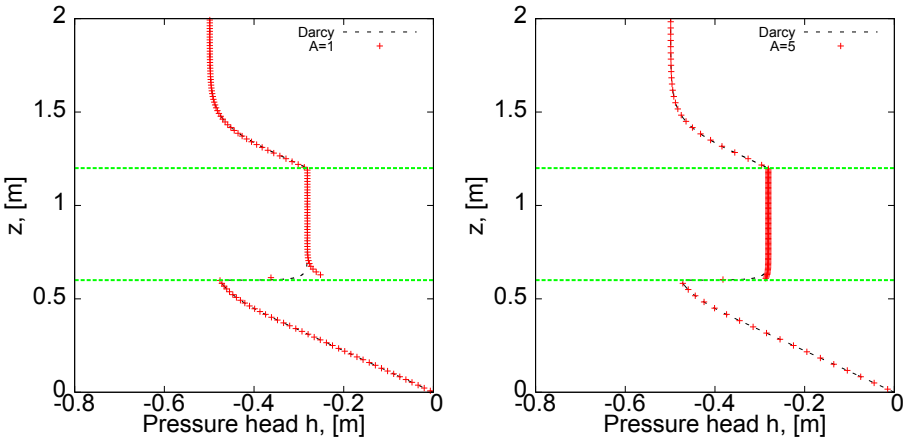

Figure 5.14: Both pictures show pressure head infiltration curves in three layered variably-saturated tube, obtained with the L method and contrasted to Darcy's law, for K_s ratio equal 100. The uniform grid is used on the left picture ($A = 1$) and the non-uniform rescaling: the middle layer is 5 times finer than the two other layers, is used on the right picture ($A = 5$).

a three-layered soil tube of 2 m length when the pressure head $h = 2$ m at the base is suddenly reduced to the atmospheric value at $t = 0$, a tough example borrowed from Marinelli and Durnford [135], is compared to RKA solution in Figure 12 of [72]. With the implicit method, larger time step values becomes possible but one LBE step is much cheaper.

5.6.6 Anisotropic heterogeneous grids

The anisotropy of the diffusion/convection terms appears in Richards' equation because of the distinct conductivity values in the vertical and horizontal directions. A similar effect appears using a linear transformation of the coordinates from the orthorhombic (rectangular) discretization grid to the cuboid computational grid. The anisotropic coordinate transformation enabled a correct describing of the steady state flow through unconfined "elongated" 25 $m \times 5$ m aquifer on the square computational domains. Very similar results are obtained with all three anisotropic LBE techniques (TRT-E, L and MRT methods) and plotted in Figure 5 of [71]. Once again, the anisotropic techniques can be efficiently tested against the solutions of the given method itself which are obtained without using of coordinate transformations.

More difficult situation takes place in multi-dimensions when the anisotropic

coordinate transformations are also heterogeneous for two soils. Such situations are examined in Figure 5.15. These simulations are performed with implicit tracking of interlayer boundary. Indeed, when the numerical solution is get with the continuous velocity, the physical vertical velocity u_z is continuous only if the rescaling from u_z' to u_z is uniform for each sub-domain. In considered case, $u_z^{(i)} = u_z^{'(i)}/(\mathcal{U}L_z^{(i)})$ and the using of implicit tracking becomes possible only if the modeled equations (5.36) are divided by $L_z^{(i)}$-value in each i^{th} sub-domain. This in principle will cause different time scaling in the sub-domains, but this is not relevant for the steady state.

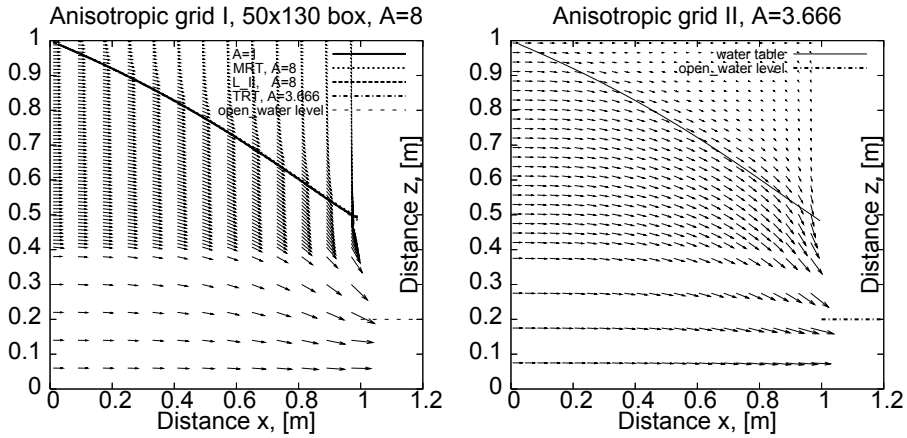

Figure 5.15: Two pictures show unconfined flow in a square 1 m^2-aquifer filled with homogeneous Silty Clay Loam using non-uniform coordinate transformations. Open water level corresponds to $h+z=0.2$. Left picture: grid I $[50\times 130]$ with $\mathcal{L}=50m^{-1}$, $L_x=1$, $L_z^{(1)}=0.5$ and $L_z^{(2)}=4$, i.e., $10/120$ grid points repartition. Right picture: grid II $[100\times 52]$ with $\mathcal{L}=20m^{-1}$, $L_x=5$, $L_z^{(1)}=1$ and $L_z^{(2)}=3.666$, i.e., $8/44$ grid points repartition between bottom and top layers. The velocity is output for each second grid point. These pictures are extracted from Figure 6 of [71].

The results obtained here tell us that the global characteristic quantities, the discharge values and the water table position are in very close agreement for all considered methods: MRT model with the anisotropic (velocity) eigenvalues, L model with the anisotropic eigenvalues of the coordinate links, and TRT-E model, with the anisotropic equilibrium functions. Also, the detailed analysis has shown that neither the pressure head nor the vertical velocity manifest any significant oscillations on the interface. In contrast, it was detected that the solutions differ for

tangential velocity, which oscillates on the interface and especially for the MRT and TRT-E models. The latter analysis [73] confirmed that the case of the heterogeneous anisotropy requires an introduction of the explicit interface corrections for the populations traveling across the interface. They are given by relations (4.26) and (4.27), and take into account an eventual possibility of the non-uniform refining (via relations (4.24)). These corrections have not been yet verified for variably saturated flow. However, the observed results confirm the predictions of the analysis: without any (flux) correction (4.27), the L model with the vertical strategy and equal eigenvalue functions $\Lambda_q^{-(i)}$ for all interface cut links enforces the continuity of the pressure and all flux components, hence the continuity of $u_x^{\prime(i)} L_z^{(i)}$ and then the continuity of the physical values: $u_x^{(i)} = u_x^{\prime(i)} L_z^{(i)} / (\mathcal{U} L_x)$. This explains the observed smooth fields obtained with the L model. Altogether, we emphasize that the TRT-E model needs the interface corrections when the equilibrium weights become discontinuous. This indicates a certain preference for the L model in heterogeneous anisotropic soil.

5.6.7 Concluding remarks

The Lattice Boltzmann formulations for Richard's equation manifest them as a promising tool for modeling of variably saturated flow. We show that the choice of the diffusion variable determines not only the form of the diffusion term (e.g., specific integral transform) but also the robustness of the numerical scheme. One striking difference between the LBE and the direct discretization methods, e.g., the moisture content form [177], the mixed form of Celia et al [29] or Kirchhoff-transform of Ross [167], is that the altering of the primary equilibrium variables does not necessitate any modification of the LBE solving procedure. In author's belief, a dynamic switch from one equilibrium formulation to another would give a well performing method for a large spectre of problems, from the drainage to imbibing.

One of the problems to be solved is the extension of the method for large (kilometric-scale) aquifers. Keeping this application in mind, the anisotropic rescaling of the coordinates was proposed. This technique was found efficient for isotropic aquifers with a large length disproportion, [71]. It was also demonstrated there that the non-uniform mesh transformations may play a role of the adaptive grid refining. However, adaptive heterogeneous refining in sub-domains needs a careful control of the continuity of the obtained solutions. Finally, the adaptive time stepping was introduced into LBE Richard's schemes based on the adequate rescaling of the equilibrium and non-equilibrium components. This procedure makes possible a dynamical adjusting of the stability criteria in dry and saturated zones. The

routine use of such techniques needs however further numerical assessment, for a wide spectre of flow scenarios.

5.6.8 Appendix: exact solutions of Richard's equation

Several extensions of the known analytical solutions [10, 23, 207] were proposed in [68]. They enabled an efficient inspection of the LBE and finite-element approaches for a large range of possible solutions and their coupling on the saturated front.

Non-linear unsaturated model

We consider the infiltration before ponding following Broadbridge and White [23] and Watson et al. [207]. The hydraulic conductivity $K(\tilde{\theta}) = K_s K_r(\tilde{\theta})$ and the soil water diffusivity $D(\tilde{\theta})$ as functions of effective moisture content, $\tilde{\theta} = \frac{\theta-\theta_s}{\theta_s-\theta_r}$, are prescribed as:

$$K_r(\tilde{\theta}) = \frac{\mathcal{C}-1}{\mathcal{C}-\tilde{\theta}}(\beta_1\tilde{\theta}+\beta_2\tilde{\theta}^2)\ ,\ D(\tilde{\theta}) = D_0\frac{\mathcal{C}^2}{(\mathcal{C}-\tilde{\theta})^2}\ ,\ \beta_1+\beta_2=1\ ,\ \mathcal{C}>1\ . \quad (5.50)$$

A very easy variation of the sharpness of the infiltration curves is possible with the help of the parameter $\mathcal{C}$, as illustrated in Figure 5.16. The Kirchhoff transform [118] $\Psi = \int_{-\infty}^{\tilde{\theta}} D(\tilde{\theta}')d\tilde{\theta}'$ becomes for this model:

$$\Psi(\tilde{\theta}) = D(\tilde{\theta})\mathcal{C}^2/(\mathcal{C}-\tilde{\theta})\ . \quad (5.51)$$

Using the scaling $L = D_0\mathcal{C}/(U(\mathcal{C}-1))$, $U = K_s/\bar{\theta}_s$, $\bar{\theta}_s = \theta_s-\theta_r$, $T = L/U$, $t_\star = t/T$, $\tau = mt_\star$ and the parameters $m = 4\mathcal{C}(\mathcal{C}-1)$, $m_0 = m/4$, $\rho = R_\star/m$, $R_\star = i_r/K_s$, $B_\star = {h_1}^2/m - C_1\beta_2$, $\rho_\star = \rho - \frac{1}{2}(C_1+C_2)$, $h_1 = \sqrt{m}(C_2-2\rho)$, $h_0 = \sqrt{m_0}(\mathcal{C}-1)\beta_2$, $\mu_0 = (\mathcal{C}-1+h_0/h_1)$, we construct the analytical solution in a form [23] for 1D infiltration into a semi-infinite sec column $z \le H$: $\tilde{\theta}(t=0,z) = 0$, subject to constant flux $\vec{u_r}(t,z=H) = -i_r\vec{1}_z$, $\forall\, t$:

$$\tilde{\theta}(t_\star,\zeta) = \mathcal{C}(1-\frac{C_1}{2\rho-C_2-u^{-1}\partial_\zeta u})\ ,\ C_1 = \beta_2+\frac{\beta_1}{\mathcal{C}}\ ,\ C_2 = -\beta_2-\frac{\beta_1}{2\mathcal{C}}\ , \quad (5.52)$$

ζ is related to the dimensionless depth variable $z_\star = \frac{H-z}{L}$:

$$\begin{aligned} z_\star &= \frac{1}{\mathcal{C}C_1}(-h_1\zeta/\sqrt{m} - \ln[u] + B_\star\tau/4)\ ,\ u = \exp(-\frac{\zeta^2}{\tau})[u_1+\frac{1}{2}(u_2-u_3)]\ , \\ u_1 &= \exp[a_+^2]\ ,\ u_2 = g(b_+)+g(b_-)\ ,\ u_3 = g(a_+)+g(a_-)\ ,\ g(x) = \exp(x^2)\mathrm{erfc}(x)\ , \\ a_\pm &= \frac{(\zeta\pm\rho_\star\tau)}{\sqrt{\tau}}\ ,\ b_\pm = \frac{(\zeta\pm\tau\sqrt{B_\star/4})}{\sqrt{\tau}}\ ,\ . \end{aligned} \quad (5.53)$$

When $C_1 = 0$, the solution is $\tilde{\theta}(t_\star, Z)$ and Z is related to dimensionless depth $z_\star$:

$$\begin{aligned}
\tilde{\theta}(t_\star, Z) &= \mathcal{C} - m_0/\mu(t_\star, Z)\ ,\ \mu(t_\star, Z) = \mathcal{C} - 1 + \mu_0(-\frac{\sqrt{t_\star}h_1}{\sqrt{\pi}}\exp[-{\alpha_+}^2]\exp[h_1 Z] \\
&+ \frac{1}{2}\exp[h_1 Z]\mathrm{erfc}[\alpha_+](1 + h_1 Z + h_1^2 t_\star) - \frac{1}{2}\mathrm{erfc}[\alpha_-])\ ,\ \alpha_\pm = \frac{Z \pm h_\star}{2\sqrt{t_\star}}\ ,\ h_\star = t_\star h_1 \\
\sqrt{m_0} z_\star &= (\mathcal{C} - 1)Z + \frac{\mu_0}{2}((h_\star + Z)\exp[h_1 Z]\mathrm{erfc}[\alpha_+] - h_\star \mathrm{erf}[\alpha_-] - Z\mathrm{erfc}[\alpha_-] - h_\star) \qquad (5.54)
\end{aligned}$$

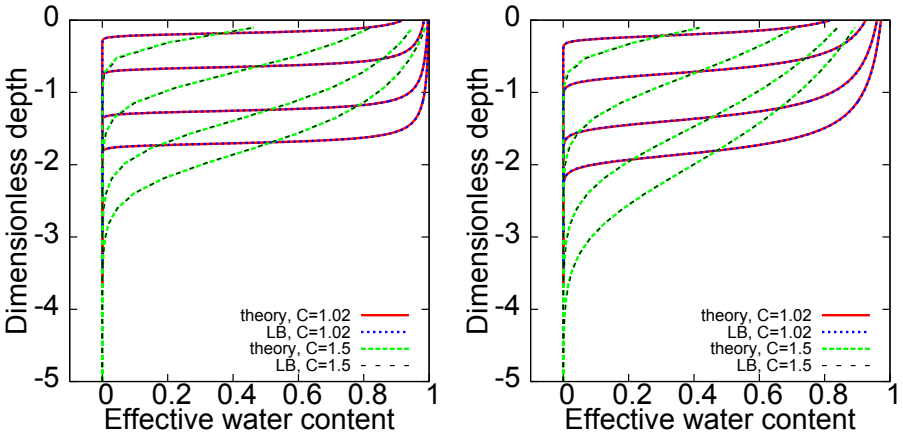

Figure 5.16: Temporal evolution $\tilde{\theta}(t_\star, -z_\star)$ during constant rate rainfall at dimensionless time $t_\star \approx 0.125, 0.5, 1.0, 1.375$ for $\mathcal{C} = 1.02$ ("sharp" profiles) and $\mathcal{C} = 1.5$ ("smooth" profiles). Left picture: $\beta_1 = 0$, $\beta_2 = 1$. Right picture: $\beta_1 = C/(C-1)$, $\beta_2 = -1/(C-1)$.

"Soil independent" solution. When $\beta_1 = 0$, the non-dimensional reference solution may be represented in soil independent form [23, 177]. The physical solution is governed by a selected value of the parameter $\mathcal{C}$. When $\beta_2 = 1$, the solution is:

$$\begin{aligned}
\partial_{t^+}\theta^+ &- \partial_{z^+}K^+ = \partial_{z^+}D^+(\theta^+)\partial_{z^+}\theta^+\ ,\ 0 \le \theta^+ \le \frac{1}{\mathcal{C}}\ , \\
\theta^+ &= \tilde{\theta}/\mathcal{C}\ ,\ z^+ = z_\star \mathcal{C}\ ,\ t^+ = t_\star m_0 = \tau/4\ , \\
K^+(\theta^+) &= \frac{K_r(\tilde{\theta})}{m_0} = \frac{{\theta^+}^2}{(1-\theta^+)}\ ,\ D^+(\theta^+) = \frac{D_\star(\tilde{\theta})\mathcal{C}^2}{m_0} = \frac{1}{(1-\theta^+)^2}\ , \\
\Psi(\theta^+) &= 1/(1-\theta^+)\ . \qquad (5.55)
\end{aligned}$$

The solution with the infiltration rate R^+ is a function of $\{t^+, z^+, R^+\}$ only. Analytical solution to Eq. (5.55) is given by relation (5.53) with $C_1 = 1$, $C_2 = -1$, $\tau =$

$4t^+$, $\rho = R^+/4$, $\rho_\star = \rho$, $R_\star = R^+ m_0$, $h_2 = (1+2\rho)$,$h_1/\sqrt{m} = -h_2$, $B_\star = h_2^2 - 1$:

$$\begin{aligned}
\theta^+(t^+,\zeta) &= (1 - \frac{1}{h_2 - u^{-1}\partial_\zeta u}) , \\
z^+ &= h_2\zeta - \ln[u] + h_2^2 t^+ , \; h_2 = (1+2\rho) , \; \rho = R^+/4 , \\
u &= \exp(-\frac{\zeta^2}{\tau})[u_1 + \frac{1}{2}(u_2 - u_3)] , \; g(x) = \exp(x^2)\mathrm{erfc}(x) , \\
u_1 &= \exp[a_+^2] , \; u_2 = g(b_+) + g(b_-) , \; u_3 = g(a_+) + g(a_-) , \\
a_\pm &= \frac{(\zeta \pm \rho\tau)}{\sqrt{\tau}} , \; b_\pm = \frac{(\zeta \pm \tau\sqrt{B_\star/4})}{\sqrt{\tau}} , \; B_\star = h_2^2 - 1 , \; \tau = 4t^+
\end{aligned} \tag{5.56}$$

The function $u(\zeta)$ being computed as above.

Exact time-dependent solution for variably saturated soil

An interesting class of the exact solutions is proposed by Barry et al [10] for variably-saturated Richard's equation. We extend them is for Brooks and Corey-Mualem hydraulic conductivity function [24, 143] (with β as an empiric parameter):

$$K_r(h) = (-\alpha h)^{-\beta} , \; \alpha = -1/h_s , \; h \le h_s . \tag{5.57}$$

The principal idea of this class of solutions consists in a specific relation between the retention curve and the relative conductivity function $K_r(h)$:

$$\begin{aligned}
\tilde{\theta}(h) &= \gamma \int_{-\infty}^{h} \frac{1}{h' + B} \partial_{h'} K_r(h') dh' , \; \gamma^{-1} = \int_{-\infty}^{h_s} \frac{1}{h' + B} \partial_{h'} K_r(h') dh' , \; h \le h_s , \\
\tilde{\theta} &= 1 , \; h \ge h_s ,
\end{aligned} \tag{5.58}$$

Under this condition, the solution in the unsaturated zone takes the form

$$h = \frac{a_1 + Z}{A(t)} - B , \; A(t) = 1 + W[-\exp(tK_s/\gamma - 1)] , \; h \le h_s , \; Z \ge 0 , \tag{5.59}$$

with Z positive downwards, a_1 and B being some constants and $W(x)$ being the upper portion of the Lambert function in infiltration case. The solution for $A(t)$ is obtained with the condition $A(0) = 0$, assuming that the flux is infinite at $t = 0$ (dry soil). Taking $\partial_t \tilde{\theta} \equiv 0$ in the saturated zone, the general solution inside this part of the domain becomes:

$$h = h_w(t) + M(t)Z , \; h \ge h_s , \; Z \ge 0 , \; h(t, Z = 0) = h_w(t) , \tag{5.60}$$

where $h_w(t)$ and $M(t)$ are some functions. The continuity of the pressure on the saturation front prescribes: $M(t) = 1/A(t)$, $h_w(t) = a_1/A(t) - B$. A simplest exact solution which is valid over both zones is given by $h_w(t) = 0$:

$$h = \frac{Z}{A(t)} \ , \ h(t, Z = 0) = 0 \ , \ B = 0 \ , \ a_1 = 0 \ , \quad \forall h \ . \tag{5.61}$$

Then the retention function (5.58) takes a form of the BCM model but λ is replaced here with $\beta + 1$:

$$h = h_s \tilde{\theta}^{\frac{-1}{\lambda}} \ , \ h \leq h_s \ , \ \lambda = \beta + 1 \ . \tag{5.62}$$

Differently selecting the starting point $t = t_0$, one can validate the numerical method either in unsaturated or in saturated domain, or both. The infiltration into variably saturated soil is demonstrated in Fig. 5.17. Exact solution (5.61) is used to set the initial and boundary conditions, with $h(t) = h(t, Z_0 = 0.6m)$ at the top and $h(t) = (H + Z_0)/A(t)$ at the bottom. The scaling factors are $\mathcal{L} = 1/100$ and $\mathcal{U} = 1$ for the computational and physical characteristic length and velocity, respectively. The computations are started at $t = t_0 = 0.1h$ when the pressure head at the bottom is about $-80\,m$. The results show that in the saturated zone ($t > 60h$) the error with respect to local steady state decreases approximately linear with the number of iterations. The pressure distribution is linear in the saturated zone but its slope varies in time. With a properly selected boundary value $h(\tilde{t})$, e.g., for the anti-bounce-back rule, the LBE solution in saturated domain is exact, provided that local steady state is reached.

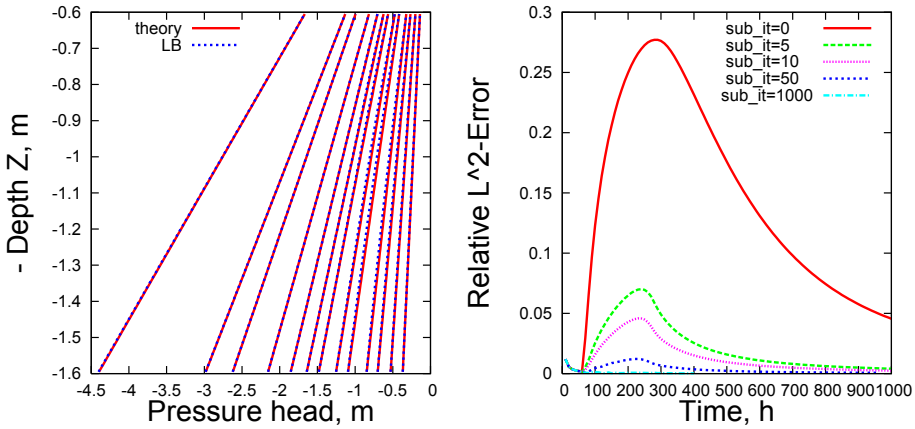

Figure 5.17: Pressure head profiles obtained with only 10 sub-steps in the saturated zone (see right picture) are compared to the exact solution (5.61). Left to right: $t/10 = 2,4,5,6,9,11,13,17,21,31,41,61,100$ h. Unsaturated flow ($t < 60h$), variably saturated flow ($t < 300h$) and fully saturated flow ($t > 300h$). The right picture compares the L^2-error without sub-iterations to those without sub-steps and with $5,10,50,1000$ sub-steps.

Chapter 6

Exact LBE solutions

Exact bulk analytical solutions of the evolution equation offer a deep understanding of the method. Although available analytical solutions for macroscopic conservation laws are mostly simple, the ”kinetic” equivalents, which are exact solutions of populations, are less trivial. When they are built, their exact numerical validation becomes possible either prescribing the exact solution for incoming populations or constructing exact (specific) boundary schemes. A special case we have met is when the closure relations are not exact but their mismatch with the populations in bulk has no any impact on the conserved quantities. Several exact solutions below illustrate these three situations. We conclude this work drawing the table of particular “magic” values which are derived in our studies.

6.1 Steady polynomial hydrodynamic solutions

When the bulk steady solutions for the macroscopic variable are given by the polynomial distributions in space, the Chapman-Enskog series (1.30)- (1.33) hold their non-equilibrium solution provided that they may satisfy the solvability conditions (1.7).

6.1.1 Couette and Poiseuille Stokes flow

For arbitrarily rotated channels in two dimensions (see sketch in Fig. 6.1), and periodic along the third coordinate axis, it is most suitable to look for the populations in the rotated coordinate system:

$$x' = x\cos\alpha + y\sin\alpha\ ,\ y' = -x\sin\alpha + y\cos\alpha\ . \tag{6.1}$$

“Simple” flows are either solutions in a “parallel” (“non-inclined”, $\alpha = 0^\circ$) or “diagonal” ($\alpha = 45^\circ$) channel. In simply-oriented channels, the distance to boundary

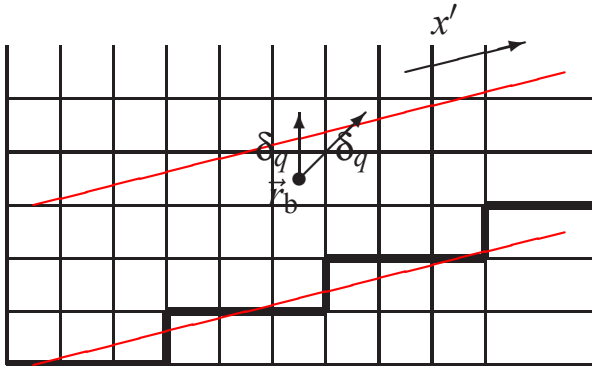

Figure 6.1: Inclined channel at regular grid with imaginary boundaries along the $x-$axis. A boundary surface cuts at $\vec{r}_{\rm b}+\delta_q\vec{c}_q$ the link between boundary node $\vec{r}_{\rm b}$ and an outside one at $\vec{r}_{\rm b}+\vec{c}_q$. This distance is used for linear or parabolic multi-reflection schemes. The bounce-back is commonly applied for stair-case discretization, which is plotted for the lower boundary.

δ_q takes equal values for all relevant cut links, and it is denoted hereafter δ. We look for translation invariant solutions $u_{x'}(y')=j_{x'}(y')/\rho_0$ for

Couette type flow:

$$\partial^2_{y'}u_{x'}=0\ ,\ u_{x'}(\pm\frac{H}{2})=u^{\pm}\ , \tag{6.2}$$

and Poiseuille flow:

$$\partial^2_{y'}u_{x'}=\nabla_{x'}P-F_{x'}\ ,\ u_{x'}(\pm\frac{H}{2})=0\ . \tag{6.3}$$

These flows are exact solutions of the evolution equation with the Stokes equilibrium, which is given by relation (1.42) with $g_S=0$, in arbitrarily rotated channels. The exact non-equilibrium solution can be found in [56, 60, 66]. It was first constructed for the MRT models (cf., relations (B.3) and (B.4) of [66]), and, with the argument of the rotational invariance of the relevant basis vectors, the exact populations are (again, with equal weights for all moving components):

$$\begin{aligned} g_S=0\ \ (\text{Stokes})\quad &: \\ f_q(y') &= t^\star_q[P(y')+(j_{x'}(y')-\frac{1}{2}F_{x'})c_{q\,x'}+\frac{\partial_{y'}j_{x'}(y')}{\lambda^+}c_{q\,x'}c_{q\,y'}] \\ &+ \frac{\nu}{\lambda^-}t^\star_q\partial^2_{y'}j_{x'}c_{q\,x'}(1-3c^2_{q\,y'})\ ,\ P=c_s^2\rho\ ,\ S^-_q=t^\star_qF_{x'}c_{q\,x'} \end{aligned} \tag{6.4}$$

Originally derived for the forcing driven flows in periodic (open) channels, the solution (6.4) is also valid for the constant pressure-drop driven flow ($\nabla_{x'}P=const$),

and for any linear combination of the pressure drop and forcing. The last term, which is related to the curvature) and all forcing terms vanish for the Couette flow. It is interesting that the mass of the outgoing populations does not return to the node of departure on the exact solution (6.4) in arbitrarily rotated channel (see Appendix A.2 of [60]). The equivalent link-wise form [75] of the solution, where the forcing is hidden in e_q^-, is:

$$\begin{aligned} g_S = 0 \ \text{(Stokes)} \quad &: \\ f_q(y') &= [e_q^+ + e_q^- + n_q^+ + n_q^-](y') \ , \ e_q^+ = P_q^\star(y') \ , \ P_q^\star = t_q^\star c_s^2 \rho(y') \ , \\ e_q^- &= j_q^\star + \Lambda^- F_q^\star \ , \ j_q^\star = t_q^\star j_{x'} c_{q\,x'} \ , \ F_q^\star = t_q^\star F_{x'} c_{q\,x'} \ , \ S_q^- = 0 \ , \\ n_q^+(y') &= n_q^{+(S)} = \frac{\partial_q j_q^\star(y')}{\lambda^+} \ , \ n_q^- = n_q^{-(S)} = \frac{\partial_q P_q^\star - \Lambda^+ \partial_q^2 j_q^\star}{\lambda^-} \ . \end{aligned} \tag{6.5}$$

Here, $n_q^{\pm(S)}$ denotes the Stokes non-equilibrium component, to be contrasted later to Navier-Stokes one. The bounce-back rule (3.1) plus the prescribed momentum quantity $w_q^{(u)} = -2\rho_0(\vec{u}(\vec{r}_w)\cdot\vec{c}_q)$ places the boundaries midway the normal outgoing link but only for the parallel and diagonal Couette flow. For Poiseuille flow this is achieved with the help of two solutions (3.3) for Λ^{eo}. Linear schemes, as the BFL rule and "magic" linear family MGLI($\alpha^{(u)}$) respect arbitrarily prescribed walls in Couette flow. The MGLI family also gets exact simply oriented Poiseuille flows of arbitrary width. This can be achieved with the TRT/MRT models owing to a special solution for Λ^{eo}:

$$\begin{aligned} \Lambda^{eo} &= \frac{3}{4}\delta^2 \ \text{for parallel flow , and} \\ \Lambda^{eo} &= \frac{3}{2}\delta^2 \ \text{for diagonal flow .} \end{aligned} \tag{6.6}$$

The effective width of the parallel flow is larger than the assumed one when $\Lambda^{eo} > \frac{3}{4}$. This solution is valid for forcing and pressure gradient driven flows using the "magic" schemes, owing to their parametrization properties. In contrast, two solutions are different using the schemes which are not exactly parametrized, as the BFL rule [20] and three population scheme [212]. This is demonstrated by relations (2.32) of [75] for respectively ULI/DLI and YLI schemes.

The solution (2.18) in [75] enables the MGLI schemes to get exact solutions for arbitrarily rotated Stokes Poiseuille flow. This can be achieved with any model (including the BGK) by applying the following expression for δ_q *when computing the coefficients of a given MGLI scheme*:

$$\delta_q \to \delta_q + \frac{\delta_q^2 - \frac{4\Lambda^{eo}}{3}}{H_q - 2\delta_q} \ , \ \forall \ \Lambda^{eo}. \tag{6.7}$$

Unlike the coefficients of the parabolic multi-reflection schemes, which are computed with the local distance δ_q, their solution with relation (6.7) depends on H_q, which is the channel width along the $q^{th}-$link. The LSOB schemes [60, 61] and the parabolic velocity schemes, MULI($\alpha^{(u)}$) and MGMR(C) families, which are described in Section 3.3.2, get exact Couette and Poiseuille flows in arbitrarily rotated channels, but compromising (in case of the $M_q^{(u)}$ schemes) the link-wise implementation for diagonal corner links which are commonly present in stair-wise discretization on the cuboid computational grid, see Fig. 6.1 and [74, 75].

When the pressure drop is imposed at the channel ends, one gets the same solution as in a periodic channel provided that the established pressure gradient is constant. This can be achieved for any distance to inlet/outlet with the help of the mixed schemes $M_q^{(m)}$, when they combine the parabolic pressure schemes from the PMR(k) family (see Table 3.2) and the parabolic $M_q^{(u)}-$schemes. In simple channels, the linear schemes, or even the bounce-back scheme with the correction given by relation (3.4) of [75], are sufficient as the $M_q^{(u)}$ components of the mixed scheme.

Altogether, arbitrarily rotated Stokes Couette and Poiseuille flows are exact bulk solutions of the method. In open simple channels, they are exact numerical solutions of the TRT/MRT schemes with the MGLI boundary schemes when Λ^{eo} is selected with relations (6.6). In arbitrarily rotated channels, they are exact solutions of the BGK/TRT/MRT schemes with the parabolic multi-reflections, for any Λ^{eo}, and with the MGLI schemes using the definition (6.7). When a given link-wise velocity scheme is not exact for these flows in a simply-oriented open channel, one shifts the effective location of the solid walls but the velocity profile, either linear or parabolic, is correct and invariant along the boundary. This situation changes for the rotated walls where the accommodation (Knudsen-type) boundary layers appear. Their numerical solutions are examined in [60] for the bounce-back rule. The analytical solutions are available only in the "global" form prescribed above by relations (2.24)- (2.25), which depend on the bulk solution via the closure relations at each extremity (see $\delta g_q^{\pm}(\vec{r}_{b_2})$ and $\delta g_q^{+}(\vec{r}_{b_1})$).

6.1.2 Flows in pipes

One-dimensional flows in a pipe of circular or triangular cross-sections are among the rare flows with polynomial velocity distributions. The solution of the Poisson equation in a circular pipe of radius R with a flow direction along the $x-$axis is:

$$u_x = -\frac{F_x}{4\nu}(r^2 - R^2)\ ,\ r^2 = y^2 + z^2\ ,\ 0 \le r \le R\ . \tag{6.8}$$

This solution extends the channel Poiseuille flow to three-dimensions. Again, the parabolic profile (6.8) is an exact solution of the LBE Stokes scheme, e.g., based on the LSOB approach or parabolic multi-reflection schemes. The relation (6.5) gives the populations in this flow, with the help of the substitutions: $x' \to x$ and $y' \to (y,z)$. This solution can also be expressed in circular coordinates. Actually, the numerical computing of the exact link-wise expansion is simpler using suitable (exact) link-wise finite-difference operators (as relations (2.7)) directly on the prescribed velocity field.

The solution for triangular (equilateral) pipe is borrowed from [129]. Let h be the side of equilateral triangle; then the velocity $u_x(y,z)$ is proportional to product of three heights values, $h_1(y,z)$, $h_2(y,z)$ and $h_3(y,z)$, dropped from the point (y,z) to the sides of triangle:

$$u_x(y,z) = \frac{2}{\sqrt{3}h}\frac{F_x}{\nu}h_1(y,z)h_2(y,z)h_3(y,z)\ . \tag{6.9}$$

The velocity field is expressed as a third order polynomial in space and the steady state Chapman-Enskog expansion (1.33) gives the exact solution, which is prescribed by relation (6.5), where $\partial_q j_q^\star(z')$ is replaced with $\partial_q j_q^\star(y,z) + (\Lambda^{eo} - \frac{1}{12})\partial_q^3 j_q^\star$. The term with the third order derivatives vanishes when $\Lambda^{eo} = \frac{1}{12}$, in agreement with relation (1.34).

In their actual form the $M_q^{(u)}-$schemes are not exact for the third order polynomial velocity profiles (except when $\Lambda^{eo} = \frac{1}{12}$) and their extension to them needs some efforts. On the same time, the improved LSOB node-based scheme [61] (illustrated in Appendix A.1 of [60]) was able to do this rather simply, extending the list of the locally unknown derivatives. The critical point is to keep the uniqueness of the solution in the presence of sharp corners. Altogether, the solutions in pipes with complex cross-sections provide worthwhile numerical tests for singular geometries.

6.1.3 Two phase Couette and Poiseuille flows

Exact piece-wise linear and piece-wise parabolic solutions for two phase Couette and Poiseuille flows with a planar interface

$$\begin{aligned} \mu^{(R)}\Delta\vec{u}^{(R)} &= -F^{(R)}\ ,\ y < y^{(I)}\ , \\ \mu^{(B)}\Delta\vec{u}^{(B)} &= -F^{(B)}\ ,\ y > y^{(I)}\ , \end{aligned} \tag{6.10}$$

are useful for understanding the LBE immiscible models. The surface tension should not then play any role for flat interface ($y = y^{(I)}$), where the Stokes equations (6.10) are constrained by the continuity of the velocities and normal shear

stress tensor components. The interface conditions are given by relations (4.9) where $u_z \equiv 0$. Exact LBE solutions were first constructed in [57] and summarized in Table 1 of [58] for implicit (Model 1) and semi-explicit (Model 2) interface tracking. Their link-wise analysis for the TRT operators can be respectively found in Sections 4.1.3 and 4.2.4 of [72]. The population solution is given again by relations (6.4) and (6.5), where the eigenvalues are set by the collision parameters of each of two phases.

Figure 6.2: Two phase Poiseuille flow is obtained with **implicit interface tracking** and the bounce-back, for $\nu^{(R)}/\nu^{(B)} = 10^2$, $F^{(B)}/F^{(R)} = 10$. The pictures plot the reduced, by the interface value, horizontal momentum $j_x/j_x(y^{(I)})$, for a range of Λ^{eo} values. Data: $\Lambda^{+(R)} = 1$, $\Lambda^{+(R)}\Lambda^{-(R)} = \Lambda^{-(B)}\Lambda^{-(B)}$, $F^{(R)} = 5 \times 10^{-4}$ on the coarse grid (left picture) and $F^{(R)} = \frac{5}{4} \times 10^{-4}$ on the fine grid (right picture). *The solution is exact when* $\Lambda_{eo} = \frac{3}{16}$ *in agreement with the boundary and interface analysis.*

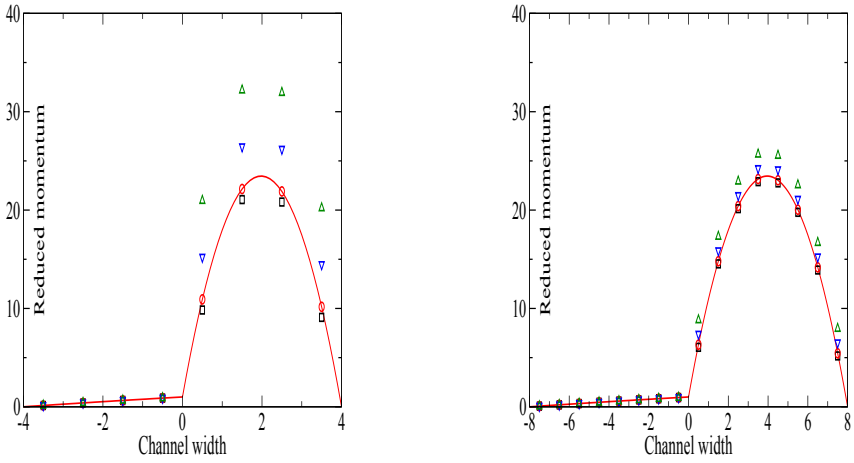

Implicit interface tracking.

The populations simply traverse the interface and enter into collision with the populations of other phase. First-order accurate continuity conditions on the static interface (midway the interface links) are recalled by relations (4.11) to (4.13) in Chapter 4. They enforce the continuity of the equilibrium momentum variable and the continuity of stress components, j_x and $\nu\partial_z j_x$ here. Selecting equal values for free parameters, $\lambda^{-(R)} = \lambda^{-(B)}$, and locating the interface midway the link, the solution is exact for piece-wise linear velocity profiles and piece-wise parabolic profiles when two forcing are equal. When $F^{(R)} \neq F^{(B)}$, exact piece-wise parabolic

solution requires to set:

$$\Lambda^{eo(R)} = \Lambda^{eo(B)} = \frac{3}{16}\,. \tag{6.11}$$

In fact, the Taylor form of the interface link-wise closure relations for the parabolic flow is the same as for the bounce-back condition, for any viscosity and forcing ratios. Then the interface and bounce-back "magic" solutions coincide, for the parallel and, quite likely, for the diagonal flows (cf. relations (3.3)), and the the bounce-back gets exact solutions. The role of the magic parameter is illustrated in Fig. 6.2. In general, these and semi-explicit interface (exact) numerical solutions require the exact boundary schemes which are described above for one phase flow. Taking $c_s^{2(\mathrm{R})} \neq c_s^{2(\mathrm{B})}$, the steady solution remains the same, and given by relations (6.4) and (6.5) with $P^{(\mathrm{R})} = P^{(\mathrm{B})}$, but the derived velocity $u_x^{(R)} = j_x/\rho^{(R)}$ and $u_x^{(B)} = j_x/\rho^{(B)}$ becomes discontinuous on the interface.

Semi-explicit interface tracking.

The special (interface) collision operator is applied in the grid nodes where two phases coexist (see picture 6.3). The interface values of the equilibrium components, forcing and relaxation parameters, are derived from the continuity conditions. These conditions are summarized by relations (81) to (84) of [72]. They adjust the continuity of the tangential shear stress component $\nu\partial_z j_x$ with the help of the harmonic mean value for the interface kinematic viscosity:

$$\nu^{(I)} \;=\; \frac{2\nu^{(R)}\nu^{(B)}}{\nu^{(R)}+\nu^{(B)}}\,. \tag{6.12}$$

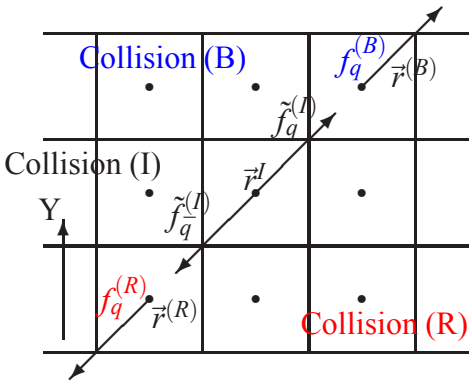

Figure 6.3: Sketch for explicit interface tracking.

When the forces are equal, one can again take equal (arbitrary) free eigenvalues, $\lambda^{-(R)} = \lambda^{-(B)} = \lambda^{-(I)}$. Otherwise, if the interface forcing value is set equal

to arithmetic mean of bulk quantities, then the interface value $\Lambda^{eo(I)}$ should be set equal to $\frac{3}{8}$, then both $\lambda^{-(R)}$ and $\lambda^{-(B)}$ values are set equal to $\lambda^{-(I)}$. This set-up yields the exact piece-wise parabolic solutions for any viscosity and forcing ratios in all bulk points, *bot not on the interface itself*. We stress that the interface tangential momentum components, $\vec{j}_x^{(I)} = \sum_{q=1}^{Q-1} f_q^{(I)} c_{qx}$ differ from the expected continuous (mean) value of bulk components: $\frac{(j_x^{(R)} + j_x^{(B)})}{2} = j_x^{(R)}(y^{(I)}) = j_x^{(B)}(y^{(I)})$. The momentum value derived from the interface populations is:

$$j_x^{(I)} = [\frac{(j_x^{(R)} + j_x^{(B)})}{2} + \frac{\delta j_x}{4}](y^{(I)}) \; , \; \delta j_x = [\partial_y j_x^{(B)} - \partial_y j_x^{(R)}](y^{(I)}) \; . \tag{6.13}$$

This tells us that the equating of the macroscopic values to conserved moments should be used with a care (or avoided) on the interfaces.

6.1.4 Channel solution beyond the Chapman-Enskog expansion

The exact solution for parallel Poiseuille flow modeled with the non-linear equilibrium term $E_q^{(u)}(\vec{j}, \rho_0)$ is constructed in Section 3.2.1 of [75]. We show that the solution gets a Knudsen-type correction $\delta g_q^{\pm}$, given in general form by relation (2.24), which compensates the mismatch in the closure relations. This solution is quantified exactly for several principal boundary schemes: bounce-back, linear interpolations and the parabolic schemes. This correction has no projections on mass and momentum for parallel flow. Let us build this solution.

In the presence of the non-linear equilibrium term $E_q^{(u)}$, the Chapman-Enskog solution is decomposed into two parts: the Stokes component $g_q^{\pm(S)} = \lambda^{\pm} n_q^{\pm(S)}$ (where $n_q^{\pm(S)}$ is given by relations (6.5)) and the Navier-Stokes component $g_q^{\pm(NS)}$, given by the terms $g_q^{+(2)} + g_q^{+(4)}$ and $g_q^{-(1)} + g_q^{-(3)}$ in relations (1.31)- (1.33). Taking $S_q^- = 0$ (the forcing is put into equilibrium) and $\alpha_{\varepsilon^\star} = 0$ (the standard equilibrium), this solution is:

$$\begin{array}{lcl} g_q^{\pm ch} & = & g_q^{\pm(S)} + g_q^{\pm(NS)} \; , \; g_q^{\pm(S)} = \lambda^{\pm} n_q^{\pm(S)} \; , \\ g_q^{+(S)} & = & \partial_q j_q^{\star}(y) \; , \; g_q^{-(S)} = \partial_q P_q^{\star} - \Lambda^{+} \partial_q^2 j_q^{\star} \; , \; P_q^{\star} = t_q^{\star} P \; , \\ g_q^{+(NS)} & = & \rho_0 T_q H^{+}(y) c_{qy}^2 \; , \; g_q^{-(NS)} = \rho_0 T_q H^{-}(y) c_{qy} \; , \; T_q = t_q^{\star}(3c_{qx}^2 - 1) \; , \end{array} \tag{6.14}$$

where

$$\begin{array}{lcll} E_q^{(u)}(y) & = & \frac{\rho_0 u_x^2(y)}{2} T_q & , \quad u_x(y) = \frac{j_x(y)}{\rho_0} \; , \\ H^{-}(y) & = & H^{-(1)}(y) + H^{-(3)}(y) & , \quad H^{+}(y) = H^{+(2)}(y) + H^{+(4)}(y) \; , \\ H^{-(1)} & = & u_x \partial_y u_x & , \quad H^{-(3)} = 3(\Lambda_{eo} - \frac{1}{12})(\partial_y u_x \partial_y^2 u_x) \; , \\ H^{+(2)} & = & -\Lambda^{-}(u_x \partial_y^2 u_x + (\partial_y u_x)^2) & , \quad H^{+(4)} = -3\Lambda^{-}(\Lambda_{eo} - \frac{1}{6})(\partial_y^2 u_x)^2 \; . \end{array}$$

The exact no-slip scheme for the solution (6.14)–(6.15) must fit $O(\partial_y^4 u_x^2)$. However, although no one velocity scheme possesses such an accuracy, the macroscopic velocity solution in *open channel* is the same as one obtained with the Stokes equilibrium for all considered $M_q^{(u)}$ schemes (including the bounce-back and the BFL rules). Let us ask ourselves : why ?

The solution below answers the question. Actually, the correction $\delta g_q^{\pm}(y)$, hereafter called "Knudsen layer", appears in populations:

$$g_q^{\pm ch}(y) \;=\; g_q^{\pm (S)}(y) + g_q^{\pm (NS)}(y) + \delta g_q^{\pm}(y)\,. \tag{6.15}$$

Writing the solution in the form (6.15) we keep in mind that the bulk solution $g_q^{\pm (S)}(y) + g_q^{\pm (NS)}(y)$ is extended for boundary nodes, then we are looking for correction $\delta g_q^{\pm}(y)$ *with respect to this solution*. This decomposition is natural but it is not unique. Indeed the boundary schemes prescribe the closure relation in a form of the linear combination of the symmetric and anti-symmetric non-equilibrium components, where the individual contributions of bulk and accommodation solutions are linked.

The correction $\delta g_q^{\pm}(y)$ satisfies equation (2.11) and takes the form:

$$\delta g_q^{+} \;=\; \rho_0 T_q K^{+}(y) c_{qy}^2\,,\; \delta g_q^{-} = \rho_0 T_q K^{-}(y) c_{qy}\,, \tag{6.16}$$

where

$$K^{\pm}(y) \;=\; k_1^{\pm} r_0^{z} + k_2^{\pm} r_0^{-z}\,, r_0 = \frac{2\sqrt{\Lambda^{eo}}+1}{2\sqrt{\Lambda^{eo}}-1}\,,\; \Lambda^{eo} \neq \frac{1}{4}\,,\; \Lambda^{eo} \neq 0\,, \tag{6.17}$$

and the coefficients $k_1^{\pm}$ and $k_2^{\pm}$ are related as (the "upper" and "down" relations (6.18) are equivalent using the definition of r_0)

$$k_1^{\mp} \;=\; 2\Lambda^{\pm} k_1^{\pm} \frac{1-r_0}{1+r_0}\,,\; k_2^{\mp} = 2\Lambda^{\mp} k_2^{\pm} \frac{r_0-1}{1+r_0}\,. \tag{6.18}$$

When $\Lambda^{eo} = \frac{1}{4}$, the accommodation is non-zero only in the boundary nodes $y = y_b^{\pm}$:

$$\begin{aligned} \Lambda^{eo} = \frac{1}{4} \;:\; K^{\pm}(y_b^{-}) \;&=\; k_1^{\pm}\,,\;,\; K^{\pm}(y_b^{+}) = k_2^{\pm}\,, \quad k_1^{-} = 2\Lambda^{+} k_1^{+}\,,\;,\; k_2^{-} = -2\Lambda^{+} k_2^{+}\,, \\ K^{\pm}(y) \;&=\; 0\,,\; y_b^{-} < y < y_b^{+}\,. \end{aligned} \tag{6.19}$$

Two remaining coefficients in relations (6.18) and (6.19) are set by the closure relations at two boundary nodes $y = y_b^{\pm}$. These relations are elaborated for the bounce-back, "magic" linear and quadratic schemes, and the MR1 scheme (see relations (3.18) and (3.19) in [75]), then confirmed on the numerical solutions.

Figure 6.4: Normalized symmetric components $K^{\pm}(y)/H^{\pm}(0)$ of the Knudsen layer solution is plotted for two discretizations of the parabolic Poiseuille flow. The numerical solution is exactly located on the analytical curve (6.17). The closure relation correspond to parabolic MULI scheme used in these computations. The accomodation oscillates when $\Lambda^{eo} < \frac{1}{4}$. When $\Lambda^{eo} = \frac{1}{4}$, it vanishes for all bulk points (see symbols). Data: $\nabla_x P = 0$, $\nu = 1$, $F_x = 10^{-3}$ (coarse grid) and $F_x = \frac{1}{8} \times 10^{-3}$ (fine grid).

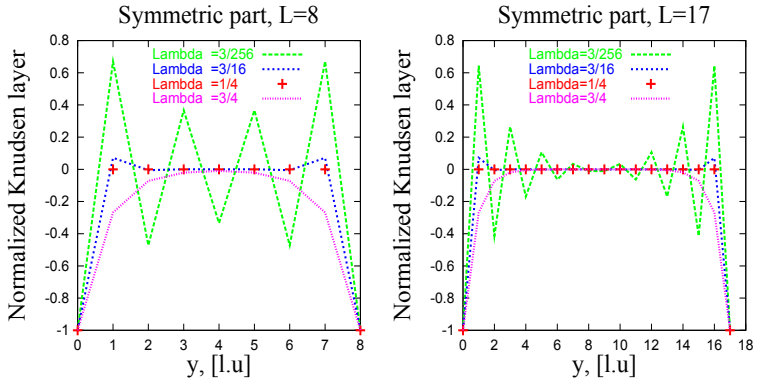

This particular accommodation solution does not have any impact on the pressure and velocity provided that the same (or equivalent) $M_q^{(u)}-$scheme is applied for all incoming links at a given wall, their closure relations being *equivalent for all those cut links*.

In summary, this solution confirms an existence of the non-equilibrium accommodation layers which are not described by the Chapman-Enskog solution. They reduce exponentially away the walls and do not impact the parallel parabolic flow using the common hydrodynamic boundary schemes. A way to quantify their impact in rotated channels is still to be found. The solution above reduces to Couette flow dropping the two last terms in expansion (6.15), $H^{-(3)}$ and $H^{+(4)}$.

6.1.5 Navier-Stokes flows in inclined channels

The possibilities to reach the one-dimensional (translation invariant) solution $j_{x'}(y')$ and constant pressure distributions in arbitrarily rotated periodic channels based on the Navier-Stokes-type equilibrium function are examined in Appendix B of [76]. Assuming that this solution exists, then the non-equilibrium populations are given by the fourth-order accurate expansion (6.14)-(6.15), replacing there $x \to x'$ and $y \to y'$ and, in the presence of the free equilibrium parameter $\alpha_{\varepsilon^\star}$ (see relation (1.42)), replacing $t_q^\star(3c_{qx}^2 - 1)$ by $t_q^\star(3c_{qx}^2 - 1) - 2\alpha_{\varepsilon^\star}\varepsilon_q^\star$. The equivalent di-

rectional finite-difference form of these relations is derived from the recurrence equations in Appendix B of [76]. Then we take the moments of this solution and check them with respect to solvability conditions (1.13). We find that they can be satisfied on the rotated Couette profile, but not for the Poiseuille profile, in general. In fact, the condition of mass conservation, $\sum_{q=0}^{Q-1} g_q^+(y)$ and the condition of momentum conservation $\sum_{q=1}^{Q-1} g_q^-(y) c_{qy'}$ in diagonal and arbitrarily rotated parabolic flow are consistent only for a particular value of free equilibrium parameter $\alpha_{\varepsilon^\star}$ (see relation (1.42)):

$$\alpha_{\varepsilon^\star} = -\frac{1}{k_{\varepsilon^\star}} \, , \; k_{\varepsilon^\star} = 24 \, . \tag{6.20}$$

We assume here that the components of fourth order polynomial vectors $\varepsilon_q^\star$ as given in Section 1.5.1, otherwise $\alpha_{\varepsilon^\star} = -\frac{1}{C k_{\varepsilon^\star}}$ if $\varepsilon_q^\star$ is multiplied with C. Except the parallel and diagonal channels, the momentum equation $\sum_{q=1}^{Q-1} g_q^-(y) c_{qx'} = F_{x'}$ is consistent only when the third-order terms vanish in the expansion (see $H^{-(3)}$ term in relations (6.15)), i.e., if only:

$$\Lambda^{eo} = \frac{1}{12} \, . \tag{6.21}$$

Again, one can build exact numerical solution using relations (6.20) and (6.21) with help of exact incoming populations. We believe that this example is quite important. It shows that even if the macroscopic solution is given by the polynomial distribution, its exact LBE solution may not exist when the Chapman-Enskog expansion cannot satisfy the solvability conditions of the prescribed solution. Otherwise speaking, not every polynomial distribution is compatible with the LBE discretization scheme.

6.1.6 Linear velocity/parabolic pressure solution

The inverse situation, when the exact velocity solution is linear and pressure distribution is parabolic, represents exact steady solution of the incompressible Navier-Stokes equation:

$$\begin{aligned} u_x(x,y) &= ax + by \, , \; u_y(x,y) = bx - ay \, , \\ P(x,y) &= P^{ex}(x,y) \, , \; \vec{F}(x,y) \equiv 0 \, , \text{ or} \, , \\ \vec{F}(x,y) &= -\nabla P^{ex}(x,y) \, , \; P \equiv P_0 \, , \\ P^{ex}(x,y) &= P_0 - \rho_0 \frac{(a^2+b^2)}{2}(x^2+y^2) \, . \end{aligned} \tag{6.22}$$

This solution (without forcing) was used to validate the accuracy of the boundary conditions in [112]. The exact Dirichlet velocity and pressure schemes are specified in Section 3.3.1 of [75]. They enabled us to validate the multi-reflection at the third order, when these particular schemes maintain the curvature of pressure distribution and a linear variation of the forcing (the both are the components of the non-equilibrium term $g_q^{+(2)}$). However, these schemes are not robust in general. Also, using any non-exact but correctly parametrized boundary scheme for this example, one can easily check the parametrization properties described in Section 2.4.3: the dimensionless pressure and velocity solutions on the fixed grid, hence their errors with respect to the exact solution, should not change at given Reynolds and Λ^{eo} values when the characteristic (e.g., boundary) velocity values and viscosity vary.

6.1.7 "Solid rotation" solution

The following solution to incompressible Navier-Stokes equation is interesting in the context of the LBE evolution equation:

$$\begin{aligned} \vec{u}(x,y) &= \vec{u}^{\tau}(r)\ ,\ \vec{u}^{\tau}(r) = \Omega\vec{i_z}\otimes\vec{r}\ ,\ \text{i.e. } u_x^{\tau} = -\Omega y\ ,\ u_y^{\tau} = \Omega x\ , \\ P(x,y) &= P_0 + \rho_0\frac{\Omega^2 r^2}{2}\ ,\ r^2 = x^2+y^2\ . \end{aligned} \tag{6.23}$$

It is shown in Appendix A of [74] that the populations are constant along any link and equal to their local equilibrium value:

$$\begin{aligned} e_q^{\pm}(x+c_{qx},y+c_{qy}) &= e_q^{\pm}(x,y)\ ,\ \text{then} \\ f_q^{\pm}(x,y) &= e_q^{\pm}(x,y)\ ,\ g_q^{+}\equiv 0\ ,\ g_q^{-}\equiv 0\ ,\forall\ \{x,y\}\ ,\ \forall q\ . \end{aligned} \tag{6.24}$$

Any boundary scheme, which is accurate with respect to the equilibrium components, gets this solution exactly. In the moving coordinate system $\vec{u}^m(r) = \vec{u}(r) - \vec{u}^{\tau}(r)$, the velocity is equal to zero, $\vec{u}(x,y)\equiv 0$, the pressure (6.23) can be then obtained with the help of the centrifugal force:

$$\vec{F}(x,y) = \rho_0\Omega^2\vec{r}\ ,\ \nabla P = \vec{F}\ . \tag{6.25}$$

Only properly parametrized schemes maintain this solution, owing to equivalence of their closure relations with respect to the pressure gradient and forcing (see in Section 3.3.1).

6.2 Parallel and diagonal Brinkman flow

The Brinkman flow in a channel parallel to arbitrarily inclined $x'-$axis obeys the equation (5.6). The solution for $j_{x'} = \rho_0 u_{x'}$ is governed by the ratio F_0:

$$j_{x'}(y') = k_1 e^{2By'} + k_2 e^{-2By'} \ , \ B = \frac{\sqrt{F_0}}{2} \ , \ F_0 = \frac{F_c}{\nu_e} \ , \tag{6.26}$$

where the coefficients k_1 and k_2 are fixed by the boundary conditions. Exact solution of the TRT scheme satisfies equation (5.9) and takes the form:

$$j_{x'}(y') \quad = \quad k_1 r^{y'} + k_2 r^{-y'} \ , \tag{6.27}$$

$$\text{where} \quad r^{\Theta} = s \ , \ s = \frac{1+P}{1-P} \ , \ P^2 = \frac{b^2\Theta^2}{1+b^2\Theta^2} \ . \tag{6.28}$$

Here, s is a root of the equation $s^2 - 2s(2b^2\Theta^2+1) + 1 = 0$, $\Theta^2 = 1$ for parallel flow and $\Theta^2 = \frac{1}{2}$ for diagonal flow, and P is given in relations (5.9). This numerical solution is equal to the exact solution (6.26) when $r = e^{2B}$, i.e.,

$$P \quad = \quad \tanh\left[B\Theta\right] . \tag{6.29}$$

One may satisfy this equation either with a special solution for $F_0^{num}(B, \Lambda^{eo}, \Theta)$ (formulas (32) of [76]) or with the specific function $\Lambda^{eo}(B,\Theta)$:

$$\Lambda^{eo}(B,\Theta) \quad = \quad \frac{3(1 - B^2\Theta^2 \coth^2\left[\Theta B\right])}{4B^2(1-3\Theta^2)} \ , \text{ when } F_0^{num} = F_0 = 4B^2 \ . \tag{6.30}$$

These solutions can be used to validate the code computing the incoming boundary populations with the exact solution (see relations (22),(A.3) of [76]):

$$n_q^-(y') = \frac{3}{\lambda^-} c_{q\,y'}^2 F_q^\star(y') \ , \ n_q^+(y') \quad = \quad \frac{(1+\bar{\delta}\nu_e)}{\lambda^+} \bar{\Delta}_q j_q^\star(y') \ , \tag{6.31}$$

where $\bar{\delta}\nu_e$ is given by relation (5.9). Alternatively, one may use special exact boundary schemes, as the MR1 scheme [66, 74] for $\delta_q = 0$, but they are restricted to node location of the walls in parallel flow. It is recommended to verify the whole set-up stating from the exact initialization of populations, because of possible degeneration of the solutions using these exact schemes.

Finally, we emphasize that the effective TRT macroscopic solution remains the same in the presence of the Navier-Stokes equilibrium term only in parallel channel. Like for the Poiseuille flow, the exact diagonal flow becomes possible only for one particular configuration of the non-linear term, given by the solution (6.20). Altogether, these solutions extend the class of the exact LBE solutions to exponential velocity distribution in the presence of space variable forcing.

6.3 Solutions for the AADE

6.3.1 Linear and parabolic solutions

The linear and parabolic solutions for one velocity component $u_{x'}(y')$ in the arbitrarily inclined channels keep their form for diffusion equations replacing $u_{x'}(y')$ with the diffusion variable $\mathcal{D}(s)$ and the forcing with the mass source quantity $M(y')$, then

$$-M(y') = \partial_\alpha K'_{\alpha\beta} \partial_\beta \bar{\mathcal{D}}(s) \; . \tag{6.32}$$

The diffusion tensor is not restricted to be isotropic: the irrelevant coefficients do not have any impact for translation invariant solutions. The boundary schemes for the AADE can be designed then with the same methodology as for the hydrodynamic solutions. Along these lines, first multi-reflection type diffusion schemes, discussed in the Section 3.3.6, were validated for linear and parabolic distributions of the diffusion variable (see sections 8.2.1 and 8.2.2 of [70]). The anti-bounce back scheme gets exact parabolic solution provided that the macroscopic solution is redefined with $\frac{1}{2}M$, then using the following equilibrium and collision configuration:

$$c_e = \frac{1}{3} \; , \; S_q^+ = \frac{1}{3} t_q^\star M \; , \; \bar{\mathcal{D}}(s) = s \; , \; s = \rho^{\text{eq}} + \frac{M}{2} \; , \; \text{and} \quad \Lambda^{eo} = \frac{3}{16} \; . \tag{6.33}$$

Using again the equilibrium distribution (1.48), and without any redefinition of the conserved quantity, the anti-bounce back scheme is exact only when the source correction $-\frac{2}{\lambda^+} S_q^+$ is removed "by hand" from the closure relation :

$$s = \rho \; , \; f_q^{\text{p.c.}(p)} = -\frac{2}{\lambda^+} S_q^+ \; , \; \text{and} \; \; \Lambda^{eo} = \frac{1}{8} \; , \; \forall \, c_e \; . \tag{6.34}$$

This solution was proposed in [69], when the shifting with the half mass quantity was not yet defined. The linear and parabolic equivalents of the hydrodynamic solutions are useful for validation of the Dirichlet boundary schemes in the presence of mass source quantity.

6.3.2 Heterogeneous saturated vertical flow

The vertical saturated flow in heterogeneous media is a primary test of the continuity relations. We consider piece-wise linear and parabolic distributions of pressure head variable $h(y)$ which obeys equation (6.32) in each horizontal layer i of the vertical column, with $M = 0$ for linear solutions and $M = M^{(i)}$ for parabolic solutions. Both pressure head and normal flux $\vec{u}^{(i)} = -\mathbf{K}^{(i)} \nabla h^{(i)}$ should be continuous

on the soil boundaries; then the vertical Darcy velocity u_y is constant on the piece-wise linear profile $h^{(i)}(y)$. The boundary pressure values can be prescribed exactly midway the grid nodes using the anti-bounce back rule for the linear solution and with the parabolic, diffusion or pressure, schemes for the parabolic distributions. Of course, this test is suitable for any one-dimensional solution with heterogeneous diffusion coefficients.

Implicit interface tracking

The necessary conditions for pressure continuity on the flat horizontal implicit interface are given by the relations (4.18). The TRT-E and L models, described in Section 1.6.4, yield them with so-called "vertical strategies" for eigenvalues and free parameters. They are given respectively by relations (94) and (95) in [72] and relations (B.8) and (B.13) in [73]. Using the vertical strategy, the L model holds then condition (4.24), $\Lambda_q^{-(i)}/\Lambda_q^{-(j)} = K_{zz}^{(i)}/K_{zz}^{(j)}$, for all vertical links. This condition is valid also for the eigenvalue functions $\Lambda_q^{-(i)}$ and $\Lambda_q^{-(j)}$ assigned to the diagonal links provided that the off-diagonal elements $K_{\alpha\beta}^{'(i)}$ either vanish or are proportional to $K_{zz}^{(i)}$.

The vertical strategy of the TRT-E model is based on the necessary condition (4.19). It appears that this condition is also sufficient for the vertical flow: the interface accommodation terms have no trace on the pressure and flux distributions. In contrast, when the necessary condition is not respected, the solution is discontinuous on the interface, even if the obtained vertical flux is constant. This is illustrated on the left picture in Figure 4.2.

The formula (99) of [72] for $\Lambda^{eo(i)}$ extends the piece-wise linear profiles to piece-wise parabolic solutions, in the presence of the mass source $M^{(i)}$. This solution assigns the special $\Lambda^{eo(i)}$ values, which become equal to $\frac{3}{16}$ using the equilibrium set-up (6.33) for each layer. Then the anti-bounce-back is able to maintain the parabolic solution exactly. The equal values $\Lambda_q^{eo(i)}$ for all links are available only with the TRT-E model, in general (anisotropic) case.

Semi-explicit tracking

Tracking of the interface boundary with the special collision matrix is examined in Section 5.2 of [72]. The interface update rules (eigenvalues, equilibrium, sources) are determined here by formulas (120)-(124) such that the continuity conditions for the vertical saturated flow are exact. When the bulk collision configurations are selected with the vertical strategies, the interface vertical component $K_{zz}^{'(I)}$ becomes equal to the harmonic mean value, for both TRT-E and L models (see relations

(115)-(117) and (123)-(124) in [72]):

$$K_{zz}^{'(I)} = \frac{2K_{zz}^{'(i)}K_{zz}^{'(j)}}{K_{zz}^{'(i)} + K_{zz}^{'(j)}} \, . \tag{6.35}$$

This is likewise as the well known vertical approximation for the inverse of the resistance coefficient (e.g., in [15]). However, likely for the hydrodynamic velocity on the interface between two immiscible fluids, the interface pressure solution (obtained as a local population mass) differs from its continuous value (cf. relation (6.13)):

$$h'^{(I)} \quad = \quad (\frac{(h'^{(i)} + h'^{(j)})}{2} + \frac{\delta h'}{4})(y^{(I)}) \, , \; \delta h' = (\partial_z \bar{\mathcal{D}}^{(j)} - \partial_z \bar{\mathcal{D}}^{(i)})(y^{(I)}) \, . \tag{6.36}$$

The deficiency term vanishes only when the vertical diffusion coefficients are homogeneous. Once again, one should be careful about the precision of the conserved and diffusion variables obtained on the interfaces.

The formula (119) of [72] for interface value $\Lambda^{eo\,(I)}$ extends the piece-wise linear solutions to piece-wise parabolic, in the presence of the mass source $M^{(i)}$, then $\Lambda^{+(R)} = \Lambda^{+(B)} = \Lambda^{+(I)}$. This solution reduces to two phase Poiseuille flow solution, $\Lambda^{+(I)} = \frac{3}{8}$ when the mass quantity and then linear diffusion variable are redefined with half of mass source quantity, using again the equilibrium set-up (6.33).

6.3.3 "Optimal rule": linear convection-diffusion solution

Let us consider linear stationary 1D convection diffusion problem

$$\nu \frac{\partial^2 s}{\partial y'^2} - UH \frac{\partial s}{\partial y'} = 0 \, , \; U > 0 \, , \; 0 \leq y' = y/H \leq 1 \, , \; s(0) = 1 \, , \; s(1) = 0, \tag{6.37}$$

The exact LBE solution was found in [87] for two-dimensional Navier-Stokes configuration, with $s(y)$ being the solution for $u_x(y)$ and U for $u_y(y)$, with ν as kinematic viscosity. Let us present this solution as follows:

$$s(y' = jh) = \frac{\chi^j - \chi^n}{1 - \chi^n} \, , \; \chi = \frac{1 + Pe}{1 - Pe} \, , \; Pe = \frac{Re}{2} \, , \; Re = \frac{UH}{\nu} \, , \; h = \frac{1}{n} \, , \; j = 0, ..., n \tag{6.38}$$

We discuss this solution in Section 8.3 of [70] for the advection-diffusion model and in Section 6 of [67] for the hydrodynamic model. The isotropic diffusion model yields this solution with the linear equilibrium ($E_q^{(u)} = 0$). The solution (6.38) would coincide with the exact solution

$$s(y') = \frac{e^{Re\,y'} - e^{Re}}{1 - e^{Re}} \, , \tag{6.39}$$

provided that ν (either viscosity or the diffusion coefficient) is incremented by the quantity $-\nu^{l.}$:

$$\nu \quad \rightarrow \quad \nu - \nu^{l.} \ , \ \nu^{l.} = -\nu \times Pe \times f(Pe) \ , \ f(Pe) = \coth(Pe) - \frac{1}{Pe} \ . \quad (6.40)$$

In this solution, $\nu^{l.}$ represents the apparent (exact) correction of the numerical scheme with respect to the exact solution. This quantity is exactly the same as for the finite-element methods [36], then it is called "optimal rule" for explicit upwind correction. That means that the LBE numerical scheme is equivalent to used there discretization scheme for these solutions. The central-difference equivalent can be easily derived from the sum of the recurrence equations for 1D linear convection-diffusion equilibrium function. In agreement with the predictions (2.19) for 1D steady problem without (space-dependent) sources, the solution does not depend on Λ^{eo}.

The reader can find in [67] an attempt to introduce the artificial numerical diffusion into the LBE scheme when the local Reynolds number exceeds the critical value. On the other side, with the specific choice of the eigenvalue function Λ^{-}, the equilibrium term $sE_q^{(u)}(\vec{U},1)$ can cancel the negative numerical diffusion $\nu^{l.}$ (this is given by relations (68)-(69) of [69]). Again, these findings can be numerically validated using parabolic diffusion or pressure schemes for $\delta_q = 0$.

6.3.4 Temperature wave

This example is built in Section 7.6 of [69]. It enables us to examine the diffusion models with solution-dependent diffusion coefficients, as the *temperature wave* exact solution [192]:

$$s(x,t) = \begin{cases} [\tilde{d}(t-x)]^{\frac{1}{\tilde{d}}} & , \quad x \leq t, \\ 0 & , \quad x \geq t. \end{cases} \quad (6.41)$$

It satisfies the following equation and the boundary condition $s(0,t)$:

$$\frac{\partial s}{\partial t} - \frac{1}{\tilde{d}+1} \frac{\partial^2 s^{\tilde{d}+1}}{\partial x^2} = 0 \ , \ s(x,0) = 0 \ , \ s(0,t) = (\tilde{d}t)^{\frac{1}{\tilde{d}}} \ , \ \tilde{d} > 0 \ . \quad (6.42)$$

Since the diffusion variable appears in the inner derivatives, this equation can be modeled exactly with the TRT model and non-linear isotropic equilibrium (1.48), $E_q\overline{\mathcal{D}}(s) = \frac{s^{\tilde{d}+1}}{(\tilde{d}+1)\Lambda^{-}} t_q^{\star}$ (cf. relations (1.50),(1.52)). The exact time-dependent Chapman-Enskog expansion is given by relations (61) of [69], for $\tilde{d} = 1$ where $\partial_t s = -\partial_x s$. Incoming populations on the upstream boundary and downstream the front are

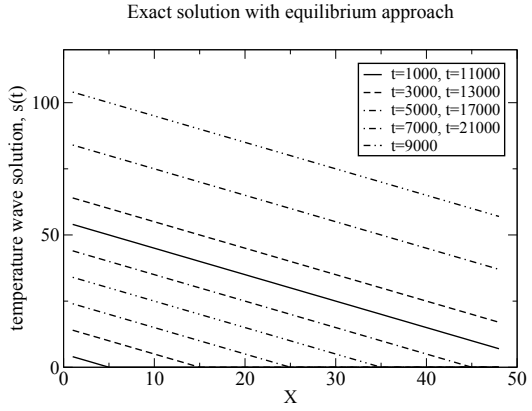

Figure 6.5: Exact solution obtained with the equilibrium approach using $\lambda^- = \lambda^+ = -1$ for $\tilde{d} = 1$. Imaginary boundary nodes are found at $x = 0$ and $x = 49$.

then either computed exactly or with a particular exact scheme, $f_q(\vec{r}+\vec{c}_q, t+1) = e_q(\vec{r}, t)$. This scheme is exact for any exact solution of the LBE scheme provided that all eigenvalues are equal to -1. Without this exact front tracking, the solution is not exact any more but the front is sharp.

Alternatively, the solution based on the standard linear equilibrium function with $\mathcal{D}(s) = s$ was considered. Then the eigenvalue function Λ^- varies as $s^{\tilde{d}}$. It was conjectured that an exact (finite) expansion cannot be found in this case because of the variation of Λ^- and its next derivatives in the series.

This problem demonstrates the role of the non-linear equilibrium diffusion functions which may prescribe the integral transformations of the diffusion term. This idea is exploited above for the Kirchhoff transform of the Richard's equation.

6.3.5 Coordinate transformations

The anisotropic diffusion tensors can be validated with the help of coordinate transformations of the laplace-operator described by relations (1.47). This is worked out in Section 8.4 of [70], where the solutions of the diffusion equation in square computational domain

$$-M = K'_{yy}\partial^2_{y'}s + K'_{zz}\partial^2_{z'}s\ ,\ \{y', z'\} \in [H \times H]\ , \tag{6.43}$$

for zero boundary values $s(y', H) = 0$ and $s(H, z') = 0$ are checked against the known solution for Stokes flow, $j_x(y, z)$, in a pipe of rectangular cross-section. One

should keep in mind that even if this (developed in series) solution is not an exact solution of the LBE evolution operator, it is useful to validate the anisotropic techniques. More generally, the anisotropic coordinate transformation may be efficiently tested against the solutions of the same numerical scheme on the uniform grids. The coordinate transformations give a possibility to reach the effects of adaptive grid refining in sub-domains. However, the interlayer conditions should be then respected. These situations are studied in [71] and illustrated in Fig. 5.14 for variably saturated flow.

6.3.6 Anisotropic eigenvalues for rotated channels

This (unpublished) solution shows how the exponential solution (6.26) in arbitrarily oriented channel can be get with the help of the anisotropic eigenvalues by the L-model. Let us consider one-dimensional diffusion equation:

$$-M = \nu_e \partial^2_{y'} \psi \, , \, M = -F_c \psi \, . \tag{6.44}$$

and the diffusion equilibrium function (1.48), with:

$$\begin{aligned} \psi &= \rho + \frac{1}{2} M \, , \, e_0 = \psi + \Lambda^+ M - \sum_{q=1}^{Q-1} e_q^+ \, , \, S_0^{\pm} = 0 \, , \\ e_q^+(\vec{r},t) &= t_q \psi + \Lambda^+ M_q \, , \, M_q = t_q^m M \, , \, t_q = \frac{t_q^\star}{C} \, , \, t_q^m = \frac{t_q^\star}{C^m} \, , \\ e_q^-(\vec{r},t) &= 0 \, , \, S_q^{\pm} = 0 \, , \, q = 1, \ldots, Q-1 \, . \end{aligned} \tag{6.45}$$

Likely the Brinkman flow in simple channels, the finite-difference equivalent of the L-operator is obtained with the help of recurrence equations:

$$\begin{aligned} F_0 \psi &= (\frac{\Lambda_q^-}{C \nu_e} + \bar{\delta}_q \nu_e) \Delta^2_{y',q} \psi \, , \, c_{q\,y'} \neq 0 \, , \text{ where} \\ \bar{\delta}_q \nu_e &= F_0 [\Theta_q^2 (\Lambda_q^e - \frac{1}{4}) - \frac{\Lambda_q^e}{C^m} + \frac{\Lambda_q^-}{2C^m} (r-1)] \, , \, r = \frac{C^m}{C} \, , \, F_0 = \frac{F_c}{\nu_e} \, . \end{aligned} \tag{6.46}$$

The solutions of Eqs. (6.46) are given by relations (5.9) and (6.28) replacing there: $\Delta^2_{y',\Theta} \to \Delta^2_{y',q}$, $\Theta \to \Theta_q$ and $b^2 \to b_q^2 = \frac{F_0}{4(\frac{\Lambda_q^-}{C\nu_e} + \bar{\delta}_q \nu_e)}$. The idea is to satisfy all link relations with a proper solution of the eigenvalue functions Λ_q^-, which yields the relation $r_q = e^{2B}$ for each separate link. This is achieved with: :

$$\Lambda_q^- = \frac{C^m \nu_e B^2 \Theta_q^2 \coth^2 [\Theta_q B]}{r + 2\nu_e B^2 (r-1) + 4\nu_e B^2 \Lambda^+ (C^m \Theta_q^2 - 1)} \, , \, c_{q\,y'} \neq 0 \, . \tag{6.47}$$

The solution becomes isotropic for the parallel and diagonal orientations of the channel, $\Theta_q \equiv \Theta$, similar to the TRT solution of Brinkman flow in section 6.2. Exact populations are:

$$n_q^+(y') = \frac{M(y')}{\lambda^+} t_q^\star c_{q\,y'}^2 \ , \ n_q^-(y') = \frac{t_q^\star}{\lambda_q^- \Lambda_q^-}\left(\frac{\Lambda_q^- \overline{\Delta}_q \psi}{C} - \overline{\delta}_q \nu_e \overline{\Delta}_q M(y')\right) . \qquad (6.48)$$

This solution is obtained as follows: first substitute $n_q^+(y')$ into recurrence equation (2.6), derive from it an expression for $\Lambda_q^- \Delta_q^2 g_q^-$, then substitute this expression, together with $e_q^+(y')$, into recurrence equations (2.5) and derive from there the solution for $g_q^-(y')$. Again, one can compute relations (6.48) with the finite-difference operators on the exact distributions $\psi(y')$ and $M(y')$, using relations (6.47) for Λ_q^-, relation (6.46) for $\overline{\delta}_q \nu_e$ and relation (6.45) for e_q^+. This solution can be useful for validation of coding for fully anisotropic L- operator.

6.4 Concluding remarks, and table of "magic" values

The derived solutions for magic combinations Λ^{eo} play different roles and they are of different importance. Of special interest is $\Lambda_q^{eo} = \frac{1}{4}$. The L operator is restricted in our study to all equal symmetric eigenvalues, for the sake of consistent modeling of the mass conservation equation. Then the L operator with $\Lambda_q^{eo} = \frac{1}{4}$ reduces to a special sub-class of the TRT operator, given by $\Lambda^{eo} = \frac{1}{4}$, where the BGK operator is represented by $\tau = 1$. The non-equilibrium components are given as the explicit (directional finite-difference) functions of the equilibrium components when $\Lambda^{eo} = \frac{1}{4}$. This simplifies greatly both the form of the solution and the analysis of the scheme. Besides that, the accommodation layers are localized in the boundary nodes when $\Lambda^{eo} = \frac{1}{4}$. Finally, this value possesses the optimal stability properties for the AADE, at least.

In author's opinion, other derived values are less significant but some of them are quite useful. Let us mention $\Lambda^{eo} = \frac{1}{12}$ and $\Lambda^{eo} = \frac{1}{6}$, which annihilate the coefficients of the third and fourth order spatial errors, hence they are helpful for improvement of the accuracy and the convergence with grid refining. As a particular effect, the arbitrarily rotated Navier-Stokes Poiseuille flow becomes compatible with the TRT scheme only when $\Lambda^{eo} = \frac{1}{12}$ (and only for one special form of the non-linear term described in the text). Let us mention the first observed magic value, $\Lambda^{eo} = \frac{3}{16}$, which locates the straight walls midway the grid nodes in Stokes and Navier-Stokes Poiseuille flows. Extension of the bounce-back to linear magic boundary schemes makes possible to place them at an arbitrary distance δ, when $\Lambda^{eo} = \frac{3\delta^2}{16}$. It should be remembered that the stability bounds decrease when

$\Lambda^{eo} \rightarrow 0$ then very small magic values should be used with care in the limit of zero transport coefficients. Last, the magic values should be set while refining the grid or altering the characteristic parameters, at given physical numbers. This makes the steady solutions of the Lattice Boltzmann Equation physically consistent for all orders and its transient solutions conditionally consistent, at least.

Λ^{eo}	**Purpose**	See
	Bulk: generic properties	
$\frac{1}{4}$	Explicit finite-difference form of the Chapman-Enskog expansion	Eqs. (1.36), (1.38
$\frac{1}{4}$	Explicit finite-difference form of the recurrence equations	Eqs. (2.9), (2.11)
$\frac{1}{4}$	Equivalent stability properties for any value of diffusion coefficient	Eq. (1.75)
$\frac{1}{12}$	Annihilates third order errors of spatial approximation	Eq. (1.34)
$\frac{1}{6}$	Annihilates fourth order errors of spatial approximation	Eq. (1.35)
	Bulk: linear diffusion equation	
$\Lambda^{eo}(\Lambda^{-})$	Annihilates k^2-correction for isotropic diffusion	Eq. (1.69)
$\frac{1}{6}$	Annihilates k^2- anisotropic component in diffusion coefficient	Eq. (1.71)
$\frac{1}{12}$	BGK: annihilates k^2-correction for advective velocity	Eq. (1.73)
	Bulk: rotated Poiseuille flow with Navier-Stokes equilibrium	
$\frac{1}{12}$	Necessary compatibility condition	Eq. (6.21)
	Bulk: Brinkman channel flow	
$\frac{1}{4}$	Principal anisotropic correction vanishes for arbitrarily-rotated flow	Eq. (5.15)
$\frac{3}{8}$	Equivalent to finite-difference scheme for parallel flow	Eq. (5.9)
$\frac{3}{4}$	Equivalent to finite-difference scheme for diagonal flow	Eq. (5.9)
$\Lambda^{eo}(B,\Theta)$	Exact parallel and diagonal Brinkman flow	Eq. (6.30)
	Boundary: generic property for any steady bulk solution	
$\frac{1}{4}$	Accommodation is localized at boundary nodes	Eqs. (2.26), (6.19
	Boundary: parallel Poiseuille flow (Stokes or Navier-Stokes)	
$\frac{3}{16}$	Bounce-back, $\delta_q \equiv \frac{1}{2}$	Eq. (3.3)
$\frac{3\delta^2}{4}$	"Magic" linear schemes MGLI($\alpha^{(u)}$), $\forall\ \delta_q = \delta > 0$	Eq. (6.6)
	Boundary: diagonal Poiseuille flow (Stokes or Navier-Stokes)	
$\frac{3}{8}$	Bounce-back, $\delta_q \equiv \frac{1}{2}$	Eq. (3.3)
$\frac{3\delta^2}{2}$	"Magic" linear schemes MGLI($\alpha^{(u)}$), $\forall\ \delta_q = \delta > 0$	Eq. (6.6)
	Boundary: exact parabolic solutions of diffusion equation	
$\frac{3}{16}$	Anti-bounce-back with $\frac{M}{2}$ redefinition, $\delta_q \equiv \frac{1}{2}$	Eq. (6.33)
$\frac{1}{8}$	Anti-bounce-back and source correction, $\delta_q \equiv \frac{1}{2}$	Eq. (6.34)
	Implicit interface: exact solution in straight channel	
$\frac{3}{16}$	Two-phase Poiseuille flow with the bounce-back, $\forall \nu^{(i)}, \forall \vec{F}^{(i)}$	Eq. (6.11)
$\frac{3}{16}$	Heterogeneous vertical flow with anti-bounce-back	Sec. 6.3.2
	Explicit interface: exact solution in straight channel	
$\frac{3}{8}$	Two-phase Poiseuille flow with the different values of forcing	Sec. 6.1.3
$\frac{3}{8}$	Stratified parabolic flow with the different values of mass source	Sec. 6.3.2

Table 6.1: Several magic values from this work.

Chapter 7

Bibliography

7.1 References

Bibliography

[1] A. S. Abdul and R. W. Gillham. Laboratory studies of the effects of the capillary fringe on streamflow generation. *Water Resour. Res.*, 20(6):691–708, 1984.

[2] B. Ahrenholz, J. Tölke, and M. Krafczyk. Lattice-Boltzmann simulations in reconstructed parametrized porous media. *Int. J. Comput. Fluid Dyn.*, 20(6):369-377, 2006.

[3] B. Ahrenholz, J. Tölke, P. Lehmann, A. Peters, A. Kaestner, M. Krafczyk, and W. Durner. Prediction of capillary hysteresis in a porous material using lattice-Boltzmann methods and comparison to experimental data and a morhphological pore network model. *Adw. Water. Res.*, doi:10.1016/j.adwartres.2008.03.009, 2008.

[4] C. K. Aidun and Y. Lu. Lattice Boltzmann Simulation of Solid Particles Suspended in Fluids, *J. Stat. Phys.,* 81(1/2):49-61, 1995.

[5] M. G. Ancona. Fully-Lagrangian and Lattice-Boltzmann Methods for Solving Systems of Conservation Equations. *J. of Comp. Physics*, 115:107-120, 1994.

[6] B. Andreianov, F. Boyer, and F. Hubert, Discrete duality finite volume schemes for Leray-Lions-ttype elliptic problems on general 2D meshes. *Numer. Methods Partial Differential Equations*, 23(1):145-195, 2007.

[7] S. Ansumali and I. V. Karlin. Kinetic boundary conditions in the lattice Boltzmann method. *Phys. Rev. E*, 66:26311-1–6, 2002.

[8] A. N. Alexandrou, E. Duc, and V. Entov. Inertial, viscous and yield stress effects in Bingham fluid filling of a 2-D cavity. *J. of Non-Newtonian Fluid Mech.* 96:383–403, 2001.

[9] S. Ansumali, I.V. Karlin, S. Arcidiacono, A. Abbas, and N. I. Prasianakis. Hydrodynamics beyond Navier-Stokes: Exact Solution to the Lattice Boltzmann Hierarchy. *Phys. Rev. Lett.*, 98:124502-1–4, 2007.

[10] D. A. Barry, J.-P. Parlange, G. C. Sander, and M. Sivaplan. A class of exact solutions for Richards' equation. *J. of Hydrology*, 142:29–46, 1993.

[11] J. Becker, M. Junk, D. Kehrwald, and G. Thömmes. A Lattice Boltzmann Method for multiphase flows. *6^{th} International Conference on Multiphase Flow*, ICMF 2007, Leipzig, Germany, July 9-13, 2007.

[12] R. Benzi, S. Succi, and M. Vergassola. The lattice Boltzmann equation: theory and applications. *Physics Reports*, 222:145-197, 1992.

[13] A. N. Brooks, and T. J. R. Hughes. Streamline Upwind/Petrov-Galerkin Formulations for convection Dominated Flows with Particular Emphasis on the incompressible Navier-Stokes Equations. *Computer Methods in Applied Mechanics and Engineering*, 32:199-259, 1982.

[14] G. R. Burgos, A. N. Alexandrou, and V. Entov On the determination of yield surfaces in Herschel-Bulkley fluids. *J. of Rheol.* 43:463–483, 1999.

[15] M. Bakker and K. Hemker. Analytic solutions for groundwater whirls in box-shaped, layered anisotropic aquifers. *Adv. Water. Resour*, 27:1075–1086, 2004.

[16] E. Beaugendre, A. Ern, I. Ginzburg, and C. Kao. Finite element modeling of variably saturated flows in hillslopes with shallow water tables. *in Computational methods in Water resources*, Ed. by C. T. Miller, 1427-1429, Elsevier, 2004.

[17] E. Beaugendre, A. Ern, T. Esclaffer, E. Gaume, I. Ginzburg, and C. Kao. A seepage face model for the interaction of shallow water tables with the ground surface: Application of the obstacle-type method. *J. of Hydrology*, 392(1-2):258-273, 2006.

[18] E. B. Belov, S. V. Lomov, I. Verpoest, T. Peters, D. Roose, R. S. Parnas, K. Hoes, and H. Sol. Modelling of permeability of textile reinforcements: lattice Boltzmann method. *Composites Science and Technology*, 64(7-8):1069–1080, 2004.

[19] L. Boltzmann. Lectures on gas theory. Translated by S.G. Brusch. University of California Press, Berkley and Los-Angeles. 1964.

[20] M. Bouzidi, M. Firdaouss, and P. Lallemand. Momentum transfer of a Boltzmann-lattice fluid with boundaries. *Phys. Fluids,* 13:3452-3459, 2001.

[21] M. Bouzidi, D. d'Humières, P. Lallemand, and L.-S. Luo, Lattice Boltzmann equation on a two-dimensional rectangular grid, *J. Comput. Physics*, 172:704-717, 2001.

[22] H. C. Brinkman. A calculation of the viscous force excerted by a flowing fluid on a dense swarm of particles. *Appl. Sci. Res. A*, 1:27-34, 1949.

[23] P. Broadbridge and I. White. Constant Rate Rainfall Infiltration: A Versatile Nonlinear Model. 1. Analytic Solution . *Water Resour. Res.*, 24(1): 145–154, 1988.

[24] R. H. Brooks and A. T. Corey, Hydraulic properties of porous media. *Hydrol.Pap.*, 3, Colo. State Univ., Fort Collins, 1964.

[25] J. M. Buick and C. A. Greated. Gravity in a lattice Boltzmann model. *Phys. Rev. E*, 61:5307–5320, 2000.

[26] A. Caiazzo and M. Junk. Boundary forces in lattice Boltzmann: Analysis of Momentum Exchange algorithm . *Computers and Mathematics with Applications*, 55:1415-1423, 2008.

[27] A. Caiazzo. Analysis of lattice Boltzmann nodes initialization in moving booundays points. *Progress in Computational Fluid Dynamics*, 8(1-4):3-11, 2008.

[28] A. Cancelliere, C. Chang, E. Foti, D. Rothman, S. Succi. The permeability of random medium: Comparison of simulations with theory. *Phys. Fluids A*, 2:2085-2088, 1990.

[29] M. A. Celia, E. T. Boulotas, and R. L. Zarba. A general mass-conservative numerical solution for the unsaturated flow equation. *Water Resour. Res.*, 26(7):1483–1496, 1990.

[30] C. Cercignani. Theory and Application of the Boltzmann Equation. *Scottish Academic*, New-York, 1975.

[31] S. Chapman. On the law of distribution of velocities, and on the theory of viscosity and thermal conduction, in a non-uniform simple monoatomic gas. *Phil. Trans. Roy. Soc. A*, 216:279, 1916.

[32] H. Chen, S. Chen, and W. H. Matthaeus. Recovery of the Navier-Stokes equations using a lattice-gas Boltzmann method. *Phys. Rev. A*, 45:R5339-5342, 1992.

[33] S. Chen, D. Martinez, and R. Mei. On boundary conditions in lattice Boltzmann methods. *Physics of Fluids*, 8:2527-2536, 1996.

[34] S. Chen, and G. D. Doolen. Lattice Boltzmann method for fluid flows. *J. of Fluid Mechanics*, 30:329-393, 1998.

[35] S. Chen, K. Diemer, G. D. Doolen, D. Eggert, C. Fu, S. Gutman, and B. J. Travis. Lattice Gas Automata for Flow Through Porous Media. *Physica D*, 47:72–84, 1991.

[36] I. Christie, D. F. Griffiths, A. R. Mitchell, and O. C. Zienkiewicz, Finite element methods for second order differential equations with significant first derivatives. *Int. J. for Numerical Methods in Engineering*, 10:1389-1396, 1976.

[37] B. Chopard and M. Droz, Cellular Automata Modeling of Physical Systems, Cambridge: Cambridge University Press, 1998.

[38] D. S. Clague, B. D. Kandhai, R. Zhang, P. M. A. Sloot. Hydraulic permeability of (un)bounded fibrous media using the lattice Boltzmann method. *Phys. Rev. E*, 61(1):616–625, 2000.

[39] T. P. Clement, W. Wise, F. J. Molz, and M. Wen . A comparison of modeling approaches for steady-state unconfined flow. *J. Hydrol.*, 181:189–209, 1996.

[40] R. Cornubert, D. d'Humières, and D. Levermore. A Knudsen layer theory for lattice gases. *Physica D*, 47:241–259, 1991.

[41] O. Dardis and J. McCloskey. Permeability porosity relationships from numerical simulations of fluid flow. *Geophys. Res. Lett.*, 25:1471-1474, 1998.

[42] A. R. Davies, J. L.Summers, and M. C. T.Wilson, On a dynamic wetting model for the finite-density multi-phase lattice Boltzmann method. *Int. J. of Computational Fluid Dynamics*, 20(6):415-427, 2006.

[43] A. P. Deshpande, A. Srikanth, and N. Praveen. Quantitative Estimation of Permeability with Lattice Boltzmann Simulations: Representative Porous Media from Composite Processing. *The Canadian J. of Chemical Engineering*, 83(5):808-815, 2005.

[44] F. Dubois and P. Lallemand, On lattice Boltzmann scheme, finite volumes and boundary conditions. *Progress in Computational Fluid Dynamics*, 8(1-4):11-25, 2008.

[45] F. Dubois, Equivalent partial differential equations of a lattice Boltzmann scheme. *Computers and Mathematics with Applications*, 55:1441-1449, 2008.

[46] DYNAS: Cooperative Research Initiative "Dynamics of shallow water tables", http://www-rocq.inria.fr/estime/DYNAS.

[47] E. C. Du Fort and S. P. Frankel, Stability conditions in the numerical treatment of parabolic differential equations. *M.T.A.C.*, 7:135, 1953.

[48] G. Drazer and J. Koplik. Tracer dispersion in two dimensional rough fractures. *Phys. Rev. E* 63:056104-1-056104-11, 2001.

[49] D. A. Edwards, M. Shapiro, P. Bar-Yoseph, and M. Shapira, The influence of Reynolds number upon the apparent permeability of spatially periodic arrays of cylinders, *Phys. Fluids A.*, 2(1):45-55, 1990.

[50] D. Enskog. The kinetic theory of Phenomena in fairly rare gases. *Dissertation*, Upsala, 1917.

[51] O. Filippova and D. Hänel. Boundary-Fitting and Local Grid Refinement for Lattice-BGK Models. *Int. J. of Modern Physics*, 9:1271-1279, 1998.

[52] D. M. Freed. Lattice-Boltzmann Method for Macroscopic Porous Media Modeling. *Int. J. Modern Phys. C*, 9:1491–1503, 1998.

[53] U. Frisch, D. d'Humières, B. Hasslacher, P. Lallemand, Y. Pomeau, and J. P. Rivet. Lattice gas hydrodynamics in two and three dimensions. *Complex Sys.*, 1:649–707, 1987.

[54] C. Ghaddar. On the permeability of unidirectional fibrous media: A parallel computational approach. *Phys. Fluids.*, 7(11):2563-2586, 1995.

[55] M. A. Gallivan, D. R. Noble, J. G. Georgiadis, and R. O. Buckius. An evaluation of the bounce-back boundary condition for lattice Boltzmann simulations. *Int. J. Num. Methods in Fluids*, 25:249-263, 1997.

[56] I. Ginzbourg and P. M. Adler. Boundary flow condition analysis for the three-dimensional lattice Bolzmann model. *J. Phys. II France*, 4:191–214, 1994.

[57] I. Ginzbourg. Boundary conditions problems in lattice gas methods for single and multiple phases. PHD Thesis, University Paris VI, 1994.

[58] I. Ginzbourg and P. M. Adler. Surface Tension Models with Different Viscosities. *Transport in Porous Media*, 20:37-75, 1995.

[59] I. Ginzbourg, L. Giraud, and D. d'Humières. Magic parameters for the efficient Lattice Boltzmann computations. unpublished, 1995.

[60] I. Ginzbourg and D. d'Humières. Local Second-Order Boundary method for Lattice Boltzmann models. *J. Stat. Phys.*, 84(5/6):927–971, 1996.

[61] I. Ginzbourg and D. d'Humières. Local Second-Order Boundary method for Lattice Boltzmann models. Part II. Application to Poisson equation in complicated geometries. *unpublished*, 1996.

[62] I. Ginzburg and G. Wittum. Two-Phase Flows on interface refined grid modelled with VOF, staggered finite volumes, and spline interpolants. *J. of Comp. Phys.*, 166:302–335, 2001.

[63] I. Ginzburg, P. Klein, C. Lojewski, D. Reinel-Bitzer, and K. Steiner, Parallele Particelcodes für industielle Anwendungen, Abschlussbericht, Fraunhofer ITWM, Kaiserslautern, 2001.

[64] I. Ginzbourg. Introduction of upwind and free boundary into lattice Boltzmann method. *in Discrete Modelling and Discrete Algorithms in Continuum Mechanics*, eds. T. Sonar & I. Thomas, 97–109, Logos-Verlag, Berlin, 2001.

[65] I. Ginzburg and K. Steiner. A free-surface Lattice Boltzmann method for modelling the fillling of expanding cavities by Bingham Fluids. *Phil. Trans. R. Soc. Lond. A*, 360:453-466, 2002.

[66] I. Ginzburg and D. d'Humières. Multi-reflection boundary conditions for lattice Boltzmann models. *Phys. Rev. E*, 68:066614-1-30, 2003.

[67] I. Ginzburg and K. Steiner. Lattice Boltzmann model for free-surface flow and its application to filling process in casting. *J. Comp. Phys.*, 185:61–99, 2003.

[68] I. Ginzburg, J.-P. Carlier, and C. Kao. Lattice Boltzmann approach to Richards' Equation. *in Computational methods in Water resources*, Ed. by C. T. Miller, 583-597, Elsevier, 2004.

[69] I. Ginzburg. Equilibrium-type and Link-type Lattice Boltzmann models for generic advection and anisotropic-dispersion equation. *Adv. Water Resour.*, 28:1171–1195, 2005.

[70] I. Ginzburg. Generic boundary conditions for Lattice Boltzmann models and their application to advection and anisotropic-dispersion equations. *Advances in Water Resour.*, 28:1196–1216, 2005.

[71] I. Ginzburg. Variably saturated flow described with the anisotropic Lattice Boltzmann methods. *J. Computers & Fluids*, 25:831–848, 2006.

[72] I. Ginzburg. Lattice Boltzmann modeling with discontinuous collision components. Hydrodynamic and advection-diffusion equations. *J. Stat. Phys*, 126:157–203, 2007.

[73] I. Ginzburg and D. d'Humières. Lattice Boltzmann and analytical modeling of flow processes in anisotropic and heterogeneous stratified aquifers. *Adv. Water Resources*, 30:2202–2234, 2007.

[74] I. Ginzburg, F. Verhaeghe, and D. d'Humières. Two-relaxation-time Lattice Boltzmann scheme: about parametrization, velocity, pressure and mixed boundary conditions. *Com. Comp. Phys*, 3:427–478, 2008.

[75] I. Ginzburg, F. Verhaeghe, and D. d'Humières. Study of simple hydrodynamic solutions with the two-relaxation-times Lattice Boltzmann scheme. *Com. Comp. Phys*, 3:519–581, 2008.

[76] I. Ginzburg. Consistent Lattice Boltzmann schemes for the Brikman model of porous flow and infinite Chapman-Enskog expansion. *Phys. Rev. E*, 77:0666704:1-12, 2008.

[77] C. Le Potier. Schéma volumes finis pour des opérateurs de diffusion fortement anisotropes sur des maillages non structurés, *C. R. Math. Acad. Sci. Paris*, 340(12):921-926, 2005.

[78] L. Giraud. Fluides visco-élastiques par la méthode de Boltzmann sur réseau. PhD, Université Paris VI, 1997.

[79] L. Giraud, D. d'Humières, and P. Lallemand, A lattice Boltzmann model for Jeffreys viscoelastic fluid, *Europhys. Lett.* 42:625-630, 1998.

[80] P. M. Gresho. Incompressible Fluid Dynamics: Some Fundamental Formulation Issues. *Ann. Rev. Fluid Mech.*, 23, Annual Reviews, Inc. Palo Alto, CA, 1991.

[81] D. Grunau, S. Chen, and K. Eggert. A lattice Boltzmann model for multiphase fluid flows. *Phys. Fluids*, A5:2557-2572, 1993.

[82] A. K. Gunstensen, D. H. Rothman, S. Zaleski, and G. Zanetti. Lattice Boltzmann Model of Immiscible Fluids, *Physical Review A*, 43(8):47-52, 1991.

[83] Z. Guo and C. Zheng. An extrapolation method for boundary conditions in Lattice Boltzmann method. *Physics of Fluid*, 14(6):2007-2010, 2002.

[84] Z. Guo and C. Zhao. Lattice Boltzmann model for incompressible flows through porous media, *Phys. Rev. E*, 66:036304-1-10, 2002.

[85] A. K.Gunstensen and D. H. Rothmann . Microscopic Modeling of Immiscible Fluids in Three Dimensions by a Lattice-Boltzmann Method. *Europhys.Lett.* 18:157-161, 1992.

[86] Z. Guo, C. Zheng, and B. Shi. Discrete lattice effects on the forcing term in the lattice Boltzmann method. *Phys. Rev. E*, 65:066308-1–6, 2003.

[87] X. He, Y. Zou, L.-S. Luo, and M. Dembo. Analytic Solutions of Simple Flows and Analysis of Nonslip Boundary Conditions for the Lattice Boltzmann BGK Model. *J. Stat. Phys.*, 87:115–135, 1997.

[88] X. He and L.-S. Luo, A priori derivation of the lattice Boltzmann equation. *Physical Review E*, 55:R6333-4, 1997.

[89] X. He and L.-S. Luo. Lattice Boltzmann Model for the Incompressible Navier-Stokes Equation. *J. Stat. Phys*, 88:927–945, 1997.

[90] K. Hemker, E. van der Berg, and M. Bakker. Ground Water Whirls. *Ground Water*, 42:234–242, 2004.

[91] F. J. Higuera and J. Jiménez. Boltzmann approach to lattice gas simulations. *Europhys. Lett.*, 9:663–668, 1989.

[92] F. J. Higuera, S. Succi, and R. Benzi. Lattice Gas Dynamics with Enhanced Collisions. *Europhys. Lett.*, 9:345–349, 1989.

[93] A. C. Hindmarsch, P. M. Grescho, and D. F. Griffiths. The stability of explicit time-integration for certain finite difference approximation of the multi-dimensional advection-diffusion equation. *Int. J. Num. Methods in Fluids*, 1984(4):853–897.

[94] C. W. Hirt and R. P. Harper, Flow modeling for casting analysis. Technical Note FSI-88-TN7, Flow Science Int., Los Alamos, NM, 1988.

[95] D. J. Holdych, D. R. Noble, J. G. Georgiadis, and R. O. Buckius, Truncation error analysis of lattice Boltzmann methods, *J. of Comput. Physics*, 193(2):595-619, 2004.

[96] S. Hou, X. Shan, Q. Zou, G. D. Doolen, and W. E. Soll. Evaluation of Two Lattice Boltzmann Models for Multiphase Flows . *J. Comput. Physics*, 138:695–713, 1996.

[97] D. d'Humières, P. Lallemand, and U. Frisch, Lattice Gas models for 3D hydrodynamics. *Europhys. Lett.*, 2:291-297, 1986.

[98] D. d'Humières. Generalized Lattice-Boltzmann Equations. AIAA Rarefied Gas Dynamics: Theory and Simulations. *Progress in Astronautics and Aeronautics*, 59:450–548, 1992.

[99] D. d'Humières, M. Bouzidi, and P. Lallemand. Thirteen-velocity three-dimensional lattice Boltzmann model. *Phys. Rev. E*, 63:066702-1–7, 2001.

[100] D. d'Humières, I. Ginzburg, M. Krafczyk, P. Lallemand, and L.-S. Luo. Multiple-relaxation-time lattice Boltzmann models in three dimensions. *Phil. Trans. R. Soc. Lond. A*, 360:437–451, 2002.

[101] A. Hollis, I. Halliday and C. M. Care. Enhanced, mass-conserving closure scheme for lattice Boltzmann equation hydrodynamics, *J. Phys. A: Math. Gen.*, 39:10589-10601, 2006.

[102] P. Lallemand, D. d'Humières, L.-S. Luo, and R. Rubenstein. Theory of the lattice Boltzmann method: Three-dimensional model for linear visco elastic fluids, *Phys. Rev. E*, 67:021203-1–19, 2003.

[103] D. d'Humières and I. Ginzburg. Viscosity independent numerical errors for Lattice Boltzmann models: from recurrence equations to "magic" collision numbers. *to appear in Computers & Mathematics with Applications*, 2008.

[104] D. d'Humières and I. Ginzburg, Some analytical results about the stability of Lattice Boltzmann models. in preparation, 2008.

[105] M. W. Heemels, M. H. J. Hagen, and C. P. Lowe. Simulating Solid Colloidal Particles Using the Lattice-Boltzmann Method. *J. Comp. Phys.* 164:48–61, 2000.

[106] S. Hou, J. Sterling, S. Chen, and G.D. Doolen. A Lattice Boltzmann Subgrid Model for High Reynolds Number Flows. *Fields Institute Communications* 6:151-165, 1996.

[107] The HYDRUS-2D Software Package for Simulating the Two-Dimensional Movement of Water, Head, and Multiple Solutes in Variably-Saturated Media, Version 2, Riverside, California: US Salinity Laboratory, 1999.

[108] T. Inamuro, M. Yoshino, and F. Ogino. A non-slip boundary condition for lattice Boltzmann simulations. *Physics of Fluids,* 7(12):2928-2930, 1995.

[109] T. Inamuro, M. Yoshino, and F. Ogino. Lattice Boltzmann Simulation of Flows in a Three-dimensional Porous Structure. *Int. J. Num. Meth. Fluids*, 29:737-748, 1999.

[110] S. Izquierdo and N. Fueyo. Preconditioned Navier-Stokes schemes from the generalised lattice Boltzmann equation. *Progress in Computational Fluid Dynamics*, 8(1-4): 189-196, 2008.

[111] S. Izquierdo and N. Fueyo. Characteristic non-reflecting boundary conditions for open boundaries in lattice Boltzmann methods. *Physical Review E*, 78 (4):046707, 2008.

[112] M. Junk and Z. Yang. Asymptotic Analysis of Lattice Boltzmann Boundary Conditions. *J. Stat. Phys.*, 121:3–37, 2005.

[113] M. Junk and Z. Yang. Outflow boundary conditions for the lattice Boltzmann method. *Progress in Computational Fluid Dynamics*, 8(1-4):38-48, 2008.

[114] Q. Kang, D. Zhang, and S. Chen, Unified lattice Boltzmann method for flow in multiscale porous media. *Phys. Rev. E*, 66:056307-11, 2000.

[115] G. E. Karniadakis and A. Beskok. Micro Flows: Fundamentals and Simulation. Springer, New York, 2002.

[116] Y. Keehm, T. Mukerji, and A. Nur. Permeability Prediction from Thin Sections: 3D Reconstruction and Lattice-Boltzmann Flow Simulation. *Geophys. Res. Lett.*, 31:L04606-1-10, 2004.

[117] D. Kehrwald. Numerical analysis of immiscible lattice BGK. *PhD. diss, Univ. Kaiserslautern, Germany*, 2002.

[118] G. Kirchhoff, Vorlesungen über die Theorie der Wärme, Barth, Leipzig, 1894.

[119] S. H. Kim, H. Pitsch, and I. D. Boyd. Slip velocity and Knudsen layer in the lattice Boltzmann method for microscale flows. *Phys. Rev. E*, 77:026704-12, 2008.

[120] A. Koponen, D. Kandhal, E. Hellen, M. Alava, A. Hoekstra, M. Kataja, K. Niskanen, P. Sloot, and J. Timonen. Permeability of three-dimensional random fiber webs. *Phys. Rev. Lett.*, 80:716-720, 1998.

[121] C. Körner, M. Thies, T. Hoffmann, N. Thürey, and U. Rüde. Lattice Boltzmann Model for Free Surface flow for modeling Foaming. *J. Stat. Phys*, 121:179–197, 2005.

[122] Y. K. Kwok and K. K.Tam Stability analysis of three-level difference schemes for initial-boundary problems for multidimensional convective-diffusion equations *Communications in Num. Methods in Engineering*, 271:595-605, 1993.

[123] A. J. C. Ladd. Numerical simulations of particulate suspensions via a discretized Boltzmann equation. Part 1. Theoretical foundation. *J. Fluid Mech.*, 271:285-309, 1994.

[124] A. J. C. Ladd. Numerical simulations of particulate suspensions via a discretized Boltzmann equation. Part 2. Numerical results. *J. Fluid Mech.*, 271:311–339, 1994.

[125] A. J. C. Ladd. Moderate Reynolds number flows through periodic and random arrays of aligned cylinders. *J. Fluid Mech.*, 349:31-66, 1997.

[126] B. Lafaurie, C. Nardone, R. Scardovelli, S. Zaleski, and Zanetti. Modeling Merging and Fragmentation in Multiphase Flows with SURFER. *J. Comput. Phys*, 113:134-147,1994.

[127] P. Lallemand and L.-S. Luo. Theory of the lattice Boltzmann method: Dispersion, dissipation, isotropy, Galilean invariance, and stability. *Phys. Rev. E*, 61:6546–6562, 2000.

[128] P. Lallemand and L.-S. Luo. Lattice Boltzmann method for moving boundaries. *J. Comput. Phys.*, 184(2):406-421, 2003.

[129] L. Landau and E. Lifchitz. Fluid Mechanics, Moscou, Mir, 1971.

[130] M. Latva-Kokko and D. H. Rothman. Diffusion properties of gradient-based lattice Boltzmann models of immiscible fluids. *Phys. Rev. E.*, 71:056702-7, 2005.

[131] J. Latt, Y. Grillet, B. Chopard, and P. Wittwer. Simulating an exterior domain for drag force computations in the Lattice Boltzmann method. *Math. Comput. Simul.*, 72:169-172, 2006.

[132] L.-S. Luo. Theory of the lattice Boltzmann method: Lattice Boltzmann models for nonideal gases. *Phys. Rev. E*, 62(4):4982-4996, 2000.

[133] R. S. Maier, R. S. Bernard, and D. W. Grunau. Boundary Conditions for the Lattice Boltzmann Method. *Phys. Fluids*, 8:1788-1801, 1996.

[134] R. S. Maier, D. M. Kroll, Y. E. Kutsovsky, H. T. Davis, and R. S. Bernard. Simulation of flow through bead packs using the lattice Boltzmann method. *Phys. Fluids*, 10:60-74, 1998.

[135] Marinelli, F., and Durnford, D. S., Semianalytical solution to Richards' Equation for layered porous media, *J. of Irrigation and Drainage Engineering*, 124(6):290-299, 1998.

[136] N. Martys. Improved approximation of the Brinkman equation using a lattice Boltzmann method. *Phys. Fluids*, 13(6):1807-1810, 2001.

[137] A. R. Mitchell and D. F. Griffiths. The Finite Difference Method in Partial Differential Equations. Chichester, Wiley, 1980.

[138] G. R. McNamara, and G. Zanetti, Use of the Boltzmann equation to simulate lattice-gas automata, *Phys. Review Letters*, 61(20):2332-2335, 1988.

[139] R. Mei, L.-S. Luo, and W. Shyy. An Accurate Curved Boundary Treatment in the Lattice Boltzmann Method. *J. Comput. Phys.*, 155:307-330, 1999.

[140] R. Mei, L.-S. Luo, P. Lallemand, and D. d'Humières. Consistent initial conditions for lattice Boltzmann simulations. *J. Comp. & Fluids*, 35(4):855–862, 2006.

[141] C. T. Miller, G. A. Williams, C. T. Kelly, and M. D. Tocci, Robust solution of Richard's equation for nonuniform porous media, *Water Resour. Research* **34**:2599–2610, 1998.

[142] Miller C.T., Abhishek, C., Sallerson, A.B, Prins, J.F., and Farthing, M.W., A comparison of computational and algorithmic advances for solving Richards' equation. "Computational methods in water resources", Edited by C. T. Miller, Proc. of the CMWR XV, June 13-17, Chapel Hill, NC, USA, vol. **2**, 1131-1145, Elsevier; 2004.

[143] Y. Mualem, A new model for predicting the hydraulic conductivity of unsaturated porous media. *Water Resour. Res.* 12:513–522, 1976.

[144] R. M. H. Merks, A. G. Hoekstra, and P. M. A. Sloot. The Moment Propagation Method for Advection-Diffusion in the Lattice Boltzmann Method: Validation and Péclet Number Limits. *J. Comp. Phys.* 183:563–576, 2002.

[145] X. Nie, Y. Qian, G. D. Doolen, and S. Chen. Lattice Boltzmann simulation of the two-dimensional Rayleigh-Taylor instability. *Phys. Rev. E* 58(5):6861-6864, 1998.

[146] X. Nie and N. S. Martys. Breakdown of Chapman-Enskog expansion and the anisotropic effect for lattice-Boltzmann models of porous media. *Phys. Fluids*, 19:011702-1–4, 2007.

[147] D. R. Noble, S. Chen, J. G. Georgiadis, and R. O. Buickius. A consistent hydrodynamic boundary condition for the Lattice Boltzmann method. *Phys. Fluids*, 7:203–209, 1995.

[148] U. D'Ortona, D. Salin, M. Cieplak, R.B. Rybka, and J. R. Banavar. Two-color nonlinear Boltzmann cellular automata: Surface tension and wetting. *Phys. Review E*, 51:3718–3751, 1995.

[149] C. Pan, M. Hilpert, and C. T. Miller. Pore-scale modeling of saturated permeabilities in random sphere packings. *Phys. Rev. E*, 64(6):066702-1–9, 2001.

[150] C. Pan, M. Hilpert, and C. T. Miller. Lattice Boltzmann simulation of two-phase flow in porous media. *Water Resource Research*, 40(1):W01501:1–14, 2004.

[151] C. Pan, L.-S. Luo, and C. T. Miller. An evaluation of lattice Boltzmann schemes for porous media simulation. *J. Computer & Fluids*, 35(4):898–909, 2006.

[152] B. Palmer and D. R. Rector. Lattice-Boltzmann algorithm for simulating thermall flow in compressible fluids. *J. Comput. Phys.* 161: 1–20, 2000.

[153] T. C. Papanastasiou. Flows of materials with yield. *J. of Rheol.*, 31:385–404, 1987.

[154] Y. Peng and L.-S. Luo, A comparative study immersed-boundary and interpolated bounce-back methods in LBE. *Progress in Computational Fluid Dynamics*, 8(1-4):156-167, 2008.

[155] R. Peyret and T. Taylor. Computational methods for Fluid Flow. Springer Series in Computational Physics. 1983.

[156] M. Pilotti, S. Succi, and G. Menduni. Energy dissipation and permeability in porous media. *Europhys. Lett.*, 60(1):72-78, 2002.

[157] C. M. Pooley and K. Fyrtado, Eliminating spurious velocities in the free-energy lattice Boltzmann method, *Phys. Review E*, 77(4):046702-9, 2008.

[158] S. Popinet and S. Zaleski. A front-tracking algorithm for the accurate representation of surface tension, *Int. J. Numer. Meth. Fluids*, 30:775-793, 1998.

[159] V. Pot and A. Genty. Sorbing and Non-Sorbing Solute Migration in Rough Fractures with a Multi-Species LGA Model: Dispersion Dependence on Retardation and Roughness, *Transp.Porous Media*, 59:175-196, 2005.

[160] V. Pot and A. Genty. Dispersion Dependence on retardation in a real fracture geometry using lattice-gas cellular automaton, *Adv. Water Res.*, 30:273-283, 2007.

[161] Y. Qian, D. d'Humières, and P. Lallemand. Lattice BGK models for Navier-Stokes equation. *Europhys. Lett.*, 17:479–484, 1992.

[162] Y.-H. Qian. Fractional propagation and the elimination of staggered invariants in lattice-BGK models. *Int. J. of Modern Physics*, 8:753-761, 1997.

[163] D. Raabe. Overview of the lattice Boltzmann method for nano-and microscale fluid dynamics in matherials science and engineering. *Modeling Simul.Mater.Sci.Eng.*, 12:R13-R46, 2004.

[164] T. Reis and T. N. Phillips. Alternative approach to the solution of the dispersion relation for a generalized lattice Boltzmann equation. *Phys. Rev. E.*, 77, 026702-8, 2008.

[165] M. Rheinländer. Stability and multiscale analysis of an advective lattice Boltzmann scheme. *Progress in Computational Fluid Dynamics*, 8(1-4):56-68, 2008.

[166] L. A. Richards, Capillary conduction of liquids through porous mediums, *Physics*, 1 318-333, 1931.

[167] P. J. Ross. Efficient Numerical Methods for Infiltration Using Richard's Equation. *Water Resour.Res.* 26:279–290, 1990.

[168] D. H. Rothman. Cellular-automaton fluids: A model for flow in porous media. *Geophysics*. 53:509-518, 1988.

[169] D. H. Rothmann and S. Zaleski. Lattice Gas Dynamics Automata - Simple Model for Complex Hydrodynamics. Camb. Univ. Press, ISBN: 0-521-55201-X, 1997.

[170] M. Sbragaglia and S. Succi. Analytical calculation of slip flow in lattice Boltzmann models with kinetic boundary conditions. *Phys. Fluids*, 17:093602-1–8, 2005.

[171] R. Scardovelli and S. Zaleski. Direct Numerical Simulation of Free-Surface and Interfacial Flow, *Ann. Rev. Fluid Mech.* 31:567-603, (1999).

[172] K. Schladitz, S. Peters, D. Reinel-Bitzer, A. Wiegmann, and J. Oscher. Design of acoustic trim based on geometric modeling and flow simulation for nonwoven. *Comp. Mat. Sci.*, 38:56–66, 2006.

[173] B. Servan-Camas and F. T. C. Tsai. Lattice Boltzmann method for two relaxation times for advection-diffusion equation: Third order analysis and stability analysis. Adw. Water. Res., 31:1113-1126, 2008.

[174] X. Shan and H. Chen. Lattice Boltzmann model for simulating flows with multiple phases and components. *Phys. Rev. E*, 47:1815-1819, 1993.

[175] X. Shan and G. D. Doolen. Multi-component lattice-Boltzmann model with interparticle interaction, *J. Stat. Phys.*, 81(1/2):379–393, 1995.

[176] X. Shan and G. Doolen. Diffusion in a multicomponent lattice Boltzmann equation model. *Phys. Rev. E*, 54:3614–3620, 1996.

[177] D. Short, W. R. Dawes, and I. White. The practicability of using Richard's equation for general purpose soil water dynamics models, *Environment International*, 21(5):723-730, 1995.

[178] P. A. Skordos. Initial and boundary conditions for the Lattice Boltzmann method. *Phys. Rev. E*, 48:4823–4842, 1993.

[179] R. G. M. Van der Sman and M. H. Ernst. Diffusion lattice Boltzmann scheme on an orthorhombic lattice. *J. Stat. Phys.*, 94 (1/2):203–217, 1999.

[180] R. G. M. Van der Sman and M. H. Ernst. Advection-diffusion lattice Boltzmann scheme for irregular lattices. *J. Comput. Phys.* 160(2):766–782, 2000.

[181] V. Sofonea and R. F. Sekerka. Boundary conditions for the upwind finite difference Lattice Boltzmann model: Evidence of slip velocity in micro-channel flow. *J. Comp. Phys.*, 207:639–659, 2005.

[182] M. Spaid and F. Phelan. Lattice Boltzmann method for modeling microscale flow in fibrous porous media. *Phys. Fluids*, 9(9):2468-74, 1997.

[183] M. Stiebler, J. Tölke, and M.Krafczyk. An upwind discretization scheme for the finite volume lattice Boltzmann method. *Computers and Fluids*, 35(8/9):814-820, 2005.

[184] M. Stiebler, J. Tölke, and M. Krafczyk. Advection-diffusion lattice Boltzmann schemes for hierarchical grids. *Computers and Mathematics with Applications*, 55:1576-1584, 2008.

[185] J. C. Strikwerda. Finite Difference schemes and Partial Differential Equations. Pacific Grove, Wadsworth & Brooks Cole. 1989.

[186] S. Succi, E. Foti, and F. Higuera. 3-Dimensional flows in complex geometries with the lattice Boltzmann method, *Europhys. Lett.*, 10:433, 1989.

[187] S. Succi, The lattice Boltzmann equation for fluid dynamics and beyond. Numerical mathematics and scientific computation. Oxford Universiy Press, Oxford 2001.

[188] S. Suga. Numerical schemes obtained from Lattice Boltzmann equations for advection diffusion equations. *Int. J. Modern Physics C*, 17(11):1653-1577, 2006.

[189] M. C. Sukop and D. T. Thorne, Jr. Lattice Boltzmann Modeling. An Introduction for Geoscientists and Engineers Springer-Verlag Berlin Heidelber, 2006.

[190] M. R. Swift, E. Orlandini, W. R. Osborn, and J. M. Yeomans. Lattice Boltzmann simulation of liquid-gas and binary fluid systems. *Phys. Review E*, 54:5041–5052, 1996.

[191] L. Szalmas. Lattice Boltzmann method with optimized boundary layer at finite knudsen numbers. *Int. J. of Modern Physics C.*, 19(2):249-257, 2008.

[192] A. Tichonov and A. Samarsky. *Equations of mathematical physics.* Moscow. Nauka. 1977.

[193] M. Thies. Lattice Boltzmann Modeling with Free Surfaces Applied to Insitu Gas Generated foam Formation, PhD-Thesis, Erlangen, Germany, 2005.

[194] J. W. Thomas. Numerical Partial Differential equations. Finite Difference Methods. Berlin, Springer-Verlag, 1995.

[195] G. Thömmes, J. Becker, M. Junk, A. K. Vaikuntam, D. Kehrwald, A. Klar, K. Steiner, and A.Wiegmann. A Lattice Boltzmann Method for immiscible multiphase flow simulations using the Level set Method. Berichte des Fraunhofer ITWM, N. 134, 2008.

[196] N. Thürey. A single-phase free-surface Lattice Boltzmann method, Friedrich-Alexander-Universtität Erlangen-Nürnberg, Diplomarbeit, 2002.

[197] N. Thürey and U. Rüde. Stable free surface flows with the lattice Boltzmann method on adaptively coarsened grids *Computing and Vizualization in science*, DOI:10.107/S00791-008-0090-4.

[198] J. Tölke. Gitter-Boltzmann-Verfaren zur Simulation von Zweiphasenströmungen, PhD Thesis, TU München, 2001.

[199] J. Tölke, M. Krafczyk, M. Schulz, and E. Rank. Lattice Boltzmann simulations of binary fluid flow through porous media, *Phil. Trans. R. Soc. Lond. A*, 360:535–545, 2002.

[200] J. Tölke, S. Freudiger, and M. Krafczyk. An adaptive scheme for LBE multiphase flows simulations on hierarchical grids. *Computers and Fluids*, 35(8/9): 820-830, 2006.

[201] M. Th. Van Genuchten. A closed-form equation for predicting the hydraulic conductivity of unsaturated soils. *Soil Sci. Soc. Am. J.*, 44: 892–89, 1980.

[202] M. A. Van der Hoef, R. Beetstra, and J. A. M. Kuipers, Lattice-Boltzmann simulations of low-Reynolds-number flow past mono- and bidisperse arrays of spheres: results for the permeability and drag force. *J. Fluid Mech.*, 528:233–254, 2005.

[203] R. Verberg and A. J. C. Ladd. Simulation of low-Reynolds-number flow via a time-independent lattice-Boltzmann method. *Phys. Rev. E*, 60:3366-3373, 1999.

[204] R. Verberg and A. J. C. Ladd. Lattice-Boltzmann model with sub-grid scale boundary conditions. *Phys. Rev. Lett.*, 84(10):2148-2151, 2000.

[205] T. Vogel, M. Th. van Genuchten, and M. Cislerova. Effect of the shape of the soil hydraulic functions near saturation on variably saturated flow predictions. *Adv. in Water Resour.*, 24:133–144, 2001.

[206] H.-J. Vogel, J. Tölke, V. P. Schulz, M. Krafczyk, and K. Roth. Comparison of Lattice-Boltzmann Model, a Full-Morphology Model, and a Pore Network Model for Determining Capillary Pressure-Saturation Relationships. *Vadoze Zone J.*, 4:380–388, 2005.

[207] K. K. Watson, V. A. Sardana, and G. C. Sander. Comparison of analytical and numerical results for constant flux infiltration. *J. of Hydrology*, 165:101–112, 1995.

[208] J. A.White, R. I.Borja, and J. T. Fredrich. Calculating the effective permeability of sandstone with multiscale lattice Boltzmann/finite element simulations. *Acta Geotechnica*, 1(4):195-209, 2006.

[209] G. A. Williams and C. T. Miller. An evaluation of temporally adaptive transformation approaches for solving Richards' equation. *Adv. Water. Res.*, 22(8):831-840, 1999.

[210] D. Wolf-Gladrow. *Lattice gas cellular automata and lattice Boltzmann models: an introduction.* Springer 2000, Lecture notes in mathematics, 1725, ISBN 3-540-66973-6.

[211] J. R. Womersley. Method for the calculation of velocity, rate of flow and viscous drag in arteries when the pressure gradient is known. *J. Physiol.*, 127:553–563, 1955.

[212] D. Yu, R. Mei, L.-S. Luo, and W. Shyy. Viscous flow computations with the method of lattice Boltzmann equation. *Progress in Aerospace Sciences*, 39:329–367, 2003.

[213] G. Zanetti. Hydrodynamics of lattice-gas automata. *Phys. Rev. A*, 40:1539–1548, 1989.

[214] X. Zhang, A. G. Bengough, L. K. Deeks, J. W. Crawford, and I. M. Young. A lattice BGK model for advection and anisotropic dispersion equation. *Adv. Water Resour.*, 25:1–8, 2002.

[215] X. Zhang, J. W. Crawford, A. G. Bengough, and I. M. Young. On boundary conditions in the lattice Boltzmann model for advection and anisotropic dispersion equation. *Adv. Water Resour.*, 25:601-609, 2002.

[216] X. Zhang, A. G. Bengough, L. K. Deeks, J. W. Crawford, and I. M. Young, A novel three-dimensional lattice Boltzmann model for solute transport in variably saturated porous media, *Water Resour. Res.*, 38:1167–1177, 2002.

[217] J. G. Zhou. Lattice Boltzmann modeling for shallow water flows. ISBN 3-540-40746-4, Springer-Verlag, Berlin Heidelberg, 2004.

[218] D. P. Ziegler. Boundary Conditions for Lattice Boltzmann Simulations. *J. Stat. Phys.*, 71(5/6):1171-1177, 1993.

[219] J. Zhu and B. P. Mohanty. Analytical solutions for steady state vertical infiltration. *Water Resour. Res.*, 38:1145–1149, 2002.

[220] Q. Zou and X. He. On pressure and velocity boundary conditions for the lattice Boltzmann BGK model. *Phys. Fluids*, 9:1591–1598, 1997.

7.2 Errata

Several important type errors in published author's papers have been detected during the work on this thesis. They are listed bellow.

- Paper [67]: Fig.3-Fig.7: ν^{exp} should be multiplied by 10^{-3}. Fig. 16 should read: $\nu^{exp} = 9.42 \times 10^{-7}\ m^2/s$.
- Paper [66]: Replace in relations (B.4)-(B.6): $\lambda_\nu \rightarrow -\lambda_\nu$ (using notations there, the eigenvalues are positive).
- Paper [68]:
  1. The length scale is defined as $\mathcal{L} = L/L'$ (physics/LBE). In fact, the data in examples for $\mathcal{L}$ corresponds to $1/\mathcal{L}$.
  2. Replace in relation (28): $\tilde{\mathcal{K}}_s \rightarrow \tilde{K}_s = \frac{K_s}{(\theta_s - \theta_r)}$
  3. Replace "lower portion of Lambert function" $\rightarrow$ "upper portion of Lambert function."
- Paper [73]: Relations (48), (49) should change sign.
- Paper [75]: Table 2, change sign for MR(k): $-\alpha^{(u)}\Lambda^-(m_q^{(F)} - F_q^\star) \rightarrow \alpha^{(u)}\Lambda^-(m_q^{(F)} - F_q^\star)$.
- Paper [76]:
  1. Appendix B: $\{\varepsilon_0^\star = -4\ ,\ \varepsilon_I^\star = 2\ ,\ \varepsilon_{II}^\star = -1\}$ for $d2Q9$ should be replaced $\{\varepsilon_0^\star = 4\ ,\ \varepsilon_I^\star = -2\ ,\ \varepsilon_{II}^\star = 1\}$ for solution (B.13).
  2. Relation (B5), change sign for both terms for solution (B.6). They should read: $E_q^{(u)}(\vec{j}, \tilde{\rho}, \alpha_{\varepsilon^\star}) = \frac{j_{x'}^2}{2\tilde{\rho}} w_q\ ,\ w_q = -(2\alpha_{\varepsilon^\star}\varepsilon_q^\star + t_q^\star(1 - 3c_{q\,x'}^2))$
  3. Change in relation (B9): $-3 \rightarrow 6$, then in relation (B.12): $-9 \rightarrow 18$.